STRUCTURAL AND FUNCTIONAL STUDY OF HUMAN MXA PROTEIN

Dissertation zur Erlangung des akademischen Grades des Doktors der Naturwissenschaften (Dr. rer. nat.)

eingereicht im Fachbereich Biologie, Chemie, Pharmazie der Freien Universität Berlin

vorgelegt von

SONG GAO 高 嵩

aus Wuhan, China

Februar, 2011

Die vorliegende Arbeit wurde von September 2007 bis Februar 2011 am

Max-Delbrück-Centrum für Molekulare Medizin

unter der Anleitung von

Prof. Dr. Oliver Daumke

angefertigt.

1. Gutachter: Prof. Dr. Udo Heinemann

2. Gutachter: Prof. Dr. Oliver Daumke

Disputation am Mai 24, 2011

CONTENT

1 ABSTRACT

The interferon-inducible Mx proteins are key mediators of innate immunity against life-threatening pathogens such as influenza viruses. It belongs to the dynamin superfamily of large GTPases which are known to have an essential role in membrane remodeling activities in cells. It has been proposed that the middle domain (MD) and GTPase effector domain (GED) of dynamin-like GTPases constitute a stalk which mediates oligomerization and transmits conformational changes from the guanine-nucleotide-binding (G) domain to the target structure, but the molecular architecture of this stalk was not known. Therefore, the functional mechanism of Mx proteins as well as the whole dynamin superfamily remains an open question.

The aim of my PhD project was the structure characterization of MxA protein and to contribute to the understanding of the mechanism of Mx proteins and dynamin superfamily by structure-based functional studies.

In this thesis, the crystal structure of the stalk of human MxA (hsMxA) is reported. It folds into a four-helical bundle and tightly oligomerizes in the crystal in a criss-cross pattern involving three distinct interfaces and one loop. Mutations in each of these interaction sites interfered with native assembly, oligomerization, membrane binding and antiviral activity of hsMxA. Based on these results, structural models were proposed for oligomerization and stimulated GTP hydrolysis of Mx protein and dynamins that are consistent with previous structural predictions and have functional implications for all members of the dynamin family. Accompanying the stalk structure is a crystal structure of full-length hsMxA in the nucleotide-free form which shows a three-domain architecture composed of the G domain, the stalk and the bundle signaling element (BSE). The full-length hsMxA oligomerizes in the crystal as the isolated stalk. The studies on the interactions between different domains elicit a hypothesis of the functional mechanism of Mx proteins and the dynamin superfamily.

2 INTRODUCTION

This thesis focuses on the Myxovirus resistance (Mx) proteins. Functionally, they are found in higher eukaryotes and their expression is triggered by interferons (IFNs) to act against a wide range of viruses, including influenza A virus (FLUAV). Structurally, they belong to dynamin superfamily of large GTPases that carry out their function by assembly on templates inducing GTP hydrolysis. Hence, the interferon system, influenza A virus and the dynamin superfamily will be discussed in the introduction as important background information.

2.1 Interferons

2.1.1 Classification of interferons

The immune system protects the organism from diseases by identifying and killing pathogens or tumor cells. Pathogens that can be detected range from viruses to mulicellular parasitic worms. According to the functional mechanism and effects, immunity can be classified into two types, innate immunity and adaptive immunity (Janeway, Travers et al. 2005). The innate immunity provides non-specific defenses against pathogenic challenges but does not confer long-lasting effects to these protections, while adaptive immunity, activated by the innate immune system, generates highly specialized cells and systematic processes that eliminate invading pathogens and acts in a retentive manner (Janeway, Travers et al. 2005). Recently a third form of immunity was discovered and termed 'intrinsic immunity'. It is characterized by constant expression of genetically coded proteins specifically targeted against eukaryotic retroviruses (Sheehy, Gaddis et al. 2002; Bieniasz 2004).

A major function of the vertebrate innate immune system is the recruitment of certain immune cells to infection sites through a special type of small protein called cytokines, which act as the signaling mediator between the cells (Janeway, Travers et al. 2005). Among the cytokines, interferons (IFNs) are the earliest discovered examples and represent a large family of protein carrying strong antiviral functions (Isaacs and Lindenmann 1957; Pestka, Krause et al. 2004; Platanias 2005). The IFN family is mainly comprised of two types of related cytokines: Type I IFNs and Type II IFN (Pestka, Langer et al. 1987). The Type I group consists of 7 classes, IFN-α, IFN-β, IFN-

ε, IFN-κ, IFN-ω, IFN-δ, and IFN-τ. IFN-α has 13 subspecies and other IFNs only have one (Pestka 1997; LaFleur, Nardelli et al. 2001; Conklin, Grant et al. 2002). IFN-α, IFN-β, IFN-ε, IFN-κ and IFN-ω are found in humans whereas IFN-δ and IFN-τ are described only in pigs and cattle, respectively (Platanias 2005). Type II IFN contains only IFN-γ. Type I and Type II IFNs are structurally distinct: they bind different receptors (see 2.1.4) and are encoded by separate chromosomal loci. Genes encoding Type I IFNs are clustered on human chromosome 9 and Type II IFN gene is located on chromosome 12 in humans (Pestka, Krause et al. 2004). In recent years, another class of IFN-like molecules have been discovered and named IFN-λ1, IFN-λ2 and IFN-λ3 (also known as interleukin (IL)-29, IL28A and IL28B) (Kotenko, Gallagher et al. 2003; Sheppard, Kindsvogel et al. 2003). Genes encoding IFN-λs are clustered on human chromosome 19 (Kotenko, Gallagher et al. 2003). IFN-λs have a similar but independent functional mechanism from Type I IFNs and are sometimes referred as Type III interferons (Kotenko, Gallagher et al. 2003; Sheppard, Kindsvogel et al. 2003; Haller, Kochs et al. 2007). In the IFN family, IFN-α, IFN-β and IFN-γ are currently the most important and well-characterized members. IFN-α, IFN-β and IFN-λ are the mediators for the expression of Mx proteins. Therefore these IFNs will be stressed accordingly in the following parts.

2.1.2 Overview of interferon functions

Type I IFNs are expressed at a low level in almost all cell types, although hematopoietic cells are the main producers of IFN-α while IFN-β is mostly secreted in fibroblasts (IFN-α and IFN-β were therefore originally termed leukocyte and fibroblast IFN, respectively) (Bach, Aguet et al. 1997). Generally speaking, viruses or double-stranded (ds) RNA can induce human cells to produce IFN-α and IFN-β, and the ratio of the expressed IFNs varies by the organism, tissue, and viral species. IFN-α and IFN-β are mainly involved in innate immune response against viral infection. Some IFN-α species also exhibit other functions such as antiproliferation and stimulation of cytotoxic activities of natural killer (NK) cells and T cells and up-regulation of major histocompatibility complex (MHC) class I antigen expression in cells (Ortaldo, Herberman et al. 1984; Kotenko, Gallagher et al. 2003; Pestka, Krause et al. 2004).

Major production of IFN-γ takes place in CD4+ T helper cell type 1 (T_h1) lymphocytes and CD8+ cytotoxic lymphocytes when these cells are stimulated with specific antigens or mitogens such as staphylocolccal enterotoxin A or B, during the adaptive

immune response (Young 1996; Bach, Aguet et al. 1997). IFN-γ is also secreted by NK cells, B cells, NKT cells and possibly professional antigen-presenting cells (APCs) (Schroder, Hertzog et al. 2004). The most distinguishing feature of IFN-γ from other IFNs is its versatile immunomodulatory activity, although IFN-γ is also involved in the immediate cellular response to viral infections. This activity directly affect Th1-type response development, B cell promotion and local leukocyte endothelial interactions (Huang, Hendriks et al. 1993). Other important functions of IFN-γ include macrophage stimulation, NK cell promotion and up-regulation of the Class I & II antigen presentation pathway in normal cells (Wallach, Fellous et al. 1982; Mach, Steimle et al. 1996; Boehm, Klamp et al. 1997).

As a relatively new member of the IFN family, IFN-λ has not yet been intensively studied yet. It is usually co-expressed with type I IFNs by virus infected cells and has antiviral activity against certain viruses that may or may not be suppressed by Type I IFNs, but in a similar way as Type I IFNs (Sheppard, Kindsvogel et al. 2003; Pestka, Krause et al. 2004; Robek, Boyd et al. 2005; Ank, West et al. 2006). It also can up-regulate MHC class I antigen expression in the cells (Kotenko, Gallagher et al. 2003). Besides, IFN-λ may have a limited antiproliferative activity (Maher, Sheikh et al. 2008).

2.1.3 Induction of interferon expression

The induction of IFN expression is regulated at the transcriptional level. For type I IFNs, the best understood example for regulation is IFN-β (Fig. 1). The IFN-β gene (*IFNB*) promoter can interact with several transcription factors that cooperatively enhance the *IFNB* transcription level (Haller, Kochs et al. 2007). Of these transcription factors, interferon regulatory factor 3 (IRF-3) is thought to play the central role (Hiscott 2007). Phosphorylation is required for IRF-3 activation. On the other hand, the initial antigenic substances that are recognized in the innate immune response and collectively termed pathogen-associated molecular patterns (PAMPs) are detected by so-called pattern recognition receptors (PRRs) at the first step. As briefly mentioned before, the PAMPs for type I IFNs are mainly viral specific dsRNA and 5' triphosphorylated single-stranded RNA (ssRNA). They can be captured by the RNA helicase RIG-I and MDA5, the PRRs responsible for type I IFN induction, in the cytoplasm of infected cells (Yoneyama, Kikuchi et al. 2004; Kato, Takeuchi et al. 2006). RIG-I and MDA5 can activate an adaptor called IFN-β promoter stimulator 1 (IPS-1) which subsequently activates IKK-like kinases IKKε and TBK-1 (Kawai,

Takahashi et al. 2005). Further, some Toll-like receptors which are membrane PRRs can also sense certain PAMPs and activate these IKK-like kinases (Beutler 2004; Uematsu and Akira 2007).

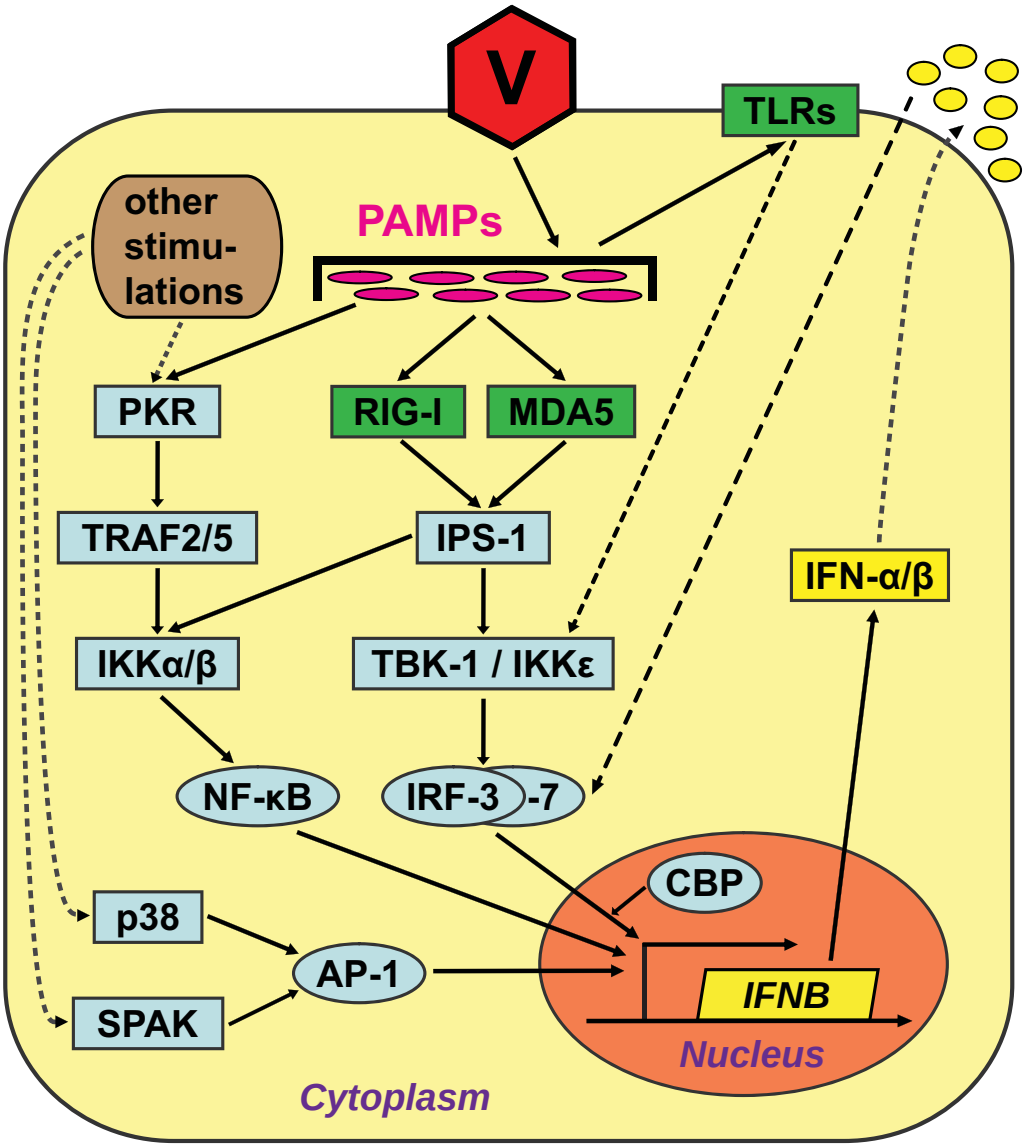

Figure 1. Type I IFN induction. Viral PAMPs (magenta) are recognized by PRRs (green) and lead to the activation of IRF3 and NF-κB. NF-κB and AP-1 can also be induced by other non-PAMP related stimulation. NF-κB is activated via the PKR pathway as well as by IPS-1. IRF-7 is predominantly induced by IFNs and later enhances IFN gene transcription as a positive feedback. Figure modified from Haller, Kochs et al. 2007.

IKKε and TBK-1 have been both demonstrated to phosphorylate IRF-3. Phosphorylated IRF-3 subsequently dimerizes and translocates into the nucleus to cooperate with the transcriptional activator CREB-binding protein (CBP) and initiate *IFNB* transcription. Another IRF family member, IRF-7, is also an important enhancer which is favored by the majority of INF-α promoters and is absolutely essential for

INF-α expression. Unlike the constitutive expression of IRF-3, IRF-7 gene is INF inducible (Honda, Yanai et al. 2005). Therefore, *IFNB* is transcribed in the early response, whereas INF-α species are expressed in relatively higher amounts but with delayed kinetics (Marie, Durbin et al. 1998; Honda, Yanai et al. 2005). Two essential partners of IRFs, nuclear factor κB (NF-κB) and activated protein-1 (AP-1, ATF-2/cJun particularly), are promoted as a more general stress response. They work together to enhance *IFNB* transcription (Fig. 1) (Haller, Kochs et al. 2007).

Induction of IFN-γ expression appears to be more complex, as different pathways are found in distinct cell types. On the cellular level, IFN-γ production can be stimulated by cytokines secreted by APCs, mostly IL-12 and IL18, and negatively regulated by IL-4, IL-10, transforming growth factor-β (TGF-β) and glucocorticoid (Munder, Mallo et al. 1998; Fukao, Matsuda et al. 2000; Golab, Zagozdzon et al. 2000; Fukao, Frucht et al. 2001; Schindler, Lutz et al. 2001; Sen 2001). On the genetic level, transcription factors such as YY1, nuclear factor of activated T cells (NFAT), AP-1, NF-κB and signal transducer and activator of transcription proteins (STATs) are found to bind the IFN-γ gene (*IFNG*) promoter regions (Cippitelli, Sica et al. 1995; Xu, Sun et al. 1996; Ye, Cippitelli et al. 1996; Sica, Dorman et al. 1997; Sweetser, Hoey et al. 1998; Kiani, Garcia-Cozar et al. 2001). Some other transcriptional factors like high mobility group A1 (HMGA1) and T-bet, a key lineage commitment factor in T_h1 cell differentiation, are also demonstrated to be involved in the regulation of *IFNG* expression (Szabo, Kim et al. 2000; Afkarian, Sedy et al. 2002; Chau, Keane-Myers et al. 2005). Like type I IFNs, positive feedback effect also exists as an important up-regulatory means in IFN-γ induction (Schroder, Hertzog et al. 2004).

The induction of IFN-λ expression is overall similar to that of Type I IFNs. IFN-λ gene transcription is also controlled by the IRF and NF-κB pathways when viral or other PAMPs are present (Onoguchi, Yoneyama et al. 2007). It has also been shown that IFN-λ1 induction is largely dependent on IRF-3 as with *IFNB*, whereas IFN-λ2/3 expression mainly relies on IRF-7 as in the case of INF-α. Moreover, IFN-λ2/3 has delayed kinetics in comparison to IFN-λ1 in the immune response, which is analogous to the later response of INF-α compared to INF-β (Osterlund, Pietila et al. 2007). Despite these similarities, however, the induction of IFN-λs has also been reported to possess substantial differences from that of Type I INFs. Firstly, IFN-λs and Type I IFNs are not always expressed in the same cell types. Exceptions are found in macrophages which express Type I IFNs but not IFN-λ1 in response to influenza A

virus, while under the same conditions, type II epithelial cells produce IFN-λ1 but not IFN-β (Wang, Oberley-Deegan et al. 2009). Secondly, distinct from the cooperative manner of transcription factors in the Type I IFN promoter activation, IRF and NF-κB regulate IFN-λ1 induction independently, as the binding sites for IRF and NF-κB have been found spatially separated on the IFN-λ1 gene promoter (Thomson, Goh et al. 2009). In addition, NF-κB seems to be the key controller of IFN-λ production, rather than IRFs that play dominant role in IFN-α/β expression (Iversen, Ank et al. 2010).

2.1.4 Interferon-induced signaling pathways

In the immune response, secreted IFNs are sensed by certain membrane-inserted receptors and initiate the corresponding signal transduction pathways that result in the expression of numerous IFN-stimulating genes (ISGs). Type I, II and III IFNs bind to distinct membrane associated receptor complexes. Each one of the receptor chains interacts with a member of the Janus activated kinase (Jak) family (Darnell, Kerr et al. 1994; Ihle 1995). The Jak-STAT pathway is the first signaling pathway shown to be activated by IFNs (Fu, Schindler et al. 1992; Schindler, Shuai et al. 1992; Shuai, Schindler et al. 1992; Silvennoinen, Ihle et al. 1993). The models of the IFN-mediated signaling mechanism via this pathway have been well established since then, and are summarized below.

In the case of Type I IFNs, the receptor is composed of two subunits, IFN-αR1 and IFN-αR2 (Uze, Lutfalla et al. 1990). IFN-αR1 and IFN-αR2 are constitutively associated with tyrosine kinase 2 (Tyk2) and Jak1, respectively (Fig. 2). When a monomeric Type I IFN is bound (Pestka, Kelder et al. 1983), the receptor chains undergo a structural rearrangement and their associated Jaks are rapidly auto-phosphorylated (Silvennoinen, Ihle et al. 1993). In a major pathway for Type I IFNs, activated receptor complexes subsequently regulate the phosphorylation of STAT1 and STAT2. Phosphorylated STAT1 and STAT2 dimerize and recruit a non-phosphorylated factor IRF-9 to form a heterotrimer called ISG factor 3 (ISGF3) (Darnell 1997), which enters the nucleus and binds to IFN-stimulated response elements (ISRE) to initiate the transcription of certain ISGs such as *MX1*, *IRF3* and *OAS1* that possess this promoter (Donnelly and Kotenko 2010). Besides ISGF3, activated Type I IFN receptor is also responsible for the activation and homo- or heterodimer formation of other STATs (Darnell, Kerr et al. 1994; Stark, Kerr et al. 1998). While ISGF3 is the only complex that binds ISRE, these activated STAT dimers bind another type of element known as IFN-γ activated site (GAS) elements and thereby induce the transcription of

GAS-presenting ISGs (Fasler-Kan, Pansky et al. 1998; Matikainen, Sareneva et al. 1999). It has been proposed that different combination of STATs may be induced to target the transcription of specific genes with distinct functions (Platanias 2005).

The functional IFN-γ receptor complex consists of two different chains, IFN-γR1 and IFN-γR2, which tetramerize in a 2:2 stoichiometry (Hemmi, Bohni et al. 1994). Different from Type I IFNs, IFN-γ binds its receptor in a dimeric form and only has direct contact with two IFN-γR1 chains which are assembled with two IFN-γR2 chains prior to IFN-γ-binding (Krause, Mei et al. 2002; Pestka, Krause et al. 2004) (Fig. 2). IFN-γR1 and IFN-γR2 are associated with kinases Jak1 and Jak2, respectively (Schroder, Hertzog et al. 2004).

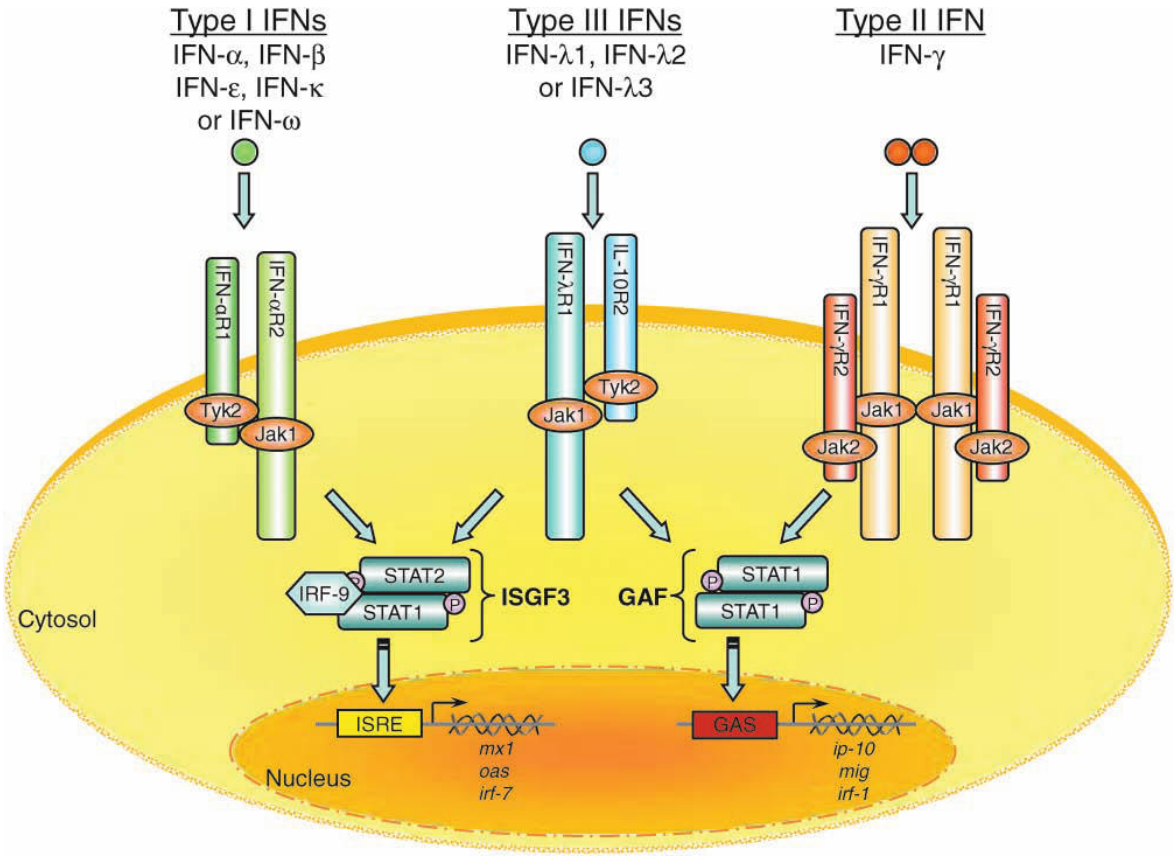

Figure 2. A schematic model of the IFN receptor signaling pathway. GAF: IFN-γ activated factor. Figure excerpted from Donnelly and Kotenko 2010.

Jak1 and Jak2 are activated via cross-phosphorylation upon IFN-γ engagement and, in most cases, subsequently regulate the phosphorylation of STAT1 (Boehm, Klamp et al. 1997; Stark, Kerr et al. 1998; Aaronson and Horvath 2002). Activated STAT1 proteins homodimerize and transloctate into the nucleus to bind GAS elements and initiate the transcription of corresponding ISGs (Fig. 2) (Aaronson and Horvath 2002).

IFN-λ receptor complexes are also composed of two distinct subunits, IFN-λR1 (also known as IL-28 receptor α, IL-28Rα or IL-28RA) and IL-10R2 (or IL-10Rβ), which interact with Jak1 and Tyk2, respectively (Kotenko, Gallagher et al. 2003; Platanias 2005). Upon binding of monomeric IFN-λ, the activated receptor complex induces downstream gene transcription in a similar manner as in the Type I IFN receptor signaling pathway (Fig. 2) (Donnelly and Kotenko 2010).

The classical Jak-STAT pathway has proved to be insufficient for generating all of the diverse biological functions for IFNs. Much evidence has been found that some other signaling elements, such as Crk proteins (Ahmad, Alsayed et al. 1997), mitogen-activated protein kinases (MAPKs) (Uddin, Majchrzak et al. 1999), phosphatidyl-inositol 3-kinase (PI3K) (Uddin, Yenush et al. 1995), and signaling pathways are required for the versatility of IFNs (Platanias 2005). These elements and pathways either cooperate with STATs to contribute to the Jak-STAT pathway or operate independently to regulate the transcription of target ISGs (Platanias 2005).

2.1.5 Structural study of interferons

IFNs are composed of between 160 and 210 amino acid residues. So far, crystal structures of IFN-α, IFN-β, IFN-τ, IFN-γ and IFN-λ as well as the IFN-γ-IFN-γR1 complex have been solved (Pestka, Krause et al. 2004; Gad, Hamming et al. 2010). These IFN structures are very similar in topology, as they all contain 5 α-helices (Fig. 3A-E) and helices A, B, C and E assemble to form a left-handed four-helix bundle, which comprises the core of the single globular domain (except in the case of IFN-γ when not bound to its receptor) (Pestka, Krause et al. 2004). On the other hand, substantial differences, which are predicted to be functionally important, are also evident among the IFNs. A major example is the AB loop which varies significantly even within Type I IFN subfamily. AB loops have been proven to be crucial for IFN-αR1 binding via mutagenesis studies (Pestka, Krause et al. 2004). The crystal structure of the IFN-γ-IFN-γR1 complex also shows that flexible AB loops become ordered when IFN-γ binds to IFN-γR1 (Walter, Windsor et al. 1995). These findings suggest that the structural diversity of AB loops defines the biological differences between IFNs. Other structural differences between IFNs are the number of disulfide bonds, and local variances of certain helices (Pestka, Krause et al. 2004).

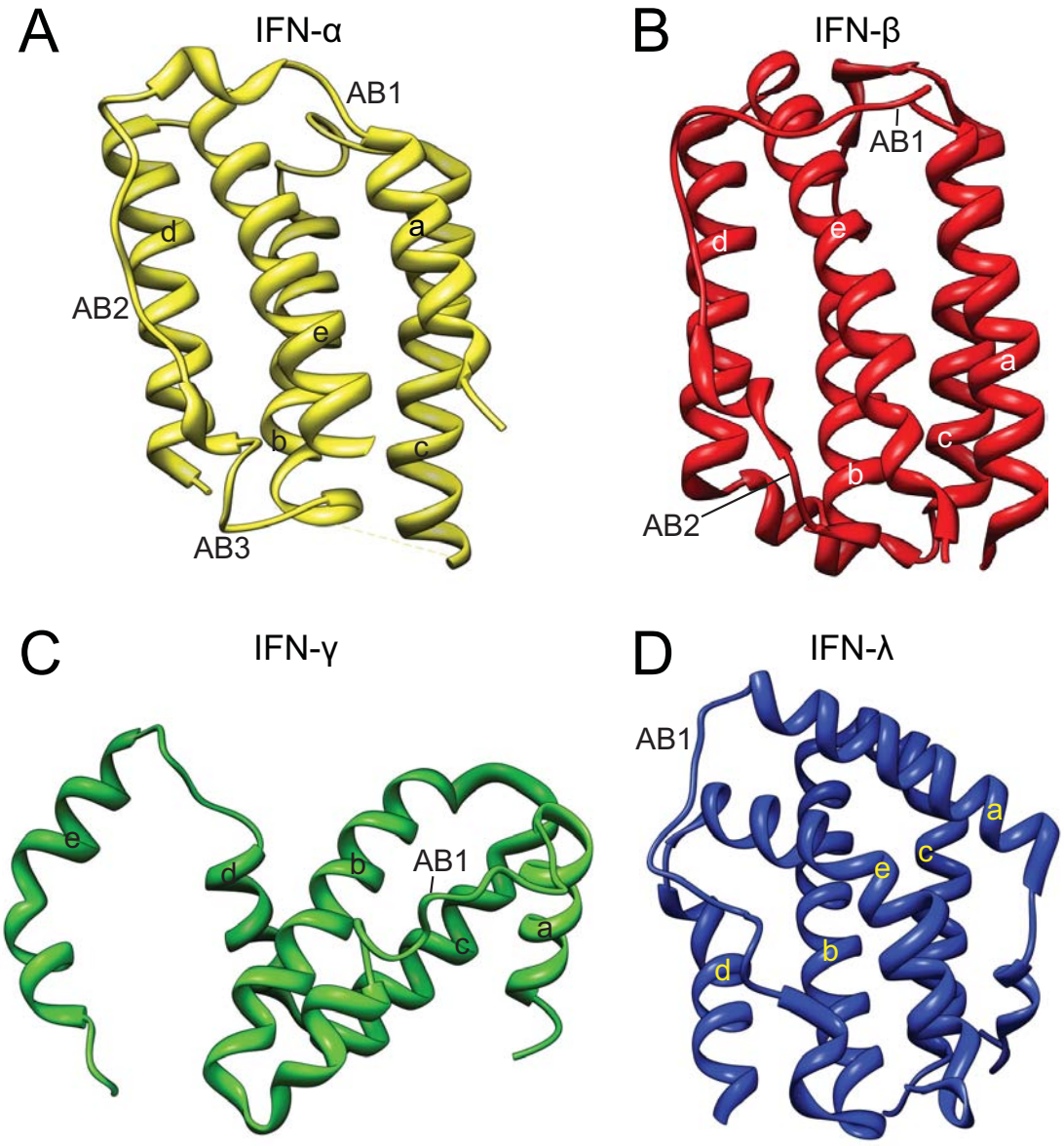

Figure 3. Crystal structures of IFNs, shown in ribbon representation. All the structures in other figures of this thesis are shown in ribbon representation as well, unless specified. A) Human IFN-α2b (protein data bank (PDB) code 1RH2, shown in yellow) (Radhakrishnan, Walter et al. 1996). B) Murine IFN-β (1WU3, shown in red) (Senda, Saitoh et al. 1995). C) Bovine IFN-γ (1RFB, shown in green) (Samudzi and Rubin 1993). D) Human IFN-λ3 (3HHC, shown in blue) (Gad, Dellgren et al. 2009). The five α-helices are labeled a, b, c, d and e from the amino- to carboxyl-terminus of the protein. The loop connecting helices A and B is specified. In some IFNs, parts of the AB loop may form one or two 3^{10} helices. Therefore, the regions of the AB loop separated by 3^{10} helices are named AB1, AB2 and so on, as specified in human IFN-α2b and murine IFN-β.

2.1.6 Clinical application of interferons

Due to their high potential of antiviral and other features, IFNs have been widely applied in therapeutic treatment against relevant diseases for many years. Before the emergence of DNA banks and entire genome sequences, IFN-α was purified to homogeneity for the first time in the late 1970s (Rubinstein, Rubinstein et al. 1978; Rubinstein, Rubinstein et al. 1979) and then became the first approved biotherapeutic. It has been approved for the treatment of chronic hepatitis B (Mazzella, Saracco et al. 1999), hepatitis C (Roffi, Mels et al. 1995; Pianko and McHutchison 2000), several cancers and other diseases (Goldstein and Laszlo 1988). INF-β was purified and sequenced in the early 1980s (Stein, Kenny et al. 1980; Friesen, Stein et al. 1981) and approved for the treatment of genital herpes (Ophir, Brenner et al. 1995) and relapsing-remitting multiple sclerosis (Silberberg 1994; Wingerchuk and Noseworthy 2002). IFN-γ was also used clinically against chronic granulomatous disease (GCD) (Todd and Goa 1992) and osteopetrosis (Key, Ries et al. 1992). Moreover, although not yet approved, IFNs have also been shown to be effective for the treatment of laryngeal papillomatosis (Lundquist, Haglund et al. 1984) and for the prevention of rhinovirus caused common colds (Farr, Gwaltney et al. 1984; Hayden, Albrecht et al. 1986). Recombinant human IFN-ω and bovine IFN-τ have also been used in clinical trials since 1981. Recombinant IFN-λ is now being probed and evaluated initially as a potential therapeutic alternative to IFN-α for hepatitis C (Miller, Klucher et al. 2009; Donnelly and Kotenko 2010). Despite this, the detailed physiological mechanisms underlying many IFN therapeutic activities still remain undefined.

2.2 Influenza A virus

2.2.1 Overview of influenza A virus

Influenza viruses are members of the Orthomyxoviridae family and feature a negative-sense ssRNA genome (Samuel 2010). There are three types of influenza viruses, namely the influenza A, B and C viruses. All three types can infect humans but influenza A virus (FLUAV) is the major threat to public health as it has caused several notorious pandemics in last 100 years, such as the Spanish flu in 1918, Asian flu in 1957, Hong Kong flu in 1968, Russian flu in 1977, as well as the recent swine flu in 2009 (Gamblin and Skehel 2010). In addition to humans, FLUAV can also infect avians and some other mammals.

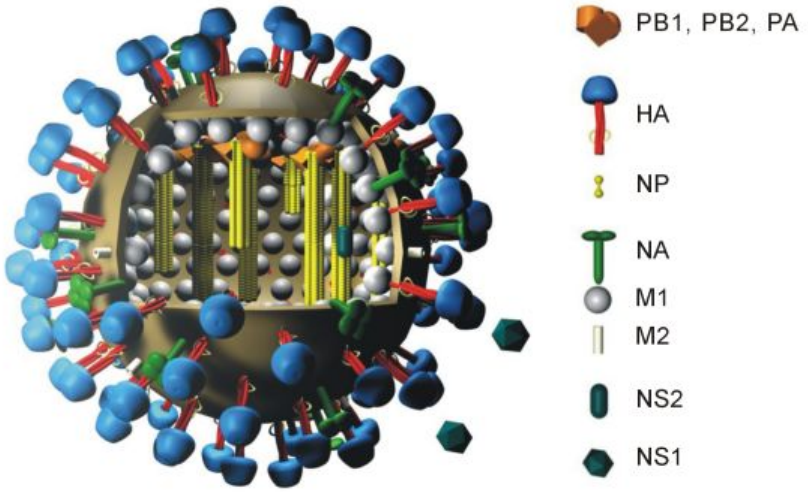

Figure 4. Schematic model of FLUAV, showing the major components of the virus particle. Figure excerpted from Wikipedia Commons (Author: Dr. Markus Eickmann, 2005)

FLUAV genomic RNA is segmented into eight parts encoding 10 major proteins (Fig. 4): hemagglutinin (HA), neuraminidase (NA), nucleoprotein (NP), Matrix protein 1 (M1), M2, NS1, NS2 (also known as nuclear export protein, or NEP), polymerase acidic (PA), polymerase basic 1 (PB1), and PB2 (Ghedin, Sengamalay et al. 2005). HA and NA are surface glycoproteins, both recognizing sialic acid (Klenk, Faillard et al. 1955; Gottschalk 1957). HA binds the sialic acid receptor on the surface of the host cell and thus mediates membrane fusion necessary for the entry of the virus (Skehel and Wiley 2000). NA facilitates the release of mature virions by cleaving the terminal sialic acid residues from glycan structures on the host cell surface (Palese, Tobita et al. 1974; Liu, Eichelberger et al. 1995). There are 16 HA (H1-16) and 9 NA (N1-9) subtypes which are

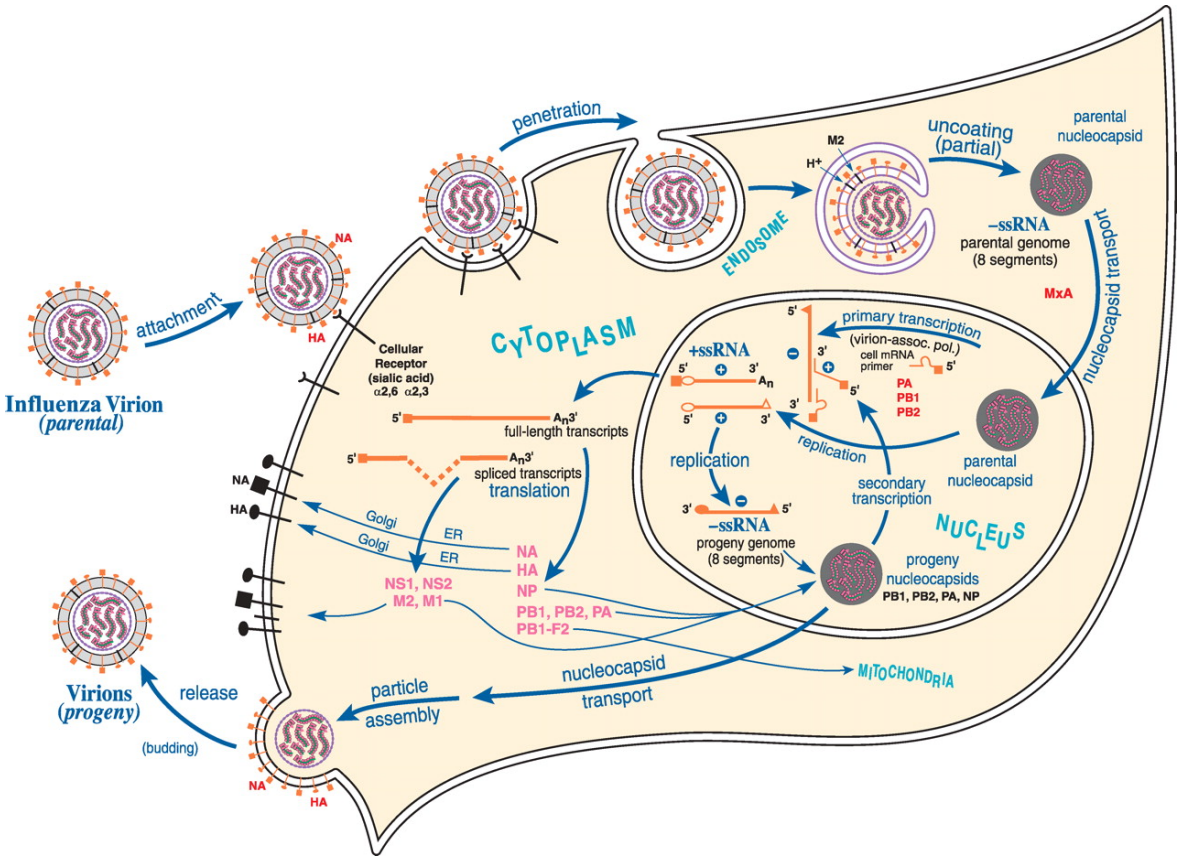

Figure 5. The FLUAV multiplication cycle. MxA protein is also included in the figure as it inhibits FLUAV multiplication. ER: endoplasmic reticulum. Figure adapted from Samuel 2010.

used as antigenic difference for the classification of FLUAV (WHO 1980). FLUAV NPencapsidates the viral genome to form ribonucleoprotein (RNP) particles so that the genome is packed and segmented (Portela and Digard 2002). The M1 protein forms a coat inside the viral envelope and regulates the import of RNPs of the parental virion into and the export of newly assembled viral RNPs from the host cell nucleus (Martin and Helenius 1991; Whittaker, Bui et al. 1996). The M2 protein is a proton channel integral to the viral envelope and mediates the acidification of the viral interior, thereby facilitating the dissociation of M1 protein from the viral NP, which is a crucial step for the unpacking of the viral genome (Schnell and Chou 2008). The NS1 protein regulates the transport of viral mRNA and other poly adenine (poly(A)) containing mRNA from the nucleus and can probably suppress interferon response in infected cells (Alonso-Caplen, Nemeroff et al. 1992; Lu, Wambach et al. 1995). The NS2 protein is responsible for the nuclear export of viral RNPs (O'Neill, Talon et al. 1998; Neumann, Hughes et al. 2000). PA, PB1 and PB2 form a heterotrimeric RNA-dependent RNA polymerase complex. The influenza polymerase catalyzes the replication and transcription of viral RNA in the host cell nucleus with the assistance of viral NP (Newcomb, Kuo et al. 2009; Boivin, Cusack et al. 2010). As the polymerase

lacks the proofreading activity, the nascent viral RNA genome has a high mutation rate, which is essential for the evolutionary strategy of the influenza viruses (Drake 1993).

The life cycle of FLUAV in an infected cell, illustrated in Fig. 5, begins with the binding of the parental virion to host cells via the interaction between viral HA and cellular sialic acid (Wagner, Matrosovich et al. 2002). Subsequent endocytosis takes the viral particles into the cytoplasm where they disassemble to release viral RNA, accessory proteins and RNA polymerase subunits. (Lakadamyali, Rust et al. 2003). These molecules form a complex before being translocated into the nucleus, where the viral positive-sense RNA (cRNA) is transcribed and negative-sense RNA is replicated (Cros and Palese 2003). The synthesized cRNA either stays in the nucleus or is exported to the cytoplasm and translated. The newly-translated viral proteins are (i) imported into the nucleus to form more viral RNPs (NP, PA, PB1 and PB2, etc.), (ii) trafficked through the Golgi apparatus to the cell surface (HA and NA, etc.), or (iii) remaining in the cytoplasm to affect the host cell, for example, by hampering the translation of the host cell mRNA (NS1 and NS2, etc.) (Kash, Goodman et al. 2006). The replicated negative-sense viral RNA genome and other core proteins such as NP and polymerase subunits are reassembled into the progeny nucleocapsids and migrate from the nucleus to the plasma membrane that already contains inserted HA and NA molecules. The nucleocapsids then bud off from the infected cell with a host membrane coat and thereby acquire HA and NA (Nayak, Hui et al. 2004). After the cleavage of sialic acid residues by NA, the mature progeny virions are formed and released from the host cell, which dies after this infection cycle (Wagner, Matrosovich et al. 2002).

2.2.2 Structural studies of influenza virus

The molecular structures of the FLUAV components have elicited broad interest for many years because of the important hints they may provide for the development of anti-influenza drugs. Up to now, full-length or partial structures of FLUAV HA, NA, NP, M1, M2, NS1 and polymerase complex have been solved by X-ray crystallography or NMR. They are summarized in the following paragraphs.

The crystal structure of HA has been solved for several subtypes. In all cases, HA has three individual domains: a receptor binding domain for sialic acid binding, a vestigial esterase domain and a fusion domain (Skehel and Wiley 2000). Functional HA forms a homotrimer and each monomer contains two peptide chains from a necessary

proteolytic cleavage of a single precursor (Fig. 6A, B) (Steinhauer 1999; Gamblin and Skehel 2010). Functional NA is a four-leaf-clover-shaped homotetramer. The monomer is predominantly made of β-strands which are organized in a propeller-shaped structure (Fig. 6C) (Varghese, Laver et al. 1983). The active site for sialic acid binding and hydrolysis sits almost at the center of the 'leaf' (Colman, Varghese et al. 1983). The 'leaves' are attached to the viral membranes via a thin 'stalk' whose length is variable in different viral strains (Gamblin and Skehel 2010).

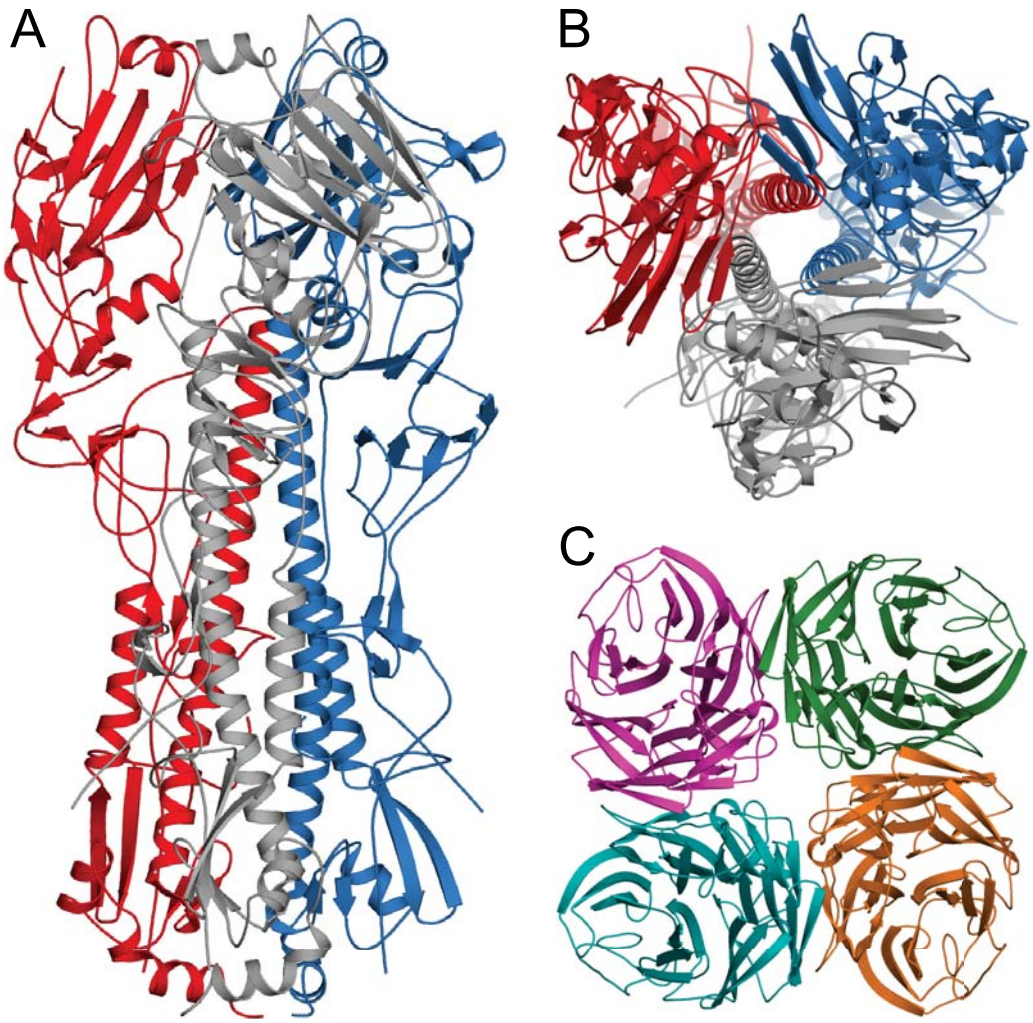

Figure 6. The crystal structures of FLUAV HA and NA. A) Side view of an HA homotrimer from an H3 subtype (PDB code 2VIU) (Fleury, Wharton et al. 1998). The three monomers are colored in red, blue and gray, respectively. B) top view of the same HA trimer. C) top view of an NA homotetramer from an N2 subtype (1NN2) (Varghese and Colman 1991). The four monomers are individually colored in magenta, green, orange and cyan.

The FLUAV NP alone shows a monomer-oligomer equilibrium in solution (Ye, Krug et al. 2006). However, the oligomerization state of NP is largely dependent on the presence of RNA (Ng, Zhang et al. 2008). The two available crystal structures of

FLUAV NP both show that the NP forms a crystallographic trimer (Fig. 7A, B). Each monomer can be divided into a 'head' domain, a 'body' domain and a tail loop by the relative positions (Fig. 7A), while at the cleft formed by the 'head' and 'body' domains a number of positively charged amino-acid residues that may serve as the binding template for viral genome RNA are located (Fig. 7C) (Ye, Krug et al. 2006; Ng, Zhang et al. 2008).

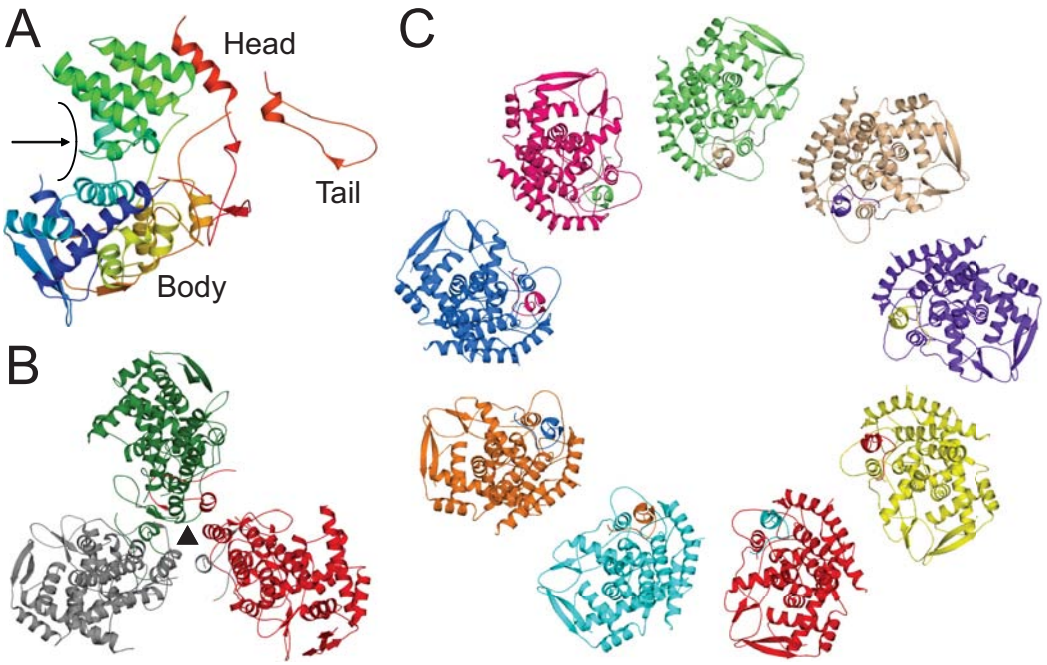

Figure 7. The crystal structures of FLUAV NP and its oligomerization model. A) side view of an NP monomer from avian H5N1 subtype in rainbow colors from N- (purple) to C-terminus (red) (PDB code 2IQH) (Ye, Krug et al. 2006) The 'head' and 'body' domains as well as the tail loop are labeled and the potential RNA binding site is indicated by an arrow. B) top view of a crystallographic trimer of the NP molecule in A. The individually monomers are colored in red, green and gray, and the 3-fold symmetry center is indicated by a black triangle. C) a nonameric model of functional NP based on an electron density map from a cryo-EM reconstruction (2WFS) (Coloma, Valpuesta et al. 2009). Note that all the monomers are interlinked with their neighboring molecules via the tail loop.

The FLUAV M1 is composed of two domains. The C-terminal domain has been shown to mediate the binding of M1 to viral RNPs though its structure still remains unknown (Baudin, Petit et al. 2001). The crystal structure of the M1 N-terminal domain shows an α-helix-dominated dimer in the asymmetric unit of the crystals in both acidic and neutral environments (Fig. 8A) (Sha and Luo 1997; Harris, Forouhar et al. 2001). As one face of the dimer has a large stripe of positive charges, it has been proposed that the M1 dimer may be the building unit that further oligomerizes to elongated helices

or ribbons and thereby forms the layer under the viral membranes (Harris, Forouhar et al. 2001). The M2 proton channel has three domains: an N-terminal domain outside the viral particle, a transmembrane domain and a C-terminal domain inner domain. A crystal structure of the M2 transmembrane domain shows a homotetrameric helical composition (Fig. 8B) (Stouffer, Acharya et al. 2008). The channel is gated by conserved histidine and tryptophan residues, and the drug amantadine is seen to

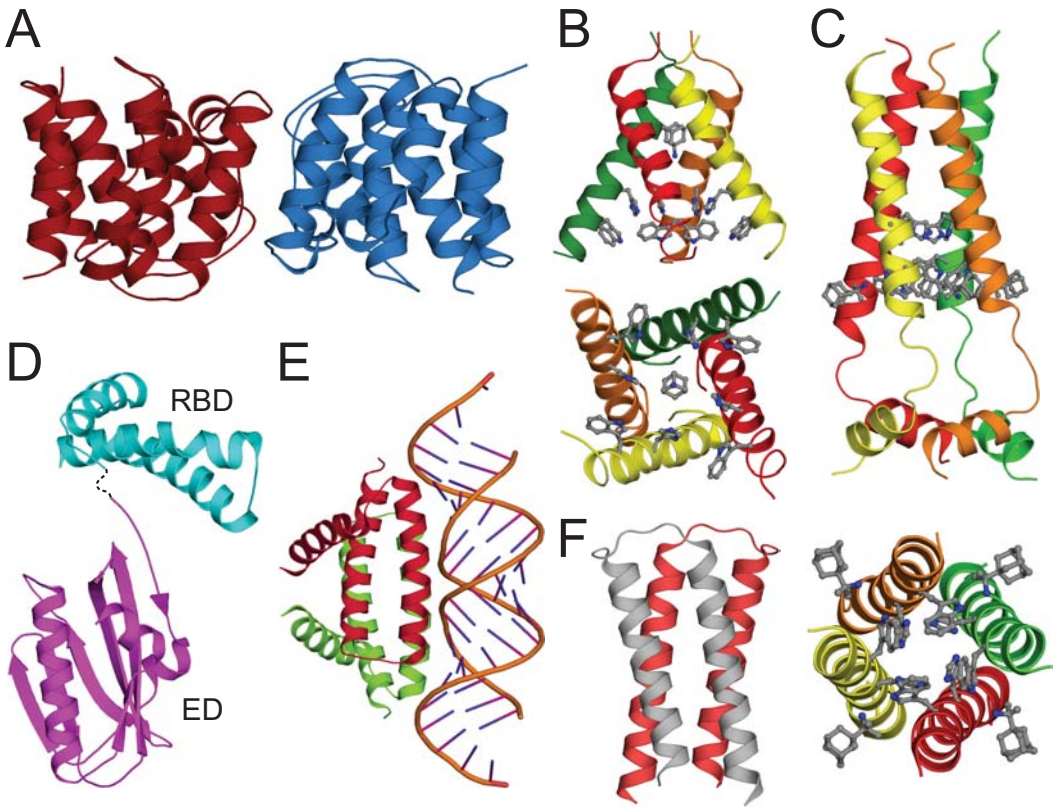

Figure 8. The crystal and NMR structures for FLUAV M1, M2 and NS1. A) Side view from a crystal structure of an M1 N-terminal domain homodimer from an H1N1 subtype (PDB code 1AA7) (Sha and Luo 1997). The two monomers are colored in red and blue. B) Two views of a crystal structure of homotetrameric M2 from an avian H9N2 subtype (3C9J) (Stouffer, Acharya et al. 2008). The individual chains are colored in red, green, orange and yellow. The proton gating residues His37 and Trp41, as well as the inhibitor amantadine are shown as ball-and-stick models. C) Two views of an NMR structure of the M2 tetramer from an H9N2 strain (2RLF) (Schnell and Chou 2008), colored in the same way as in B. His37, Trp41 and the inhibitor rimantadine are shown as ball-and-stick models. The C-terminal segments of M2 are resolved in this structure. Note the different binding position of the inhibitors in B and C. D) The NS1 protein from an H5N1 subtype (3F5T) (Bornholdt and Prasad 2008). The RBD and ED are colored in cyan and magenta, respectively. E) The RBD homodimer of NS1 from an H1N1 subtype complexed with dsRNA (2ZKO) (Cheng, Wong et al. 2009). The two monomers are colored in red and light green, respectively. F) The homodimer of NS2 M1-binding domain from an H1N1 strain (1PD3) (Akarsu, Burmeister et al. 2003). The two monomers are colored in grey and light red, respectively.

block the channel (Fig. 8B). The structure of M2 has also been determined by NMR, where additional portions of the C-terminal domain are resolved and form basement of the tetrameric channel (Fig. 8C) (Schnell and Chou 2008). The channel looks more 'closed' than in the previous structure and a different inhibitor, rimantadine, binds each helix from outside the channel (Fig. 8C). The NS1 protein is composed of an N-terminal RNA binding domain (RBD) for double-stranded RNA binding and an effector domain (ED) that is essential for RBD activity and nuclear export (Wang, Riedel et al. 1999) (Nemeroff, Barabino et al. 1998). Each of the two domains carries a nuclear localization signal (NLS). RBD is a three-helical assembly while ED is made of three helices and seven twisted β-strands (Fig. 8D) (Bornholdt and Prasad 2008). The binding of the dsRNA of NS1 requires the dimerization of RBD, as confirmed in a recently solved crystal structure (Fig. 8E), (Cheng, Wong et al. 2009). For the NS2 protein, only the structure of the M1-binding domain is known, which comprises a helix-turn-helix motif that forms a homodimer primarily via several hydrophobic residues (Fig. 8F). The surface-exposed Trp78 residue has been suggested to be crucial for the binding of the NS2 protein to M1 (Akarsu, Burmeister et al. 2003).

Concerning the FLUAV RNA polymerase complex, no full-length structure for either the entire complex or its subunits has been solved. However, structures of individual domains and complexed subunit fragments have been solved and have provided a considerable amount of information about the architecture and functional mechanism of the complex. The PA subunit contains an N-terminal domain and a C-terminal PB1-binding domain, based on limited proteolysis studies (Guu, Dong et al. 2008). The crystal structure of the N-terminal domain verified the PD-(D/E)*X*K-family-like endonuclease character that was previously thought to be present in the PB1 subunit (Fig. 9A) (Li, Rao et al. 2001; Dias, Bouvier et al. 2009; Yuan, Bartlam et al. 2009). The C-terminal part of PA was shown to bind the N-terminal region of PB1 (Gonzalez, Zurcher et al. 1996). The crystal structures of the PB1-binding domain of PA complexed with a short peptide from the PB1 N-terminus confirmed this result, where the PB1-binding domain resembled the head of a wolf biting the bone-like peptide from PB1 (Fig. 9B) (He, Zhou et al. 2008; Obayashi, Yoshida et al. 2008). The PB1 subunit is predicted to possess a central RNA polymerase domain according to the mapping of several conserved polymerase motifs (Poch, Sauvaget et al. 1989). However, attempts at the expression of crystallizable PB1 full-length or fragmental constructs remain unsuccessful (Boivin, Cusack et al. 2010). Therefore besides the

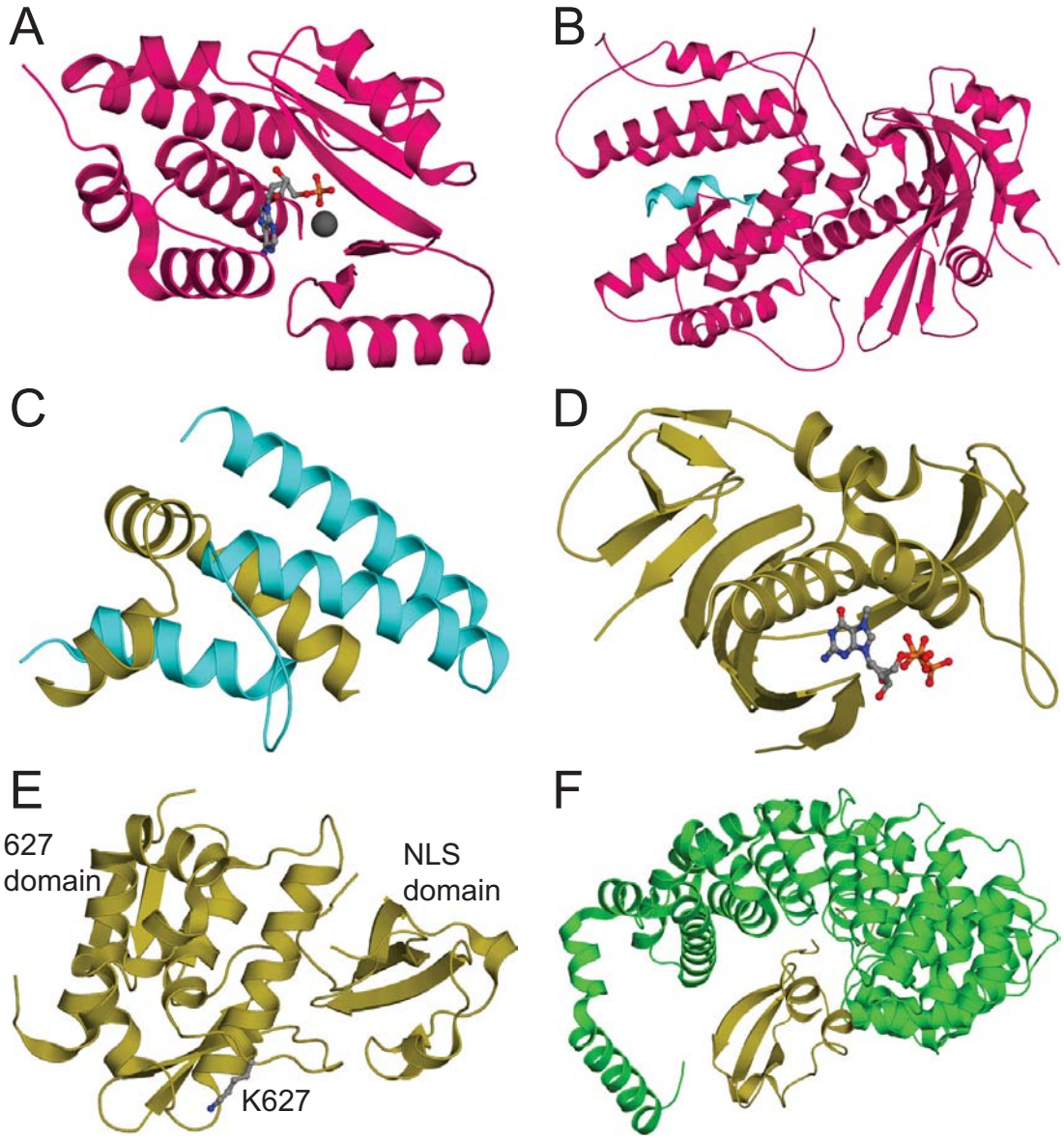

Figure 9. The crystal structures of FLUAV polymerase fragments and complexes. A) The endonuclease domain of PA from an H5N1 subtype, bound with AMP (PDB code 3HW5) (Zhao, Lou et al. 2009). The AMP molecule is shown as a ball-and-stick model and the catalytic Mg^{2+} ion is shown as a gray sphere. B) The PB1 binding domain of PA (colored in pink) complexed with a short peptide at the N-terminus of PB1 (colored in cyan), from an H1N1 subtype (2ZNL) (Obayashi, Yoshida et al. 2008). C) The complex of the interaction regions of PB1-PB2, including the C-terminal fragment of PB1 (colored in cyan) and N-terminal fragment of PB2 (colored in olive), from an H1N1 subtype (3A1G) (Sugiyama, Obayashi et al. 2009). D) The cap-binding domain of PB2 bound with m^7GTP, from an H3N2 subtype (2VQZ) (Guilligay, Tarendeau et al. 2008). The m^7GTP molecule is shown as a ball-and-stick model. E) The 627 domain and the NLS domain of PB2 from an H3N2 subtype (2VY6) (Tarendeau, Crepin et al. 2008). Both domains are indicated and the Lys627 is highlighted as a ball-and-stick model. F) The NLS domain of PB2 from an H3N2 strain in complex with the human importin α-1 subunit (2JDQ) (Tarendeau, Boudet et al. 2007). The NLS domain is colored in olive and the importin α-1 subunit is colored in green.

short N-terminal peptide, the known structural information of PB1 is only its C-terminal region complexed with an N-terminal portion of PB2, where two short fragments both fold into α-helices and tightly associate with each other (Fig. 9C) (Sugiyama, Obayashi et al. 2009). Full-length PB2 is also insoluble, therefore a new library-based construct screening strategy ESPRIT (Yumerefendi, Tarendeau et al. 2010) was used to search for soluble PB2 fragments, which successfully led to a number of domain structures. The central region of PB2 was found to have a cap binding function (Ulmanen, Broni et al. 1981; Blaas, Patzelt et al. 1982). The crystal structure of this region bound with m^7GTP confirmed that it is indeed a cap binding domain with a novel fold (Fig. 9D) (Guilligay, Tarendeau et al. 2008). The C-terminal portion of PB2 is responsible for host interaction and forms a well-folded structure composed of two domains: the 627 domain and the NLS domain (Fig. 9E) (Tarendeau, Crepin et al. 2008). The 627 domain was named after its residue Lys627, which was suggested to be the determinant point for host adaption (Tarendeau, Crepin et al. 2008). The very C-terminal NLS domain interacts with host import factors and thus mediates the adaption, as shown by crystal and NMR structures (Fig. 9F) (Tarendeau, Boudet et al. 2007).

2.3 Dynamin superfamily

2.3.1 Overview of the dynamin superfamily

The dynamin superfamily comprises a class of guanine-nucleotide-binding (G) proteins, or GTPases (hydrolases that catalyze the hydrolysis of guanosine triphosphate (GTP) to guanosine diphosphate (GDP) and phosphate), which have essential functions in cellular processes relying on membrane remodeling (Praefcke and McMahon 2004). In addition to classical dynamins, an increasing number of dynamin-related proteins have been assigned to this superfamily (Fig. 10), such as the Mx proteins (Haller, Stertz et al. 2007), the GBP/atlastin family (Prakash, Renault et al. 2000), the bacterial dynamin-like proteins (BDLPs) (Low and Lowe 2006) and the EHD ATPases (Daumke, Lundmark et al. 2007). All members share common biochemical properties and have (i) low binding affinity to nucleotides, (ii) the propensity to self-assemble and oligomerize around lipid templates and (iii) increased nucleotide hydrolysis rates promoted by oligomerization. Because of these features, the dynamin superfamily of large GTPases are distinguished from the small Ras-like and other regulatory GTPases, such as the α-subunits of heterotrimeric G-proteins and the translation factors in protein synthesis (Bourne, Sanders et al. 1991; Schweins and Wittinghofer 1994; Wittinghofer 1996; Wittinghofer 1998; Praefcke and McMahon 2004).

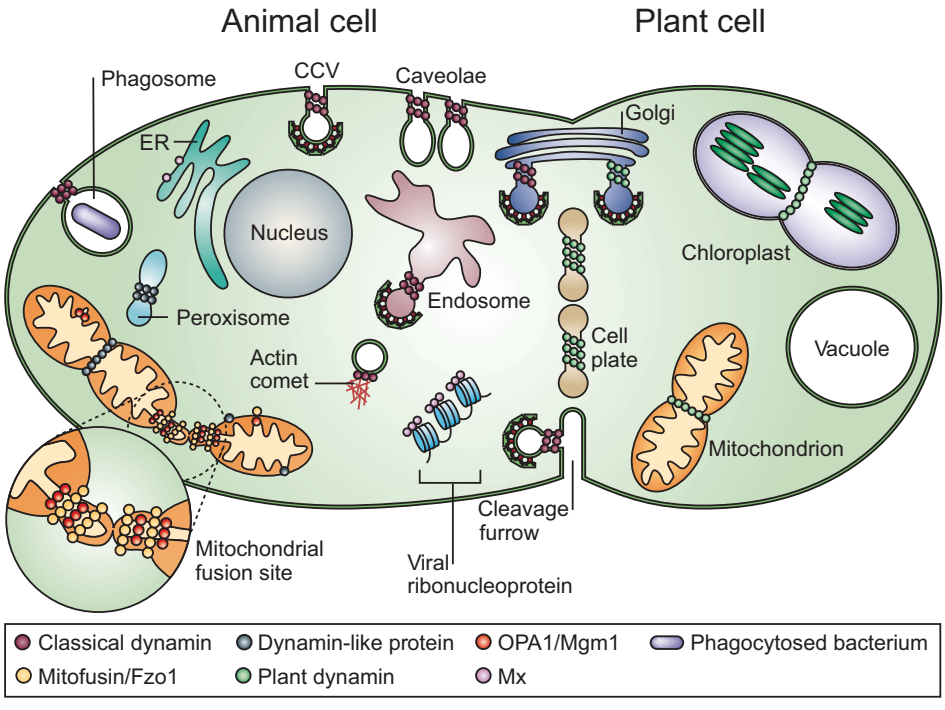

Figure 10. Dynamin superfamily members and their cellular localizations. Figure modified from Praefcke and McMahon 2004.

These distinct biochemical features of dynamin superfamily members can be explained by their special multi-domain architecture. Apart from a large N-terminal GTPase (G) domain containing around 300 amino acid residues, the members usually also have two additional domains: the so-called middle domain (MD) and the GTPase effector domain (GED) that were thought be crucial to the oligomerization and GTPase activity stimulation at least in some members, such as dynamins and Mx proteins (Fig. 11) (Sever, Muhlberg et al. 1999; Janzen, Kochs et al. 2000; Marks, Stowell et al. 2001; Ramachandran, Surka et al. 2007). Further, different members in the superfamily also carry other extra domains individually for their specific cellular functions (Fig. 11) (Praefcke and McMahon 2004).

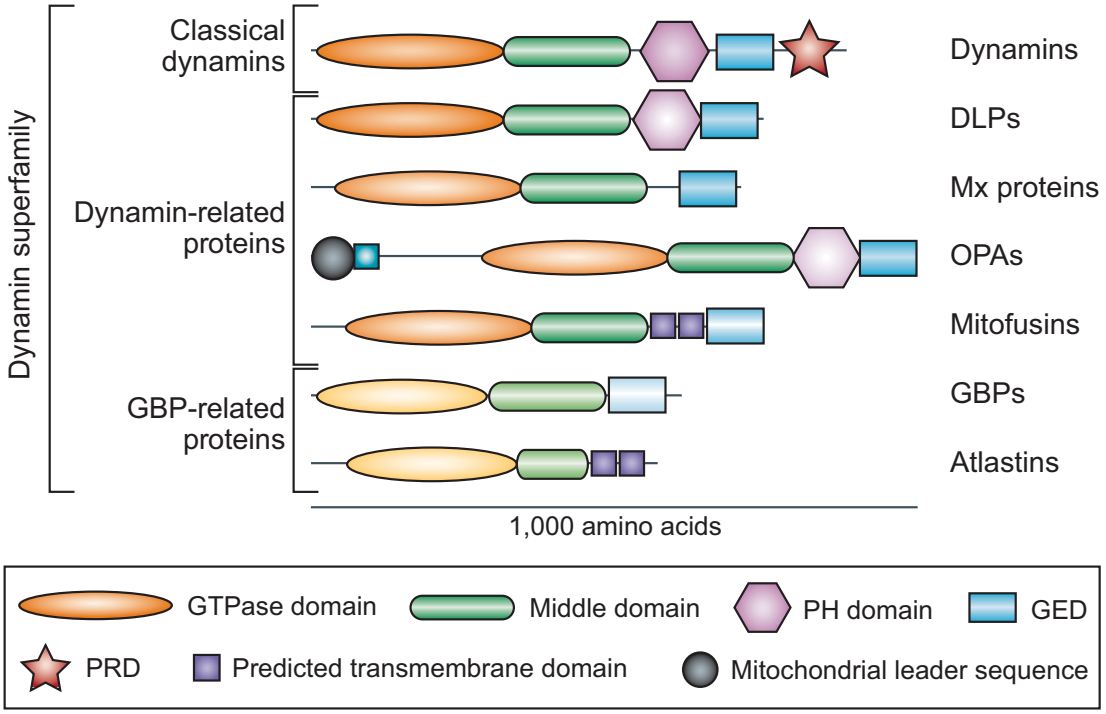

Figure 11. Domain architecture of the dynamin superfamily members. A cartoon comparison of domain organization between different family members as indicated: classical dynamins, dynamin like protein (DLPs), Mx proteins, Optic atrophy proteins (OPAs), mitofusins, guanylate-binding proteins (GBPs) and atlastins. Figure modified from Praefcke and McMahon 2004.

Primary sequence analysis indicates that the G domain of dynamin superfamily members is an extended form of the canonical GTPase fold observed in Ras and many other GTPases, as the four essential motifs, sequentially named G1-G4, are all present. All these motifs contribute to the binding and hydrolysis of GTP, and they are hallmarked by one or more conserved amino acid residues (Vetter and Wittinghofer 2001). The G1 motif has the consensus sequence of GXXXXGKS/T ("X" stands for an unspecific residue) and form the conserved phosphate-binding (P-) loop, which is

responsible for the interaction with the β- and γ-phosphate of the nucleotide (Saraste, Sibbald et al. 1990). The G2 motif contains an invariant threonine residue that binds the γ-phosphate of GTP (Bourne, Sanders et al. 1991). The G3 motif has a DXXG composition where the conserved aspartate binds a catalytic magnesium ion (Mg^{2+}) and the glycine coordinates γ-phosphate (Vetter and Wittinghofer 2001). The G4 motif has a T/NKXD signature (except for GBPs and OPAs) that is involved in the coordination of the nucleotide base and the ribose (Bourne, Sanders et al. 1991). Two conserved loop regions in the G domain were named switch I and II, as they undergo large conformational changes in the GDP- and GTP-bound form in analogy to the switch that mediates the "on" and "off" state of the molecule (Milburn, Tong et al. 1990). Switch I covers the G2 motif and the switch II overlaps with the G3 motif. In contrast to many molecular structures of the Ras-like G domain, little structural information of the much less conserved MD and GED of the main dynamin superfamily members (such as dynamins, DLPs or Mx proteins) was known. According to secondary structure prediction based on primary amino acid sequence, MD and GED fold predominantly into α-helices (Kelley and Sternberg 2009), which was also observed for some far relatives of dynamins and Mx proteins like GBPs and BDLP (see 2.3.4 and 2.3.5) (Prakash, Praefcke et al. 2000; Low and Lowe 2006). In the following paragraphs, current structural and functional studies of selected dynamin superfamily members and other Mx-related proteins will be introduced.

2.3.2 Dynamins

The first insight into dynamin function dates back to almost 40 years ago to a study on *Drosophila melanogaster* showing a temperature-sensitive paralytic phenotype as a result of mutations in a single gene, which was named from then on as *shibire* (Grigliatti, Hall et al. 1973). Further research discovered that these flies had a dramatically decreased number of neurotransmitters-filled synaptic vesicles at the presynaptic plasma membrane, where many clathrin-coated “collared pits” were accumulated instead, suggesting that the *shibire* encoded protein plays an essential role in clathrin mediated endocytosis (CME) (Kosaka and Ikeda 1983; Poodry 1990). Around 20 years ago, dynamin was isolated and purified from calf brain as a new microtubule-associated protein (MAP) and thereby obtained its name (Shpetner and Vallee 1989). The same group also proved later that dynamin has a microtubule-stimulated GTPase activity (Shpetner and Vallee 1992). Soon after the purification of calf brain dynamin, the cDNA encoding rat brain dynamin was isolated (Obar, Collins et al. 1990). Subsequent analysis indicated that this cDNA shares 81% sequence

identity to *shibire*, which revealed a global functional role for dynamins in the brain (Chen, Obar et al. 1991; van der Bliek and Meyerowitz 1991). In the middle 1990s, when several dynamin-encoding genes were isolated, it was realized that dynamin is not neuron-specific, but it has different isoforms distributed also among other tissues (Urrutia, Henley et al. 1997). Besides, functional studies on dynamins around the millennium demonstrated that dynamins are involved not only in CME, but also in many other membrane deforming events such as budding of caveoli, phagocytosis and podosome formation, as well as in actin rearrangements and cytokinesis (Fig. 10) (Henley, Krueger et al. 1998; Oh, McIntosh et al. 1998; Gold, Underhill et al. 1999; Ochoa, Slepnev et al. 2000; van Dam and Stoorvogel 2002; Orth and McNiven 2003).

Currently, there are three dynamin isoforms known in mammals. Dynamin 1 is highly abundant in brain and is concentrated in the presynapse, dynamin 2 is ubiquitously expressed, and dynamin 3 is concentrated in testis, lung and also in brain, albeit post-synaptically (Praefcke and McMahon 2004). Structurally, dynamin has five distinct domains. Apart from the G domain, MD and GED mentioned before, it also contains a pleckstrin homology (PH) domain between MD and GED, and a C-terminal proline-rich domain (PRD) (Fig. 11). The PH domain was identified first in pleckstrin and later also in other proteins involved in intra-cellular signaling (Haslam, Koide et al. 1993; Mayer, Ren et al. 1993; Saraste and Hyvonen 1995). PH domains can interact specifically with membranes containing different phosphorylated phosphoinositides (PIPs), and with other proteins like βγ-subunits of heterotrimeric G proteins ($G_{\beta\gamma}$) and protein kinase C (PKC), thereby playing an important role in the targeting of host proteins to certain cellular components (Wang, Shaw et al. 1994; Yao, Kawakami et al. 1994; Wang and Shaw 1995). The PRD is predicted to be unstructured because of its high proline content, and it can bind to other domains such as Src homology 3 (SH3) domain that is found in many proteins involved in signaling pathways (Williamson 1994; Kay, Williamson et al. 2000; Mayer 2001). For almost 20 years, researchers have been attempting to get the atomic structure of dynamin but without much success. Nevertheless, structures of the dynamin G domain and PH domain were individually solved, and a low resolution electron density map of oligomerized dynamin was obtained, as will be discussed in the following passages.

The first crystal structure of the mammalian dynamin G domain was solved as a fusion protein artificially linked to the myosin II motor domain from *Dictyostelium discoideum* (Reubold, Eschenburg et al. 2005). Apart from the extra helices not

present in classical G domains, it is noticeable that the N- and the C-terminal helix of this rat dynamin G domain form a three-helical bundle together with the myosin C-terminal helices via hydrophobic interactions (Fig. 12A). The same arrangement was also found in a previously solved fusion protein composed of *Dictyostelium discoideum* dynamin and the myosin II motor and it was suggested that this helical bundle mimics the interaction between the G domain and GED (Niemann, Knetsch et al. 2001). It was also found that the GDP-bound G domain shows no large conformational change as compared to the nucleotide-free G domain except for the switch regions (Niemann, Knetsch et al. 2001). The PH domain is a globular structure made of one α-helix and seven β-strands (Fig. 12B) (Ferguson, Lemmon et al. 1994). Two flexible loops (named variable loop 1 (VL1) and variable loop 2 (VL2)) were believed to be the binding site for lipids (Fig. 12B) (Fushman, Cahill et al. 1995; Zheng, Cahill et al. 1996).

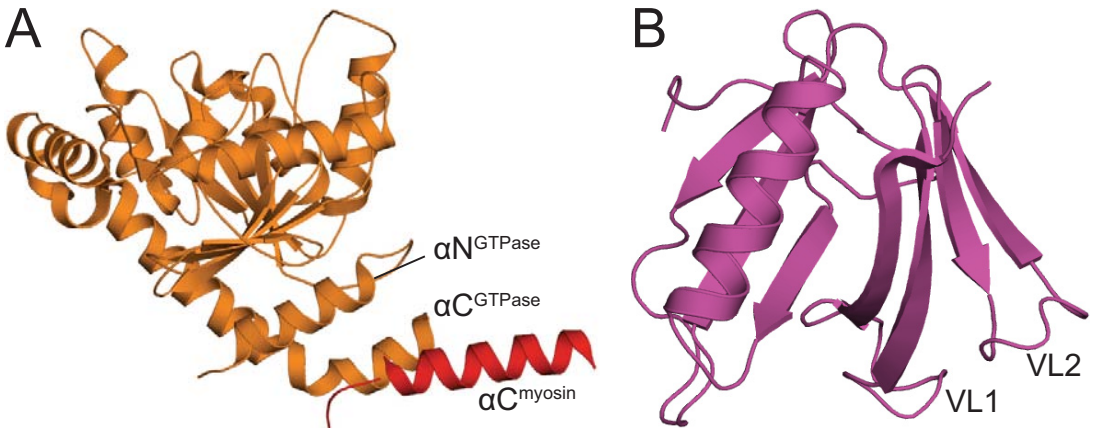

Figure 12. Crystal structures of individual domains of dynamin. A) The G domain from *Rattus norvegicus* (rat) dynamin 1 (PDB code 2AKA) (Reubold, Eschenburg et al. 2005). The G domain is colored in orange with the N- and C-terminal helices labeled accordingly. The C-terminal helix of the myosin II motor is colored in red and labeled accordingly. B) The PH domain from human dynamin 1 (1DYN) (Ferguson, Lemmon et al. 1994), the variable loops VL1 and VL2 are indicated.

Recently, a crystal structure of human dynamin 1 G domain fused with the C-terminal helix of GED (so-called minimal GTPase-GED fusion protein, GG (Chappie, Acharya et al. 2009)) was solved in the presence of GDP with aluminum tetrafluoride ($GDP{\bullet}AlF_4^-$) (Chappie, Acharya et al. 2010), which is believed to mimic the transition state of GTP hydrolysis. The GG dimerized in the crystal (Fig. 13A) with a large interface stabilized by i) dual coordination of the guanine base both *in cis* and *in trans* by the loop containing G4 motif; ii) the association of switch II with the "*trans* stabilizing loop"; and iii) a pair of symmetric salt bridges anchoring the base of the

dimer *in trans*. Moreover, the GG structure also revealed that the GTP hydrolysis occurs at this interface in a way similar to MnmE G domain dimer where a sodium ion (Na^+) was shown to be involved in the catalysis of the reaction (Scrima and Wittinghofer 2006). The C-terminal helix of GED did not contacted G domain but rather form a three-helical bundle together with the N-terminal and C-terminal helices of the G domain via extensive hydrophobic interactions, which was termed "bundle signaling element" (BSE) (Fig. 13B). The BSE did not participate in GG dimerization and was proposed to be a rigid body linking the G domain and the rest of the protein (Chappie, Acharya et al. 2010).

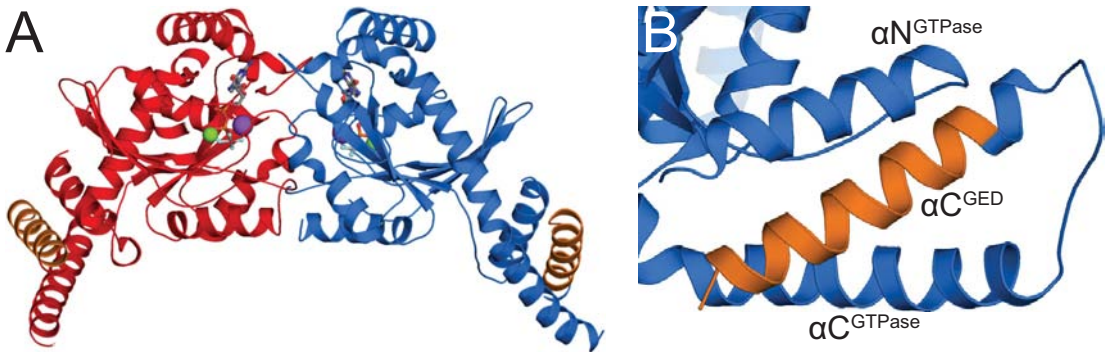

Figure 13. Crystal structure of the minimal GTPase-GED fusion protein of dynamin 1. A) The GG dimer (PDB code 2X2E) (Chappie, Acharya et al. 2010). Two monomers are individually colored in red and blue. The GED portion of both monomers is colored in orange. GDP•AlF4$^-$ is shown in ball-and-stick representation. Na^+ and Mg^{2+} are individually drawn as purple and green spheres. B) The bundle signaling element shown in details. Individual helices are labeled accordingly.

The structure of dynamin oligomer was studied *in vitro* by electron cryomicroscopy (cryo-EM), where phosphatidylinositol-4,5-bisphosphate (PIP_2) or phosphatidylserine (PS) containing lipid nanotubes, or tubules, were used as membrane templates for the assembly of a dynamin construct without the PRD. It has been observed that dynamin can form spiral-like oligomers around the lipid tubules, and the diameters or the pitches of the spiral can vary, depending on the nucleotide loading state (Praefcke and McMahon 2004). Based on these results, two models were proposed to explain the mechanism of membrane scission for dynamin: the "pinchase" model suggests that scission is realized by the constriction of the spiral (Sweitzer and Hinshaw 1998), and the "poppase" model proposes a spring-like mechano-chemical function (Stowell, Marks et al. 1999). From the cyro-EM images, low resolution electron density maps for both constricted and non-constricted dynamin oligomers were calculated using helical reconstruction or single particle methods (Zhang and Hinshaw 2001; Chen, Zhang et

al. 2004). Based on these cryo-EM studies, it was implicated that dynamin forms "T-bar" shaped dimers that serve as the building blocks of the oligomer (Fig. 14A) (Praefcke and McMahon 2004). According to this proposed dimeric model, crystal structures of the G domain and the PH domain could be fitted into the "head" and "leg" parts of the oligomer, whereas the detail of the "stalk" part which would accommodate the MD and the GED was missing (Fig. 14B) (Mears, Ray et al. 2007). Therefore the molecular basis for the assembly of dynamin still remains unclear.

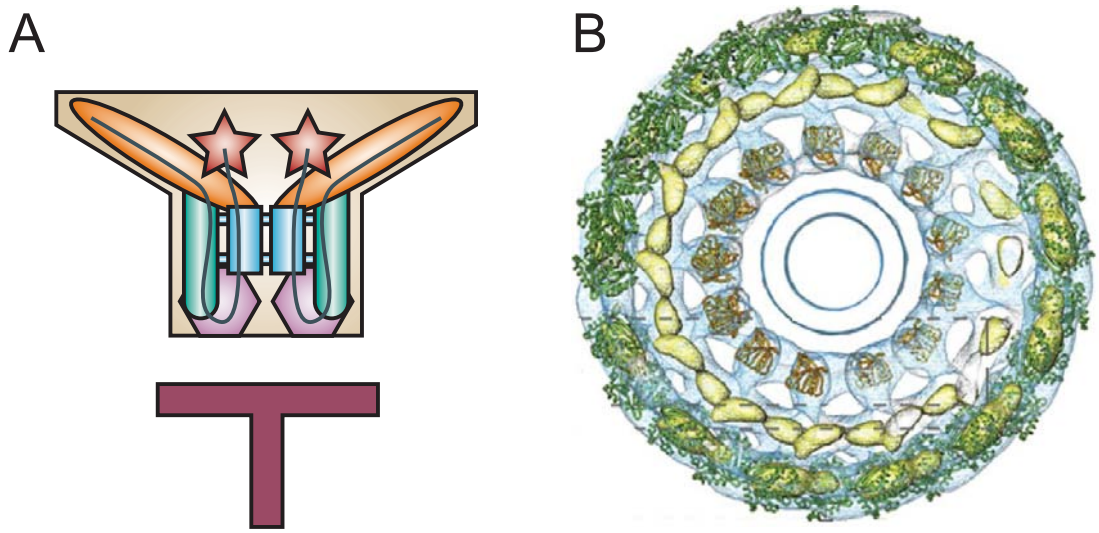

Figure 14. Studies on the oligomerization of dynamins. A) The cartoon model for a dynamin dimer as the building blocks for the oligomer, depicted as in Fig. 11. The G domains and PRDs are at the top of the dimer and make contacts with other G domains in the neighboring dimer or other partner proteins, and the PH domains reside at the bottom of the dimer to interact with the lipid substrate. The MDs and GEDs form the stalk region of the dimer and are responsible for the oligomerization. Figure modified from (Praefcke and McMahon 2004) B) A 20 Å cryo-EM electron density map of ΔPRD human dynamin 1 oligomer on a lipid tubule in a cross-section view, fitted with the crystal structures of the rat dynamin 1 G domain (green) and the human dynamin 1 PH domain (brown). Figure excerpted from Mears, Ray et al. 2007.

2.3.3 Mx proteins

Mx proteins are key mediators of the IFN-induced innate antiviral response in vertebrates (Haller, Stertz et al. 2007). Their discovery dates back on genetic studies on inborn resistance of mice to influenza viruses about 40 years ago (Lindenmann 1962; Haller and Lindenmann 1974). Mx1 protein was cloned from influenza virus-resistant mice (Horisberger, Staeheli et al. 1983) and was shown to mediate cell-intrinsic antiviral activity (Staeheli, Haller et al. 1986). The mouse Mx1 is encoded by the *Mx1* gene on chromosome 16 and most influenza virus-susceptible mouse strains

carry large deletions or nonsense mutations in this region (Staeheli, Grob et al. 1988). Later it was found in the mouse genome that another gene, named *Mx2*, which is closely linked with *Mx1* on chromosome 16, is also defective in inbred mouse strains (Staeheli and Sutcliffe 1988).

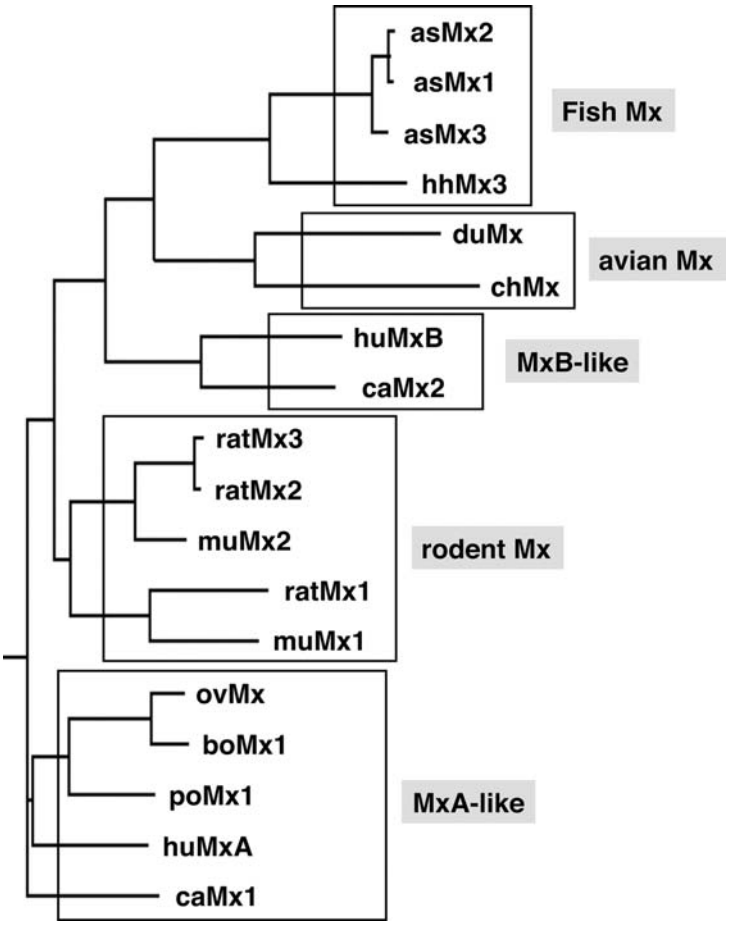

Figure 15. Phylogenetic tree of Mx proteins. According to sequence similarities, currently known vertebrate Mx proteins can be classified into five subgroups: fish Mx avian Mx, MxB-like, rodent Mx and MxA-like. as: Atlantic salmon; hh: Atlantic halibut; du: duck; ch: chicken; hu: human; ca: canine; rat: rat; mu: murine; ov: ovine; bo: bovine; po: pocine. Figure excerpted from Haller, Gao et al. 2010.

Human Mx proteins were identified from cross-interactions of a monoclonal antibody (2C12) against mouse Mx1 in human cells (Staeheli and Haller 1985). Subsequently, two proteins named MxA and MxB were found to be encoded by closely linked genes on human chromosome 21 (Horisberger, Wathelet et al. 1988; Reeves, O'Hara et al. 1988; Aebi, Fah et al. 1989). Subsequently, IFN-inducible *Mx* genes were identified in many vertebrates and their encoding proteins can be classified into several subgroups based on sequence similarities (Fig. 15) (Haller, Stertz et al. 2007).

Mx proteins have a molecular mass of around 75 kDa, and are composed of the N-terminal G domain, the MD and the C-terminal GED as described in 2.3.1. The G domain of Mx proteins share 40% sequence identity to other dynamin superfamily members whereas for MD and GED only 20% identity is observed (Staeheli, Pitossi et al. 1993). Compared to dynamin, Mx proteins usually have an extra unstructured N-terminal strech of amino acids with unknown function, and this stretch varies in the length and sequence of amino acid residues for Mx proteins from different species. As to the GTPase activity of purified histidine-tagged human MxA (His-MxA), the GTP turnover was calculated to be 27 min^{-1}, and the dissociation constant (K_d) of His-MxA to GDP and GTP were measured to be 100 µM and 20 µM, respectively (Richter, Schwemmle et al. 1995). For MD and GED, a single point mutation at Leu612 to lysine (L612K) of human MxA resulted in a non-oligomerizable form that is defective in GTP hydrolysis and rapidly degraded (Schumacher and Staeheli 1998), but still maintains some antiviral activity (Janzen, Kochs et al. 2000). Another single point mutation, E645R in human MxA, was shown to have altered specificity and mode of action against vesicular stomatitis virus (VSV) (Zurcher, Pavlovic et al. 1992). Furthermore, the region comprising residues 432-471 was shown to be the binding site of antibody

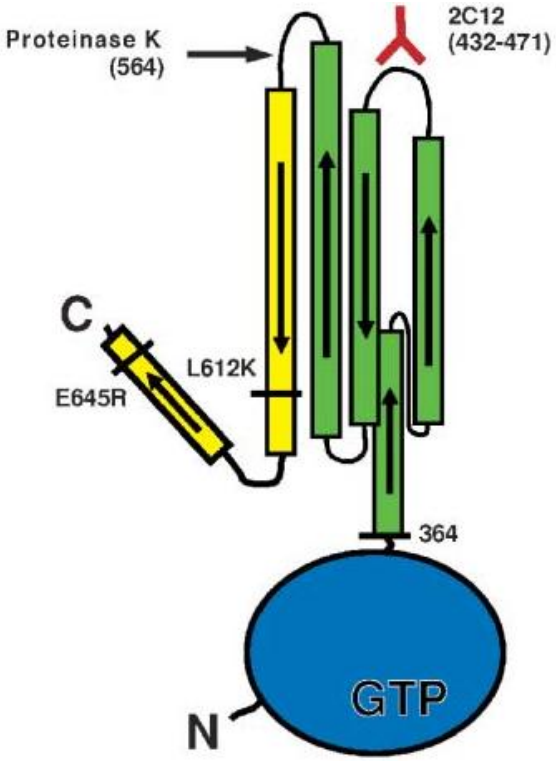

Figure 16. Hypothetical domain arrangement of human MxA. The G domain, MD and GED are colored in blue, green and yellow, respectively. The bars indicate the α-helical secondary structure. The critical positions identified in previous experiments are labeled correspondingly. Figure excerpted from Haller and Kochs 2002.

2C12 (Flohr, Schneider-Schaulies et al. 1999), and residue 564 was found to be a proteinase K cleavage site (Schwemmle, Richter et al. 1995). Based on these experimental results and the knowledge gained from the GBP1 structure (Prakash, Praefcke et al. 2000), a hypothetical domain arrangement was proposed for MxA which contains a globular G domain with MD and GED folding into an anti-parallel helical bundle (Fig. 16) (Haller and Kochs 2002).

In solution, Mx proteins self-assemble into high-order oligomers in ring-like or helical arrangement (Fig. 17A, B) (Melen, Ronni et al. 1992; Kochs, Haener et al. 2002). Human MxA was shown to bind to negatively charged membranes and form ring-like oligomers that tubulate liposomes in a way similar to dynamin (Fig. 17C) (Accola, Huang et al. 2002; Kochs, Reichelt et al. 2005). In living cells, rodent Mx proteins accumulate in distinct nuclear dots near promyelocytic leukemia (PML) nuclear bodies (NBs) in IFN-treated cells (Engelhardt, Ullrich et al. 2001), while human MxA forms punctuate granula in the cytoplasm and partially co-localizes with COPI-positive membranes of the smooth ER-Golgi intermediate compartment (Stertz, Reichelt et al. 2006). It was concluded that these Mx assemblies may serve as an intracellular storage form from where more Mx proteins can be recruited when needed (Haller and Kochs 2002).

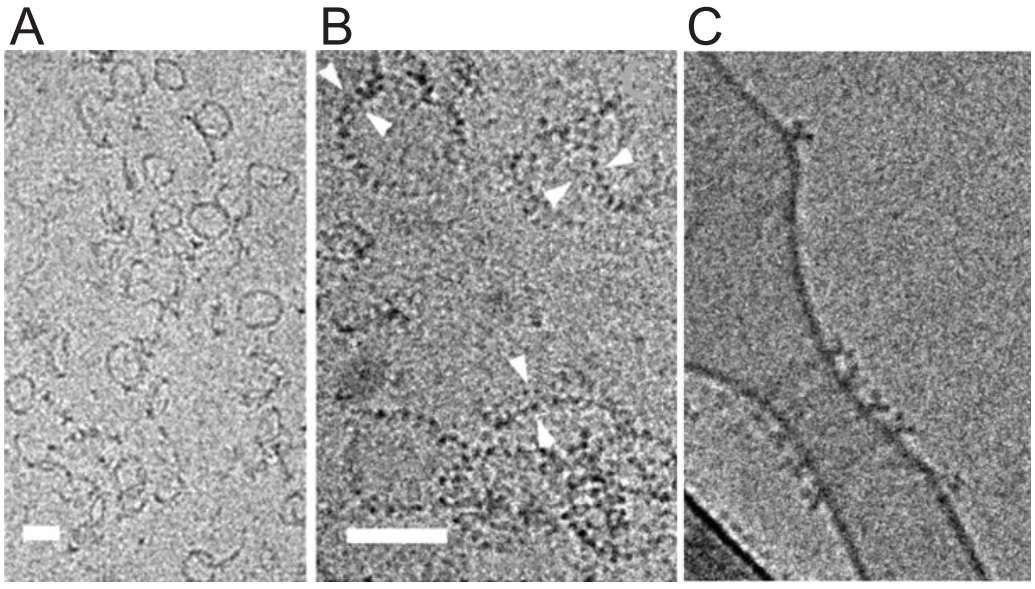

Figure 17. Cryo-transmission electron microscopy (TEM) images of human MxA self-assemblies. Scale bars = 50 nm. A) Human MxA oligomerizes into ring- and open-arc-like structures. B) Higher magnification of the rings in A reveals two parallel sets of electron-dense globular domains, indicated by arrowheads; C) Human MxA forms ring-like oligomers and tubulate PS liposomes in the presence of GTP. The T-bar shaped feature of the molecule is also observed. Figure excepted from Kochs, Reichelt et al. 2005.

Mx proteins have different specificities in their antiviral spectrum and this may be a result of their subcellular localizations to some extent. For example, rodent Mx1 has a C-terminal nuclear localization signal (NLS) and inhibits multiplication of orthomyxoviruses, such as FLUAV and Thogoto virus (THOV) which replicate in the cell nucleus (Haller, Stertz et al. 2007). In contrast, cytoplasmic rodent Mx2 confers resistance to those viruses that replicate in the cytoplasm, such as rhabdoviruses (e.g. vesicular stomatitis virus, VSV) and bunyaviruses (e.g. LaCrosse virus, LACV) (Haller and Kochs 2002). On the other hand, cytoplasmic human MxA is able to suppress a broad range of different virus classes, including members of the bunyaviruses, orthomyxoviruses, paramyxoviruses, rhabdoviruses, toga-viruses, picornaviruses, reoviruses and hepatitis B virus (HBV), a DNA virus with a genomic RNA intermediate, despite their different replication sites in the cell (Haller and Kochs 2002; Haller, Stertz et al. 2007). Recently, it was reported that human MxA can also suppress a large dsDNA virus named African swine fever virus (ASFV) (Netherton, Simpson et al. 2009). However, nucleus-localizing human MxB has no evident antiviral activities (Melen, Keskinen et al. 1996). As for avians, chicken Mx proteins also lack the ability to fight against avian influenza viruses (Haller, Staeheli et al. 2009). In the case of fish Mx proteins, Atlantic salmon Mx1 was reported to be able to inhibit the activity of an influenza-like fish virus named infectious salmon anaemia virus (ISAV) and an aquatic birnavirus called infectious pancreatic necrosis virus (IPNV) (Larsen, Rokenes et al. 2004).

From early transgenic mouse and other cell-based assays, it was demonstrated that both mouse and human Mx proteins possess intrinsic antiviral activity *in vivo* and are able to function autonomously in the absence of other type I IFN-induced factors (Haller, Stertz et al. 2007). In the last 10 years, a lot of research has been carried out in order to elucidate their antiviral mechanism. It has been suggested that Mx proteins associate with essential viral components and thereby block their functions. For example, human MxA was shown to interact with THOV and LACV NP *in vitro* in a co-sedimentation assay (Kochs and Haller 1999). This interaction was also observed in a so-called minireplicon assay that mimics the *in vivo* viral replication with a minimum viral genome. Based on these studies, it was suggested that MxA does not recognize unassembled viral components but rather assembled nucleocapsids (Weber, Haller et al. 2000). Further studies revealed that human MxA binds to the NP of bunyaviruses and forms MxA/NP copolymers residing in the smooth ER-Golgi intermediate compartment, which would lead to a depletion of NP at the replication sites of the

virus (Reichelt, Stertz et al. 2004). Based on these results, it has been proposed that Mx proteins interfere with the intracellular allocation of viral components by missorting them (Haller, Stertz et al. 2007). However, as the relevant structural information is lacking, the antiviral mechanism for Mx proteins on the molecular level still remains unclear.

2.3.4 Guanylate-binding proteins

Guanylate-binding proteins (GBPs) are a group of antiviral proteins that are also induced by IFNs. Unlike Mx proteins, GBPs are involved mostly in the IFN-γ triggered immune response, and have different antiviral spectrum and efficiency from Mx proteins (Praefcke and McMahon 2004). Currently there are seven GBPs found in humans (Vestal and Jeyaratnam 2010). Human GBP1 and GBP2 were originally identified in an extract of human fibroblasts treated with IFNs, with the most prominent effect elicited by IFN-γ (Cheng, Colonno et al. 1983). Later, it was found that GBPs can associate with agarose-bound GTP, GDP and GMP, although they lack the consensus G4 motif in the G domain (Cheng, Patterson et al. 1991). Surprisingly, they were noted surprisingly to have the distinct ability to hydrolyze GTP not only to GDP but further to GMP (Schwemmle and Staeheli 1994). As dynamin family members, GBPs are stable in the absence of nucleotide, and have lower binding affinities to guanine nucleotides and high GTPase activities than Ras (Praefcke, Geyer et al. 1999). Biochemical studies on human GBP1 suggested that it has a monomeric form in solution in the absence of nucleotide or in complex with GDP, but can dimerize or oligomerize when bound to a non-hydrolysable GTP analogue 5′-Guanylyl-β-γ-imido-diphosphate (GMP-PNP) or GDP●AlF_4^-. Therefore it was proposed that oligomerization was required for efficient GTP hydrolysis (Scheffzek, Ahmadian et al. 1998; Prakash, Praefcke et al. 2000). For the antiviral activity, human GBP1 was shown to mediate resistance to VSV and encephalomyocarditis virus (EMCV), albeit with much weaker inhibitory effects than that of human MxA for its target viruses (Anderson, Carton et al. 1999; Praefcke and McMahon 2004). Additionally, human GBP1 was also shown to have an antiproliferative function in epithelial cells (Guenzi, Topolt et al. 2001).

The crystal structure of human GBP1 in the nucleotide-free state was solved in the year 2000 and was the first full-length high-resolution structure for a dynamin superfamily member (Fig. 18A) (Prakash, Praefcke et al. 2000). According to the structure, human GBP1 is composed of a large G domain and an elongated helical domain. The switch

regions of this G domain are not completely resolved due to their flexibility and the P-loop adopts a different conformation from that observed in nucleotide-bound G domain structures, which may be a result of the absence of nucleotide. The G domain of human GBP1 also has different insertions from that of dynamin G domains, suggesting a distant relationship between these proteins (Praefcke and McMahon 2004). The helical domain comprising MD and GED is organized as a tight anti-parallel helical-bundle. The GED has an extremely long helix and leads back to the G domain at the C-terminus (Fig. 18A) (Prakash, Praefcke et al. 2000). Soon after this initial structure, the same group published the crystal structure of human GBP1 in the presence of GMP-PNP (Fig. 18B) (Prakash, Renault et al. 2000). The structure revealed some slight difference from canonical G domains for the nucleotide-binding conformation. However, except for some expected alternation in the nucleotide-binding pocket, there were few major conformational changes observed as compared to the nucleotide-free structure. It was therefore difficult to draw any conclusions about the coupling between domain movements and GTP-binding or hydrolysis (Fig. 18B) (Prakash, Renault et al. 2000; Praefcke and McMahon 2004). Later, the same

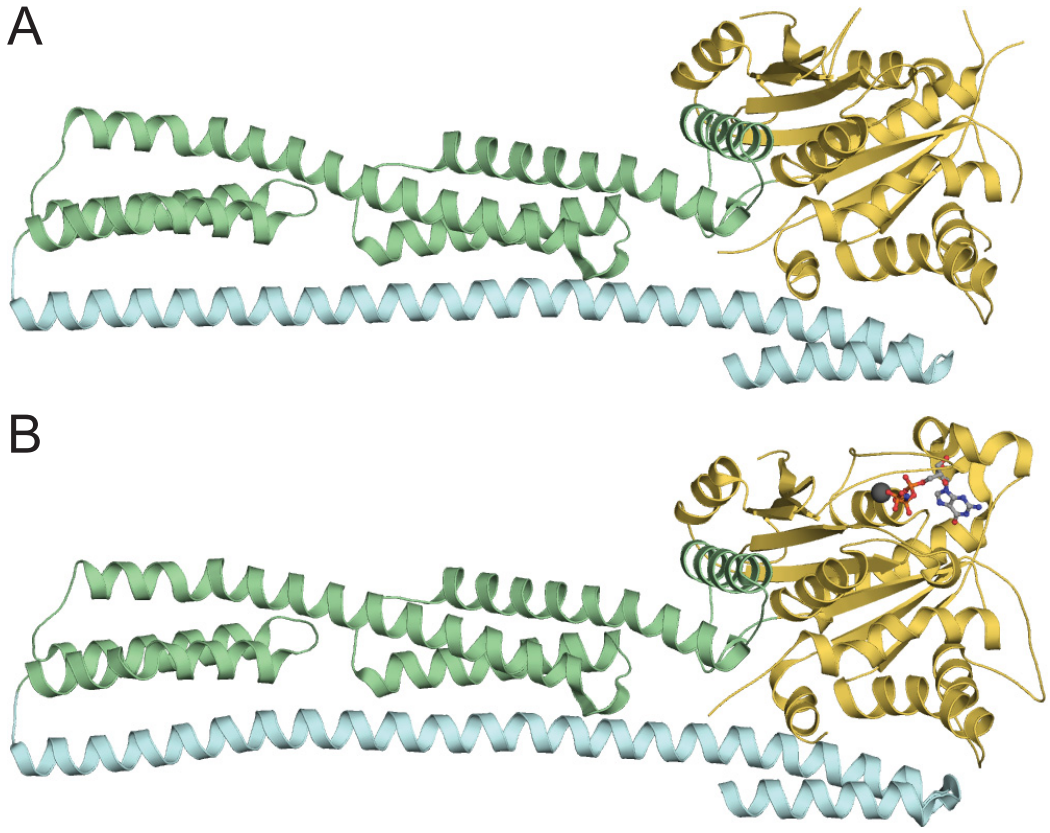

Figure 18. Crystal structures of human GBP1. A) GBP1 in the nucleotide-free state (PDB code 1DG3) (Prakash, Praefcke et al. 2000). B) GBP1 bound with GMP-PNP (in ball-and-stick representation) with a Mg^{2+} ion as a gray sphere (1F5N) (Prakash, Renault et al. 2000). The individual domains are colored according to Fig. 11.

group performed a thorough investigation of the GTP hydrolysis of human GBP1 by solving the structure of its G domain in different nucleotide-binding states (Ghosh, Praefcke et al. 2006). Their results confirmed that dimerization of G domains across the nucleotide-binding site promoted GTP hydrolysis. An arginine finger and a serine were re-oriented upon dimerization and accelerated GTP hydrolysis. There structures also explained the chemical basis for the consecutive hydrolysis of GTP to GMP. These structural studies of human GBP1 have provided valuable information about the dynamin superfamily but, due to its distant relationship to dynamins and Mx proteins, they were insufficient to explain the functional mechanism of dynamin and MxA.

2.3.5 Bacterial dynamin-like proteins

Although dynamin family members are believed to exist only in multi-cellular eukaryotes, it has been found that many Eubacteria also have hypothetical genes that are likely to encode dynamin-like proteins (DLPs) containing a G domain, MD and GED (van der Bliek 1999). As these proteins are less complex than dynamins, at least in domain organization, their structures were studied as important references to dynamins. A successful example is a tentative mitofusin-related DLP encoded by an unnamed gene with the Genbank accession code ZP_00108538 from the filamentous cyanobacterium *Nostoc punctiforme*, which was termed a bacterial DLP (BDLP) (Low and Lowe 2006). The BDLP was shown to oligomerize around tubulated liposomes in the presence of GMP-PNP, and have GTPase activity similar to that of dynamin superfamily members. The subcelluar localization of BDLP seems to be mainly on the cell periphery and BDLP tends to form punctuate patterns (Low and Lowe 2006). It was also noted that BDLP has a monomeric form in the absence of nucleotide in solution and the binding of GDP can promote its homodimerization (Low and Lowe 2006).

The crystal structures of nucleotide-free and GDP-bound full-length BDLP have been solved. In both structures, the N-terminal G domain has a globular structure, while the predicted MD and GED cooperate to form a four-helical bundle comprising a neck and a trunk, followed by a so-called tip region (Fig. 19A, B). A long helix-turn-helix structure precedes the canonical G domain and interacts extensively with the predicted MD and GED at the neck region. The G domain bends toward the neck but has hardly any contact with the predicted GED region (Fig. 19A, B). The tip region is organized into two helical layers, with the first layer derived from the predicted MD and the lower layer forming a paddle that situated between the conventional MD and

GED. Moreover, the tip region was predicted to be membrane-associating, in analogy to the PH domain of dynamins (Fig. 19A, B) (Low and Lowe 2006). It was also noticed that in both nucleotide-free and GDP-bound structures BDLP molecules form dimers in the crystal via the G domains. The GDP-bound BDLP dimer has a much larger dimeric interface which occludes the nucleotide-binding site in a way similar to that of the human GBP1 dimer. Additionally, the tip region undergoes a considerable rearrangement upon GDP-binding, which is believed to facilitate the crosstalk of the G domains (Fig. 19B) (Low and Lowe 2006). These studies on BDLP could hint at bacterial ancestry for the dynamin superfamily (Low and Lowe 2006).

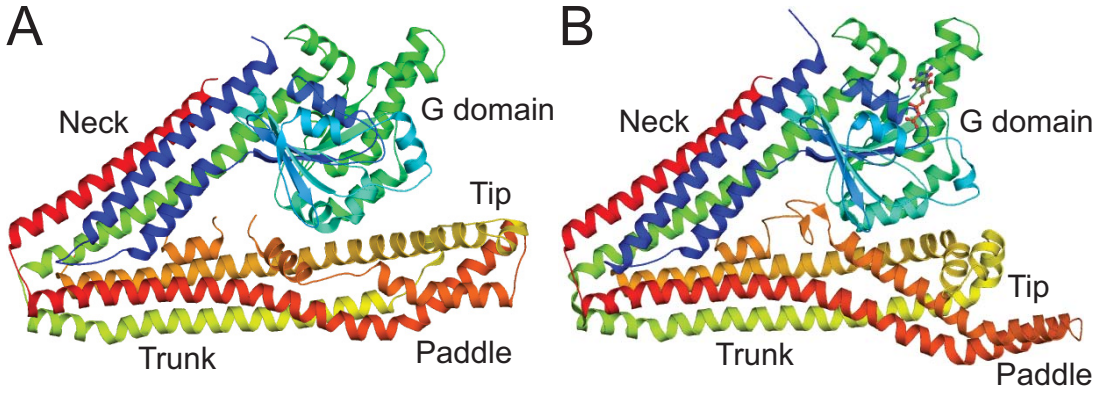

Figure 19. Crystal structures of BDLP. A) BDLP in the nucleotide-free state (PDB code 2L69) (Low and Lowe 2006). B) BDLP bound with GDP, shown in ball-and-stick representation. Note the large-scale movement at the tip region (2J68) (Low and Lowe 2006). Both structures are rendered in rainbow colors from N- (purple) to C-terminus (red). The positions of the G domain, neck, trunk, tip and paddle are indicated.

After these crystal structures, the cryo-EM reconstruction of BDLP oligomer in the presence of GMP-PNP was performed from BDLP-coated lipid tubes, resulting in an 11 Å electron density map (Fig. 20A) (Low, Sachse et al. 2009). The reconstructed electron density map reveals a tightly packed helical surface coating of BDLP oligomer with a diameter of 50 nm. And dimeric globular densities were observed for the coat that represented the asymmetric unit (Low, Sachse et al. 2009). In cross-section view, the densities were exhibited a cartwheel-like architecture where thin grooved radial spokes connected to globular densities were observed to converge centrally to the lipid tube (Fig. 20A). Based on this electron density map, the GMP-PNP-associated BDLP oligomer was modeled using the crystal structure of GDP-bound BDLP, which suggested large conformational changes of BDLP upon GMP-PNP binding (Low, Sachse et al. 2009). The modeling included two pairs of chain breaks in crystal structure, namely at Asp360 and Arg656 between the neck and trunk, and at Gly68

and Gly309 on the interface between the neck and G domain (Fig. 20B). The resulting separate G domain, neck, and trunk were accurately docked into the density as rigid bodies (Fig. 20B). Two modeled BDLP molecules in the asymmetric unit contacted each other via the G domains and trunks. The hydrophobic paddles were predicted to insert into lipid membrane (Fig. 20B) (Low, Sachse et al. 2009).

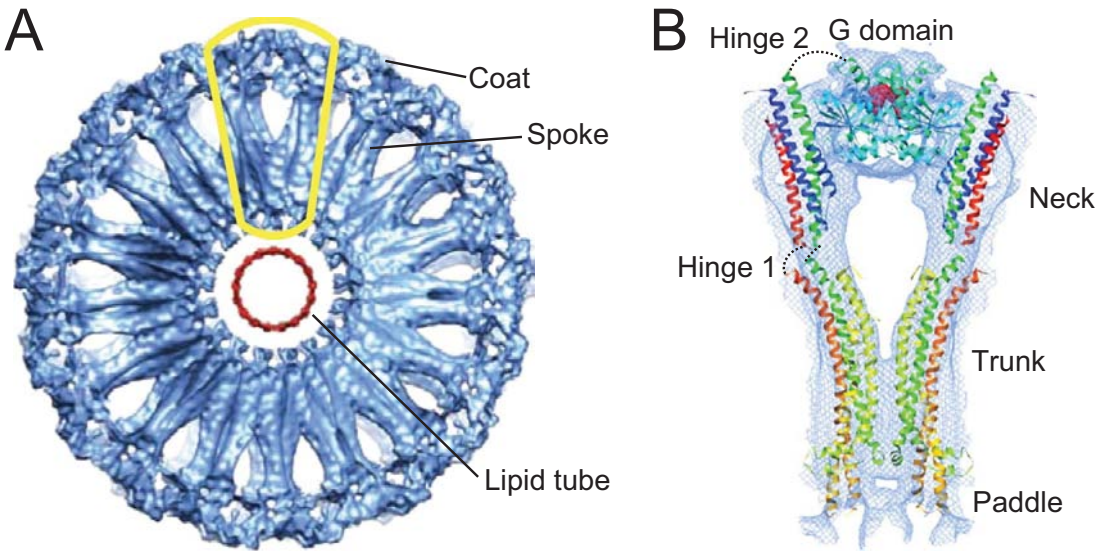

Figure 20. Cryo-EM study of GMP-PNP-bound BDLP. A) Electron density map of BDLP oligomer from Cryo-EM reconstruction in cross-section view. The coat, spoke and density in lipid tube (color in red) are indicated on the cartwheel-like architecture. The asymmetric unit is indicated by a yellow frame. B) Modeling of GMP-PNP-bound BDLP and the fitting of the model to the asymmetric unit of the density map. The hinges predicted to be responsible for the conformational changes are indicated by dashed lines. The individual parts of BDLP are labeled correspondingly to Fig. 19. Figures excerpted from Low, Sachse et al. 2009.

However, due to its remote relationship to eukaryotic dynamin superfamily members, these results are still not sufficient to unveil the detailed genuine functional mechanisms of dynamins and Mx proteins.

2.3.6 EHDs

Eps15 homology (EH)-domain-containing proteins (EHDs, also referred to as RME-1 or pincher) are a group of conserved membrane-associating ATPases with a size of approximately 60 kDa in eukaryotes. They have been found to be involved in clathrin-independent endocytosis (Shao, Akmentin et al. 2002), and recycling from endosomes (Grant, Zhang et al. 2001; Caplan, Naslavsky et al. 2002). EHDs have four members (EHD1–4) in mammals and one member in *Caenorhabditis elegans, Drosophila*

melanogaster and many eukaryotic parasites. EHDs have been recently suggested to be a new member of the dynamin superfamily as they share many common features with dynamins (Daumke, Lundmark et al. 2007). Firstly, mouse EHD2 (mEHD2) was shown to have a low binding affinity to nucleotides, with 13 μM to ATPγS and 50 μM to ADP (Daumke, Lundmark et al. 2007). Secondly, mEHD2 is also able to tubulate PIP_2 or PS liposomes *in vitro*, and form ring-like structures around lipid tubules (Daumke, Lundmark et al. 2007). Finally, mEHD2 was demonstrated to have an 8-fold stimulated ATP hydrolysis activity in the presence of saturating Folch (lipids derived from bovine brain) or PS liposomes (Daumke, Lundmark et al. 2007). A crystal structure of mEHD2 bound with a non-hydrolysable ATP analogue 5'-adenylyl-β-γ-imidodiphosphate (AMP-PNP) was also solved in 2007 (Fig. 21A) (Daumke, Lundmark et al. 2007).

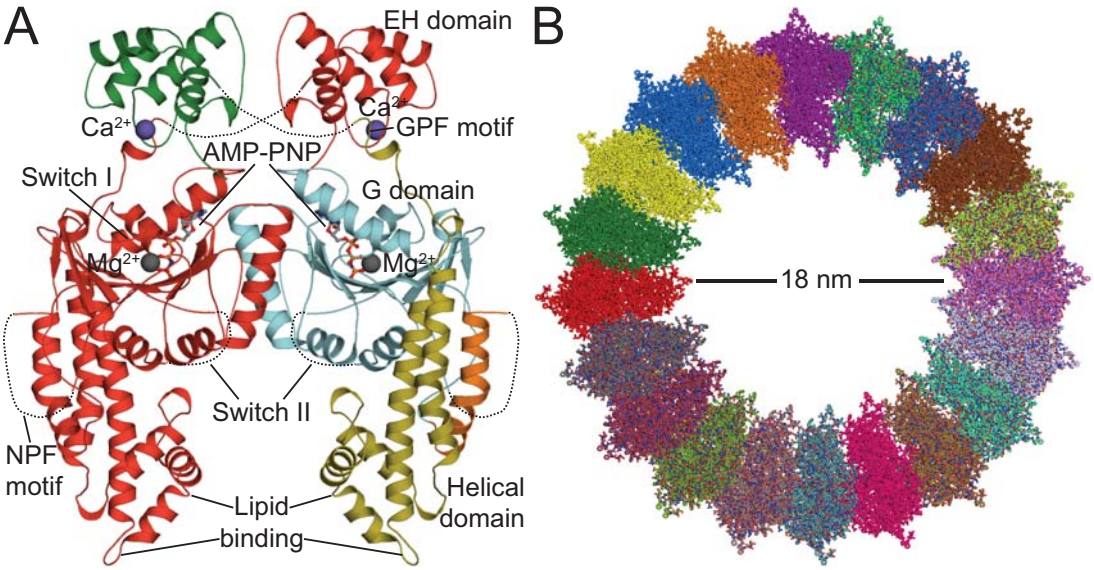

Figure 21. Crystal structure of the mEHD2 dimer and an oligomer model. A) Crystal structure of the AMP-PNP bound mEHD2 dimer (PDB code 2QPT) (Daumke, Lundmark et al. 2007). One chain of the dimer is colored in red, and the other one colored in orange, cyan, olive and green, for the N-terminal helix , G domain, helical domain and EH domain, respectively. Loops not observed in the electron density map are indicated by dashed lines. AMP-PNP is shown in ball-and-stick representation, and Mg^{2+} and Ca^{2+} are represented as gray and purple spheres, respectively. Domains, critical motifs or regions, as well as nucleotides and ions are labeled accordingly. B, the proposed ring-like model composed of 20 mEHD2 dimers, shown in different colors. The inner diameter of the model is 18 nm as indicated, which is consistent with EM studies (Daumke, Lundmark et al. 2007).

mEHD2 has an N-terminal nucleotide-binding domain, followed by a helical domain and a C-terminal EH-domain, which is known to associate with Asn-Pro-Phe (NPF)

motifs in endocytosis-related proteins (Fig. 21A). The mEHD2 nucleotide-binding domain exhibits a typical G domain fold with all G1-G4 signature motifs, although its nucleotide-binding site was found to be occupied by AMP-PNP. The mEHD2 G domain has insertions in the switch I region similar to dynamin (Reubold, Eschenburg et al. 2005). mEHD2 dimerizes via the G domain at the opposite side of the nucleotide-binding pocket, differing from human GBP1 and BDLP (Fig. 21A) (Prakash, Praefcke et al. 2000; Low and Lowe 2006). The helical domain of mEHD2 adopts a fold similar to those of the MD and GED of human GBP1 and has several conserved positively charged lysine residues at the tip, which were proved as the lipid-binding sites of mEHD2 (Fig. 21A). It was also observed that extensive contacts exist between the G domain and the helical domain. The C-terminal EH domain was connected to the helical domain by a 40-residue linker that was not fully resolved in the structure. The linker contains a Gly-Pro-Phe (GPF) motif that interacts with the EH domain. The EH domain sits on top of the G domain of the other molecule of the dimer and makes substantial contacts. The EH domains may be subject to movement when the protein associates with lipids (Daumke, Lundmark et al. 2007).

Based on the mEHD2 dimer structure, a possible mechanism of oligomerization for EHD proteins was proposed. The mEHD2 dimers were proposed to interact with each other via the conserved switch I and II regions in the nucleotide binding pocket, which were observed in human GBP1 and BDLP to comprise the dimeric interface (Prakash, Praefcke et al. 2000; Low and Lowe 2006). It was also shown that mutations at this critical interface led to a disruption of the lipid-stimulated ATPase activity (Daumke, Lundmark et al. 2007). In this way, an mEHD2 oligomer containing 20 dimers without EH-domains can be constructed (Fig. 21B) (Daumke, Lundmark et al. 2007). This predicted mEHD2 oligomer has a rather compact structure with a thickness of around 10 nm and an inner diameter of 18 nm (Fig. 21B), which are consistent with observations from EM studies. The positively charged membrane-binding sites are along one side of the oligomer and speculated to thereby generate the curvature of the membrane (Daumke, Lundmark et al. 2007). This proposed mEHD2 oligomer is the first oligomer model for the dynamin superfamily that is based on a high-resolution crystal structure, although it is still unclear whether dynamins or Mx proteins have the same orientation of the monomers in the oligomer as mEHD2.

2.4 Objective of this PhD thesis

As key mediators of innate immunity, Mx proteins confer resistance to viruses with varying specificities and effectiveness. However, little is know about the molecular mechanism of their antiviral activity. Given the efforts for structural studies on the dynamin superfamily, high-resolution structural information for full-length dynamins and Mx proteins is currently missing. Especially, little is known for the MD and GED structures which are essential for oligomerization of dynamin superfamily members. Therefore, the objective of this thesis was to determine the molecular structure of an Mx protein and carry out structure-based biochemical studies to resolve mechanistic and functional aspects of Mx proteins. The results of this work elucidate the molecular basis for oligomerization of dynamins and Mx proteins, and contribute to the understanding of the antiviral mechanisms of Mx proteins.

3 MATERIALS AND METHODS

3.1 Materials

3.1.1 cDNA clones

cDNA clones for human (*Homo sapiens*) MxA and MxB, mouse (*Mus musculus*) Mx1 and Mx2, zebrafish (*Danio rerio*) MxA and MxC, and rat (*Rattus norvegicus*) Mx1 were ordered from imaGenes (Berlin). cDNA clones for rat Mx2 and bovine (*Bos taurus*) Mx1 were ordered from Geneservice (UK).

3.1.2 Chemicals

Chemicals from the following companies were used: Amersham-Pharmacia (Freiburg), Baker (Deventer, The Netherlands), Fluka (Neu-Ulm), GERBU (Gaiberg), Jena Bioscience (Jena), Merck (Darmstadt), Pharma-Waldhof (Düsseldorf), Qiagen (Hilden), Riedel-de-Haen (Seelze), Roche (Mannheim), Roth (Karlsruhe), Serva (Heidelberg) and Sigma-Aldrich (Steinheim).

3.1.3 Enzymes

DNAase I	Roche (Mannheim)
Pfu DNA polymerase	Stratagene (Amsterdam, The Netherlands)
Restriction enzymes	New England Biolabs (Schwalbach)
T4 DNA ligase	New England Biolabs (Schwalbach)
PreScission protease	GE Healthcare (München)

3.1.4 Kits

QIAprep Spin Miniprep Kit	Qiagen (Hilden)
QIAquick Gel Extraction Kit	Qiagen (Hilden)
QuickChange Kit	Stratagene (Amsterdam)
2-log DNA ladder	New England Biolabs (Schwalbach)
Mark12 protein marker	Invitrogen (Darmstadt)
MWGF-200 Kit	Sigma-Aldrich (Steinheim)

3.1.5 Microorganisms

E. coli TG1	*K12, supE, hsdΔ5, thi, Δ(lac-proAB), F'[traD36, proAB$^+$, lacI^q, lacZΔM15]* (Promega)
E.coli BL21 (DE3) Rosetta	*F$^-$ ompT hsdSB(rB$^-$ mB$^-$) gal dcm (DE3) pRARE2 (CmR)* (Novagen) *pRARE* containing the tRNA genes *argU, argW, ileX, glyT, leuW, proL, metT, thrT, tyrU, and thru*

3.1.6 Media and antibiotics

Luria-Bertani (LB) extract	10 g/l Bactotryptone, 10 g/l NaCl, 5 mM NaOH, 5 g/l yeast
Terrific Broth (TB)	12 g/l BactoTryptone, 24 g/l Bacto-yeast-extract, 4 g/l glycerol, 17 mM KH_2PO_4, 72 mM K_2HPO_4
M9 minimium	6 g/l Na_2HPO_4, 3 g/l KH_2PO_4, 1 g/l NH_4Cl, 0.5 g/l NaCl

A preculture grown in LB medium overnight was used in 1:100 ratio to inoculate SeMet-Media (Van Duyne, Standaert et al. 1993). It was M9 medium supplied with 1 mM $MgSO_4$, 0.0042% Fe(II)SO_4, 0.2% glucose, a vitamin mix containing 1 mg/l Riboflavin, 1 mg/l Niacinamide, 0.1 mg/l pyridoxine monohydro-chloride and 1 mg/l thiamine. Shortly before induction, a amino acid mix containing L-lysine, L-phenylalanine, L-threonine, L-isoleucine, L-leucine, L-valine (100 mg/l each) and 50 mg/l L-selenomethionine (Calbiochem-Novabiochem, Schwalbach) was included (see 3.3.3).

Antibiotics from Roth (Karlsruhe) were used as follows:
Kanamycine or Ampicilline: 10 mg/l in liquid media and 50 mg/l in agar plates.
Chloramphenicol: 35 mg/l in both liquid mediums and agar plates.

3.1.7 Crystallization tools and consumables

Crystallization screens and other consumables such as glass cover slides or micro bridges were used from Hampton Research (Aliso Viejo, the USA), Jena Bioscience (Jena) and Qiagen (Hilden).

3.2 Molecular biology methods

3.2.1 Sequence alignment

Sequences alignment was performed using the ClustalW algorithm (Thompson, Higgins et al. 1994) and manually modified using Genedoc (Nicholas, Nicholas et al. 1997).

3.2.2 Agarose gel electrophoresis

Agarose gels were prepared and electrophoresis experiments are performed according to standard protocols (Sambrook, Fritsch et al. 1989).

3.2.3 DNA fragment amplification

DNA fragments were amplified by polymerase chain reaction (PCR) using *Pfu* polymerase (Stratagene, Amsterdam) following standard protocols (Sambrook, Fritsch et al. 1989). Fragments were subsequently purified using QIAquick Gel Extraction Kit (Hilden) according to the manufacturer's protocol.

3.2.4 Restriction digest

Restriction digests of target DNA fragments were performed using enzymes from New England Biolabs (Schwalbach) according to the manufacturer's protocol.

3.2.5 Ligation

Digested DNA inserts were quantified together with the vector in an ethidium bromide (EtBr) stained agarose gel using the 2-log DNA ladder (New England Biolabs, Schwalbach) as a reference. 10 ng of vector was ligated with a six fold molar excess of insert overnight at 4°C using T4 ligase (New England Biolabs, Schwalbach) following the manufacturer's protocol.

3.2.6 Extraction of plasmid DNA

DNA plasmids were isolated using QIAprep Spin Miniprep Kit from Qiagen (Hilden) according to the manufacturer's protocol.

3.2.7 Competent cells

Competent cells were prepared according to a published protocol (Chung, Niemela et al. 1989). Bacteria were grown in 200 ml LB medium from a 2 ml overnight preculture at 37 °C until an optical density at 600 nm wavelength (OD_{600}) of 0.4 and then subjected to 20 min incubation on ice. These bacteria were pelleted for 5 minutes (min) at 1,200 *g* (4°C), resuspended in 20 ml ice-cold sterile TSS buffer (85% LB medium without NaOH, 10% PEG8000, 5% DMSO, 50 mM $MgCl_2$, pH 6,5), flash frozen and stored at -80°C.

3.2.8 Transformation

DNA ligation product was transformed into competent *E. coli TG-1* cells using the heat shock method according to the standard protocol (Sambrook, Fritsch et al. 1989). For expression, plasmids were purified from *E. coli TG-1*, subsequently sequenced and transformed into *BL21 (DE3) Rosetta* cells.

3.2.9 Bacteria storage

Recombinant bacteria stocks were made from overnight culture with the addition of 33% sterile glycerol and stored at -80°C.

3.2.10 Site-directed mutagenesis

Site-directed mutagenesis experiments were carried out using the QuickChange Kit (Stratagene, Amsterdam) following the manufacturer's protocol.

3.2.11 Constructs

Construct	**Remark**
pGEX 6P1 drMxA FL (FL: full-length)	Back-up for expression
pGEX 6P1 hsMxA FL	Back-up for expression
pGEX 6P1 hsMxB FL	Back-up for expression
pGEX 6P1 mmMx1 FL	Back-up for expression
pGEX 6P1 mmMx2 FL	Back-up for expression
pGEX 6P1 rnMx1 FL	Back-up for expression
pGEX 6P1 rnMx2 FL	Back-up for expression
pGEX 6P1 btMx1 FL	Back-up for expression
pSKB-LNB drMxA FL	Expressed protein insoluble

pSKB-LNB hsMxA FL*	Expressed protein prepared in big amounts for crystallization trials and biochemical studies
pSKB-LNB hsMxB FL	Expressed protein insoluble
pSKB-LNB mmMx1 FL	Expressed protein insoluble
pSKB-LNB mmMx2 FL	Expressed protein insoluble
pSKB-LNB rnMx1 FL	Expressed protein insoluble
pSKB-LNB rnMx2 FL	Expressed protein soluble, saved as back-up
pSKB-LNB btMx1 FL	Expressed protein insoluble
pSKB-LNB hsMxA$^{23-662}$	Expressed protein insoluble
pSKB-LNB hsMxA$^{33-662}$	Expressed protein prepared in big amounts for crystallization trials and biochemical studies
pSKB-LNB hsMxA$^{38-662}$	Expressed protein insoluble
pGEX 6P1 hsMxA$^{1-361}$	Expressed protein soluble, but precipitated after cleavage of GST-tag
pGEX 6P1 hsMxA$^{1-366}$	Expressed protein soluble, but precipitated after GST cleavage
pGEX 6P1 hsMxA$^{353-662}$	Not used for expression
pGEX 6P1 hsMxA$^{361-662}$	Not used for expression
pGEX 6P1 hsMxA$^{621-662}$	Expressed protein soluble, but precipitated after cleavage of GST-tag
pGEX 6P1 hsMxA$^{622-662}$	Not used for expression
pGEX 6P1 hsMxA$^{353-662}$	Not used for expression
pSKB-LNB hsMxA$^{1-361}$	Expressed protein insoluble
pSKB-LNB hsMxA$^{1-366}$	Expressed protein insoluble
pSKB-LNB hsMxA$^{353-662}$	Expressed protein insoluble
pSKB-LNB hsMxA$^{361-662}$	Expressed protein prepared in big amounts for crystallization trials and biochemical studies
pSKB-LNB hsMxA$^{621-662}$	Expressed protein insoluble
pSKB-LNB hsMxA$^{622-662}$	Expressed protein insoluble
pSKB-LNB hsMxA$^{353-622}$	Not used for expression
pSKB-LNB hsMxA$^{361-622}$	Not used for expression
pSKB-LNB hsMxA$^{1-622}$	Expressed protein insoluble
pSKB-LNB hsMxA$^{1-654}$	Expressed protein insoluble

(dr; Danio Rerio (zebrafish); hs: *Homo sapiens* (human); mm: *Mus musculus* (mouse); rn: *Rattus norvegicus* (rat); bt: *Bos taurus* (bovine))

*Construct that yielded hsMxA stalk crystals, highlighted in red.

3.2.12 Point mutants

Construct	Point Mutants
pSKB-LNB hsMxA FL	D250N, I376D, D337K, Q358A, G392D, R408D, H412D, Y451D, D478A, E507A, M527D, S594A, H595D, F602D, L612A, L612S, K614D, L617D, L620D, E632A, K639A, R640A, R646A, R649A, QD534-535AA, EED398-400AAA, YRGR440-443AAAA, KKKK554-557AAAA, D250N+M527D, H412D+H426D, M527D+F602D, M527D+YRGR440-443AAAA, K614D+L617D+L620D, I376D+K614D+L617D+L620D, I376D+M527D+K614D+L617D+L620D, Δ533-561, M527D+Δ533-561, F602D+Δ533-561, M527D+F602D+Δ533-561, YRGR440-443AAAA+Δ533-561 (hsMxA_GBS)*, M527D+YRGR440-443AAAA+Δ533-561, M527D+L617S+YRGR440-443AAAA+Δ533-561, I376S+M527D+L617S+YRGR440-443AAAA+Δ533-561, M527D+F602D9+L617S+YRGR440-443AAAA+Δ533-561, I376S+M527D+F602A+L617S+YRGR440-443AAAA+Δ533-561
pSKB-LNB hsMxA$^{33-662}$	M527D+F602D, M527D+YRGR440-443AAAA, Δ533-561, YRGR440-443AAAA+Δ533-561 (hsMxA_GBS$^{33-662}$)*, M527D+F602D+Δ533-561, M527D+YRGR440-443AAAA+Δ533-561, I376S+M527D+F602A+L617S+YRGR440-443AAAA+Δ533-561
pSKB-LNB hsMxA$^{361-662}$	M527D+F602D, K614D+L617D+L620D, I376D+K614D+L617D+L620D, M527D+I376D+K614D+L617D+L620D
pSKB-LNB hsMxA$^{361-622}$	I376D+K614D+L617D+L620D
pSKB-LNB hsMxA$^{1-622}$	M527D+F602D, I376D+K614D+L617D+L620D

*Constructs that yielded three-domain hsMxA crystals, "_GBS" stands for G domain, BSE and stalk. The constructs are highlighted in red.

3.3 Biochemical methods

3.3.1 SDS-PAGE

SDS-polyacrylamide gel electrophoresis (SDS-PAGE) was used for separation of proteins of different molecular weight or comparison of relative protein quantities (see 3.3.13 and 3.3.14). The experiments were performed based on a standard protocol (Laemmli 1970) at denaturing, discontinuous condition.

3.3.2 Protein concentration determination

Protein concentration was determined according to (Bradford 1976) using Protein-Assay Biorad solution (Biorad). The solution was calibrated using bovine serum albumin (BSA) standards. For more accurate determination of protein concentration, absorption assays at 280 nm according to (Stoscheck 1990) were used.

3.3.3 Protein overexpression

Wildtype (wt) hsMxA and all mutants were expressed in *E.coli BL21 (DE3) Rosetta* cells. Bacteria were grown in 6 L TB medium from 60 ml overnight LB preculture at 37°C till an OD_{600} of 0.5 was reached. Then 45 µM Isopropyl-β-D-thiogalacto-pyranosid (IPTG) was added and the temperature was reduced to 19.2°C for overnight expression. The cells were collected by centrifugation at 5,000 *g* for 10 min (4°C) and the resulting pellet was resuspend in lysis buffer containing 50 mM HEPES (pH 7.5), 400 mM NaCl, 30 mM imidazole, 6 mM $MgCl_2$, 1 µM DNase, 2.5 mM β-Mercaptoethanol (β-ME), 500 µM Pefabloc SC (Roth).

3.3.4 Protein purification

Cells resuspended in lysis buffer were lysed using a microfluidizer (Microfluidics). After centrifugation at 40,000*g* for 45 min at 4°C, the soluble extract was filtered using a filter pore size of 0.2 µm.

3.3.4.1 Purification for constructs cloned in *pSKB-LNB* vector

Filtered cell extract was applied to a Ni-NTA column (GE-Healthcare, München) equilibrated with 50 mM HEPES (pH 7.5), 400 mM NaCl, 30 mM imidazole, 5 mM MgCl2, 2.5 mM β-ME. The column was extensively washed with 20 mM HEPES (pH

7.5), 800 mM NaCl, 5 mM MgCl2, 30 mM imidazole, 2.5 mM β-ME, 1 mM ATP, 10 mM KCl to remove Hsp70 which is a common contamination from E.coli and shortly with 20 mM HEPES (pH 7.5), 400 mM NaCl, 5 mM MgCl2, 80 mM imidazole, 2.5 mM β-ME. Bound MxA was eluted with 20 mM HEPES (pH 7.5), 400 mM NaCl, 300 mM imidazole, 5 mM $MgCl_2$, 2.5 mM β-ME. Unexpectedly, it was found that hsMxA can non-specifically bind to Ni-NTA in buffer containing less than 30 mM imidazole. Therefore, hsMxA eluted from the first Ni-NTA column was dialysed overnight at 4°C against 20 mM HEPES (pH 7.5), 400 mM NaCl, 2 mM $MgCl_2$, 2.5 mM β-ME in the presence of 250 µg PreScission protease to cleave off the N-terminal His-tag. The resulting protein was re-applied to a second Ni-NTA column and subsequently eluted with 20 mM HEPES (pH 7.5), 400 mM NaCl, 30 mM imidazole, 2 mM $MgCl_2$, 2.5 mM β-ME. The PreScission protease was removed via a GST column. Further purification was carried out using size-exclusion chromatography (SEC) on a Superdex200 16/60 column (GE-Healthcare) equilibrated with 20 mM HEPES (pH 7.5), 400 mM NaCl, 2 mM $MgCl_2$, 2.5 mM dithiothreitol (DTT) where it eluted in a discrete peak at approximately 300 kD. Typical yields were 1.5 mg purified human MxA protein per 1 L bacteria culture. Selenomethionine-substituted (SeMet) protein was prepared according to a standard protocol and purified in the same way as the native protein.

3.3.4.2 Purification for constructs cloned in *pGEX 6P1* vector

Filtered cell extract was applied to 15 ml reduced glutathione(GSH)-Sepharose column (GE Healthcare, München) equilibrated with 50 mM HEPES pH 7.5, 400 mM NaCl, 2.5 mM DTT. Afterwards, the column was washed with 50 mM HEPES pH 7.5, 400 mM NaCl, 2.5 mM DTT. GSH-Sepharose beads were resuspended in 1 column volume (CV) equilibration buffer and transferred to a Falcon tube and 1 mg GST-PreScission protease (GE Healthcare, München) was added to cleave the amino-terminal GST-tag. A further SEC was carried out as described in 3.3.4.1.

3.3.5 Mass spectreometry analyis of purified protein

To verify the His-tag removal of purified hsMxA, a matrix-assisted laser desorption/ ionization time-of-flight mass spectrometry (MALDI-TOF-MS) was carried out using 3,5-dimethoxy-4-hydroxy-cinnamic acid (sinapic acid) as assisting matrix with the addition of trifluoroacetic acid (TFA) (Beavis and Chait 1989). Proteins were diluted in a series from 1:3 to 1:243 from the original stock for the analysis.

3.3.6 Quality and quantity control of selected point mutants

Prior to biochemical experiments, the concentrations of wt and selected hsMxA mutants were measured by absorption at 280 nm, and validated by the Bradford method (see 3.3.2), as the mutations may cause quenching of the absorption tryptophan and tyrosine. In addition, all proteins were applied to one SDS-PAGE gel with equal sample volume and visually compared. It was thereby verified that all the proteins had the uniform concentrations for the downstream concentration-dependent experiments (Fig. 22).

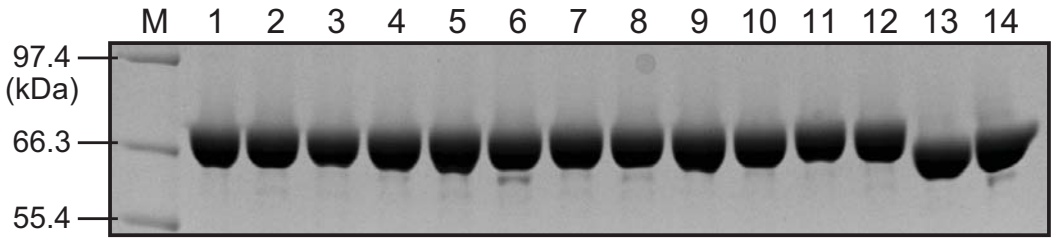

Figure 22. SDS-PAGE analysis of the concentration of wt and mutated hsMxA. M: marker, 1-14: wt hsMxA, I376D, K614D, L6147D, L620D, M527D, H595D, F602D, G392D, R408D, KKKK554-557AAAA, YRGR440-443AAAA, ΔL4 and hsMxA$^{33-662}$. Based on measured concentrations, 15 ng protein was applied to the gel for each sample. It can be observed that the proteins are homogenous and of the same quantity.

3.3.7 Nucleotide detection by HPLC

Reversed phase high-pressure liquid chromatography (HPLC) assays were carried out according to (Lenzen, Cool et al. 1995) to separate different nucleotides. The principle of the assay is based on the basis of the interaction between the hydrophobic static phase from the column and the ion pair of nucleotide and tetrabutylammonium in the mobile phase. Depending on the number of phosphates, a variable number of tetrabutylammonium ions are bound by the nucleotide which increases the retention time on the column. Furthermore, the resulting absorption peaks on the chromatograph can be used for quantification of the nucleotides. HPLC assays were used as an auxiliary method for the kinetic study of nucleotide hydrolysis (see 3.3.8).

To check if the purified protein was already loaded with nucleotide from *E. coli*, 20 µM protein sample was applied on a HPLC Ti-Series 1050 system (Hewlett Packard, Waldbronn) and separated via a reversed-phase column via a reversed-phase Hypersil ODS-2 C18 column (Thermo Scientific, Dreieich). The running buffer contained 100 mM potassium phosphate (pH 6.5), 10 mM tetrabutylammoniumbromide, 7.5%

acetonitrile. Denatured proteins were adsorbed at a C18 guard column (Knauer, Berlin). Nucleotide peaks were detected by measuring adsorption at 254 nm and compared with standard nucleotide samples.

3.3.8 Nucleotide hydrolysis assay

GTPase activities of hsMxA and the indicated mutants were determined at 37°C in 50 mM HEPES (pH 7.5), 150 mM NaCl, 5 mM KCl, 5 mM $MgCl_2$, using increasing hsMxA concentrations (0.038, 0.076, 0.15, 0.38, 0.76, 1.5 and 3.1 mg/ml, corresponding to 0.5, 1, 2, 5, 10, 20 and 40 µM, respectively; for hinge region and BSE-stalk mutants, GTPase activity was not test for 0.5 and 40 µM protein concentrations). Saturating concentrations of GTP (1-4 mM) were employed for each reaction. Reactions were initiated by the addition of protein to the final reaction solution. At different time points, reaction aliquots were 20-fold diluted in GTPase buffer and quickly transferred in liquid nitrogen. Nucleotides in the samples were separated and detected as describe in 3.3.7. Substrate GTP and hydrolysis product GDP in the samples were quantified by integration of the corresponding absorption peaks. Rates derived from a linear fit to the initial rate of the reaction (<40% GTP hydrolyzed) were plotted against the protein concentrations. To estimate k_{max}, a simple binding model was fitted to the data which describes the interaction of two GTP-bound hsMxA monomers inducing GTP hydrolysis, as previously described (Praefcke, Kloep et al. 2004).

3.3.9 Nucleotide binding assay

Fluorescence based method was used for checking the nucleotide-binding affinity of wt hsMxA and a selected mutant M527D at different protein concentrations. During the experiment, 1 µM 2'-/3'-O-(N'-Methylanthraniloyl)-GDP (mant-GDP), a fluorophore-coupled GDP analogue (Jena Bioscience) or 1 µM mant-GMP-PNP, were incubated in GTPase reaction buffer at 37°C with increasing concentrations of wt hsMxA and the M527D mutant. The peak fluorescence of an emission spectrum was recorded at an FP-6500 fluorescence spectrometer (Jasco) for each protein concentration.

3.3.10 Fast kinetics using stopped-flow assay

The experiment was according to (Kraemer, Brinkmann et al. 2002), using an RX2000 Rapid Kinetics Spectrometer Accessory (Applied Photophysics) coupled to an

Aminco Bowman Series 2 spectrofluorometer (Thermo Scientific, Dreieich). Off-rates for mant-GDP and mant-GMP-PNP were determined at 37°C by following the fluorescence after rapid mixing of 4 µM mant-nucleotide, 40 µM wt hsMxA or the M527D mutant in one syringe and a 1000-fold excess of unlabeled nucleotide (GDP or GMP-PNP, respectively) in the second syringe (excitation wavelength 366 ± 4 nm, measured emission at 435 ± 16 nm).

3.3.11 About data analysis

For data analysis for 3.3.8-10, the program GraFit5 (Erithacus Software) was used.

3.3.12 Analytical gel filtration assay

To check the oligomerization state of wt hsMxA and mutants, 1 mg of wt hsMxA or the mutants was applied to a Superdex200 10/300 analytical gel filtration column using a buffer containing 20 mM HEPES pH 7.5, 400 mM NaCl, 2 mM $MgCl_2$, 2.5 mM DTT. The column was calibrated using protein molecular weight markers from MWGF-200 Kit (Sigma-Aldrich) according to the manufacturer's protocol.

3.3.13 Right angle light scattering assay

A coupled Right angle light scattering (RALS) system and Refractive Index detector (Viscotek) was connected in line to an analytical gel filtration column Superdex200 10/300 to determine absolute molecular masses of the applied proteins. The running buffer for these experiments contained 20 mM HEPES, pH 7.5, 400 mM NaCl, 2 mM $MgCl_2$, 2 mM DTT. For each protein sample, 100 µl of a 2 mg/ml solution were applied.

3.3.14 Analytical ultracentrifugation assay

Molecular mass studies of wt hsMxA and all mutants in 20 mM HEPES, pH 7.5, 400 mM NaCl, 2 mM $MgCl_2$, 2.5 mM DTT at different protein concentrations were performed in a XL-A type analytical ultracentrifuge (Beckman, Palo Alto, CA) equipped with UV absorbance optics. Sedimentation equilibrium experiments were carried out using six-channel cells with 12 mm optical path length and the capacity to handle three solvent-solution pairs of about 70 µl liquid. Sedimentation equilibrium was reached after 2 hours (h) of overspeed at 16,000 rpm (round per minute) followed by an equilibrium speed of 12,000 rpm for about 30 h at 10°C. For some mutants, overspeed of 20,000 rpm and equilibrium speed of 16,000 rpm was used. The radial

absorbance in each compartment was recorded at three different wave lengths between 270 and 290 nm depending on the concentration used in the experiments. Molecular mass determinations employed the global fit of the three radial distributions using our program POLYMOLE (Behlke, Ristau et al. 1997) or singularly using POLYMOLA. When proteins adopt a monomer-dimer equilibrium, the molecular mass, M, can be treated approximately as a weight average parameter (M_w). This value is a composite of the monomer molecular mass (M_m) and that of the dimer (M_d) and the partial concentrations of monomers, c_m, and dimers, c_d.

$$M_w = (c_m \bullet M_m + c_d \bullet M_d) / (c_m + c_d)$$

Therefore, the equilibrium constant, K_d, can be derived with $K_d = c_m^2 / c_d$.

3.3.15 Oligomerization assay

Oligomerization assays were carried out at 2.3 mg/ml protein concentration in the absence and presence of 1 mM GTPγS. Samples were incubated at room temperature for 10 min in a buffer containing 20 mM HEPES (pH 7.5), 300 mM NaCl and 2 mM $MgCl_2$. After ultracentrifugation at 200,000 *g*, 25°C for 10 min, equivalent amounts of supernatant and pellet were loaded on SDS–PAGE.

3.3.16 Liposome co-sedimentation assay

For liposome co-sedimentation assays, the salt concentration was optimized so that wt hsMxA was not sedimented in the absence of liposomes. The final reaction conditions were 0.75 mg/ml hsMxA protein and 0.5 mg/ml unfiltered Folch liposomes fraction I (Avanti) in 20 mM HEPES (pH 7.5), 300 mM NaCl (to avoid oligomerization in the absence of liposomes, the salt concentration was optimized to 300 mM NaCl), and a 100,000 *g* spin for 20 min at 25 °C, afterwards equivalent amounts of supernatant and pellet were loaded on SDS–PAGE.

3.3.17 Other assays and techniques

Other assays and techniques whose outcome appears in 4.3.2 and 4.3.6, including cell- and virus-based assays, Influenza A virus minireplicon system, Western blot analysis and immunofluorescence analysis were performed in our collaborator's lab in Freiburg. Detailed description of these assays and techniques can be found from (Gao, von der Malsburg et al. 2010).

3.4 Crystallographic methods

3.4.1 Crystallization

For the crystals from which the hsMxA stalk structure was obtained (see 4.2), initial crystallization trials by the sitting-drop vapor-diffusion method were carried out at 20°C and 4°C. 300 nl hsMxA (15 mg/ml) were mixed with an equal volume of reservoir solution equilibrating against 85 µl reservoir solution using a Hydra II Plus One crystallization robot (Robbins Scientific). The pHClear, pHClear II, Classics, Classics II, ClassicsLite, JCSG+, Protein Complex, ComPAS, PEGs and PEGs II commercial crystal screens (Qiagen) were used for initial trials. Subsequently, manually prepared screens with different PEGs, salts and buffers combination were applied. Initial hits with tiny needles or small crystalline clusters were found after two months of set-up at 20°C in several conditions all containing low concentration of PEG3350. Refined screens were then carried out at 20°C as well as 27°C in order to accelerate the crystallization. Improved crystals were obtained from several conditions at 27°C after three weeks of set-up. Increased concentration (25 mg/ml) and volume (400 nl against 400 nl reservoir) of protein resulted in reproducible needles after two weeks incubation. Addition of Hexamine cobalt (III) chloride gave rise to further improved crystals. The final crystallization condition contained 5% PEG3350, 100 mM MES (pH 6.8), 100 mM $MgCl_2$ and 0.01 mM Hexamine cobalt (III) chloride. Crystals of selenomethionine-substituted (SeMet) protein were obtained in 5% PEG3350, 100 mM HEPES (pH 7.4), 100 mM $MgCl_2$ at 27°C after two weeks of set-up. The obtained crystals typically had dimension of 0.1 mm x 0.05 mm x 0.03 mm.

For crystals that yielded the three-domain structure of hsMxA (see 4.3), crystallization trials were initiated by the sitting-drop vapour-diffusion method were performed at 20°C. 1 µl of hsMxA_GBS or hsMxA_GBS$^{33\text{-}662}$ (see 3.2.12) at a concentration of 10-20 mg/ml were mixed with an equal volume of reservoir solution containing 7% PEG3350, 100 mM HEPES (pH 7.6), 80 mM NaCl, 2.5% 2-methyl-2,4-pentandiol (MPD) and 5% glycerol. Crystals appeared after two days and reached their final size (0.2 mm x 0.2 mm x 0.8 mm) within five days. Crystals of SeMet substituted hsMxA_GBS$^{33\text{-}662}$ were obtained in 5% PEG 3350, 100 mM HEPES (pH 7.5), 80 mM NaCl, 2% MPD and 2% ethylene glycol and had similar sizes as native crystals.

In both cases, no crystals were obtained in the presence of 1-2 mM GDP, GTPγS or GMP-PNP.

3.4.2 Cryo-protection of crystals

To prevent or alleviate the radiation damage to the crystal during diffraction data collection especially at modern synchrotron facilities, handling crystals with suitable cryo-protectant solutions becomes a necessary step.

For crystals yielding the hsMxA stalk structure, cryo-solutions were composed of protein buffer and reservoir solution from corresponding crystallization conditions mixed with equal volume, plus extra 25% glycerol, or 25% PEG200, or 25% 2-Methyl-2,4-pentanediol (MPD), or 12.5% saccharose. Crystals were soaked into 2 µl cryo-solutions at 20°C for 10 s, before flash frozen in liquid nitrogen. Crystals frozen with different cryo-protectant were tested either at an in-house copper-Kα rotating X-ray anode with an osmic mirror (λ = 1.5418 Å) or at synchrotron facility Berlin electron storage ring company for synchrotron radiation (BESSY, Berlin). The final cryo-conditions were 2.5% PEG3350, 60 mM HEPES (pH 7.4), 50 mM $MgCl_2$, 1 mM DTT, 25% PEG200 for native hsMxA crystals and 2.5% PEG3350, 60 mM HEPES (pH 7.4), 50 mM $MgCl_2$, 1 mM DTT, 25% glycerol for SeMet replace hsMxA crystals. Crystals were stored in liquid nitrogen before and if necessary, after diffraction tests.

For crystals yielding the three-domain structure of hsMxA, a cryo-solution containing 4% PEG3350, 60 mM HEPES (pH 7.6), 150 mM NaCl, 1 mM DTT, 2% MPD, 3% glycerol, 10% PEG200 was used for native crystals and 3% PEG3350, 60 mM HEPES (pH 7.5), 150 mM $MgCl_2$, 1 mM DTT, 2% MPD, 11% ethylene glycol was used for SeMet substituted protein crystals.

3.4.3 Diffraction data collection

For crystals yielding the hsMxA stalk structure, data sets were recorded at beamline MX14.1 equipped with an MX-225 detector (RAYONIX) at BESSY from single crystals at 100 K. Two data sets were used for structure determination, namely one native data set collected at a wavelength of 0.91841 Å of incident X-ray beam and detector distance of 210.15 mm for 200 images with 5 s exposure time and 1° oscillation range for each image. The data set for a SeMet replace protein crystal was obtained at selenium peak wavelength 0.97968 Å (peak wavelength of selenium absorption instantly measured by fluorescence scan) and detector distance at 288.70 mm for 360 images with 2.5 s exposure time and 1° oscillation range for each image.

For crystals yielding the three-domain structure of hsMxA, data sets for native hsMxA_GBS and hsMxA_GBS$^{33\text{-}662}$ crystals recorded at beamline MX14.1 from single crystals at a wavelength of 0.91841 Å of incident X-ray beam and detector distance of 300 mm for XXX images with 15 s exposure time and 1° oscillation range for each image. The data set for SeMet substituted hsMxA_GBS$^{33\text{-}662}$ crystal was collected at beamline X06SA at Swiss Light Source (SLS) equipped with a PILATUS 1M detector from a single crystal at a wavelength of 0.97960 Å (peak wavelength of selenium absorption instantly measured by fluorescence scan) of incident X-ray beam. 1,440 diffraction images were recorded with a total exposure period of approximately 240 s and 1° oscillation range for each image.

3.4.4 Data processing

For the hsMxA stalk structure, raw data were indexed and integrated using program sutie XDS (Kabsch 1993). The quality of the data set was then evaluated by calculating R_{symm} which compares symmetry related reflections according to Equation 2.

$$R_{symm} = \frac{\sum_{hkl}\sum_{i}\left|I_i - \langle I \rangle\right|}{\sum_{hkl}\sum_{i}\left|I_i\right|}$$

h, k, l - indices of independent reflections with the average intensity <*I*>
I_i - intensities of independent reflections.

reflections were then scaled by program XSCALE from XDS package (Kabsch 1993) and the file was converted to CCP4 format for the next step by using program XDSCONV (Kabsch 1993) and 5% of all reflections were assigned to test set (see 3.4.6).

For the three-domain hsMxA structure, reflections from native hsMxA_GBS and hsMxA_GBS$^{33\text{-}662}$ crystals were analyzed, truncated and scaled using the Diffraction Anisotropy Server (Strong, Sawaya et al. 2006) after processed using the XDS program suite. 5% of all reflections were assigned to the test set and the total number of reflections therein in was over 500, which at low resolution (worse than 3 Å) can still effectively limit the bias that may be generated in the subsequent refinement step. Raw data for SeMet substituted hsMxA_GBS$^{33\text{-}662}$ crystal were indexed, integrated and scaled as for hsMxA stalk structure.

Based on the molecular mass of the protein and the volume of the asymmetric unit, the number of protein molecules in the asymmetric unit can be estimated (Matthews 1968). The Matthew coefficient V_M is derived by Equation 3.

$$V_M = \frac{V}{M \bullet W \bullet Z}$$

MW: Molecular weight of the monomer in Dalton
V: Volume of the asymmetric unit in Å^3
Z: Number of molecules in the asymmetric unit

For protein crystals, the average Matthews coefficient is 2.5 Å^3/Da corresponding to a solvent content of 50% (Matthews 1968). V_M ranges from 1.6 to 3.5 Å^3/Da for protein crystals. The solvent content x_S of a crystal can be estimated by Equation 4.

$$x_s = 1 - \frac{1}{V_M \bullet N_A \bullet \rho_P} \sim 1 - \frac{1.23\ A^3 / Da}{V_M}$$

V_m = Matthew coefficient
N_A = Avogadro constant
ρ_P = protein density ~ 1.35 g/cm^3

3.4.5 Structure solution

Every reflection is a signal of a diffracted X-ray with indices *h*, *k*, *l* in relationship to the crystal lattice. It carries information as a property of wave containing both amplitudes and phases needed for structure determination. This information of the reflection is termed structure factor F_{hkl} and it can be represented as complex vector according to Equation 5 (Rhodes 2006).

$$F_{hkl} = A_{hkl} + iB_{hkl}$$

In this manner F_{hkl} can also be described as the composition of its amplitude $|F_{hkl}|$ and its phase angle α_{hkl} (Equation 6).

$$F_{hkl} = |F_{hkl}| \bullet (\cos\alpha_{hkl} + i\sin\alpha_{hkl}) = |F_{hkl}| \bullet e^{i\alpha hkl} = |F_{hkl}| \bullet e^{2\pi i\alpha' hkl}$$

where α and α' are the phase angle in radians and cycles, respectively.

The electron density ρ at any given point x, y, z in the real space can be calculated by Fourier synthesis according to equation 6 if the structure factors F_{hkl} of a crystal (Equation 7) are determined.

$$\rho(x,y,z) = \frac{1}{V}\sum_{h}\sum_{k}\sum_{l}\left|F_{hkl}\right| \bullet e^{-2\pi i(hx+ky+lz-\alpha'_{hkl})}$$

where V is the volume of the unit cell in the crystal and h,k,l are the indices in three dimensions of independent reflections.

In macromolecular X-ray diffraction experiments, the amplitude $\left|F_{hkl}\right|$ of every structure factor can be derived directly from the square root of the measured intensity, $(I_{hkl})^{½}$. On the other hand, the phase angle α' of every structure factor can not be directly measured but only indirectly obtained, which is often referred to as the "phase problem". There are several common methods invented to solve the phase problem for structure determination of macromolecules, including multiple isomorphous replacement (MIR), single or multiple wavelength anomalous dispersion (SAD or MAD) and molecular replacement (MR).

For the hsMxA stalk structure, the phase problem was solved by SAD. Selenium atom sites were found with SHELXD (Sheldrick 2008) using the anomalous signal of the peak data set. Initial phases were calculated and refined using the program SHELXE (Sheldrick 2008) with the graphical interface HKL2MAP (Pape and Schneider 2004). An initial model was manually built with COOT (Emsley and Cowtan 2004), where the positions of selenium atoms were used to assign the sequence. Since the native data set was non-isomorphous to the SeMet one, MR with the initial model was carried out against the native data using MOLREP (Vagin and Teplyakov 1997).

For the three-domain hsMxA structure, The phase problem was solved by MR using Phaser (McCoy, Grosse-Kunstleve et al. 2007), with the nucleotide-free rat dynamin 1 G domain (Reubold, Eschenburg et al. 2005) and the hsMxA stalk as search models. An anomalous difference Fourier map was calculated by fast Fourier transform (FFT) in CCP4 using the processed SeMet substituted hsMxA_GBS$^{33\text{-}662}$ data and phases of the refined model to aid the assignment of amino acid sequence. Model building was done with COOT.

3.4.6 Structure refinement

Refinement is iteratively carried out to improve the initial phases and the geometry of the model. During refinement, an input model is improved by minimizing a geometrical and a crystallographic energy term. The geometrical term of a model comprises the empirical chemical parameters, including bond length and angles, torsion angles, planar restraints, chiral centre restraint, non-bonded interactions, hydrogen bonds, and van-der-Waals interaction. The crystallographic term is composed of the amplitudes of the experimentally derived reflections $|F_{obs}|$. During the refinement process, new structure factors (F_{calc}) are calculated from the input model by Fourier transform. An important statistical parameter indicating quality of a model can be derived from R_{cryst} which compares measured and calculated amplitudes of structure factors according to Equation 8.

$$R_{cryst} = \frac{\sum \left| |F_{obs}| - |F_{calc}| \right|}{\sum |F_{obs}|}$$

The refinement process is generally accompanied by manual real-space model building. With the calculated phases and the measured reflection intensities, electron density maps can be obtained. However, the calculated phases may contain bias from the potentially incorrect or inaccurate input model. To reduce bias, a test set of reflections is excluded from refinement process (typically 5–10% of the reflections). These reflections are used for calculating an R_{free} value (Brunger 1992; Brunger 1997; Weiss 2001) as an independent parameter to better monitor the refinement process.

For the hsMxA stalk structure, the program Refmac5 was used for refinement (Murshudov, Vagin et al. 1997). According to the resolution of hsMxA stalk structure, the temperature (B) factors of every atom and then the position were refined by Refmac5. All hydrogen atoms were considered in the refinement to improve geometrical parameters of the model. 5% of the reflections were used as test set (see 3.4.4). 10 cycles of TLS (translation, libration, screw-rotation displacement) refinement using two TLS groups (Winn, Murshudov et al. 2003) were included in each refinement step, followed by 10 cycles of maximum likelihood restrained refinement.

For the three-domain hsMxA structure, refinement was carried out by CNS (version 1.3) employing a deformable elastic network (DEN) (Brunger, Adams et al. 1998; Schroder, Levitt et al. 2010). A homology model of the hsMxA G domain was calculated based on the nucleotide-free G domain of rat dynamin 1 (PDB code 2AKA) (Reubold, Eschenburg

et al. 2005) using the SWISS-MODEL server (Arnold, Bordoli et al. 2006) and was used, together with the published hsMxA stalk, to set up DEN restraints. At the final stage of refinement, TLS refinement was carried out for the model with 3 TLS groups, in combination with the script for jelly body restraints using Refmac5.

3.4.7 Structure validation

Before finalized, refined models are often checked for their geometry term to improve their stereochemical conformity. Common issues concerned in this step include Ramchandran rotamers (Ramachandran, Ramakrishnan et al. 1963), atom contact and clash, and C_β deviations, etc. The final models for both hsMxA stalk and three-domain hsMxA were validated by the programs Procheck (Laskowski, MacArthur et al. 1993) and MolProbity (Chen, Arendall et al. 2010).

3.4.8 Structure analysis and figure preparation

The program LIGPLOT (Wallace, Laskowski et al. 1995) was used for checking and plotting contacting amino acids at the dimer interfaces. Interface areas were calculated using CNS (Version 1.2) (Brunger, Adams et al. 1998) (Brunger 2007). Figures were prepared using PyMol (DeLano 2002), Molscript (Kraulis 1991), and Raster3D (Merritt and Murphy 1994). The conservation plot was calculated using the Consurf server (Landau, Mayrose et al. 2005) and visualized using ccp4mg (Potterton, McNicholas et al. 2004). The model of the oligomerized stalks was created using Swiss PdbViewer (Guex and Peitsch 1997) and manually fitted in the electron density map of oligomerized dynamin (Mears, Ray et al. 2007) using Chimera (Pettersen, Goddard et al. 2004). The oligomer was extended using superpose and pdbset from ccp4. The hydrophobic surface representation was generated using VASCo (Steinkellner, Rader et al. 2009).

4 RESULTS

4.1 Production of human MxA protein

4.1.1 Expression screen to obtain soluble Mx proteins

For structural and biochemical studies, sufficient amounts of purified proteins are indispensible. To achieve this, an expression screen for Mx proteins from different species was conducted (see 3.2.11). His-tagged versions of eight different full-length hsMxA clones were expressed in bacteria (see 3.3.3) and purified in small scale. Overexpression was seen for all the Mx protein constructs in *pSKB-LNB* vector after overnight incubation (Fig. 23). IPTG concentrations from 30 to 100 µM were tested for induction and at 45 µM IPTG the promoter on *pSKB-LNB* vector was already fully activated (data not shown). Of all eight constructs, only human MxA and rat Mx2 turned out to be soluble (data not shown). All further experiments were consequently carried out using human MxA (hsMxA).

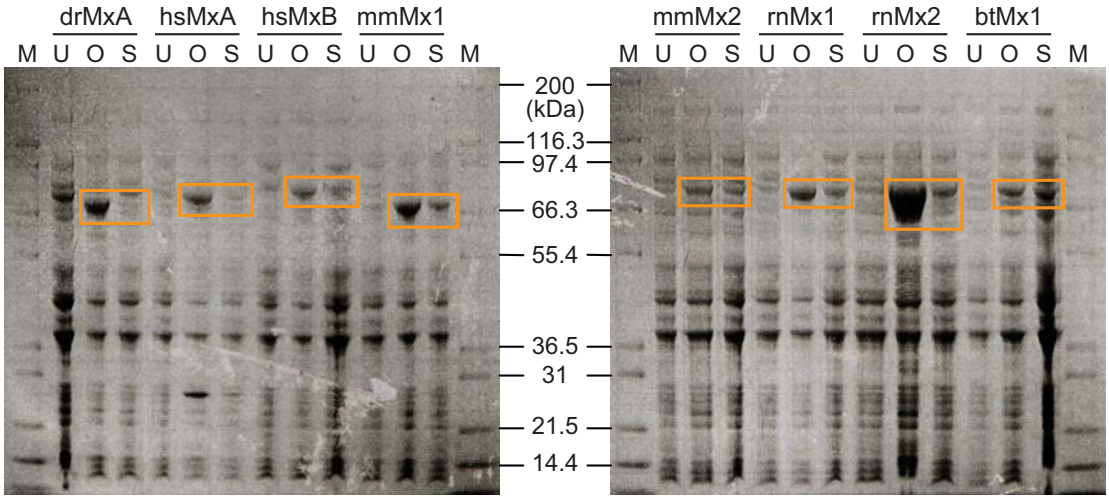

Figure 23. Overexpression test for different Mx constructs. M: marker; U: uninduced sample; O: expression profile after overnight incubation at 19.2°C, S: expression profile after incubation at 37°C for 4 hours. Abbreviations for the species are same as in 3.2.11. Target protein bands are highlighted by orange rectangles. Molecular masses of the marker are indicated.

4.1.2 Purification of human MxA protein and its truncations

To obtain sufficient amount of soluble protein, expression of His-tagged hsMxA was scaled up (see 3.3.3). The purification of His-tagged hsMxA comprised two affinity chromatography and one size exclusion chromatography step (see 3.3.4.1). The two-

step Ni-NTA purification resulted in hsMxA of over 95% purity, as assessed by SDS-PAGE (Fig. 24A). It was noted that hsMxA eluted as a trimer or tetramer during the final size-exclusion step (Fig. 24B). Complete removal of the His-tag from purified hsMxA was confirmed by MALDI-TOF-MS (see 3.3.5) (Fig. 24C). Purified hsMxA was confirmed to be nucleotide-free by HPLC (see 3.3.7) (Fig. 24D).

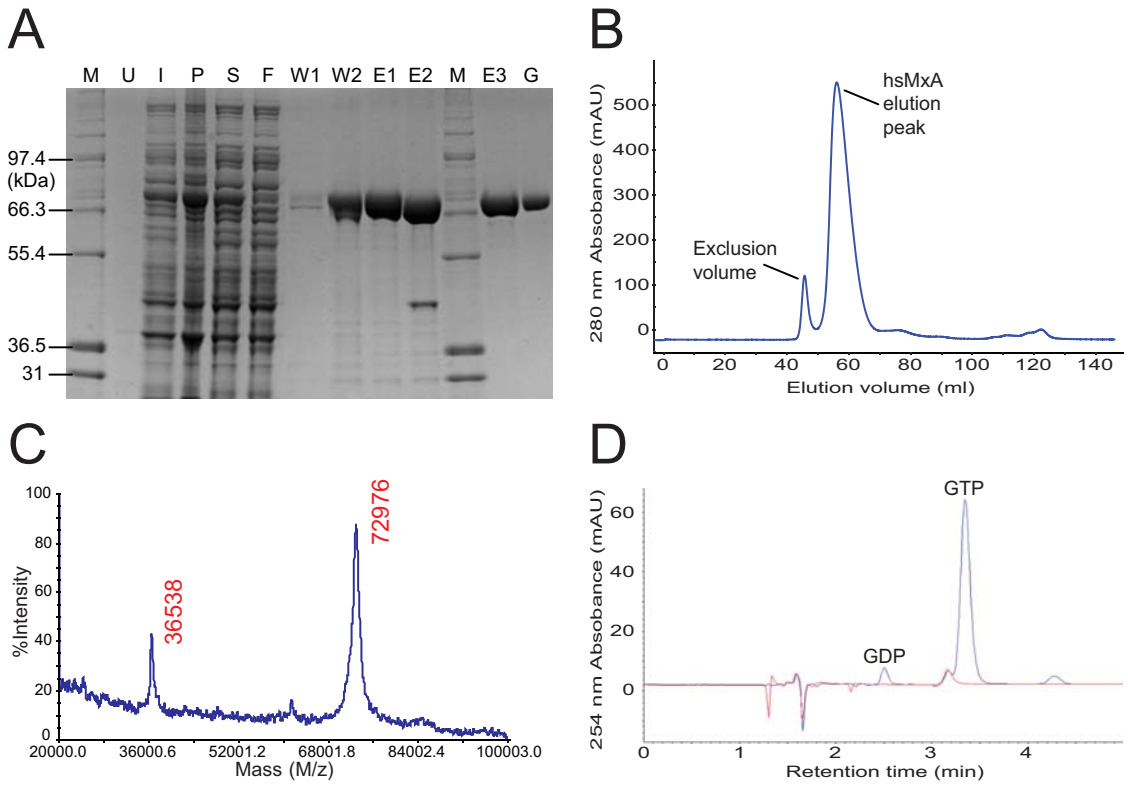

Figure 24. Purification of hsMxA. A) SDS-PAGE of hsMxA purification. M, protein molecular weight marker; U, non-induced bacteria culture; I, induced bacteria; P, pellet after ultra-centrifugation of the cell lysate; S, soluble extract of the cell lysate; F, flow-through of the soluble extract on Ni-NTA column; W1, flow-through of the high-salt and ATP wash; W2, flow-through of the high-imidazole wash; E1, elution after first Ni-NTA; E2; E1 after digestion and dialysis overnight; E3, elution after second Ni-NTA; G, after size-exclusion/gel filtration. The molecular weights of the marker are indicated. B) gel filtration profile of hsMxA purification. hsMxA elutes as a single peak. C) MALDI-TOF-MS verification of purified hsMxA. Clear signals for hsMxA at the expected molecular weights were observed. D) The nucleotide-loading was analyzed by HPLC. The profile for GTP standard is shown in blue, and the profile for purified hsMxA is shown in red. The GTP and GDP peaks are indicated.

As hsMxA has a non-conserved N-terminal sequence which was predicted to be unstructured, three N-terminal truncation constructs, namely hsMxA$^{23-662}$, hsMxA$^{33-662}$ and hsMxA$^{38-662}$ were designed for the purpose of obtaining hsMxA variants having fewer flexible regions and therefore a higher probability of

crystallization (see 3.2.11). Of these truncations, only hsMxA$^{33-662}$ could be expressed and purified, using the same protocol as for full-length hsMxA.

4.1.3 Buffer optimization for human MxA protein

The stability of a protein in solution depends on pH, oxidation-reduction (redox) environment, ionic strength, and the presence of necessary ligands, if applicable. Therefore buffer optimization was carried out for hsMxA FL and hsMxA$^{33-662}$ by varying buffers, pH, ionic strength (Na^+ and imidazole), and additives and ligands including Mg^{2+} and guanine nucleotides. The stability of the protein was monitored by determining the ratio of pellet/supernatant fraction after ultracentrifugation (see 3.3.15) at 200,000 *g* for 10 min at 4°C, with the assumption that a stable protein remains in the supernatant.

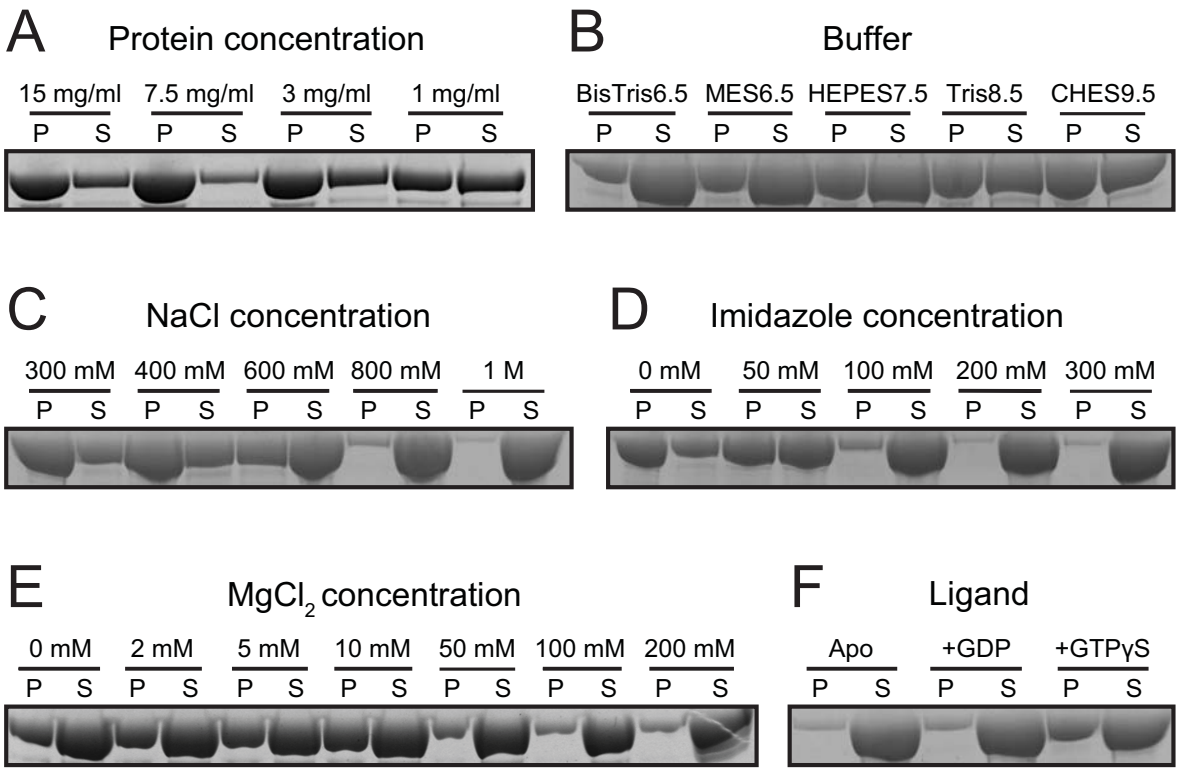

Figure 25. Buffer optimization based on ultracentrifugation assays. A) hsMxA$^{33-662}$ stability at different protein concentrations. B) Influence of the buffers and corresponding pH for hsMxA$^{33-662}$. Numbers after the name of each buffer indicate the pH values. C-E) hsMxA FL under different NaCl, imidazole, or $MgCl_2$ concentrations, respectively. F, hsMxA FL in the absence and presence of 1 mM guanine nucleotides with 1 M NaCl and 5 mM $MgCl_2$. Unless specified, proteins were tested at a concentration of 15 mg/ml in 50 mM HEPES pH 7.5 and 300 mM NaCl. For B and C, proteins that were used were from the supernatant of a previous ultra-centrifugation run and were therefore "pre-screened" for stability. P and S stand for pellet and supernatant fraction, respectively, after SDS-PAGE.

hsMxA at different concentrations was tested in the ultracentrifugation assay. It was observed that hsMxA aggregates in a concentration-dependent manner (Fig. 25A), which is a typical feature of dynamin superfamily members, although this aggregated hsMxA species may contain functional oligomers (2.3.1). hsMxA was observed to have less aggregation in weakly acidic or neutral environments (Fig. 25B). Furthermore, high ionic strength prevented aggregation of hsMxA (Fig. 25C) and high imidazole concentration also stabilized the protein (Fig. 25D). $MgCl_2$ as an additive in low concentrations did not affect the protein's stability, but it acted as a stabilizing agent in concentrations of 50 mM or higher (Fig. 25E). Finally, it was found that upon binding of GTP analogues, hsMxA had the propensity to aggregate or oligomerize even in 1 M NaCl (Fig. 25F). Additionally, GDP-binding also promoted the aggregation of hsMxA. Based on these assays, the final buffer for hsMxA contained 20 mM HEPES pH 7.5, 400 mM NaCl, 2 mM $MgCl_2$ and 2.5 mM DTT. The protein is stable in this buffer for at least three days at room temperature and up to one week at 4°C.

4.2 Structure of the human MxA stalk

4.2.1 Crystallization of the human MxA stalk

Initial crystallization trials were carried out using purified hsMxA FL or hsMxA$^{33-662}$ at 10-15 mg/ml at 4°C and 20°C in the absence or presence of GDP, GMP-PNP, or GTPγS, using various commercial screens and "home-made" conditions. Both sitting drop and hanging drop setups were applied (see 3.4.1). However, the proteins tended to precipitate in most of the conditions, and the addition of GDP further increased precipitation. No crystals were observed within the first month after the setup of all crystallization trays.

The first crystals for hsMxA FL were observed after two months in conditions containing 5-7% PEG3350 or PEG4000, and different salts in 50 mM or 100 mM concentration at weakly acidic pH and 20°C in hanging drops (Fig. 26A-D). Interestingly, some of these crystals were grown in the presence of 1 mM GDP or GMP-PNP additive. Overall, these crystals were tiny needles or rods and did not diffract X-rays.

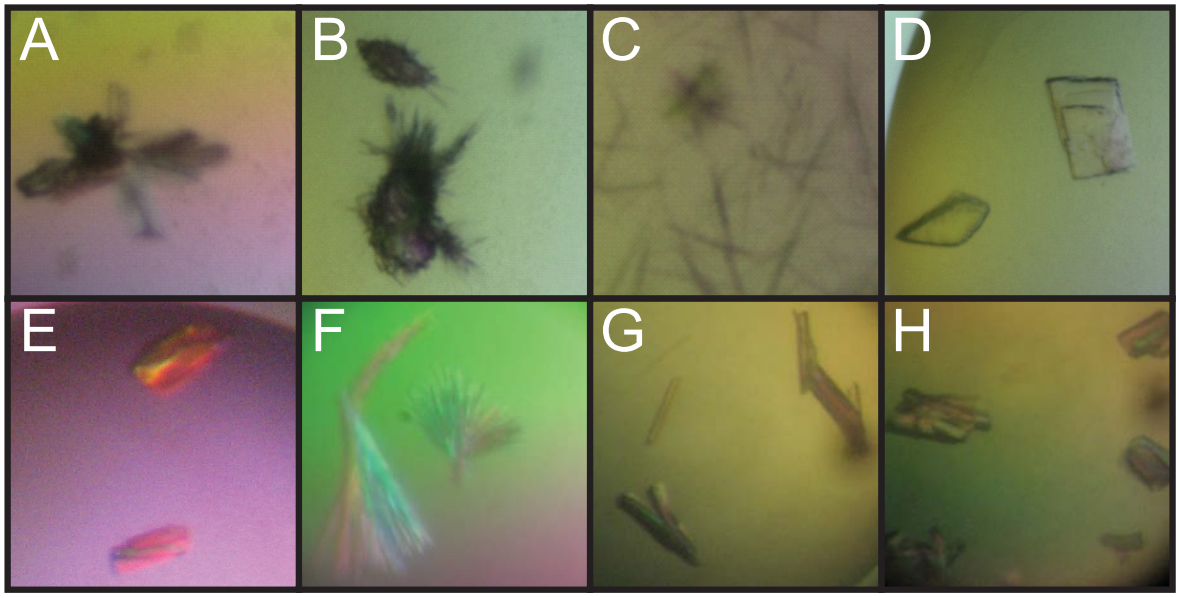

Figure 26. Crystals of hsMxA stalk. A) and B) Initial apo hsMxA crystals. C) Initial hsMxA crystals grown with GDP. D) Initial hsMxA crystals grown with GMP-PNP. E-G) Refined crystals of apo hsMxA. H) Refined crystals of SeMet apo hsMxA.

Initial crystallization conditions were refined in order to obtain single crystals suitable for X-ray diffraction. The incubation temperature was increased to 27°C which

accelerated the crystallization to two weeks. Crystals were not sensitive to most widely used cryo-protectants, such as glycerol, PEG200, or saccharose, and behaved robustly during the freezing step. Final crystals were had dimension of 0.1 mm × 0.05 mm × 0.03 mm (Fig. 26E-G) and diffracted X-rays to a resolution of 2.4 Å at a synchrotron beamline. Crystals of SeMet hsMxA stalk (Fig. 26H) were obtained from similar conditions yielding as for native crystals and diffracted X-rays to 2.8 Å at the synchrotron (see 3.4.1).

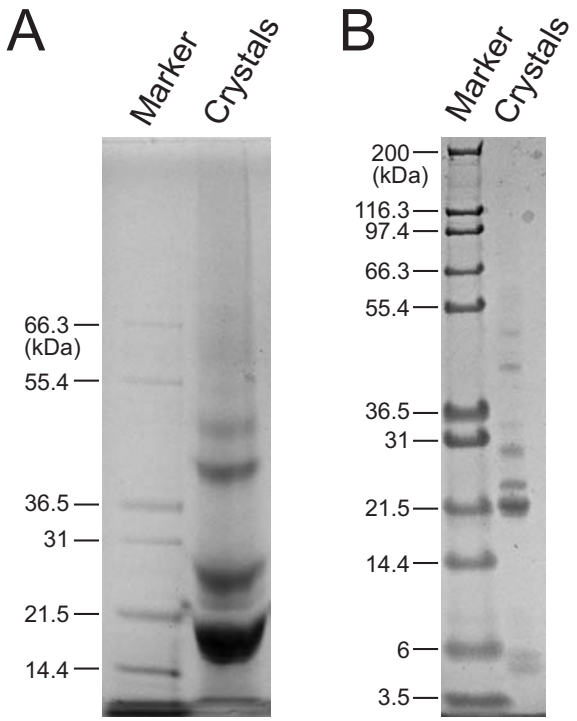

Figure 27. Analysis of dissolved hsMxA crystals. SDS-PAGE of dissolved hsMxA crystals using A) MOPS buffer and B) MES buffer.

To determine whether the crystals contained full-length hsMxA, approximately 100 hsMxA crystals were collected with a small loop, washed in reservoir solution and analyzed by SDS-PAGE in either MOPS (Fig. 27A) or MES buffer (Fig. 27B). A non-homogenous mixture of fragments of varying sizes was detected, and all fragments contained peptides of the MD and/or GED of hsMxA, as determined by in-gel digests and MALDI-TOF-MS analysis. Most of the fragments were smaller than 35 kD (size of the stalk, see 5.2.3). The inhomogeneity of these samples prevented the direct determination of the exact boundaries of each fragment. Consequently, the boundaries of the stalk model were determined solely based on evidence from the electron density.

4.2.2 Structural determination of the human MxA stalk

To determine the structure of hsMxA fragment, x-ray diffraction data of the crystals were collected at BESSY II (see 3.4.3). Crystals diffracted to a maximal resolution of 2.4 Å. The space group of the hsMxA crystals was found to be triclinic P1 based on test diffraction images. Based on subsequent Matthews coefficient calculation, the crystal should contain one full-length hsMxA per asymmetric unit. The data collection statistics are summarized in Table 1.

Table 1. Data collection statistics of native and SeMet hsMxA1 crystals.

Data collection	Native	SeMet[a]
Space group	P1	P1
Unit cell dimensions		
a, b, c (Å)	50.1, 57.4, 57.9	51.0, 57.7, 57.5
α, β, γ (°)	65.8, 88.4, 74.8	65.6, 88.9, 75.2
Wavelength (Å)	0.91841	0.97968
Resolution (Å)*	19.95-2.40 (2.46-2.40)	19.74-2.76 (2.83-2.76)
Unique reflections	21,393 (1,547)	27,647 (1,901)
Completeness (%)*	97.1 (96.7)	93.2 (86.6)
R_{symm}*, a, b	0.062 (0.387)	0.067 (0.395)
$I/\sigma(I)$*	14.91 (3.76)	7.92 (2.08)
Redundancy*	3.52 (3.54)	1.99 (1.95)

*Numbers in brackets represent values from the highest resolution shell.
[a]For the SeMet data Friedel pairs were treated as separate observations.
[b]R_{symm} is described in 3.4.4.

Using the data from SeMet substituted protein crystals, 16 Selenium atoms were found in the asymmetric unit and an initial electron density map was calculated from the anomalous signal using the SAD method and improved by solvent flattening (3.4.5). Several helical-like regions arranged in a 2-fold rotational symmetry were clearly discerned (Fig. 28). The position of 16 Selenium atoms was determined and the electron density was able to be assigned with reference to the amino acid residue sequence of hsMxA. Later, it became clear that it was indeed some proteolytic fragments from hsMxA that had been crystallized after long time incubation at a high temperature.

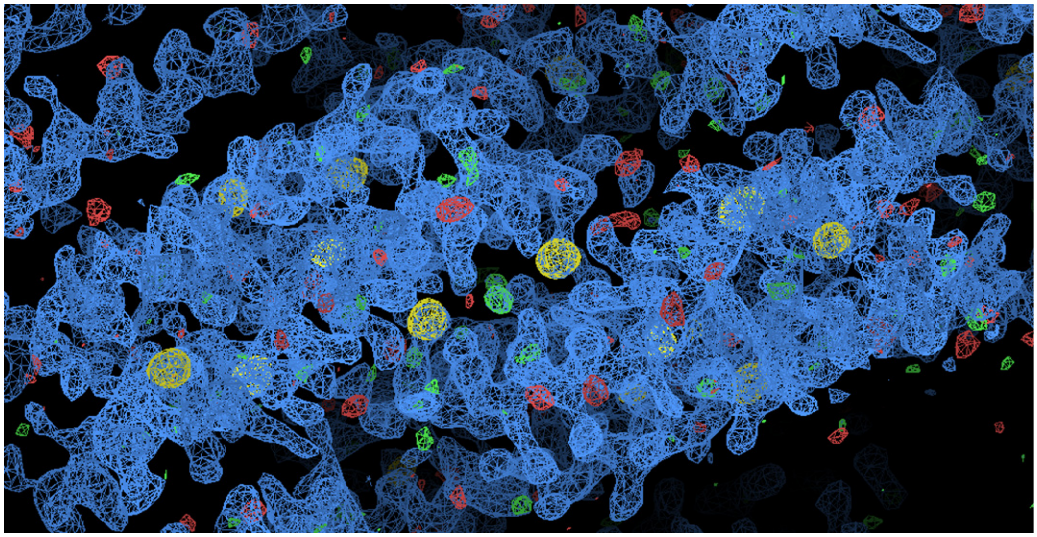

Figure 28. Initial 2*Fo-Fc*, *Fo-Fc* and anomalous difference map from a hsMxA crystal. The 2*Fo-Fc* map is shown in blue mesh at contour level of 1.2σ, the *Fo-Fc* map is shown in green (positive) and red (negative) mesh at 3σ, and the anomalous difference map is shown in yellow mesh at 4σ, indicating the positions of Selenium atoms.

The manual building of the model in real space and refinement in reciprocal space were iteratively performed until a final model with an R_{work} value of 19.3% and an R_{free} value of 25.7% was obtained. The refinement statistics are summarized in Table 2

Table 2. Refinement statistics of native hsMxA structure.

Refinement	Native
Resolution (Å)	19.95 – 2.40
R_{work}[a] / R_{free}[b]	0.193 / 0.257
Monomers / asymmetric unit	2
Number of atoms	
Protein	3,677
Ligand / Ion	0
Water	102
B-factors (Å²)	
Protein	45
Water	24
Root mean square deviations (R.m.s.d.)	
Bond lengths (Å²)	0.011
Bond angles (°)	1.152

[a] R_{work} is the same as R_{cryst} described in 3.4.6.
[b] According to Weiss 2001.

Indeed, the crystal contained two molecules (A and B) proteolytic fragment of hsMxA encompassing the MD and N-terminal portion of the GED in the asymmetric unit. The two fragments were related by non-crystallographic 2-fold rotational symmetry. The final model had an excellent geometry with 97% of all residues in the most favored region and none in disallowed region of the Ramachandran plot (Fig. 29). Molecule A, which is described in the following paragraphs regarding its structural properties, comprises residues 366–438, 448–531 and 573–633 (219 residues in total). Molecule B comprises residues 367–435, 451–531, and 576–636 (211 residues in total). The common residues of both molecules can be superimposed with a root mean square deviation of 0.7 Å.

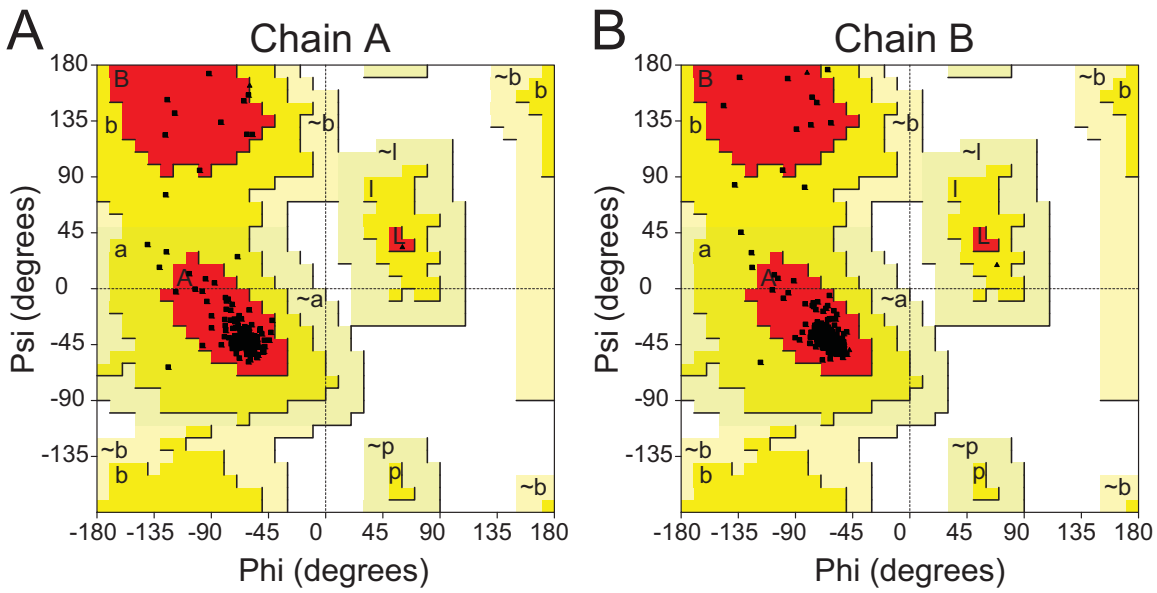

Figure 29. Ramachandran plot of both chains of the hsMxA stalk structure. A) 97.1% of all residues in chain are in the most favored region and 2.9% in allowed regions. B) 96.0% of all residues in chain B are in the most favored region and 4.0% in allowed region. No residue is in the disallowed region.

4.2.3 Structural analysis of the human MxA stalk

According to the final model, each monomer spans nearly the complete MD and the N-terminal part of the GED (amino acids 366–633) (Fig. 30A), which together fold into an elongated antiparallel four-helical bundle where the MD contributes three helices and the GED one (Fig. 30B, 31). This segment corresponds to the stalk region of dynamin (Chen, Zhang et al. 2004), and is therefore referred to it as the stalk of hsMxA. The first visible amino acid, Glu366, is 15 amino acids downstream of the last visible residue of the corresponding G domain structure in rat dynamin (Fig. 31) (see also 2.3.2). Glu366 marks the start of helix α1 in the hsMxA stalk, which is divided

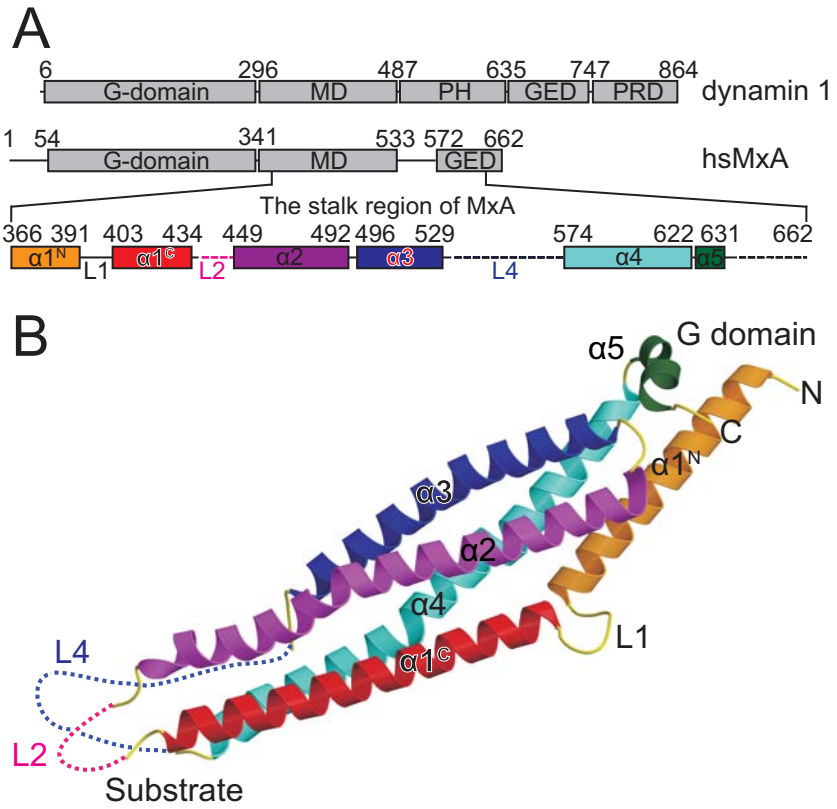

Figure 30. Structure of the hsMxA stalk. A) The domain organization of hsMxA and human dynamin 1. Secondary structure borders are shown by residue numbers and α-helices in the hsMxA stalk are colered as in B. Regions not solved in the structure are indicated by dashed lines. B) Ribbon-type representation of the hsMxA stalk with N- and C-termini labeled. The putative positions of the G domain and substrate of hsMxA are indicated. Disordered loops are shown as dashed lines.

into $\alpha1^N$ and $\alpha1^C$ (where N and C refers to the amino- and carboxyl-terminal), by a 10-amino-acid-long loop, L1, that introduces a 30° kink. A putative loop L2 (amino acids 438–447) opposite of the deduced position of the G domain is not visible in the structure. L2 was previously demonstrated to be the target of a functionally neutralizing monoclonal antibody (see 2.3.3). Helix α2 runs antiparallel to α1 back towards the G domain. It ends in a short loop, L3, followed by helix α3 that extends in parallel to α1. The 40 amino-acid-long loop L4 (residues 532–572) is sequentially in analogy to the PH domain of dynamin (Fig. 28A, 29) and is absent in the model. L4 is predicted to be unstructured and was previously shown to be proteinase K sensitive (2.3.3). At the C-terminus, the GED supplies 44 residues to helix α4 which proceeds in parallel to helix α2 back to the G domain, followed by a short helix, α5, which directs the polypeptide chain towards the N-terminus of the MD. The C-terminal 30 highly conserved residues of the GED known to be involved in antiviral specificity (2.3.3) (Zurcher, Pavlovic et al. 1992) are missing in the model. The model of hsMxA stalk was deposited into the PDB with the code accession 3LJB.

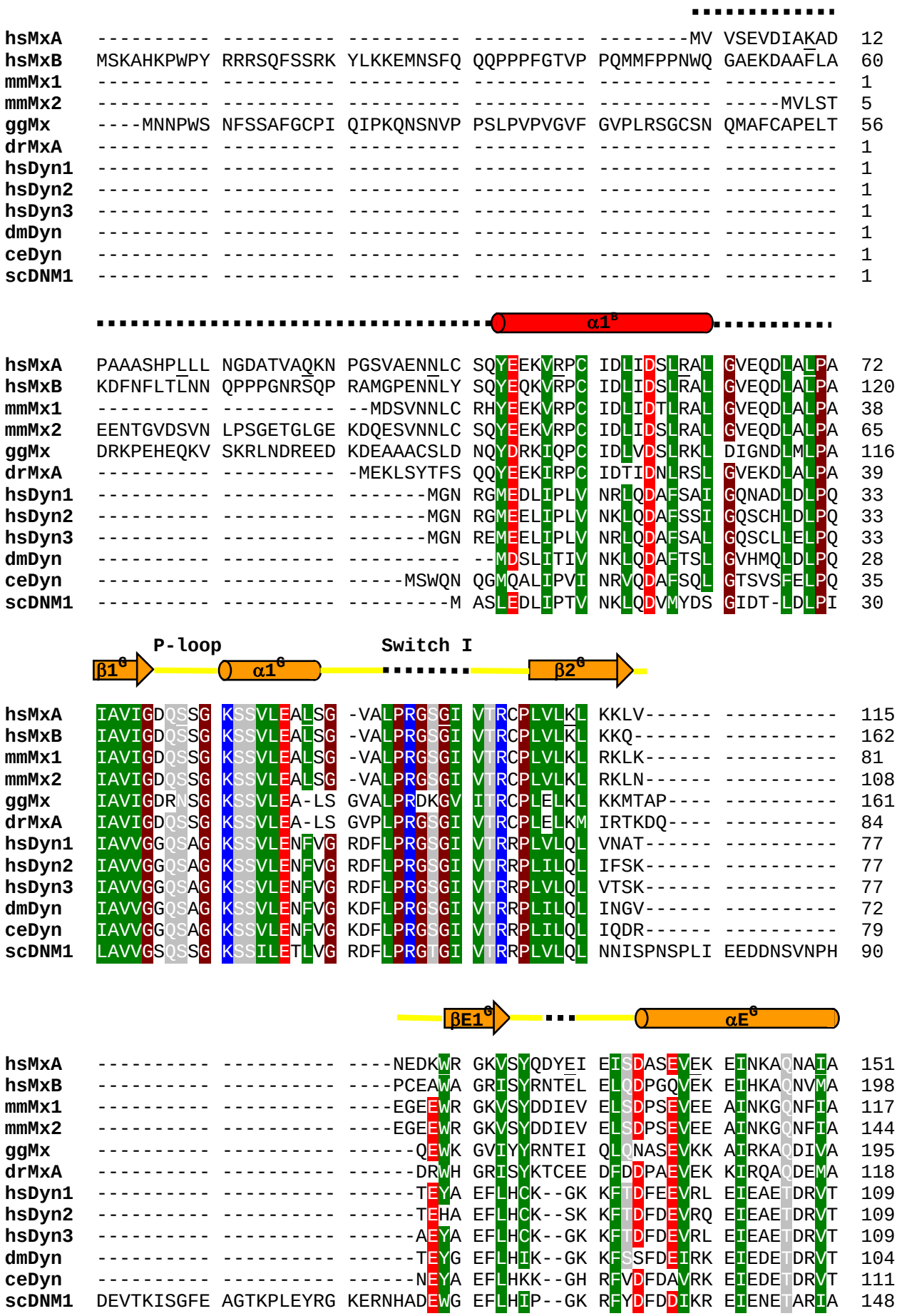


```
hsMxA   ---------- ---------- ---------- ---------- --------MV VSEVDIAKAD  12
hsMxB   MSKAHKPWPY RRRSQFSSRK YLKKEMNSFQ QQPPPFGTVP PQMMFPPNWQ GAEKDAAFLA  60
mmMx1   ---------- ---------- ---------- ---------- ---------- ----------  1
mmMx2   ---------- ---------- ---------- ---------- ---------- -----MVLST  5
ggMx    ----MNNPWS NFSSAFGCPI QIPKQNSNVP PSLPVPVGVF GVPLRSGCSN QMAFCAPELT  56
drMxA   ---------- ---------- ---------- ---------- ---------- ----------  1
hsDyn1  ---------- ---------- ---------- ---------- ---------- ----------  1
hsDyn2  ---------- ---------- ---------- ---------- ---------- ----------  1
hsDyn3  ---------- ---------- ---------- ---------- ---------- ----------  1
dmDyn   ---------- ---------- ---------- ---------- ---------- ----------  1
ceDyn   ---------- ---------- ---------- ---------- ---------- ----------  1
scDNM1  ---------- ---------- ---------- ---------- ---------- ----------  1

hsMxA   PAAASHPLLL NGDATVAQKN PGSVAENNLC SQYEEKVRPC IDLIDSLRAL GVEQDLALPA  72
hsMxB   KDFNFLTLNN QPPPGNRSQP RAMGPENNLY SQYEQKVRPC IDLIDSLRAL GVEQDLALPA  120
mmMx1   ---------- ---------- --MDSVNNLC RHYEEKVRPC IDLIDTLRAL GVEQDLALPA  38
mmMx2   EENTGVDSVN LPSGETGLGE KDQESVNNLC SQYEEKVRPC IDLIDSLRAL GVEQDLALPA  65
ggMx    DRKPEHEQKV SKRLNDREED KDEAAACSLD NQYDRKIQPC IDLVDSLRKL DIGNDLMLPA  116
drMxA   ---------- ---------- -MEKLSYTFS QQYEEKIRPC IDTIDNLRSL GVEKDLALPA  39
hsDyn1  ---------- ---------- -------MGN RGMEDLIPLV NRLQDAFSAI GQNADLDLPQ  33
hsDyn2  ---------- ---------- -------MGN RGMEELIPLV NKLQDAFSSI GQSCHLDLPQ  33
hsDyn3  ---------- ---------- -------MGN REMEELIPLV NRLQDAFSAL GQSCLLELPQ  33
dmDyn   ---------- ---------- ---------- --MDSLITIV NKLQDAFTSL GVHMQLDLPQ  28
ceDyn   ---------- ---------- -----MSWQN QGMQALIPVI NRVQDAFSQL GTSVSFELPQ  35
scDNM1  ---------- ---------- ---------M ASLEDLIPTV NKLQDVMYDS GIDT-LDLPI  30

hsMxA   IAVIGDQSSG KSSVLEALSG -VALPRGSGI VTRCPLVLKL KKLV------ ----------  115
hsMxB   IAVIGDQSSG KSSVLEALSG -VALPRGSGI VTRCPLVLKL KKQ------- ----------  162
mmMx1   IAVIGDQSSG KSSVLEALSG -VALPRGSGI VTRCPLVLKL RKLK------ ----------  81
mmMx2   IAVIGDQSSG KSSVLEALSG -VALPRGSGI VTRCPLVLKL RKLN------ ----------  108
ggMx    IAVIGDRNSG KSSVLEA-LS GVALPRDKGV ITRCPLELKL KKMTAP---- ----------  161
drMxA   IAVIGDQSSG KSSVLEA-LS GVPLPRGSGI VTRCPLELKM IRTKDQ---- ----------  84
hsDyn1  IAVVGGQSAG KSSVLENFVG RDFLPRGSGI VTRRPLVLQL VNAT------ ----------  77
hsDyn2  IAVVGGQSAG KSSVLENFVG RDFLPRGSGI VTRRPLILQL IFSK------ ----------  77
hsDyn3  IAVVGGQSAG KSSVLENFVG RDFLPRGSGI VTRRPLVLQL VTSK------ ----------  77
dmDyn   IAVVGGQSAG KSSVLENFVG KDFLPRGSGI VTRRPLILQL INGV------ ----------  72
ceDyn   IAVVGGQSAG KSSVLENFVG KDFLPRGSGI VTRRPLILQL IQDR------ ----------  79
scDNM1  LAVVGSQSSG KSSILETLVG RDFLPRGTGI VTRRPLVLQL NNISPNSPLI EEDDNSVNPH  90

hsMxA   ---------- ---------- ----NEDKWR GKVSYQDYEI EISDASEVEK EINKAQNAIA  151
hsMxB   ---------- ---------- ----PCEAWA GRISYRNTEL ELQDPGQVEK EIHKAQNVMA  198
mmMx1   ---------- ---------- ----EGEEWR GKVSYDDIEV ELSDPSEVEE AINKGQNFIA  117
mmMx2   ---------- ---------- ----EGEEWR GKVSYDDIEV ELSDPSEVEE AINKGQNFIA  144
ggMx    ---------- ---------- ------QEWK GVIYYRNTEI QLQNASEVKK AIRKAQDIVA  195
drMxA   ---------- ---------- ------DRWH GRISYKTCEE DFDDPAEVEK KIRQAQDEMA  118
hsDyn1  ---------- ---------- ------TEYA EFLHCK--GK KFTDFEEVRL EIEAETDRVT  109
hsDyn2  ---------- ---------- ------TEHA EFLHCK--SK KFTDFDEVRQ EIEAETDRVT  109
hsDyn3  ---------- ---------- ------AEYA EFLHCK--GK KFTDFDEVRL EIEAETDRVT  109
dmDyn   ---------- ---------- ------TEYG EFLHIK--GK KFSSFDEIRK EIEDETDRVT  104
ceDyn   ---------- ---------- ------NEYA EFLHKK--GH RFVDFDAVRK EIEDETDRVT  111
scDNM1  DEVTKISGFE AGTKPLEYRG KERNHADEWG EFLHIP--GK RFYDFDDIKR EIENETARIA  148
```

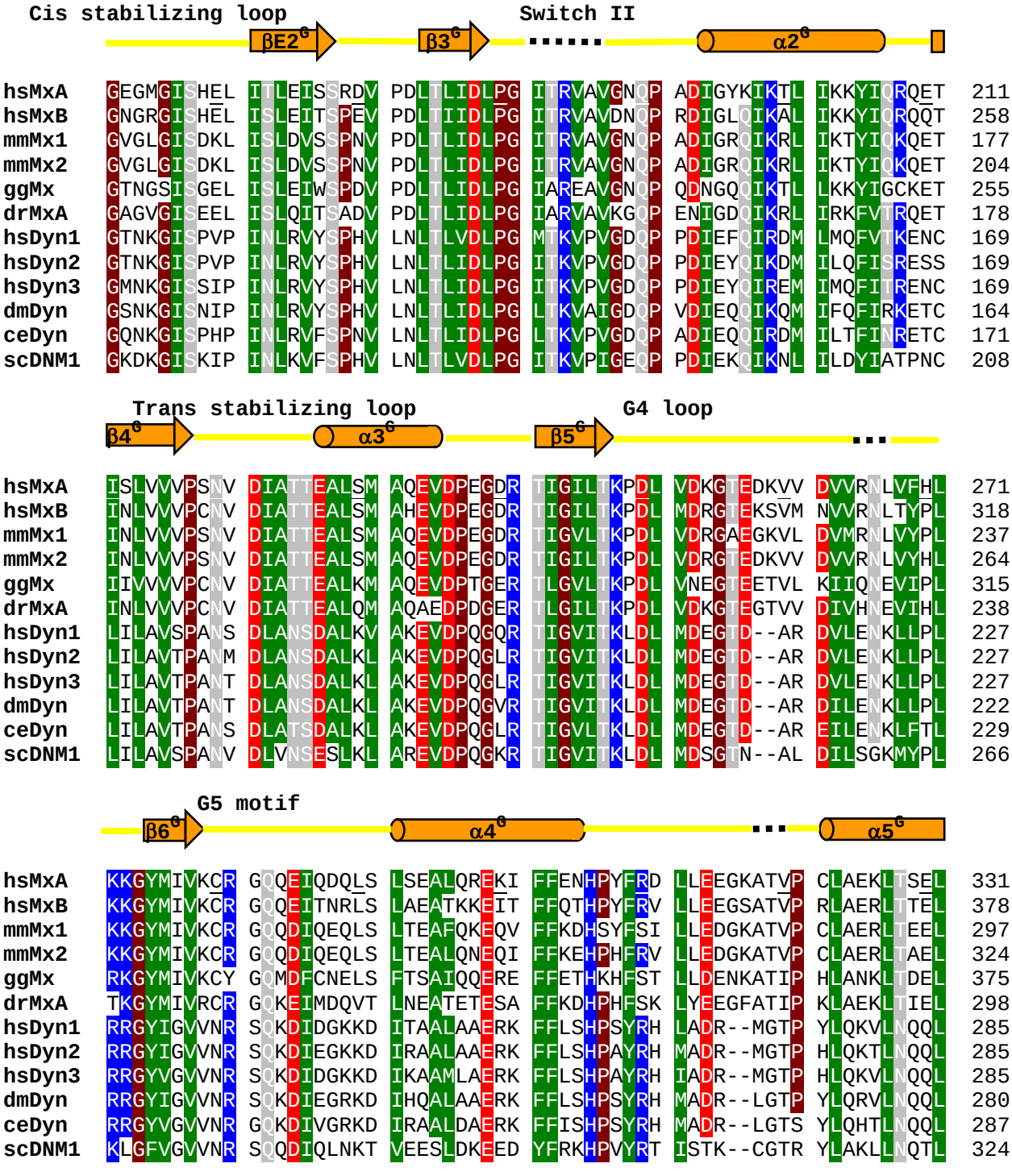
Cis stabilizing loop
Switch II
βE2G
β3G
α2G
hsMxA GEGMGISHEL ITLEISSRDV PDLTLIDLPG ITRVAVGNQP ADIGYKIKTL IKKYIQRQET 211
hsMxB GNGRGISHEL ISLEITSPEV PDLTIIDLPG ITRVAVDNQP RDIGLQIKAL IKKYIQRQQT 258
mmMx1 GVGLGISDKL ISLDVSSPNV PDLTLIDLPG ITRVAVGNQP ADIGRQIKRL IKTYIQKQET 177
mmMx2 GVGLGISDKL ISLDVSSPNV PDLTLIDLPG ITRVAVGNQP ADIGRQIKRL IKTYIQKQET 204
ggMx GTNGSISGEL ISLEIWSPDV PDLTLIDLPG IAREAVGNQP QDNGQQIKTL LKKYIGCKET 255
drMxA GAGVGISEEL ISLQITSADV PDLTLIDLPG IARVAVKGQP ENIGDQIKRL IRKFVTRQET 178
hsDyn1 GTNKGISPVP INLRVYSPHV LNLTLVDLPG MTKVPVGDQP PDIEFQIRDM LMQFVTKENC 169
hsDyn2 GTNKGISPVP INLRVYSPHV LNLTLIDLPG ITKVPVGDQP PDIEYQIKDM ILQFISRESS 169
hsDyn3 GMNKGISSIP INLRVYSPHV LNLTLIDLPG ITKVPVGDQP PDIEYQIREM IMQFITRENC 169
dmDyn GSNKGISNIP INLRVYSPHV LNLTLIDLPG LTKVAIGDQP VDIEQQIKQM IFQFIRKETC 164
ceDyn GQNKGISPHP INLRVFSPNV LNLTLIDLPG LTKVPVGDQP ADIEQQIRDM ILTFINRETC 171
scDNM1 GKDKGISKIP INLKVFSPHV LNLTLVDLPG ITKVPIGEQP PDIEKQIKNL ILDYIATPNC 208
Trans stabilizing loop
G4 loop
β4G
α3G
β5G
hsMxA ISLVVVPSNV DIATTEALSM AQEVDPEGDR TIGILTKPDL VDKGTEDKVV DVVRNLVFHL 271
hsMxB INLVVVPCNV DIATTEALSM AHEVDPEGDR TIGILTKPDL MDRGTEKSVM NVVRNLTYPL 318
mmMx1 INLVVVPSNV DIATTEALSM AQEVDPEGDR TIGVLTKPDL VDRGAEGKVL DVMRNLVYPL 237
mmMx2 INLVVVPSNV DIATTEALSM AQEVDPEGDR TIGILTKPDL VDRGTEDKVV DVVRNLVYHL 264
ggMx IIVVVVPCNV DIATTEALKM AQEVDPTGER TLGVLTKPDL VNEGTEETVL KIIQNEVIPL 315
drMxA INLVVVPCNV DIATTEALQM AQAEDPDGER TLGILTKPDL VDKGTEGTVV DIVHNEVIHL 238
hsDyn1 LILAVSPANS DLANSDALKV AKEVDPQGQR TIGVITKLDL MDEGTD--AR DVLENKLLPL 227
hsDyn2 LILAVTPANM DLANSDALKL AKEVDPQGLR TIGVITKLDL MDEGTD--AR DVLENKLLPL 227
hsDyn3 LILAVTPANT DLANSDALKL AKEVDPQGLR TIGVITKLDL MDEGTD--AR DVLENKLLPL 227
dmDyn LILAVTPANT DLANSDALKL AKEVDPQGVR TIGVITKLDL MDEGTD--AR DILENKLLPL 222
ceDyn LILAVTPANS DLATSDALKL AKEVDPQGLR TIGVLTKLDL MDEGTD--AR EILENKLFTL 229
scDNM1 LILAVSPANV DLVNSESLKL ARKVDPQGKR TIGVITKLDL MDSGTN--AL DILSGKMYPL 266
G5 motif
β6G
α4G
α5G
hsMxA KKGYMIVKCR GQQEIQDQLS LSEALQREKI FFENHPYFRD LLEEGKATVP CLAEKLTSEL 331
hsMxB KKGYMIVKCR GQQEITNRLS LAEATKKEIT FFQTHPYFRV LLEEGSATVP RLAERLTTEL 378
mmMx1 KKGYMIVKCR GQQDIQEQLS LTEAFQKEQV FFKDHSYFSI LLEDGKATVP CLAERLTEEL 297
mmMx2 KKGYMIVKCR GQQDIQEQLS LTEALQNEQI FFKEHPHFRV LLEDGKATVP CLAERLTAEL 324
ggMx RKGYMIVKCY GQMDFCNELS FTSAIQQERE FFETHKHFST LLDENKATIP HLANKLTDEL 375
drMxA TKGYMIVRCR GQKEIMDQVT LNEATETESA FFKDHPHFSK LYEEGFATIP KLAEKLTIEL 298
hsDyn1 RRGYIGVVNR SQKDIDGKKD ITAALAAERK FFLSHPSYRH LADR--MGTP YLQKVLNQQL 285
hsDyn2 RRGYIGVVNR SQKDIEGKKD IRAALAAERK FFLSHPAYRH MADR--MGTP HLQKTLNQQL 285
hsDyn3 RRGYVGVVNR SQKDIDGKKD IKAAMLAERK FFLSHPAYRH IADR--MGTP HLQKVLNQQL 285
dmDyn RRGYIGVVNR SQKDIEGRKD IHQALAAERK FFLSHPSYRH MADR--LGTP YLQRVLNQQL 280
ceDyn RRGYVGVVNR GQKDIVGRKD IRAALDAERK FFISHPSYRH MADR--LGTS YLQHTLNQQL 287
scDNM1 KLGFVGVVNR SQQDIQLNKT VEESLDKEED YFRKHPVYRT ISTK--CGTR YLAKLLNQTL 324

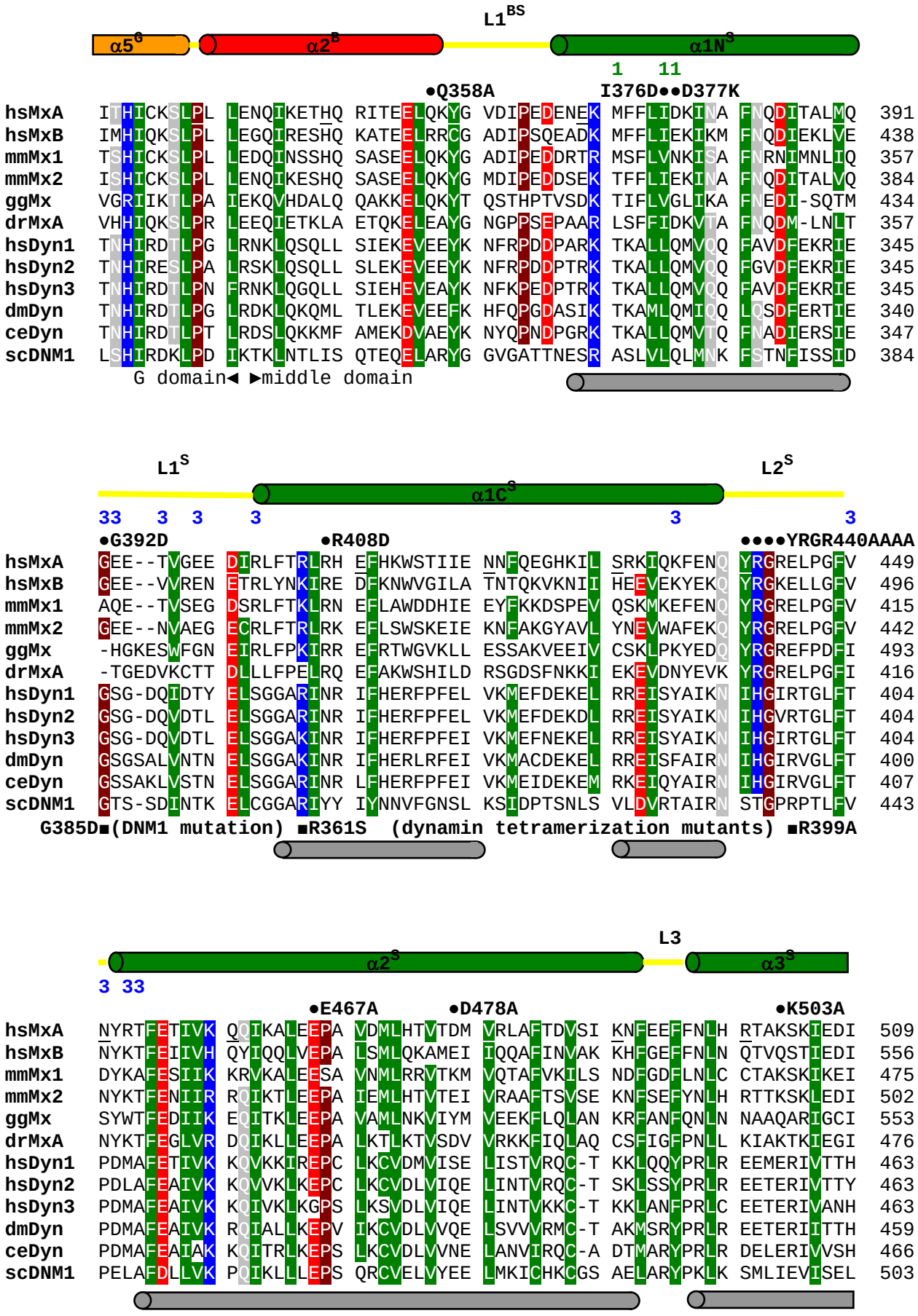
L1BS
α5G
α2B
α1NS
1 11
•Q358A
I376D••D377K
hsMxA IIHICKSLPL LENQIKETHQ RITEELQKYG VDIPEDENEK MFFLIDKINA FNQDITALMQ 391
hsMxB IMHIQKSLPL LEGQIRESHQ KATEELRRCG ADIPSQEADK MFFLIEKIKM FNQDIEKLVE 438
mmMx1 TSHICKSLPL LEDQINSSHQ SASEELQKYG ADIPEDDRTR MSFLVNKISA FNRNIMNLIQ 357
mmMx2 ISHICKSLPL LENQIKESHQ SASEELQKYG MDIPEDDSEK TFFLIEKINA FNQDITALVQ 384
ggMx VGRIIKTLPA IEKQVHDALQ QAKKELQKYT QSTHPTVSDK TIFLVGLIKA FNEDI-SQTM 434
drMxA VHHIQKSLPR LEEQIETKLA ETQKELEAYG NGPPSEPAAR LSFFIDKVTA FNQDM-LNLT 357
hsDyn1 TNHIRDILPG LRNKLQSQLL SIEKEVEEYK NFRPDDPARK TKALLQMVQQ FAVDFEKRIE 345
hsDyn2 TNHIRESLPA LRSKLQSQLL SLEKEVEEYK NFRPDDPTRK TKALLQMVQQ FGVDFEKRIE 345
hsDyn3 TNHIRDILPN FRNKLQGQLL SIEHEVEAYK NFKPEDPTRK TKALLQMVQQ FAVDFEKRIE 345
dmDyn TNHIRDILPG LRDKLQKQML TLEKEVEEFK HFQPGDASIK TKAMLQMIQQ LQSDFERTIE 340
ceDyn TNHIRDILPT LRDSLQKKMF AMEKDVAEYK NYQPNDPGRK TKALLQMVTQ FNADIERSIE 347
scDNM1 LSHIRDKLPD IKTKLNTLIS QTEQELARYG GVGATTNESR ASLVLQLMNK FSTNFISSID 384
G domain◄ ►middle domain
L1S
L2S
α1CS
33 3 3 3 3 3
•G392D
•R408D
••••YRGR440AAAA
hsMxA GEE--TVGEE DIRLFTRLRH EFHKWSTIIE NNFQEGHKIL SRKIQKFENQ YRGRELPGFV 449
hsMxB GEE--VVREN ETRLYNKIRE DFKNWVGILA TNTQKVKNII HEEVEKYEKQ YRGKELLGFV 496
mmMx1 AQE--TVSEG DSRLFTKLRN EFLAWDDHIE EYFKKDSPEV QSKMKEFENQ YRGRELPGFV 415
mmMx2 GEE--NVAEG ECRLFTRLRK EFLSWSKEIE KNFAKGYAVL YNEVWAFEKQ YRGRELPGFV 442
ggMx -HGKESWFGN EIRLFPKIRR EFRTWGVKLL ESSAKVEEIV CSKLPKYEDQ YRGREFPDFI 493
drMxA -TGEDVKCTT DLLLFPELRQ EFAKWSHILD RSGDSFNKKI EKEVDNYEVK YRGRELPGFI 416
hsDyn1 GSG-DQIDTY ELSGGARINR IFHERFPFEL VKMEFDEKEL RREISYAIKN IHGIRTGLFT 404
hsDyn2 GSG-DQVDTL ELSGGARINR IFHERFPFEL VKMEFDEKDL RREISYAIKN IHGVRTGLFT 404
hsDyn3 GSG-DQVDTL ELSGGAKINR IFHERFPFEI VKMEFNEKEL RREISYAIKN IHGIRTGLFT 404
dmDyn GSGSALVNTN ELSGGAKINR IFHERLRFEI VKMACDEKEL RREISFAIRN IHGIRVGLFT 400
ceDyn GSSAKLVSTN ELSGGARINR LFHERFPFEI VKMEIDEKEM RKEIQYAIRN IHGIRVGLFT 407
scDNM1 GTS-SDINTK ELCGGARIYY IYNNVFGNSL KSIDPTSNLS VLDVRTAIRN STGPRPTLFV 443
G385D■(DNM1 mutation) ■R361S (dynamin tetramerization mutants) ■R399A
L3
α2S
α3S
3 33
•E467A
•D478A
•K503A
hsMxA NYRTFETIVK QQIKALEEPA VDMLHTVTDM VRLAFTDVSI KNFEEFFNLH RTAKSKIEDI 509
hsMxB NYKTFEIIVH QYIQQLVEPA LSMLQKAMEI IQQAFINVAK KHFGEFFNLN QTVQSTIEDI 556
mmMx1 DYKAFESIIK KRVKALEESA VNMLRRVTKM VQTAFVKILS NDFGDFLNLC CTAKSKIKEI 475
mmMx2 NYKTFENIIR RQIKTLEEPA IEMLHTVTEI VRAAFTSVSE KNFSEFYNLH RTTKSKLEDI 502
ggMx SYWTFEDIIK EQITKLEEPA VAMLNKVIYM VEEKFLQLAN KRFANFQNLN NAAQARIGCI 553
drMxA NYKTFEGLVR DQIKLLEEPA LKTLKTVSDV VRKKFIQLAQ CSFIGFPNLL KIAKTKIEGI 476
hsDyn1 PDMAFETIVK KQVKKIREPC LKCVDMVISE LISTVRQC-T KKLQQYPRLR EEMERIVTTH 463
hsDyn2 PDLAFEAIVK KQVVKLKEPC LKCVDLVIQE LINTVRQC-T SKLSSYPRLR EETERIVTTY 463
hsDyn3 PDMAFEAIVK KQIVKLKGPS LKSVDLVIQE LINTVKKC-T KKLANFPRLC EETERIVANH 463
dmDyn PDMAFEAIVK RQIALLKEPV IKCVDLVVQE LSVVVRMC-T AKMSRYPRLR EETERIITTH 459
ceDyn PDMAFEAIAK KQITRLKEPS LKCVDLVVNE LANVIRQC-A DTMARYPRLR DELERIVVSH 466
scDNM1 PELAFDLLVK PQIKLLLEPS QRCVELVYEE LMKICHKCGS AELARYPKLK SMLIEVISEL 503

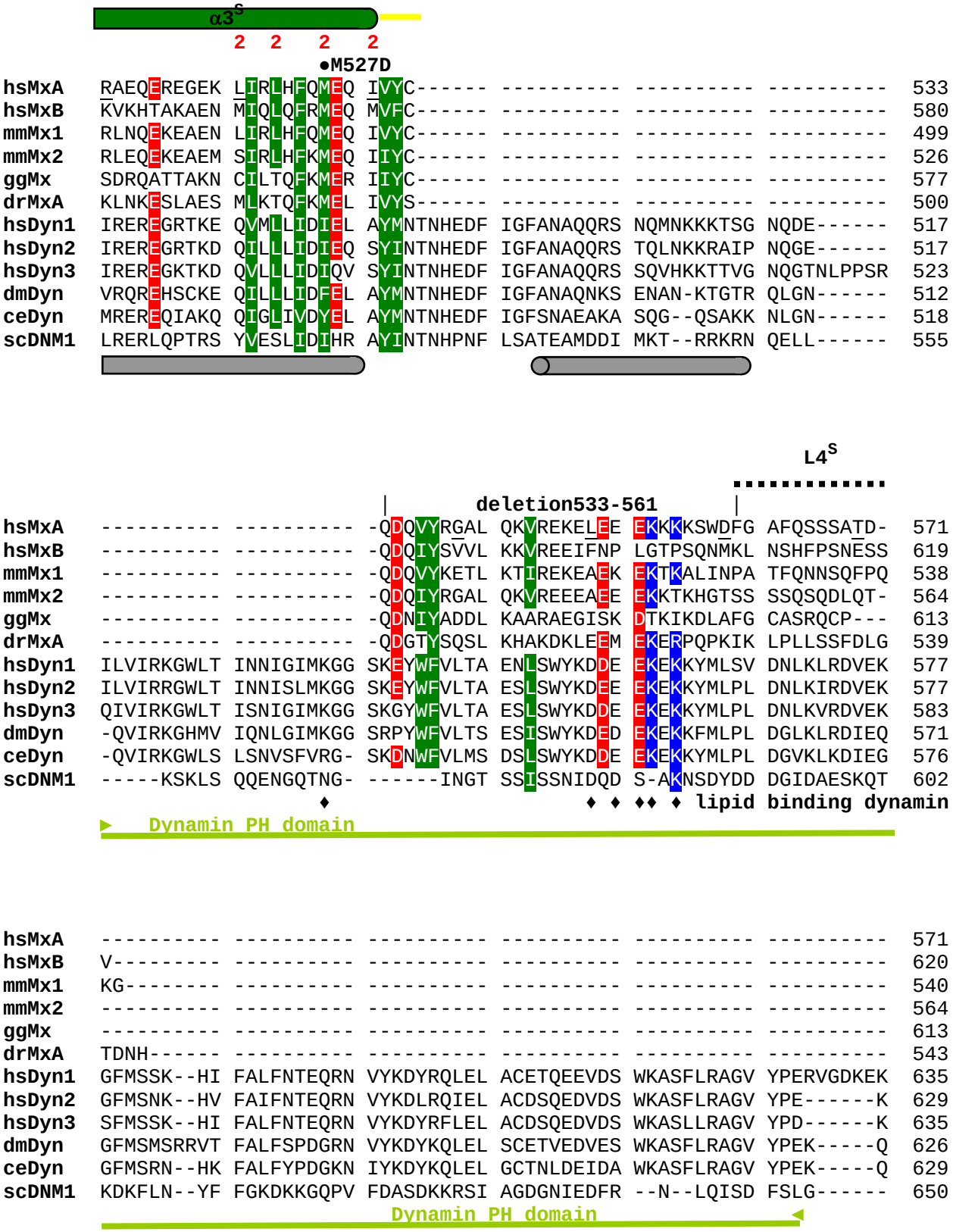
α3S
2 2 2 2
●M527D
hsMxA RAEQEREGEK LIRLHFQMEQ IVYC---------- ---------- ---------- ---------- 533
hsMxB KVKHTAKAEN MIQLQFRMEQ MVFC---------- ---------- ---------- ---------- 580
mmMx1 RLNQEKEAEN LIRLHFQMEQ IVYC---------- ---------- ---------- ---------- 499
mmMx2 RLEQEKEAEM SIRLHFKMEQ IIYC---------- ---------- ---------- ---------- 526
ggMx SDRQATTAKN CILTQFKMER IIYC---------- ---------- ---------- ---------- 577
drMxA KLNKESLAES MLKTQFKMEL IVYS---------- ---------- ---------- ---------- 500
hsDyn1 IREREGRTKE QVMLLIDIEL AYMNTNHEDF IGFANAQQRS NQMNKKKTSG NQDE---------- 517
hsDyn2 IREREGRTKD QILLLIDIEQ SYINTNHEDF IGFANAQQRS TQLNKKRAIP NQGE---------- 517
hsDyn3 IREREGKTKD QVLLLIDIQV SYINTNHEDF IGFANAQQRS SQVHKKTTVG NQGTNLPPSR 523
dmDyn VRQREHSCKE QILLLIDFEL AYMNTNHEDF IGFANAQNKS ENAN-KTGTR QLGN---------- 512
ceDyn MREREQIAKQ QIGLIVDYEL AYMNTNHEDF IGFSNAEAKA SQG--QSAKK NLGN---------- 518
scDNM1 LRERLQPTRS YVESLIDIHR AYINTNHPNF LSATEAMDDI MKT--RRKRN QELL---------- 555
L4S
deletion533-561
hsMxA ---------- ---------- -QDQVYRGAL QKVREKELEE EKKKKSWDFG AFQSSSATD- 571
hsMxB ---------- ---------- -QDQIYSVVL KKVREEIFNP LGTPSQNMKL NSHFPSNESS 619
mmMx1 ---------- ---------- -QDQVYKETL KTIREKEAEK EKTKALINPA TFQNNSQFPQ 538
mmMx2 ---------- ---------- -QDQIYRGAL QKVREEEAEE EKKTKHGTSS SSQSQDLQT- 564
ggMx ---------- ---------- -QDNIYADDL KAARAEGISK DTKIKDLAFG CASRQCP--- 613
drMxA ---------- ---------- -QDGTYSQSL KHAKDKLEEM EKERPQPKIK LPLLSSFDLG 539
hsDyn1 ILVIRKGWLT INNIGIMKGG SKEYWFVLTA ENLSWYKDDE EKEKKYMLSV DNLKLRDVEK 577
hsDyn2 ILVIRRGWLT INNISLMKGG SKEYWFVLTA ESLSWYKDEE EKEKKYMLPL DNLKIRDVEK 577
hsDyn3 QIVIRKGWLT ISNIGIMKGG SKGYWFVLTA ESLSWYKDDE EKEKKYMLPL DNLKVRDVEK 583
dmDyn -QVIRKGHMV IQNLGIMKGG SRPYWFVLTS ESISWYKDED EKEKKFMLPL DGLKLRDIEQ 571
ceDyn -QVIRKGWLS LSNVSFVRG- SKDNWFVLMS DSLSWYKDDE EKEKKYMLPL DGVKLKDIEG 576
scDNM1 -----KSKLS QQENGQTNG- ------INGT SSISSNIDQD S-AKNSDYDD DGIDAESKQT 602
♦ ♦ ♦ ♦♦ ♦ lipid binding dynamin
Dynamin PH domain
hsMxA ---------- ---------- ---------- ---------- ---------- ---------- 571
hsMxB V--------- ---------- ---------- ---------- ---------- ---------- 620
mmMx1 KG-------- ---------- ---------- ---------- ---------- ---------- 540
mmMx2 ---------- ---------- ---------- ---------- ---------- ---------- 564
ggMx ---------- ---------- ---------- ---------- ---------- ---------- 613
drMxA TDNH------ ---------- ---------- ---------- ---------- ---------- 543
hsDyn1 GFMSSK--HI FALFNTEQRN VYKDYRQLEL ACETQEEVDS WKASFLRAGV YPERVGDKEK 635
hsDyn2 GFMSNK--HV FAIFNTEQRN VYKDLRQIEL ACDSQEDVDS WKASFLRAGV YPE------K 629
hsDyn3 SFMSSK--HI FALFNTEQRN VYKDYRFLEL ACDSQEDVDS WKASLLRAGV YPD------K 635
dmDyn GFMSMSRRVT FALFSPDGRN VYKDYKQLEL SCETVEDVES WKASFLRAGV YPEK-----Q 626
ceDyn GFMSRN--HK FALFYPDGKN IYKDYKQLEL GCTNLDEIDA WKASFLRAGV YPEK-----Q 629
scDNM1 KDKFLN--YF FGKDKKGQPV FDASDKKRSI AGDGNIEDFR --N--LQISD FSLG------ 650
Dynamin PH domain

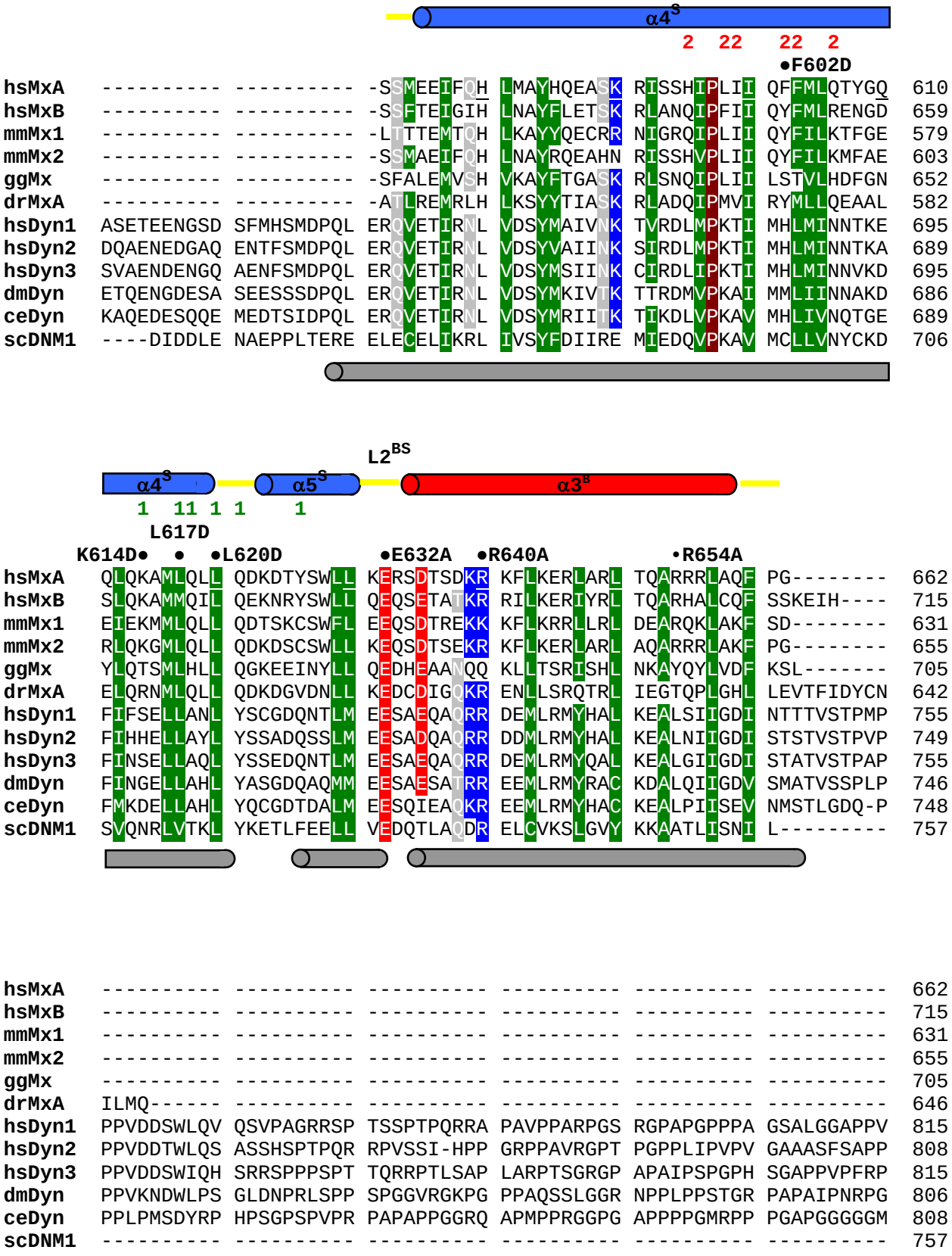
α4^S
2 22 22 2
•F602D
hsMxA ---------- ---------- -SSMEEIFQH LMAYHQEASK RISSHIPLII QFFMLQTYGQ 610
hsMxB ---------- ---------- -SSFTEIGIH LNAYFLETSK RLANQIPFII QYFMLRENGD 659
mmMx1 ---------- ---------- -LTTTEMTQH LKAYYQECRR NIGRQIPLII QYFILKTFGE 579
mmMx2 ---------- ---------- -SSMAEIFQH LNAYRQEAHN RISSHVPLII QYFILKMFAE 603
ggMx ---------- ---------- -SFALEMVSH VKAYFTGASK RLSNQIPLII LSTVLHDFGN 652
drMxA ---------- ---------- -ATLREMRLH LKSYYTIASK RLADQIPMVI RYMLLQEAAL 582
hsDyn1 ASETEENGSD SFMHSMDPQL ERQVETIRNL VDSYMAIVNK TVRDLMPKTI MHLMINNTKE 695
hsDyn2 DQAENEDGAQ ENTFSMDPQL ERQVETIRNL VDSYVAIINK SIRDLMPKTI MHLMINNTKA 689
hsDyn3 SVAENDENGQ AENFSMDPQL ERQVETIRNL VDSYMSIINK CIRDLIPKTI MHLMINNVKD 695
dmDyn ETQENGDESA SEESSSDPQL ERQVETIRNL VDSYMKIVTK TTRDMVPKAI MMLIINNAKD 686
ceDyn KAQEDESQQE MEDTSIDPQL ERQVETIRNL VDSYMRIITK TIKDLVPKAV MHLIVNQTGE 689
scDNM1 ----DIDDLE NAEPPLTERE ELECELIKRL IVSYFDIIRE MIEDQVPKAV MCLLVNYCKD 706
L2^BS
α4^S α5^S α3^B
1 11 1 1 1
L617D
K614D• • •L620D •E632A •R640A •R654A
hsMxA QLQKAMLQLL QDKDTYSWLL KERSDTSDKR KFLKERLARL TQARRRLAQF PG-------- 662
hsMxB SLQKAMMQIL QEKNRYSWLL QEQSETATKR RILKERIYRL TQARHALCQF SSKEIH---- 715
mmMx1 EIEKMMLQLL QDTSKCSWFL EEQSDTREKK KFLKRRLLRL DEARQKLAKF SD-------- 631
mmMx2 RLQKGMLQLL QDKDSCSWLL KEQSDTSEKR KFLKERLARL AQARRRLAKF PG-------- 655
ggMx YLQTSMLHLL QGKEEINYLL QEDHEAANQQ KLLTSRISHL NKAYQYLVDF KSL------- 705
drMxA ELQRNMLQLL QDKDGVDNLL KEDCDIGQKR ENLLSRQTRL IEGTQPLGHL LEVTFIDYCN 642
hsDyn1 FIFSELLANL YSCGDQNTLM EESAEQAQRR DEMLRMYHAL KEALSIIGDI NTTTVSTPMP 755
hsDyn2 FIHHELLAYL YSSADQSSLM EESADQAQRR DDMLRMYHAL KEALNIIGDI STSTVSTPVP 749
hsDyn3 FINSELLAQL YSSEDQNTLM EESAEQAQRR DEMLRMYQAL KEALGIIGDI STATVSTPAP 755
dmDyn FINGELLAHL YASGDQAQMM EESAESATRR EEMLRMYRAC KDALQIIGDV SMATVSSPLP 746
ceDyn FMKDELLAHL YQCGDTDALM EESQIEAQKR EEMLRMYHAC KEALPIISEV NMSTLGDQ-P 748
scDNM1 SVQNRLVTKL YKETLFEELL VEDQTLAQDR ELCVKSLGVY KKAATLISNI L--------- 757
hsMxA ---------- ---------- ---------- ---------- ---------- ---------- 662
hsMxB ---------- ---------- ---------- ---------- ---------- ---------- 715
mmMx1 ---------- ---------- ---------- ---------- ---------- ---------- 631
mmMx2 ---------- ---------- ---------- ---------- ---------- ---------- 655
ggMx ---------- ---------- ---------- ---------- ---------- ---------- 705
drMxA ILMQ------ ---------- ---------- ---------- ---------- ---------- 646
hsDyn1 PPVDDSWLQV QSVPAGRRSP TSSPTPQRRA PAVPPARPGS RGPAPGPPPA GSALGGAPPV 815
hsDyn2 PPVDDTWLQS ASSHSPTPQR RPVSSI-HPP GRPPAVRGPT PGPPLIPVPV GAAASFSAPP 808
hsDyn3 PPVDDSWIQH SRRSPPPSPT TQRRPTLSAP LARPTSGRGP APAIPSPGPH SGAPPVPFRP 815
dmDyn PPVKNDWLPS GLDNPRLSPP SPGGVRGKPG PPAQSSLGGR NPPLPPSTGR PAPAIPNRPG 806
ceDyn PPLPMSDYRP HPSGPSPVPR PAPAPPGGRQ APMPPRGGPG APPPPGMRPP PGAPGGGGGM 808
scDNM1 ---------- ---------- ---------- ---------- ---------- ---------- 757

```
hsMxA   ---------- ---------- ---------- ---------- ---------- ----------  662
hsMxB   ---------- ---------- ---------- ---------- ---------- ----------  715
mmMx1   ---------- ---------- ---------- ---------- ---------- ----------  631
mmMx2   ---------- ---------- ---------- ---------- ---------- ----------  655
ggMx    ---------- ---------- ---------- ---------- ---------- ----------  705
drMxA   ---------- ---------- ---------- ---------- ---------- ----------  646
hsDyn1  PSRPGASPDP FGPPPQVPSR PNRAPPGVPS RSGQASPSRP ESPRPPFDL- ----------  864
hsDyn2  IPSRPGPQSV FANSDLFPAP PQIPSRPVRI PPGIPPGVPS RRPPAAPSRP TIIRPAEPSL  868
hsDyn3  GPLPPFPSSS DSFGAPPQVP SRPTRAPPSV PSRRPPPSPT RPTIIRPLES SLLD------  869
dmDyn   GGAPPLPGGR PGGSLPPPML PSRVSGAVGG AIVQQSGANR YVPESMRGQV NQAVGQAAIN  866
ceDyn   YPPLIPTRVP TPSNGAPEIP ARPQVPKRPF ---------- ---------- ----------  838
scDNM1  ---------- ---------- ---------- ---------- ---------- ----------  757

hsMxA   ---------- - 662
hsMxB   ---------- - 715
mmMx1   ---------- - 631
mmMx2   ---------- - 655
ggMx    ---------- - 705
drMxA   ---------- - 646
hsDyn1  ---------- - 864
hsDyn2  LD-------- - 870
hsDyn3  ---------- - 869
dmDyn   ELSNAFSSRF K 877
ceDyn   ---------- - 838
scDNM1  ---------- - 757
```

Figure 31. Sequence alignment of Mx and dynamin proteins. Amino acid sequences of human MxA (Swiss-Prot accession P20591), human MxB (P20592), mouse (mm) Mx1 (P09922), mouse Mx2 (Q9WVP9), chicken (gg) Mx protein (Q90597), zebrafish (dr) MxA protein (Q8JH68), human dynamin 1 (Q05193), human dynamin2 (P50570), human Dynamin3 (Q9UQ16), *Drosophila melanogaster* (dm) dynamin (P27619), *Caenorhabditis elegans* (ce) dynamin (Q9U9I9) and *Saccharomyces cerevisiae* (sc) dynamin-related protein DNM1 (P54861) were aligned using CLUSTAL W (Thompson, Higgins et al. 1994) and manually adjusted. Residues with a conservation of greater than 70% are color-coded (D, E in red; R, K, H in blue; N, Q, S, T in grey; A, L, I, V, F, Y, W, M, C in green and P, G in brown). α-helices are shown as cylinders and β-strands as arrows with the labeling and colors as in Fig. 30B and Fig. 52B. The secondary structure prediction result from the JPred server (Cuff, Clamp et al. 1998) of the hsMxA stalk is depicted as gray cylinders under the sequences. The PH domain of dynamin is indicated by a green line with domain boundaries taken from the structure of the PH domain (Ferguson, Lemmon et al. 1994). All motifs previously described in the literature and observed in the hsMxA stalk structure are labeled accordingly. Mutations that disrupt the interfaces (described in 4.2.4) and that are introduced to other critical positions of the protein, based on the full-length hsMxA crystal structure (described in 5.4.2), are also partly specified correspondingly. Residues involved in the stalk interfaces are indicated with the numbers of individual interfaces on top the alignment. Dimerization mutants of dynamin (Ramachandran, Surka et al. 2007) and scDNM1 (■) (Ingerman, Perkins et al. 2005) and residues of dynamin involved in PIP_2 binding (♦) (Zheng, Cahill et al. 1996; Vallis, Wigge et al. 1999) are designated with the respective signs.

4.2.4 Interfaces in the human MxA oligomer

In the crystal lattice, each hsMxA stalk monomer assembled in a criss-cross pattern via crystallographic and non-crystallographic symmetry, resulting in a linear oligomer (Fig. 32A) where each stalk contributed three distinct interaction sites. Such architecture would be plausible for the arrangement of the stalks in the Mx oligomer since all G domains would be located at one side of the oligomer whereas the putative membrane or virus binding sites in L2 and L4 would be located at the opposite side (Fig. 32A). Furthermore, this organization of the criss-cross pattern is reminiscent of the dynamin stalks observed from EM reconstructions (Chen, Zhang et al. 2004; Mears, Ray et al. 2007).

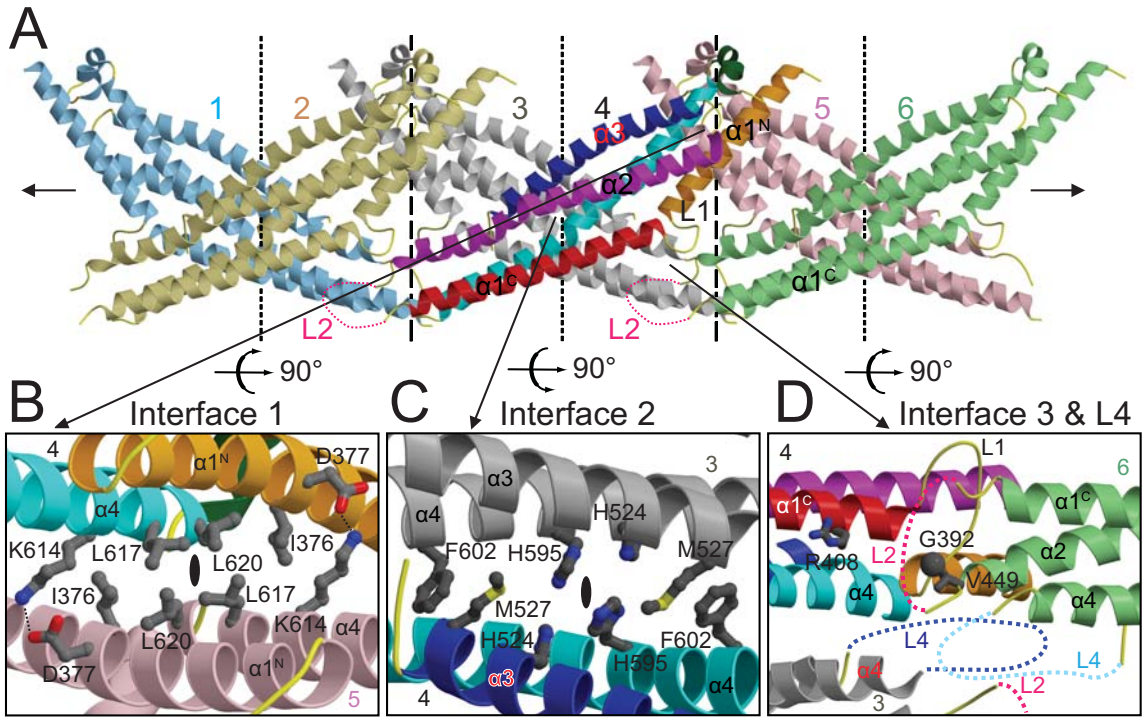

Figure 32. hsMxA stalk oligomer and interfaces. A) Ribbon-type representation of six oligomerized hsMxA stalks. The parallel non-crystallographic pseudo-two-fold axes across interface 1 and interface 2 are indicated by black dashed lines. B) Bottom view of interface 1 between monomers 4 and 5 with selected residues in the interface shown in ball-and-stick representation. Monomers 2 and 3 in panel A also associate via this interface. The position of the pseudo-two-fold axis is indicated by a filled ellipse. C) Top view of interface 2 between monomers 3 and 4 with selected residues in the interface shown in ball-and-stick representation. Monomers 1 and 2 and monomers 5 and 6 in A also have this interface in common. The position of the pseudo-two-fold axis is indicated by a filled ellipse. D) Bottom view of interface 3 and L4 with selected residues shown in ball-and-stick representation. Interface 3 mediates lateral contacts, here between monomers 4 and 6 and also between monomers 1 and 3, monomers 3 and 5 and monomers 2 and 4 in C. Contacts via L4 might stabilize opposing stalks, here between monomer 3 and 6, and monomers 1 and 4 in A.

Interface 1 covering 1,300 Å^2 is conserved among Mx proteins and dynamins and shows a two-fold symmetry between the associating monomers (Fig. 31, 32B). It is built of mostly hydrophobic residues, e.g. Ile376 from helix α1 in the MD, and Leu617 and Leu620 from α4 in the GED, and a salt bridge between Asp377 and Lys614. Interface 2 buries 1,700 Å^2 and is nearly invariant in Mx proteins but shows only limited sequence similarity to dynamins (Fig. 30). It also displays a two-fold symmetry and features a symmetric hydrophobic interaction of Met527 in helix α3 of the MD with Phe602 in helix α4 of the GED from the opposite monomer (Fig. 32C). Interface 3 occludes an area of 400-500 Å^2 and is a non-symmetric assembly interface that mediates lateral contacts between stalks oriented in parallel (Fig. 32D). It comprises loop L1 which interacts with residues in helix α2 of a neighboring stalk. Furthermore, the surface-exposed Arg408 in helix α1^C is completely conserved in Mx proteins, and lies in the vicinity of loop L2 of a neighboring monomer featuring an invariant ^{440}YRGRE motif. Loop L4 at the opposite side of the G domain is in the vicinity of the corresponding loop L4 from an opposing molecule (Fig. 32D). Due to its position, L4 might constitute a low affinity interaction site.

4.3 Characterization of the interfaces

4.3.1 Preparation of interface mutants

To investigate whether the hsMxA stalk oligomer found in the crystal lattice represents the physiologically functional assembly of hsMxA, point mutations were introduced to the corresponding interaction sites. These mutations were I376D, D377K, K614D L617D and L620D in interface 1; M527D and F602D in interface 2; G392D, R408D and a quadruple mutation YRGR440-443AAAA in L2; a quadruple mutation KKKK554-557AAAA in L4 and a deletion in L4, del533-561 (ΔL4). All hsMxA mutants were generated by site-directed mutagenesis as described in 3.2.10 and purified in the same way as wt hsMxA as described in 3.3.4.1. Almost all the mutants showed increased protein yields and eluted later than wt hsMxA in analytical gel filtration (Fig. 33), indicating that these mutants may have different features of assembly than wt hsMxA at least in solution. These mutants were subsequently analyzed in various *in vitro* and *in vivo* experiments. In the following section, results for mutants L617D, M527D, R408D and ΔL4, from interface 1, 2, 3 and L4, respectively, are shown as representatives for the disruption of the four interaction sites, whereas other mutants were tested only in certain, but not in all the experiments.

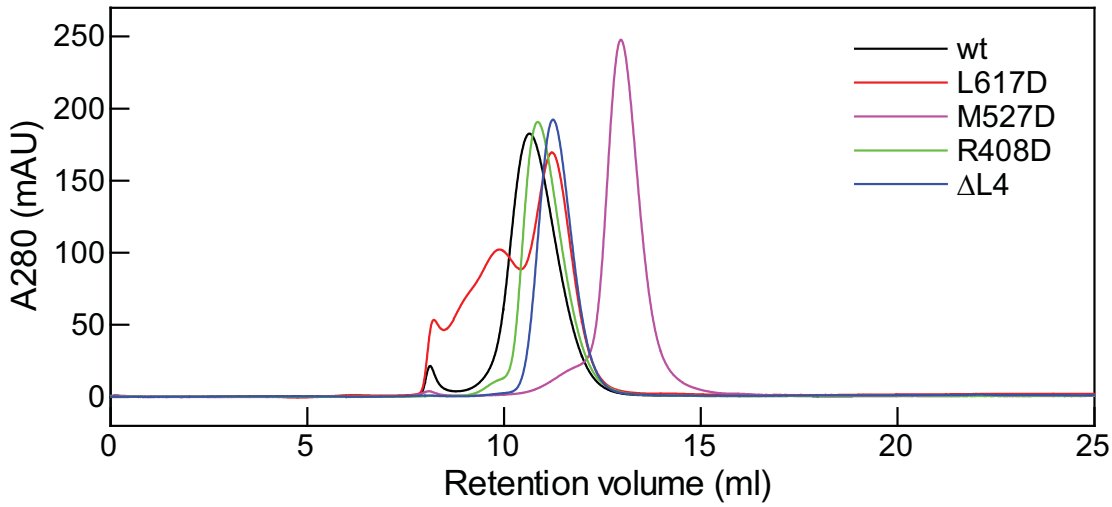

Figure 33. Analytical gel filtration experiment on wt hsMxA and mutants. The method was described in 3.3.12. wt hsMxA (black) eluted as a tetramer in gel filtration whereas mutants L617D (red) in interface 1, R408D (green) in interface 3 and ΔL4 (blue) eluted slightly later. Mutant M527D (magenta) eluted as a monomer. Note that mutants in interface 1 eluted in several peaks, possibly indicating that these mutations partially destabilize the protein.

4.3.2 Interface mutants interfere with oligomerization

To verify the role of the identified interaction sites on the native assembly of full-length hsMxA, analytical ultracentrifugation (AUC) experiments were carried out (3.3.14). wt hsMxA was shown to be a concentration-independent stable tetramer (Fig. 34A), similar to dynamin (Hinshaw and Schmid 1995). Strikingly, all the mutations caused the disruption of the tetramer, resulting in a monomer-dimer or dimer-tetramer equilibrium with a K_d in the micromolar range for mutations in interface 1 and 2, and stable dimers for mutations in interface 3 and L4 (Fig. 34A-I). These results are consistent with the analytical gel filtration experiments (Fig. 33).

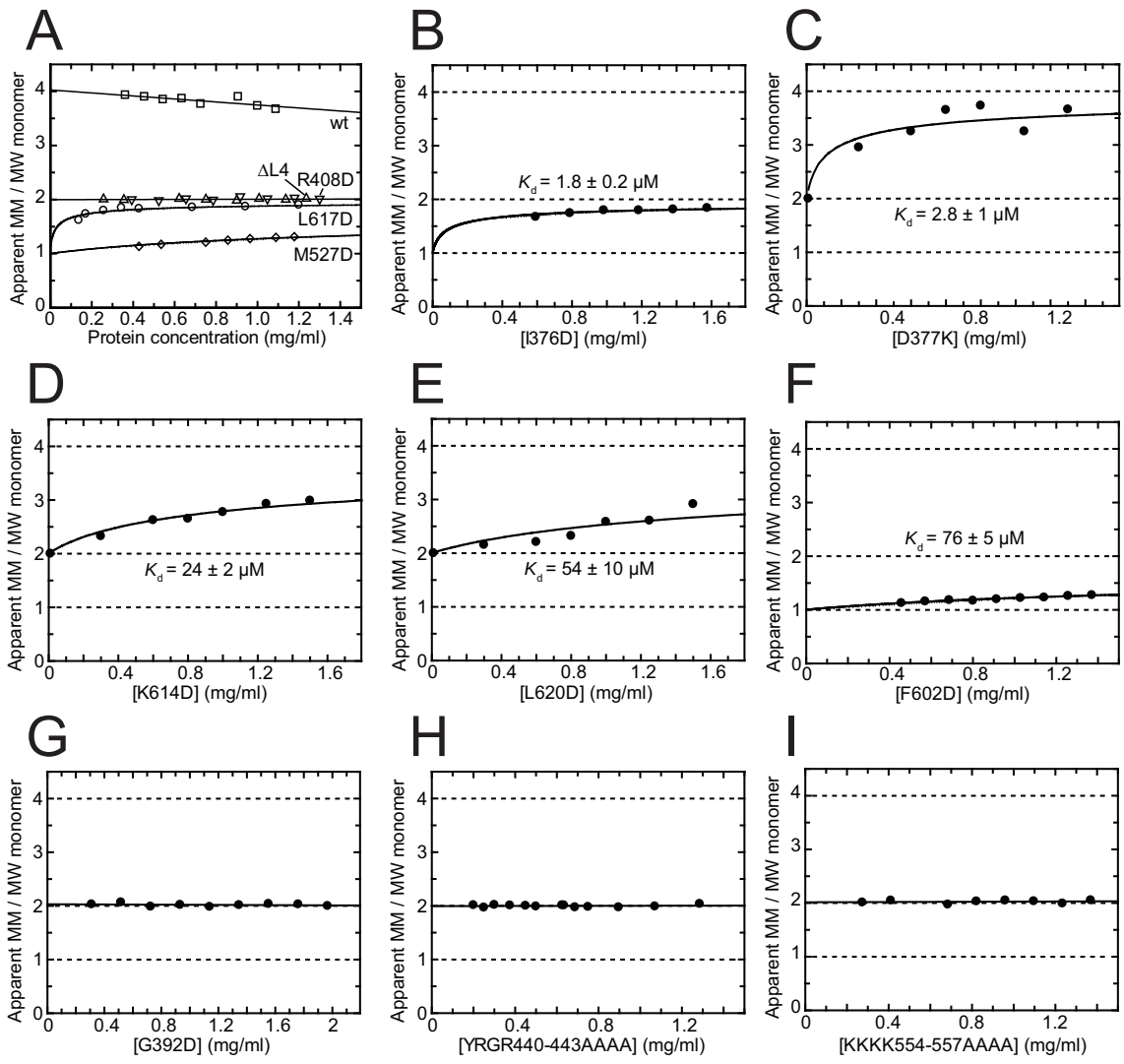

Figure 34. AUC experiments on wt hsMxA and mutants. A) Apparent molecular masses (MM) for wt hsMxA (squares) and the mutants L617D (circles), M527D (diamonds), R408D (inverted triangles) and ΔL4 (triangles) as a function of the protein concentration was calculated. Data for M527D and L617D were fitted to a monomer-dimer equilibrium function with a K_d of 55 ± 8 µM and 420 ± 140 nM, respectively. B-I) Calculated MM for other mutants that are accordingly labeled. Calculated K_d values for I376D, D377K, K614D, L620D and F602D are indicated.

It has been reported that hsMxA reversibly forms ring and spiral-like oligomers at low salt concentrations or protein concentrations greater than 1.5 mg/ml (Kochs, Haener et al. 2002). These oligomers can be sedimented by high-speed ultracentrifugation (Kochs, Haener et al. 2002). This assay was used to examine the role of the interfaces in nucleotide-dependent and independent oligomerization (3.3.15). At 2.3 mg/ml protein concentration, approximately 50% of wt hsMxA was sedimented in the absence of nucleotides (Fig. 35). Nearly all hsMxA was found in the pellet fraction when GTPγS was added at a saturating concentration. In contrast, mutants in interface 1 (I376D, D377K, K614D L617D and L620D) and interface 2 (M527D), and the ΔL4 mutant could not be sedimented by ultracentrifugation, irrespective of the presence or absence of nucleotide, indicating that these interaction sites are critical for oligomerization (Fig. 35). The mutants in interface 3 (G392D, R408D and YRGR440-443AAAA) and the second interface 2 mutant, F602D, retained the ability to form oligomers in the presence of GTPγS, albeit with reduced efficiency compared to wt protein (Fig. 35). These results confirmed that the interaction sites in the crystal are critical the oligomerization of hsMxA.

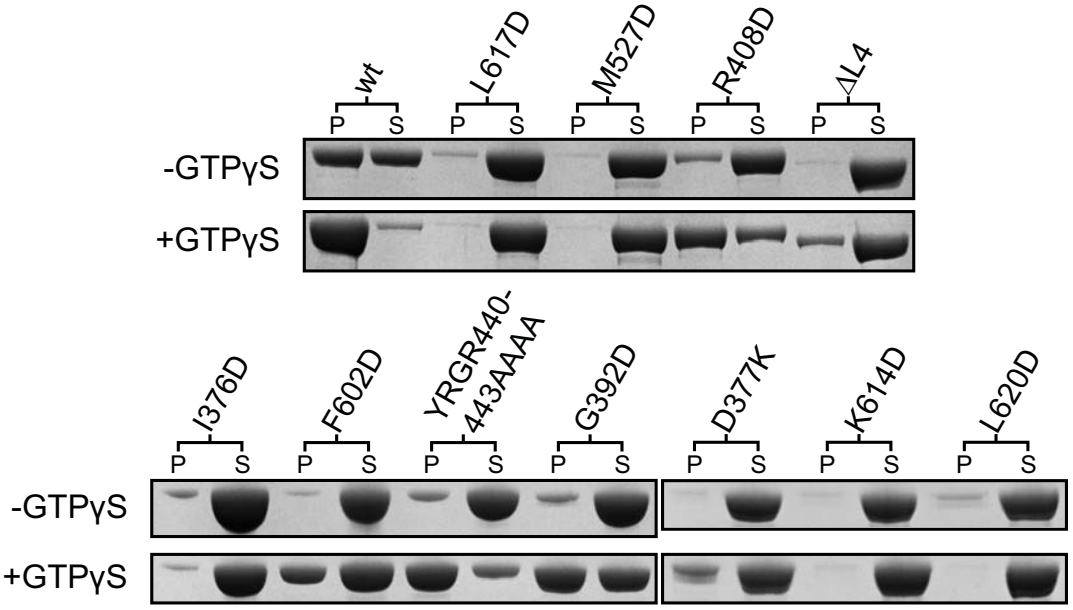

Figure 35. Sedimentation experiments for wt and selected mutants. The results obtained in the absence and presence of 1 mM GTPγS are indicated accordingly. P and S: pellet and supernatant.

To examine the role of the four interaction sites for self-assembly *in vivo*, a nuclear accumulation assay was performed by our collaborators in Freiburg (Ponten, Sick et al. 1997; Kochs, Trost et al. 1998). HA-TMxA is an artificial nuclear form of hsMxA carrying a foreign NLS and an HA-tag for detection. wt HA-TMxA and the indicated

HA-TMxA mutants were co-expressed with FLAG-tagged wt hsMxA in Vero E6 cells. When expressed alone, wt hsMxA showed mostly cytoplasmic localization. However, upon co-expression with the nuclear form of hsMxA, it accumulated predominantly in the nucleus.

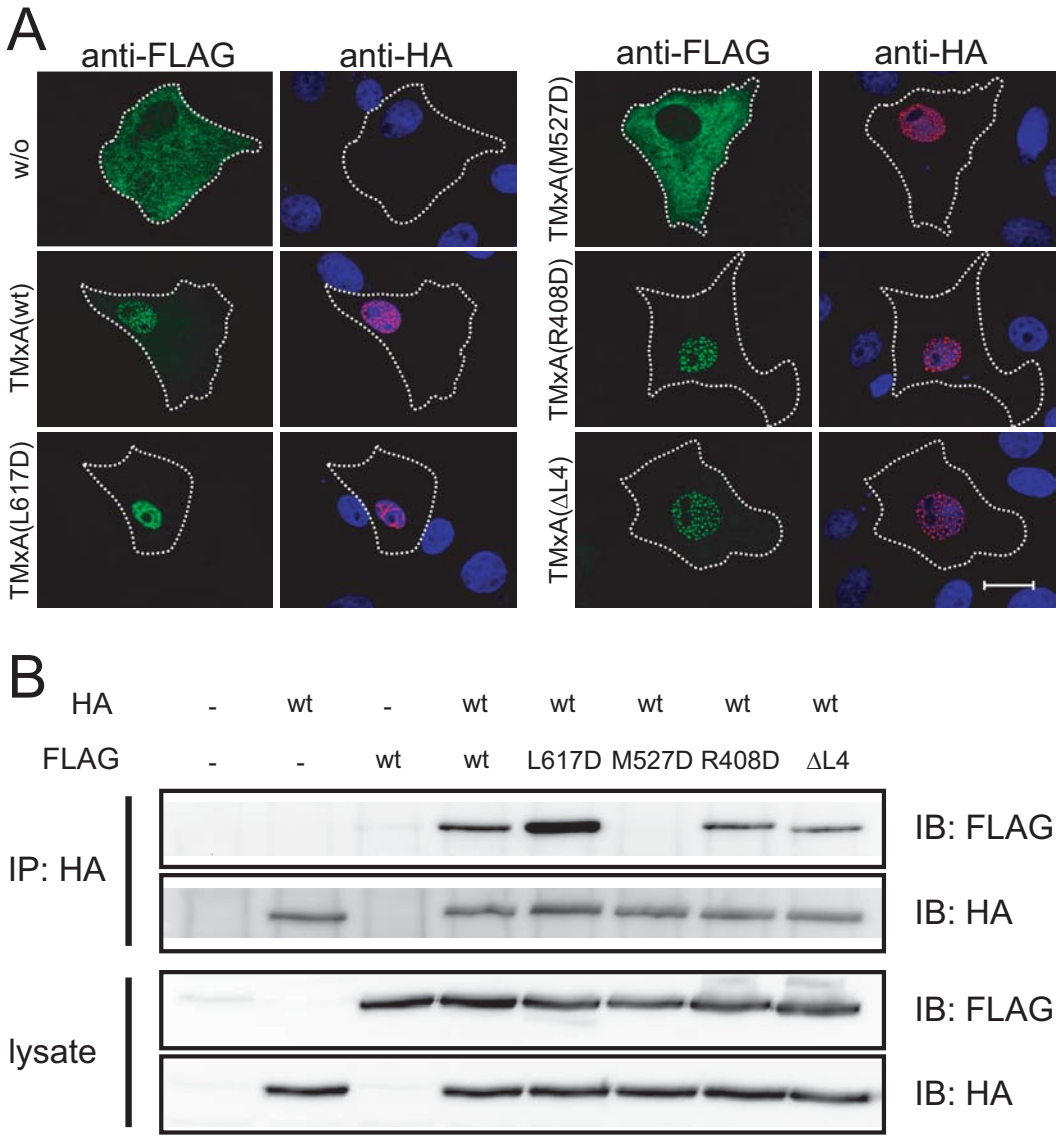

Figure 36. Study of *in vivo* assembly of wt hsMxA and mutants. A) Nuclear accumulation assay. 20 h after transfection, cells were fixed and stained with monoclonal antibodies directed against the HA-tag (red) and the FLAG-tag (green). DAPI nuclear staining (blue) is overlayed with the HA staining. In co-transfected cells, the fluorescence intensity of FLAG-tagged wt hsMxA in cytoplasm and nucleus was quantified using the Axiovision software (Zeiss, Jena) (n=20 for each experiment) (Gao, von der Malsburg et al. 2010). B) Co-immunoprecipitation assay. 293T cells were co-transfected with 1.5 µg expression plasmids encoding the indicated HA-tagged wt hsMxA and FLAG-tagged wt or mutant hsMxA constructs. After 24 h, cells were lysed and HA-tagged wt hsMxA was immunoprecipitated. After extensive washing, samples were subjected to SDS-PAGE and western blotting with antibodies directed against the HA- and FLAG-tag. Lysates represent 5% of the total input (Gao, von der Malsburg et al. 2010).

HA-tagged nuclear hsMxA proteins with mutations in interface 1 (HA-TMxA(L617D)), interface 3 (HA-TMxA(R408D)) or L4 (HA-TMxA(ΔL4)) were still able to promote nuclear accumulation of wt hsMxA. In contrast, interface 2 mutant HA-TMxA(M527D) had lost this capacity (Fig. 36A) (Gao, von der Malsburg et al. 2010). In agreement with the biochemical analysis, it was concluded that mutants in interface 1, 3 and L4 retain the ability to form dimers with wt hsMxA *in vivo*, whereas mutations in interface 2 are disruptive. These results were also confirmed in co-immuno-precipitation studies (Fig. 36B) (Gao, von der Malsburg et al. 2010).

4.3.3 Interface mutants interfere with the liposome binding

Lipid interaction is a common feature described for many dynamin-like proteins including hsMxA (described in 2.3.3). To study the role of hsMxA self-assembly on lipid binding, representative mutants in each of the interaction sites for liposome binding were tested (see 3.3.16) and compared to wt hsMxA using co-sedimentation assays followed by SDS-PAGE (Fig. 37).

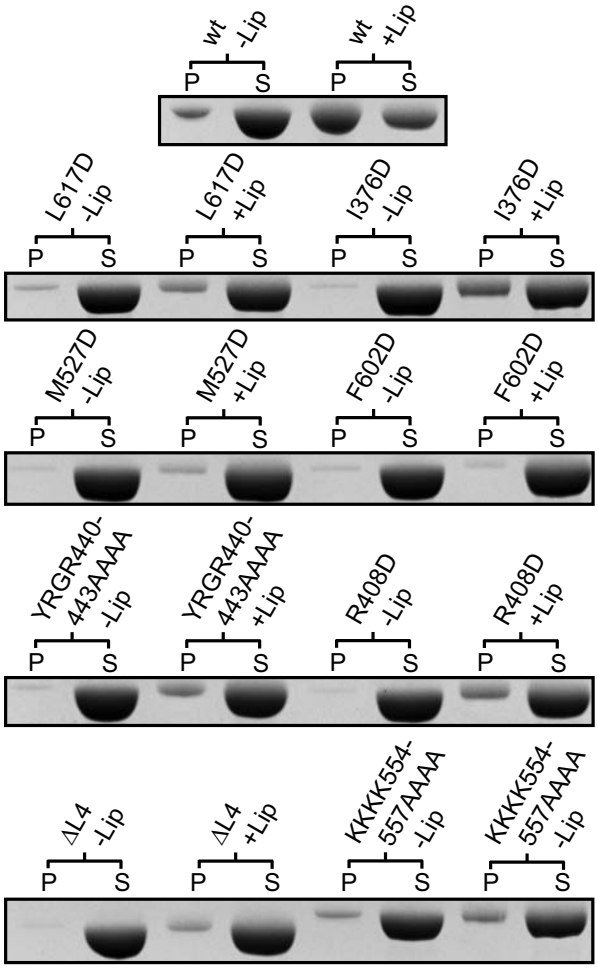

Figure 37. Folch liposome-binding assays of wt hsMxA and interface mutants. P and S: pellet fraction and supernatant.

At low hsMxA concentrations (0.75 mg/ml), approximately 60% of wt hsMxA co-sedimented with Folch liposomes. In the absence of liposomes, the protein was predominantly found in the supernatant (Fig. 37). In contrast, none of the hsMxA mutants showed significant binding to liposomes under these conditions, indicating that liposome binding requires a self-assembly competent hsMxA molecule in which all three interfaces and L4 are intact. Furthermore, the positively charged residue cluster KKKK^{554} in L4 was thought to be the potential lipid-binding site, and the KKKK554-557AAAA mutant was indeed found to lack such ability, although the reason might also be that it interrupts the native assembly of wt hsMxA (Fig. 34I).

4.3.4 Interface mutants change the GTPase activity

To probe the functional significance of each interface and L4 for assembly-stimulated GTP hydrolysis, wt hsMxA and representative mutants were analyzed in kinetics experiments, using multiple-turnover assays (excess of GTP over hsMxA) with HPLC (3.3.10) (Fig. 38).

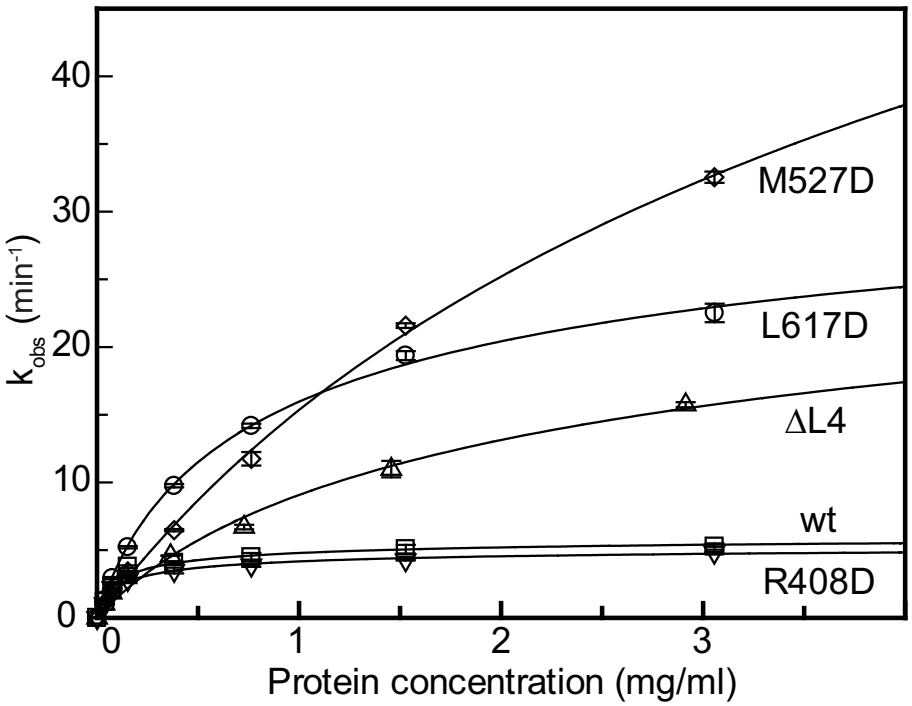

Figure 38. Kinetics of wt hsMxA and representative mutants' GTPase activities. Protein-concentration-dependent GTPase activities of wild-type hsMxA (squares) and representative mutants in each interface (L617D, circles; M527D, diamonds; R408D, inverted triangles; and DL4, triangles) were determined and fitted to a quadratic equation (see 7.2.3). The mean of k_{obs} calculated from two independent experiments is indicated with the error bar showing the range of the two data points.

When incubated with saturating concentrations of GTP (Melen, Ronni et al. 1994; Richter, Schwemmle et al. 1995), wt hsMxA showed a protein concentration-dependent specific GTPase rate with an estimated k_{max} of 6.4 min^{-1} (Fig. 38), indicating that GTP hydrolysis is stimulated by oligomerization in solution. Similar results (k_{max}= 5.6 min^{-1}) were obtained with the R408D mutant in interface 3 which can still assemble into higher-order oligomers in the presence of GTP (Fig. 35). Interestingly, the dimeric mutants L617D in interface 1 and the ΔL4 mutant displayed a six-fold increase in their maximal GTP hydrolysis rate at higher protein concentrations (k_{max}= 38 min^{-1} and 36 min^{-1}), whereas the observed GTPase rates at lower protein concentrations were comparable to wt hsMxA. The monomeric mutant M527D in interface 2 showed the highest value of the maximal GTPase rate (k_{max} = 120 min^{-1}). These results surprisingly indicate that oligomerization of hsMxA via the stalk region is not a prerequisite for assembly-stimulated GTP hydrolysis in solution.

To further elucidate the role of lipid binding in the cellular function of hsMxA, GTP hydrolysis rates of hsMxA with unfiltered Folch liposomes were measured and compared to that in liposome-free conditions to probe for any lipid-stimulated GTPase

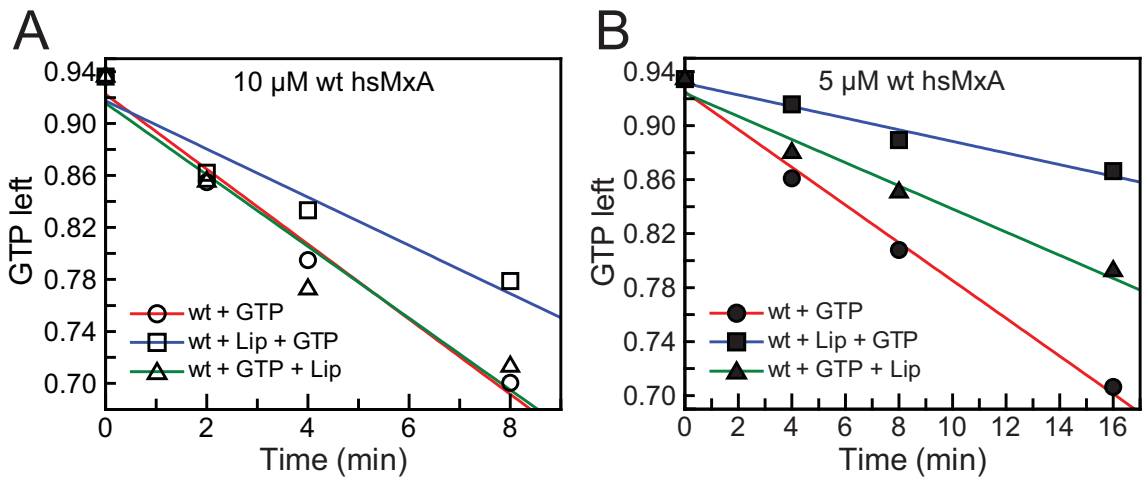

Figure 39. GTPase activity of hsMxA in presence and absence of liposomes. Hydrolysis assay was carried out for hsMxA (i) with GTP only (shown as circles for data points in the graphs), (ii) with unfiltered Folch liposomes incubated for 10 min prior to the addition of GTP (rectangle) and (iii) with the same type of liposomes added after GTP (triangle). Initial GTP concentration was 1 mM for all measurements, and unfiltered Folch liposomes were used with a final concentration of 0.5 mg/ml (see 3.3.8 and 3.3.16). The hydrolysis rates were measured at 37°C. A) Hydrolysis of GTP for 10 μM hsMxA in 8 min. All the data points were shown as void symbols. B) Hydrolysis of GTP for 5 μM hsMxA in 16 min. All the data points are shown as filled symbols. For the three sets ((i), (ii) and (iii)) of the data in both panel A and B, the linear fitting results are colored in red, blue and green, respectively.

activity. Experiments were carried out at two protein concentrations, and liposomes were supplied to the reaction system either before or after GTP was added. The results showed that at concentration of 10 µM, hsMxA alone has a GTP turnover of 2.8 min^{-1}, whereas the addition of liposomes either did not change the activity, or even reduced it to around 2.0 min^{-1} (Fig. 39A). Such effect was more obvious in the case of 5 µM protein, where the GTP turnover was further decreased to 1.5 min^{-1} and 0.5 min^{-1}, compared to 2.8 min^{-1} for liposome-free hsMxA (Fig. 39B). The same effects were also observed on hsMxA with PS liposomes (data not shown).

4.3.5 Nucleotide binding affinity

The oligomerization-dependent GTPase activity stimulation was considered to be a basic feature for classical dynamin superfamily members (see 2.3.1). However, in the GTP hydrolysis assay described in 4.3.4, it was found that non-oligomerizing hsMxA mutants had higher GTPase activity than wt hsMxA as protein concentration increases. This cannot be explained by the stalk structure and its mediated oligomerization. To clarify the contradictory results of GTP hydrolysis assays (see 4.3.4), fluorescence- and stopped-flow-based assays focusing on the difference of individual steps of GTP hydrolysis by wt hsMxA and mutant M527D were performed to seek more clues.

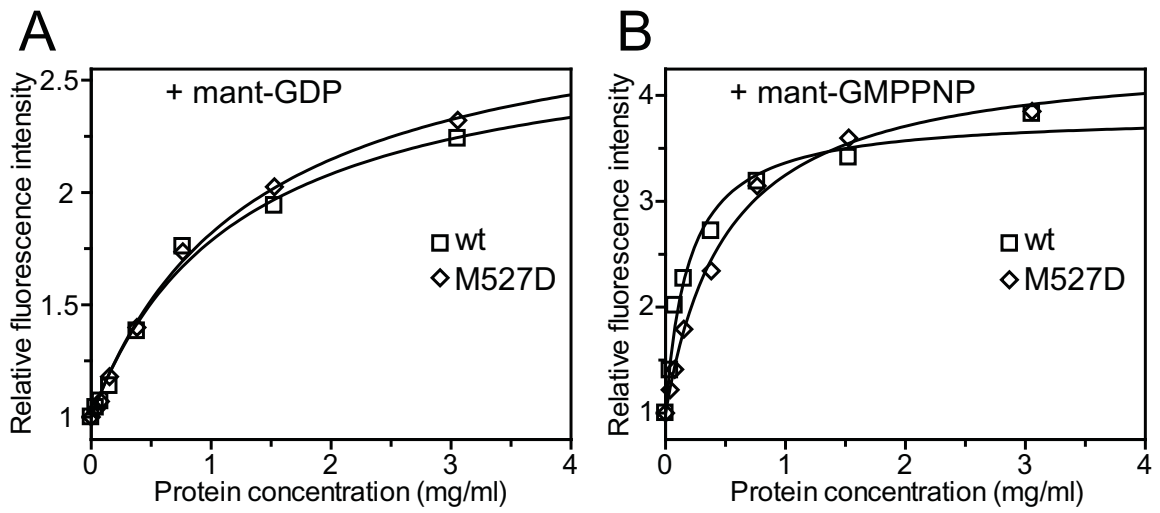

Figure 40. Fluorescence-based nucleotide binding affinity tests for wt hsMxA (□) and M527D (◇). A, binding curves for mant-GDP. B, binding curves for mant-GMP-PNP. According to (Richter, Schwemmle et al. 1995), protein binding resulted in de-quenching of mant-fluorescence, concomitant with a fluorescence increase.

A GTP hydrolysis cycle for a single G domain can be divided in three consecutive steps: (i) the binding of GTP, (ii) the cleavage of the phosphoanhydride bond, and (iii) the

release of phosphate (P_i) and GDP, finally resulting in an empty nucleotide binding pocket. The speeds of these three individual steps are incorporated into the macroscopic GTP hydrolysis rate. In the first fluorescence-based experiment, the binding affinities of wt hsMxA and M527D to either mant-GDP or mant-GMP-PNP were measured as references for the on- and off-rates of the different nucleotide for the given protein sample. As a result, it was found that the two proteins bound with similar affinities to mant-GDP (K_d = 16 µM for wt hsMxA and K_d = 18 µM for M527D), whereas wt hsMxA showed a 3-fold higher apparent affinity for mant-GMP-PNP (K_d = 2.3 µM) compared to M527D (K_d = 6.8 µM) (Fig. 40A, B).

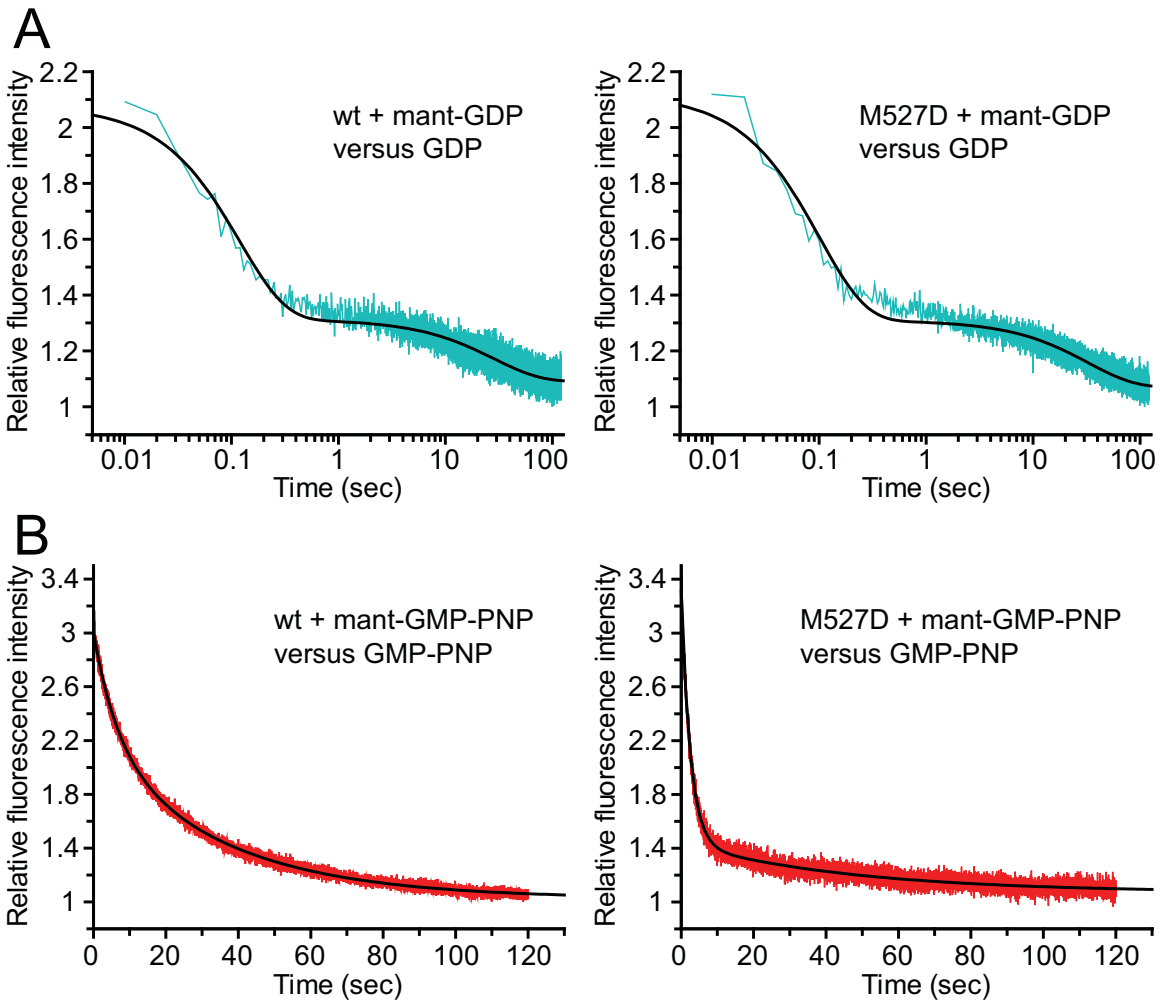

Figure 41. Fast kinetics studies of wt hsMxA and M527D. A) Raw data (cyan) and curve fits (black) for the off-rates of mant-GDP from wt hsMxA and M527D. A double exponential decay of fluorescence was observed for both reactions. k_{off1} is larger and accounts for 75% of the fluorescent decay, and the second observed off-rate, k_{off2}, is 250-fold smaller. Due to the fast fluorescence decrease, the time axis is shown in logarithmic scale. B) Raw data (red) fit with double exponential decay curve (black) for the off-rates of mant-GMP-PNP from wt hsMxA and M527D.

Next, fast kinetics experiments were performed using a stopped-flow system as described in 3.3.12, to measure the off-rates of mant-GDP and mant-GMP-PNP, which respectively mimic GDP and GDP●P_i in the GTP hydrolysis cycle, for wt and M527D (Fig. 41A, B). wt hsMxA and M527D showed similar off-rates for mant-GDP (k_{off1} = 503 min^{-1}, k_{off2} = 2.1 min^{-1} for wt hsMxA and k_{off1} = 595 min^{-1}, k_{off2} = 1.8 min^{-1} for M527D) (Fig. 41A). Furthermore, k_{off1} for mant-GMP-PNP was 2.6-fold slower for wt hsMxA (k_{off1} = 9.2 min^{-1}, k_{off2} = 1.8 min^{-1}) than for the M527D mutant (k_{off1} = 24 min^{-1}, k_{off2} = 1.3 min^{-1}) (Fig. 41B).

4.3.6 Antiviral features of the interface mutants

La Crosse virus (LACV) is a mosquito-transmitted pathogen and important cause of pediatric encephalitis in North America. hsMxA blocks its replication by binding to and sequestering the viral nucleoprotein (NP) into large intracellular deposits (Hefti, Frese et al. 1999; Kochs, Janzen et al. 2002; Reichelt, Stertz et al. 2004). To probe the significance of the identified hsMxA interaction sites and L4 in mediating these activities, a cell-based assay was performed in the lab of our collaborators in Freiburg on the complex formation of hsMxA and LACV NP (see 3.3.17) (Gao, von der Malsburg et al. 2010). Vero cells expressing wt or mutated hsMxA were infected with LACV and analyzed for complex formation of hsMxA with the viral protein as described (Gao, von der Malsburg et al. 2010). Formation of hsMxA/LACV NP complexes was quantified by generating fluorescence intensity profiles across nucleocapsid protein positive complexes. The fluorescence intensities of the signals for hsMxA and LACV NP, were determined using the Axiovision software (Zeiss, Jena). Co-localization of hsMxA and NP was considered when overlapping peaks were observed, as shown in (Fig. 42) (Gao, von der Malsburg et al. 2010). As expected, wt hsMxA redistributed the viral nucleocapsid proteins into perinuclear deposits where they co-localized (Gao, von der Malsburg et al. 2010). In contrast, the assembly-defective mutants showed no co-localization and the viral proteins accumulated near the Golgi compartment where infectious viral particles are known to be formed (Gao, von der Malsburg et al. 2010). We conclude that each of the four interaction sites is required for recognition of viral target structures and antiviral activity.

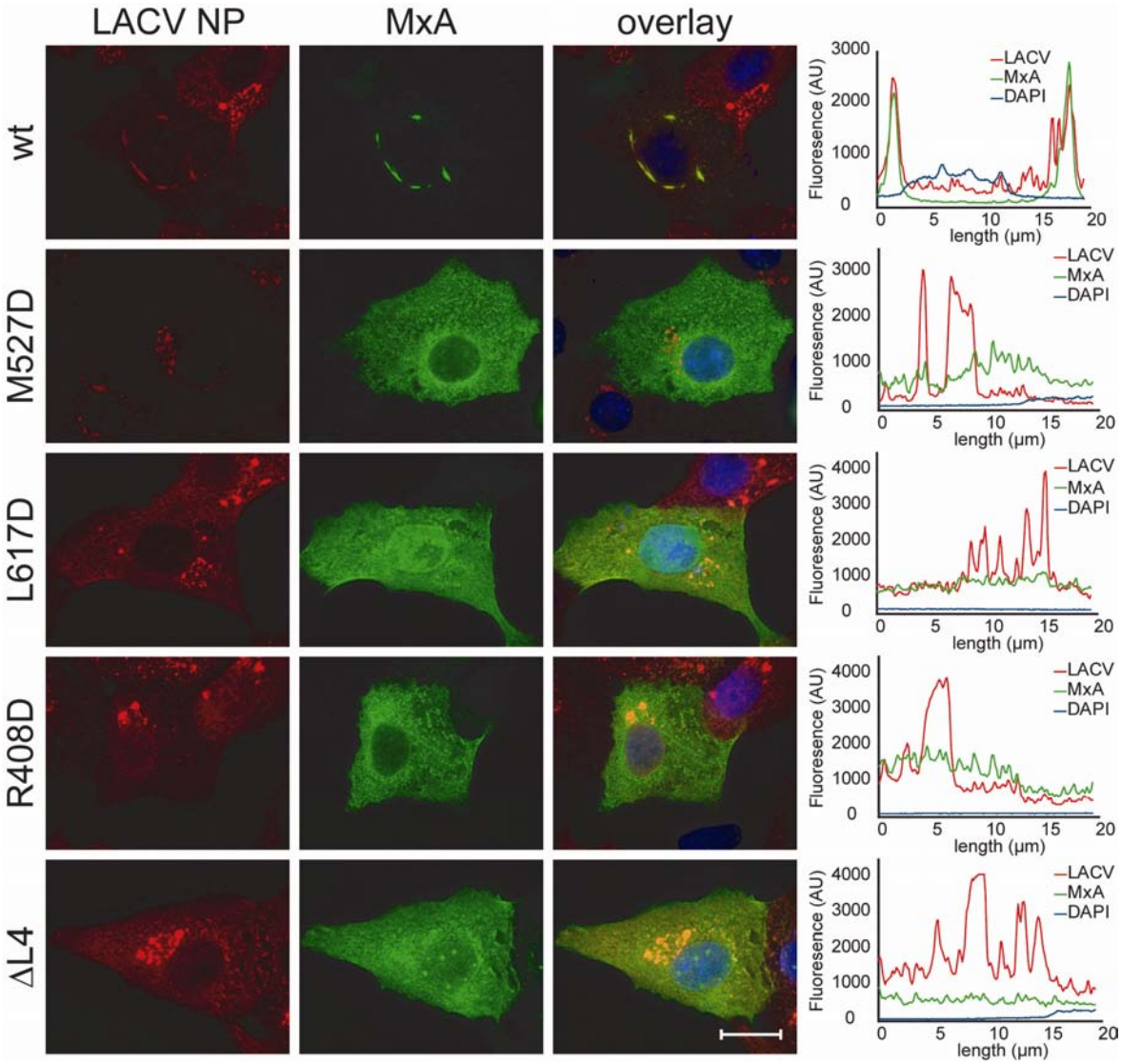

Figure 42. Complex formation of hsMxA (labeled as MxA in the figure) with the LACV nucleoprotein (NP) *in vivo*. Vero cells transfected with the indicated hsMxA constructs were infected with LACV for 16 h and then stained with antibodies specific for hsMxA (green) and LACV NP (red). In the overlays, DAPI staining is shown in blue (scale bar = 20 µm). A total number of 97% of the wt hsMxA transfected cells contained hsMxA/LACV NP complexes (n = 100), compared to 0% for all hsMxA mutants (Gao, von der Malsburg et al. 2010). The fluorescence intensities are given in arbitrary units (AU). The pictures are representative of three independent experiments.

Another antiviral assay was also carried out by our collaborators in Freiburg (see 3.3.17). In this assay, the inhibition of the polymerase complex of a highly pathogenic H5N1 influenza virus which was isolated from a fatal human case in Vietnam was assessed (Maines, Lu et al. 2005). Viral polymerase activity was determined in a mini-replicon reporter assay in which the viral components required for RNA transcription were co-expressed with the various hsMxA constructs (Dittmann, Stertz et al. 2008).

In agreement with the previous results, wt hsMxA inhibited viral replication in this assay by 80% (Fig. 43). In contrast, mutations in each of the three interfaces and L4 completely abrogated antiviral activity (Fig. 43) (Gao, von der Malsburg et al. 2010).

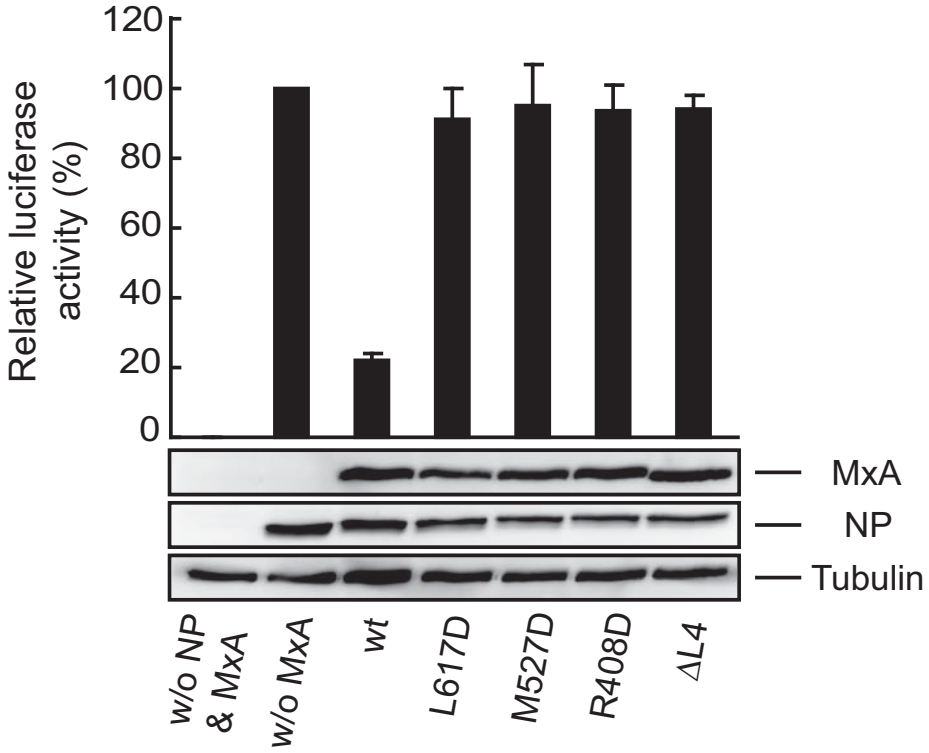

Figure 43. Minireplicon assay for FLUAV polymerase. 293T cells were co-transfected with plasmids encoding viral NP, the polymerase subunits and a reporter construct encoding firefly luciferase under the control of the viral promoter. Expression plasmids for the indicated hsMxA (labeled as MxA in the figure) constructs and for *Renilla* luciferase under a constitutive promoter were co-transfected. The activity of firefly luciferase was measured 24 h later and normalized to the activity of *Renilla* luciferase. The values without MxA expression were set to 100%. Error bars and standard deviations are indicated (n = 3). Protein expression was analyzed by western blotting using specific antibodies (Gao, von der Malsburg et al. 2010).

Taken together, the results obtained in two independent antiviral assays indicate that proper assembly of the hsMxA stalk region is essential for the antiviral function.

4.4 Model of dynamin oligomer

4.4.1 Construction of dynamin oligomer

Up to now, structural information for dynamin superfamily members in oligomerized form are available for human dynamin 1 (see 2.3.2) (Zhang and Hinshaw 2001), BDLP (see 2.3.5) (Low, Sachse et al. 2009), and a yeast dynamin-related protein Dnm1 which was published recently (Mears, Lackner et al. 2011), but not for Mx proteins. These cryo-EM studies provided low-resolution information about the 3-dimonsional (3-D) profile of the oligomers that allowed the fitting of crystal structure of individual domains into derived electron density maps. This kind of fitting was performed with the cryo-EM density map of constricted state of dynamin oligomer (see 2.3.2, Fig. 14B) (Mears, Ray et al. 2007). However, due to the missing crystal structure of the MD and GED, the corresponding criss-cross shaped middle layer of the electron densities could not be explained. As the MD and GED of hsMxA were predicted to be closely related to those of dynamins (see 2.3.1, Fig. 11) and hsMxA stalks also oligomerize in a criss-cross manner in crystals (see 4.2.4, Fig. 32A), the hsMxA stalk oligomer was used to improve the molecular scenario of dynamin oligomer (Fig. 44A-D), so as to obtain more functional hints of dynamin superfamily.

The cryo-EM studies revealed helical oligomers of dynamin, whereas the hsMxA stalk oligomer in crystals is linear. Based on the cryo-EM density map and biochemical studies (see 4.2.4 and 4.3.2-4), the dimer mediated by interface 2 was predicted to be the constitutive dimer. To accomplish the helical dynamin oligomer, the constitutive dimers made a 28° rotation against each other at interface 1, leading to larger contacts at the flexible interface 3 and L4 region which might further stabilize the oligomer (Fig. 44A). The structural models of the G domain (Yang, Tempel et al. 2010) and PH domain (Ferguson, Lemmon et al. 1994) of dynamin were fitted into the electron density map in combination with hsMxA stalks. The G domains at the top of the oligomer did not contact each other along the same helical turn, and their nucleotide binding pocket faced outward (Fig. 44A, B). The PH domains made loose contacts along the helical turn. In the front view of an exemplified tetrameric dynamin model, a T-bar-shaped arrangement of the domains could be clearly seen (Fig. 44B), corresponding to the dimeric model of dynamin (see 2.3.2, Fig. 14A) (Praefcke and McMahon 2004). The model was in good agreement with the cryo-EM electron density map (Fig. 44C, D) (Mears, Ray et al. 2007) and explained the previously undefined criss-cross region of the map.

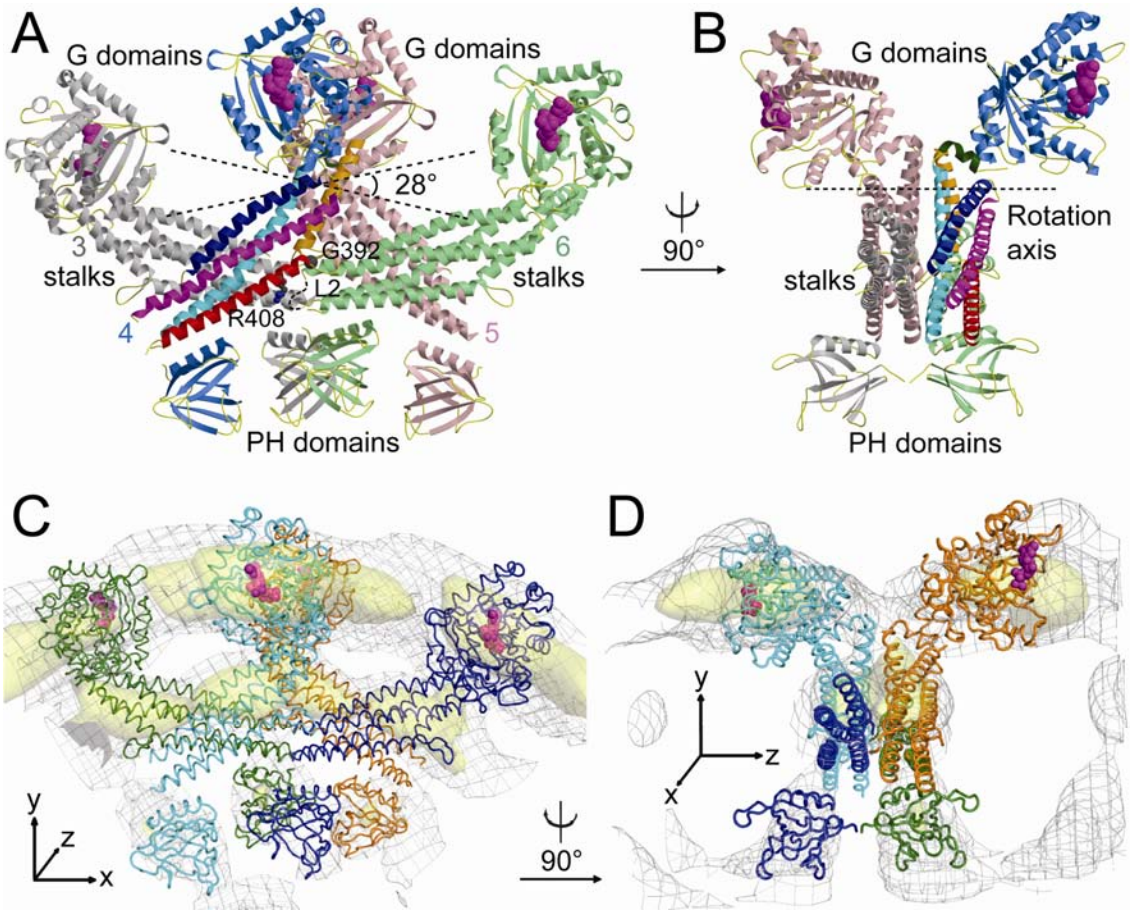

Figure 44. The tetrameric model exemplified for a dynamin oligomer. A) A tetrameric model composed of the hsMxA stalks, G domains and PH domains of dynamin as described. Stalk dimers assembled via interface 2 were rotated 28° around the indicated axis. Selected positions in interface 3 (Gly392 from L1, Arg408, L2) are indicated. The monomers are illustrated as in Fig. 32A. The GDP molecule is shown as magenta spheres. B) In the front view, the typical T-bar shape of the model becomes obvious. The G domains of each T-bar structure belong to two neighboring stalk dimers. The G domains of monomer 3 and 6, and the PH domains of monomer 4 and 5 were removed for clarity. C) and D) The fitting of the model to the EM map. Electron density is represented by a gray mesh at contour level 1.5σ and by a yellow surface at 3.5σ.(Gao, von der Malsburg et al. 2010).

4.4.2 Connectivity of individual domains of the oligomer model

The G domain was installed at the N-terminus of the hsMxA stalk according to its sequence as analyzed in 4.2.3 (Fig. 30B). The G domain was positioned in such a way that its N-terminal helix $\alpha1^G$ and incomplete C-terminal helix $\alpha5^G$ were in close proximity and almost parallel to the C-terminal helix α5 from the stalk (Fig. 45) to account for the formation of BSE (Chappie, Acharya et al. 2009). Although this helix is not resolved in the stalk structure, here it was assumed to follow the direction of α5. The $\alpha5^G$ of the G domain also has a convenient linkage with the N-terminal $\alpha1^N$ from

the stalk (Fig. 45). The PH domain was oriented so as to allow its smooth connection to the stalk via two loops that are both approximately 30 residues long (Fig. 45). Moreover, the lipid-binding loops from the PH domain faced the "bottom" of the whole molecule towards the lipid tubule (Fig. 45). The final monomer model has its three parts, namely the G domain, the stalk and the PH domain linearly aligned as in the previously proposed models (Fig. 14A).

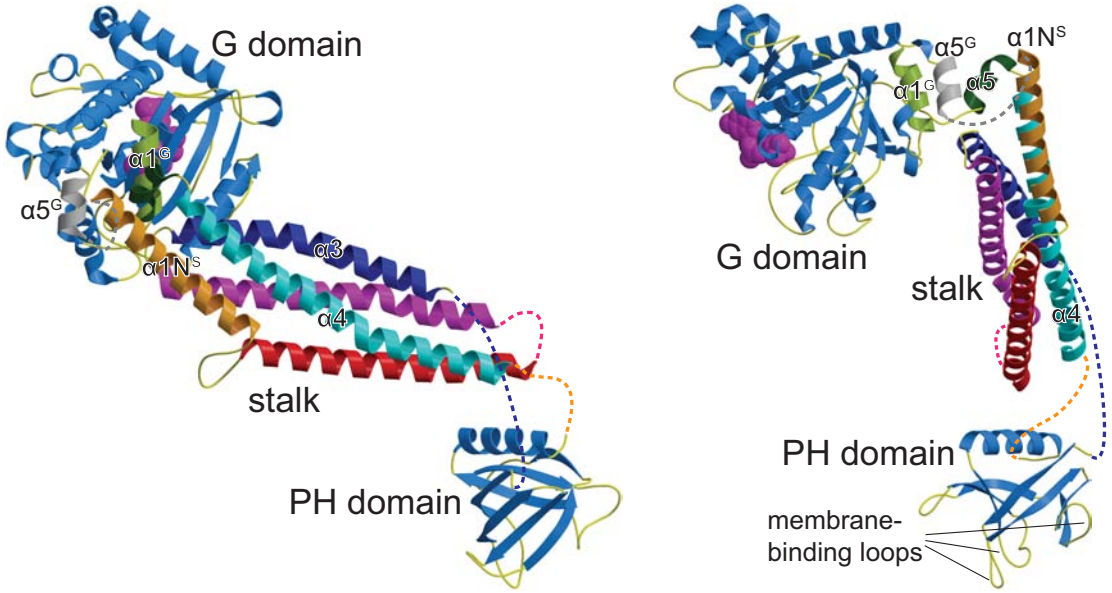

Figure 45. Two views of the modeled dynamin monomer. The G domain model was derived from a GDP-bound human dynamin 3 structure (PDB code 3L43) (Yang, Tempel et al. 2010). The PH domain model was taken from a corresponding structure of human dynamin 1 (1DYN) (Ferguson, Lemmon et al. 1994). Both domains are colored in blue. This monomer model illustrates the proposed connections between the G domain and stalk, indicated by a grey dashed line, and between the stalk and PH domain, indicated by blue and orange dashed lines. The invisible L2 is shown as a magenta dashed line. The GDP molecule is shown as magenta spheres. Individual domains, helices involved in the connections, and membrane-binding loops from the PH domain are labeled accordingly.

4.4.3 Model of a complete turn of the helical oligomer

In total, 13 dimers formed a complete turn of the modeled helical oligomer, and the 13th dimer associated with the first dimer via the highly conserved surface patches in the G domains across the nucleotide binding sites (Fig. 46). This was in agreement with the structure of a transition state dynamin G domain dimer, where at the dimeric interface the switch I and P-loop were *trans* stabilized for stimulated GTPase activity (Chappie, Acharya et al. 2010). These inter-helical-turn contacts occurred on adjacent G domains (e.g. between the 2nd and the 14th dimers, and so on) as the oligomeric

model proceeds, therefore leading to a multiplied stimulation effect on the GTPase activity of the oligomer. This helical model had an outer and inner diameter of 38 and 14 nm, respectively, which were comparable to the corresponding values obtained from previous EM studies (Praefcke and McMahon 2004).

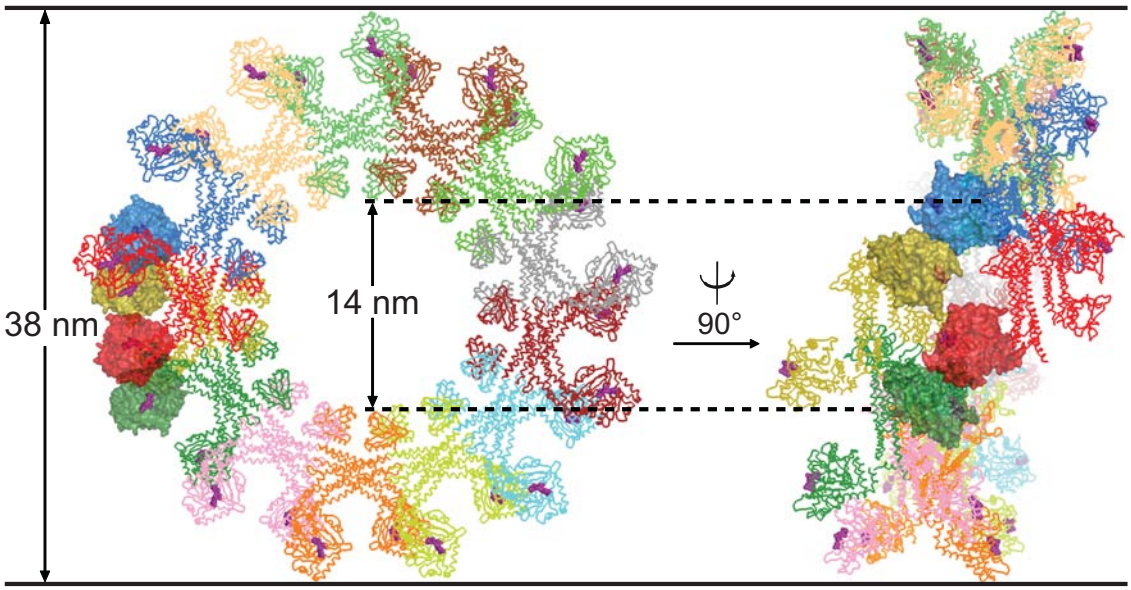

Figure 46. Two views on a complete turn of the modeled dynamin helical oligomer composed of 13-14 dimers, based on the EM electron density map of oligomerized dynamin in the constricted state. The constitutive dimers are depicted in different colors as C_α traces, while the interacting G domains in this model (green-red and blue-yellow) are highlighted by surface representations. The GDP molecule is drawn as magenta spheres. The outer and inner diameters of the helix are labeled.

In summary, the dynamin oligomeric model featured a criss-cross arrangement of the stalks (Fig. 44A, C, D) and accounted for the T-bar shape observed in side-views of oligomerized dynamin (Fig. 44B). Furthermore, it explained the connectivity of the G domain with the PH domain in oligomerized dynamin and is in agreement with the formation of a BSE between the G domain and the C-terminal part of the GED (Fig. 45). Finally, the model suggested that the G domains do not facilitate helix formation but make inter-helical contacts that promote GTPase activity, implying that GTP hydrolysis is only stimulated after formation of one complete helical turn so that G domains from neighboring turns can approach each other (Fig. 46).

4.5 The three-domain human MxA structure

4.5.1 Structure determination of a modified full-length human MxA

The stalk structure has facilitated development of a molecular scenario for the oligomerization of hsMxA and other dynamin family members. However, it is still unclear how the functions of these proteins are affected via nucleotide hydrolysis. To understand this mechanism, the full-length crystal structure of hsMxA was pursued. However, the crystallization of full-length hsMxA was mostly hindered by the oligomerization property of the protein, leading to amorphous aggregates at higher concentrations regardless of crystallization conditions. To minimize this problem, a number of oligomerization-deficient constructs based on the knowledge of the hsMxA stalk structure (Fig. 30A, B) were tested for crystallization. After extensive preliminary trials, two constructs, namely hsMxA_GBS and hsMxA_GBS$^{33-662}$ (see 3.2.12), yielded crystals, which were subsequently optimized to diffraction quality (see 3.4.1) (Fig. 47). As the constructs are modified from the native full-length protein, the related terms (e.g. crystal, structure, etc.) are named "three-domain" (the G domain, BSE and stalk) instead of "full-length", whenever applicable.

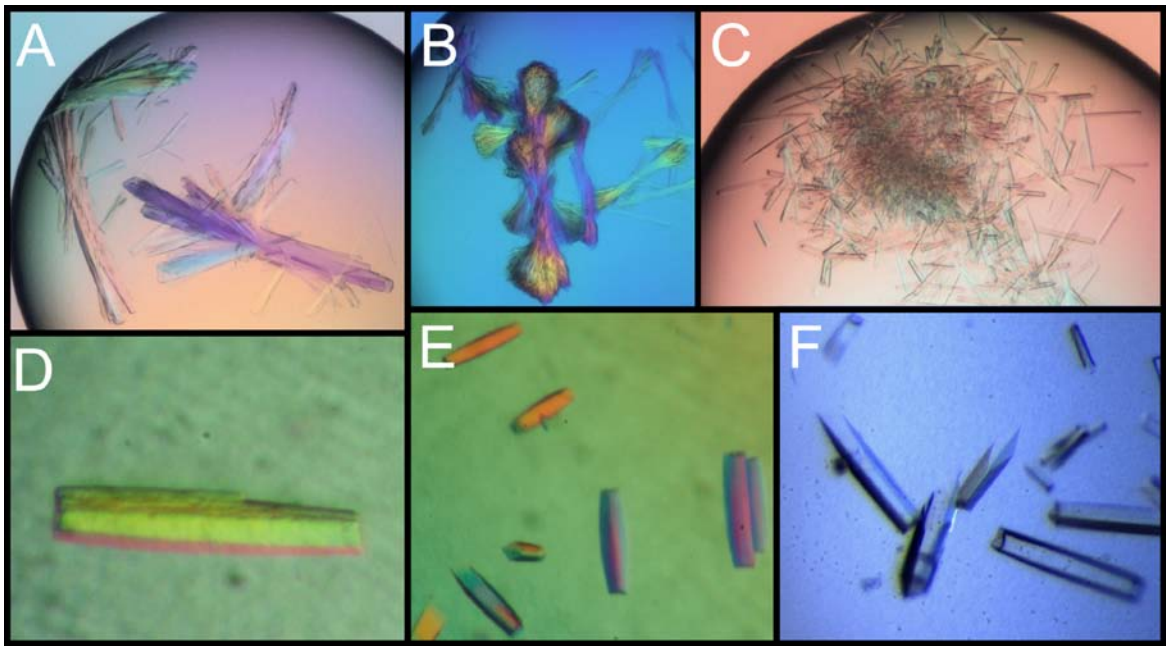

Figure 47. Crystals of three-domain hsMxA. A-C) Initial crystals from hsMxA_GBS. D-F) Optimized crystals of hsMxA_GBS and hsMxA_GBS$^{33-662}$. Crystals in F or similar conditions were used for diffraction studies.

The optimized crystals did not result in analyzable diffraction images in the first instance, but rather in smeared patterns (Fig. 48A). Therefore, the manner of handling

the crystals before diffraction was also optimized, including the freezing process and additional dehydration step (see 3.4.2). The resulting diffraction patterns were of a more satisfactory quality, although slightly anisotropic (Fig. 48B).

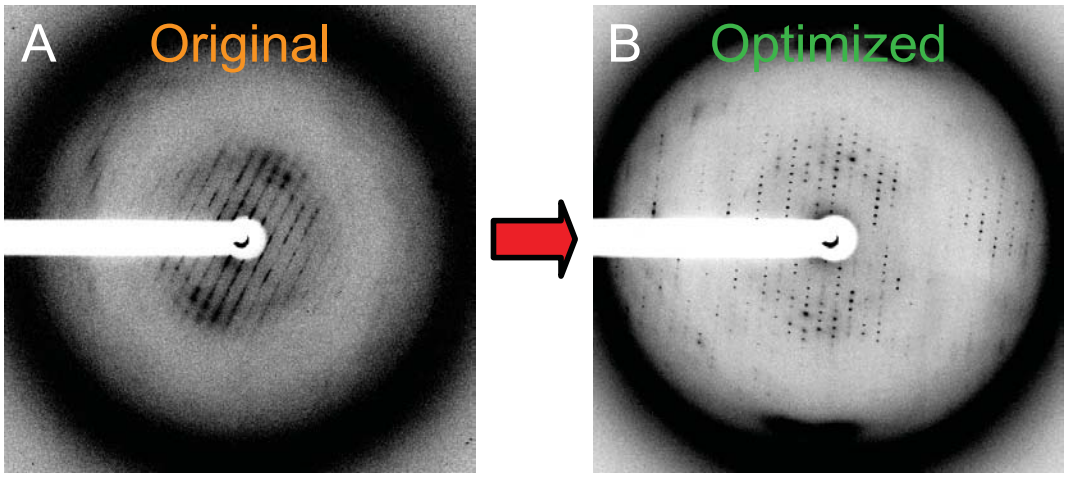

Figure 48. Improvement of X-ray diffraction of three-domain hsMxA crystals. A) Initial diffraction pattern. B) Optimized diffraction pattern.

Two native data sets and an additional SeMet data set were collected from single crystals (see 3.4.3). The data collection statistics are summarized in Table 3.

Table 3. Data collection statistics of native and SeMet three-domain hsMxA1 crystals.

Data collection	hsMxA_GBS	hsMxA_GBS$^{33\text{-}662}$	SeMet[a] hsMxA_GBS$^{33\text{-}662}$
Space group	C2	C2	C2
Unit cell dimensions			
a, b, c (Å)	146.9, 137.6, 57.7	156.8, 134.0, 58.1	150.5, 138.1, 57.6
α, β, γ (°)	90.0, 106.9, 90.0	90.0, 106.3, 90.0	90.0, 106.5, 90.0
Wavelength (Å)	0.91841	0.91841	0.97960
Resolution (Å)*	31-3.50 (4.41-3.50)#	35-3.50 (4.15-3.50)‡	50-5.60 (5.75-5.60)
Unique reflections	7,012 (1,076)	10,349 (1,699)	6,816 (532)
Completeness (%)*	50.3 (15.5)	70.6 (29.0)	98.8 (96.6)
R_{symm}*, a, b	0.064 (0.341)	0.097 (0.595)	0.077 (0.712)
$I/\sigma(I)$*	12.38 (4.30)	9.33 (2.25)	8.76 (2.01)
Redundancy*	3.14 (2.93)	3.06 (3.03)	3.54 (3.42)

*Numbers in brackets represent values from the highest resolution shell.
#The values (Å) for resolution limit along a*, b* and c* are 4.5, 5.5 and 3.5, respectively.
‡The values (Å) for resolution limit along a*, b* and c* are 4.0, 4.2 and 3.5, respectively
[a]For the SeMet data Friedel pairs were treated as separate observations.
[b] R_{symm} is described in 3.4.4.

The low completeness of two native data sets results from the anisotropic feature of the diffraction patterns (Fig. 48B, Table 3). To obtain more detailed structural information, high resolution reflections, although not complete, were included in data processing (see 3.4.4). Data sets for both hsMxA_GBS and hsMxA_GBS$^{33\text{-}662}$ were used for structure determination (see 3.4.5) (Table 3). After molecular replacement, extra positive electron densities of the C-terminal helix of the GED and of several loops were clearly discernable (Fig. 49A, B, C).

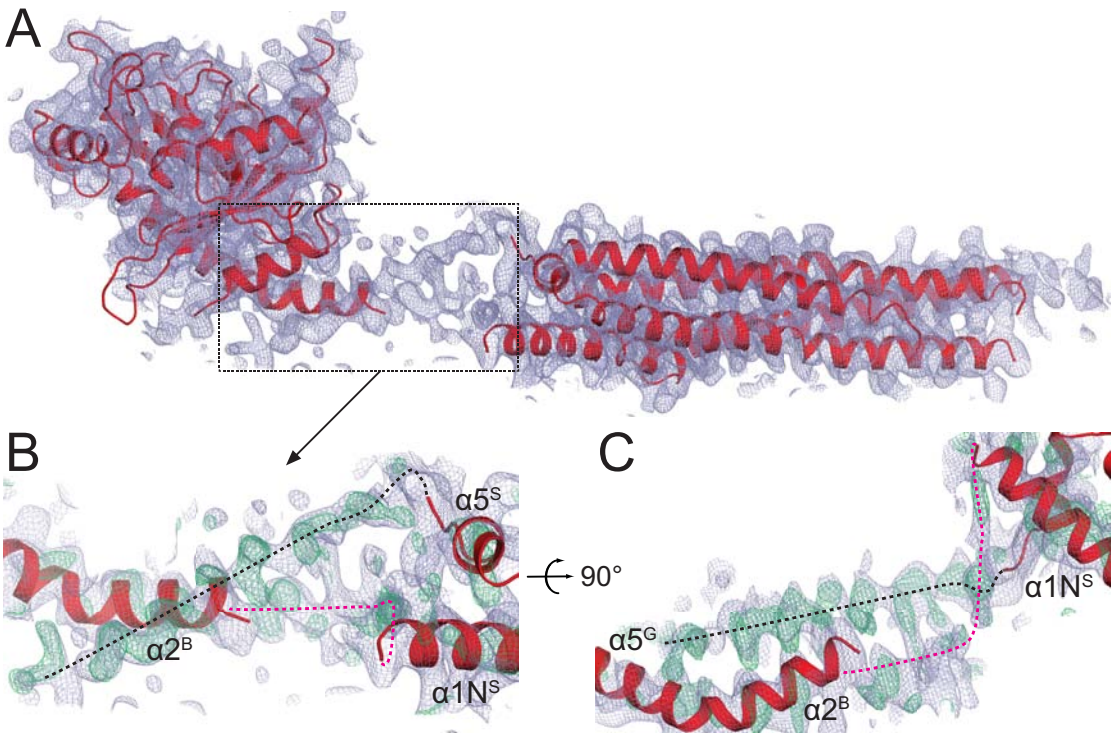

Figure 49. Molecular replacement result of three-domain hsMxA. A) 2*Fo*-*Fc* electron density map of hsMxA after phasing by molecular replacement. The two search models are shown as red ribbons. The density representing the missing parts of BSE and the hinge is clearly visible in between the G domain and the stalk. B and C, Two detailed views of the emerging density between the G domain and the stalk. The missing parts of the model are indicated by dashed lines as suggested by the emerging electron density. The magenta line represents the missing part of the α2^{B} and complete L1^{BS}, and the black line indicates the missing part of L2^{BS} and complete α3^{B}. The α1^{B} of the search model was removed for clarity. These first-instance electron density indications, showing a clearly helical shape and even some side chains, have greatly facilitated the subsequent model building. The 2*Fo*-*Fc* and *Fo*-*Fc* electron density maps are shown at 0.8σ as light blue mesh and 2.2σ as green mesh, respectively.

To verify the backbone trace of the low resolution structure, a data set of a SeMet-derivative protein crystal was collected at the peak wavelength of selenium absorption to locate selenium atoms (see 3.4.4-5) (Table 3). In total, 9 out of 12 (1 out of 3 in the G

domain, 8 out of 9 in the stalk) selenium positions were found, which confirmed correct assignment of corresponding methionines in the native structure. However, no anomalous difference density was observed for the remaining 3 methionines (Fig. 50).

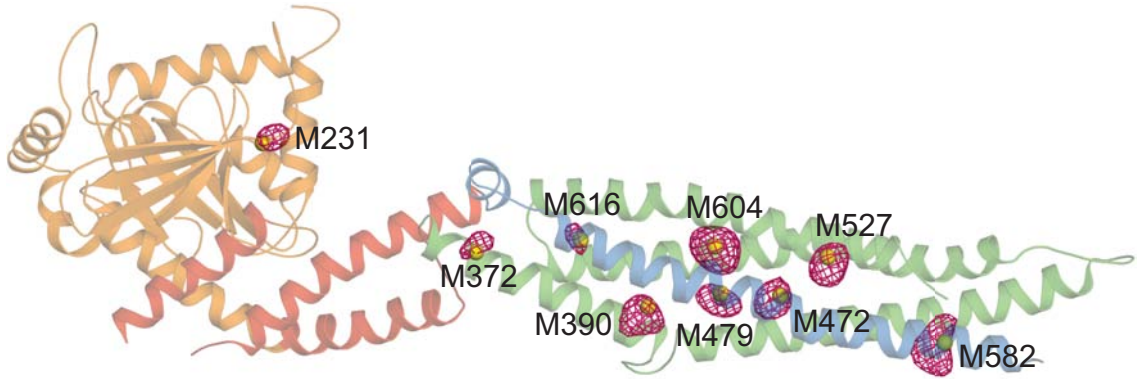

Figure 50. Verification of the three-domain hsMxA model. The anomalous difference map was shown at 3.3σ in pink, the sulphur atoms of corresponding methionines in the hsMxA model are shown as yellow spheres. The hsMxA model is shown in ribbon-representation and rendered half-transparent for clarity.

Refinement was carried out for both hsMxA_GBS and hsMxA_GBS$^{33\text{-}662}$ (see 3.4.6). No major differences were observed of the two structures since in both case the N-terminal portion could be visible only from the 45th amino acid residue of the native protein. Due to a better resolution, structure from hsMxA_GBS$^{33\text{-}662}$ was chosen for the final model. The refinement statistics are summarized in Table 4.

Table 4. Refinement statistics of native three-domain hsMxA structures.

Refinement	hsMxA_GBS	hsMxA_GBS$^{33\text{-}662}$
Resolution (Å)	31 – 3.5	35 – 3.5
R_{work}[a] / R_{free}[b]	0.306 / 0.333	0.260 / 0.294
Molecules / asymmetric unit	1	1
Protein atoms	4,642	4,510
Water / ligand / ion atoms	0	0
R.m.s.d. Bond lengths (Å²)	0.006	0.015
R.m.s.d. Bond angles (°)	0.931	1.503

[a] R_{work} is the same as R_{cryst} described in 3.4.6.
[b] According to Weiss 2001.

The final model has an excellent geometry at the given resolution, with 87 % of all residues in the most favored region and only 0.2% in disallowed regions in the Ramachandran plot, as determined by PROCHECK (see 3.4.7) (Fig. 51).

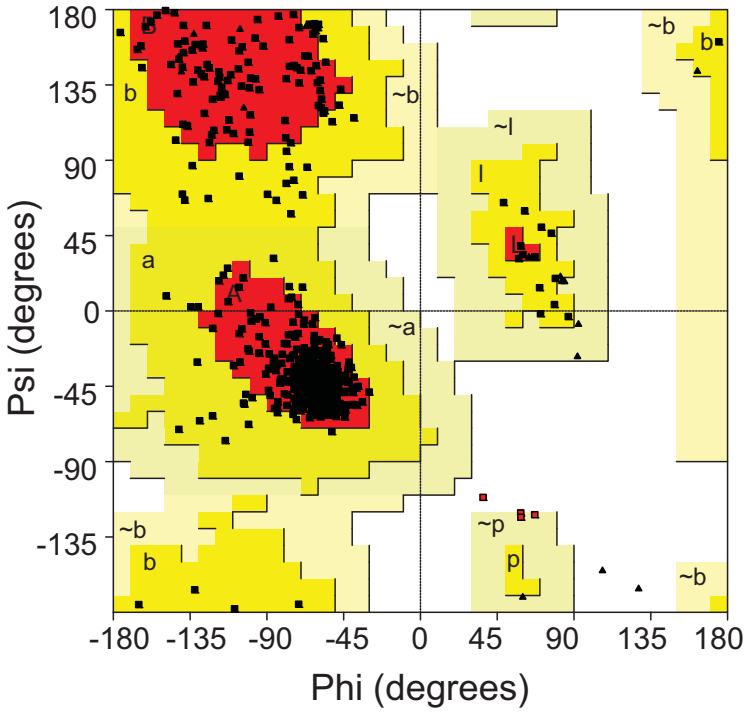

Figure 51. Ramachandran plot of the three-domain hsMxA structure. Of all residues, 87.0% are in the most favored regions. 12.2% and 0.6% are in additional and generously allowed regions, respectively. Only 1 residue is in disallowed regions.

4.5.2 Structure analysis of the three-domain human MxA

With the aid of DEN refinement and the stalk structure model, side chain density for a number of residues along the complete sequence became apparent, either already in the beginning or after a few rounds of initial refinement even at this moderate resolution, which facilitated model building in previously undefined regions, such as the missing L2 in the hsMxA stalk structure.

The hsMxA_GBS$^{33\text{-}662}$ model began at amino acid position 45 and ended at the very C-terminal residue of the native protein. It shows a three-domain architecture comprising the N-terminal G domain, the helical BSE (Chappie, Acharya et al. 2009) and the stalk (Fig. 52A, B). This arrangement was not strictly coinciding with the "traditional" domain boundaries derived from the primary sequence (Fig. 52A). The G domain of hsMxA consisted of eight central β-strands, surrounded by α-helices, and was very similar to the nucleotide-free G domain of rat dynamin. The two switch regions known to mediate nucleotide-dependent changes were not visible in the electron density, and the G4 motif, *cis*- and *trans*-stabilizing loops, shown to be involved in G domain dimerization in dynamin, were only weakly defined. The C-terminus of the G domain

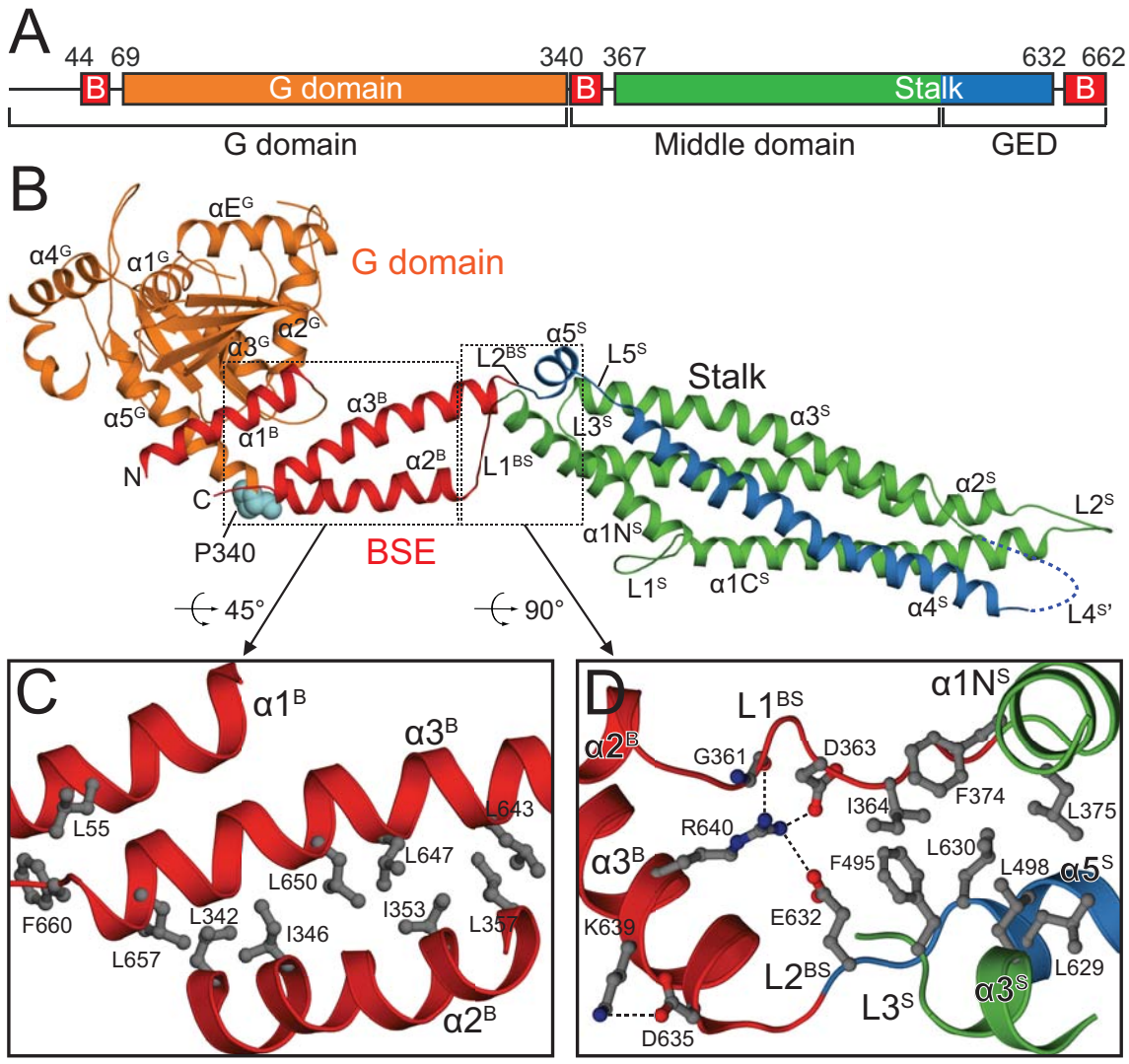

Figure 52. Structure of the three-domain hsMxA monomer. A) Schematic representation of the domain structure of hsMxA: B (bundle signaling element) in red; G domain in orange; stalk in green and blue. The conventional MD and GED are also indicated. B) Ribbon-type representation of an hsMxA monomer colored as A. with N- and C-termini, as well as most of the secondary elements labeled. The unresolved artificial loop 4 in the stalk (termed L4$^{S'}$) is indicated by a dashed line. The invariant Pro340 linking the C-terminus of G domain and BSE is shown as spheres in cyan. C) Structure of the BSE. The three-helical bundle is shown in ribbon-type and the residues involved in the inter-helix interactions are shown as ball-and-stick models. The G domain and L1^{BS} were removed for clarity. D) The hinge region between the stalk and BSE. Residues involved in interactions in the hinge region are shown in ball-and-stick representation. α2^{S} and parts of α1N^{S}, L3^{S} and α3^{S} were removed for clarity.

extended via the invariant Pro340 to the BSE (Fig. 52B). The corresponding Pro294 in dynamin were suggested to mediate conformational coupling of the G domain and BSE (Chappie, Acharya et al. 2010). The BSE was composed of a three-helical bundle formed by helices α1^{B} (where superscripts G, B, S stands for G domain, BSE and stalk; the labeling for stalk elements in the three-domain hsMxA are corresponding to those

in the hsMxA stalk, where no superscripts are used; see also Fig. 31) at the N-terminal end of the G domain, $\alpha2^{B}$ extending from the C-terminus of the G domain, and $\alpha3^{B}$ which comprised the C-terminal portion of the GED (Fig. 52B, C). $\alpha2^{B}$ and $\alpha3^{B}$ form an extensive hydrophobic network (Fig. 52C). Most of these residues are also conserved in with dynamins. In contrast, $\alpha1^{B}$ seems only weakly associated with $\alpha3^{B}$ via a conserved hydrophobic interaction between Leu55 and Phe660 (Fig. 52C).

While the globular G domain is located at one end of the BSE, the stalk of hsMxA forms an alpha-helical extension at the other end (Fig. 52B). Its structure is almost the same as that obtained from the stalk alone. The final short helix $\alpha5^{S}$ leads the stalk back to the BSE. At its N-terminus, the stalk is connected to the BSE via loop $L1^{BS}$ and at the C-terminus via loop $L2^{BS}$, both of which are clearly resolved in the electron density and appear to form a hinge between the two domains (Fig. 52D). $L1^{BS}$ is in an extended conformation and interacts loosely via hydrophobic and polar contacts with $L2^{BS}$ (Fig. 52D). $L2^{BS}$, in turn, forms further, mostly hydrophobic, contacts with $\alpha3^{S}$ and $\alpha5^{S}$ of the stalk (Fig. 52D). The highly conserved Glu632 in the middle of $L2^{BS}$ might interact with Arg640 from $\alpha3^{B}$, which simultaneously form a hydrogen bond with the oxygen atom of Gly361 and a salt bridge with Asp363 (Fig. 1D) from $L1^{BS}$. Mutations in Arg725 in dynamin corresponding to Arg640 in hsMxA lead to a reduced GTPase activity but increased endocytosis efficiency (Sever, Muhlberg et al. 1999), suggesting that these interactions contribute to the conformational coupling of the GTPase reaction with the effector function in the stalk. Interestingly, this hinge region was also shown to be present in BDLP at equivalent position and was suggested to allow the large conformational change upon GMP-PNP binding (see 2.3.5, Fig. 20B) (Low, Sachse et al. 2009).

4.5.3 The analysis of the three-domain human MxA oligomer

In the crystals, hsMxA oligomerized via the stalks which assembled in a criss-cross pattern (Fig. 53A). This arrangement via three distinct interfaces was almost identical to that observed for the isolated hsMxA stalks (Fig. 32) and described the physiologically relevant assembly of full-length hsMxA. The two-fold symmetric interface 2 in the centre of the stalks was characterized by hydrophobic residues Met527 and Phe602 (Fig. 53B), which reached into a hydrophobic pocket of the opposing molecule and mediated assembly of an hsMxA dimer (Fig. 53B). The extended shape of this dimer was in good agreement with a low resolution re-

construction of a dimeric dynamin mutant obtained by small angle X-ray scattering (SAXS) (Kenniston and Lemmon 2010), indicating that hsMxA and dynamin dimers have similar architectures. Interface 1 in the stalk was located in vicinity of the BSE and mediates oligomerization of hsMxA dimers (Fig. 53C). It included residues Ile376, Asp377, Lys614, Leu617 and Leu620. Interface 3 including loop $L1^S$ and Val449 also participated in oligomerization by mediating contacts between parallel stalks (Fig. 53D).

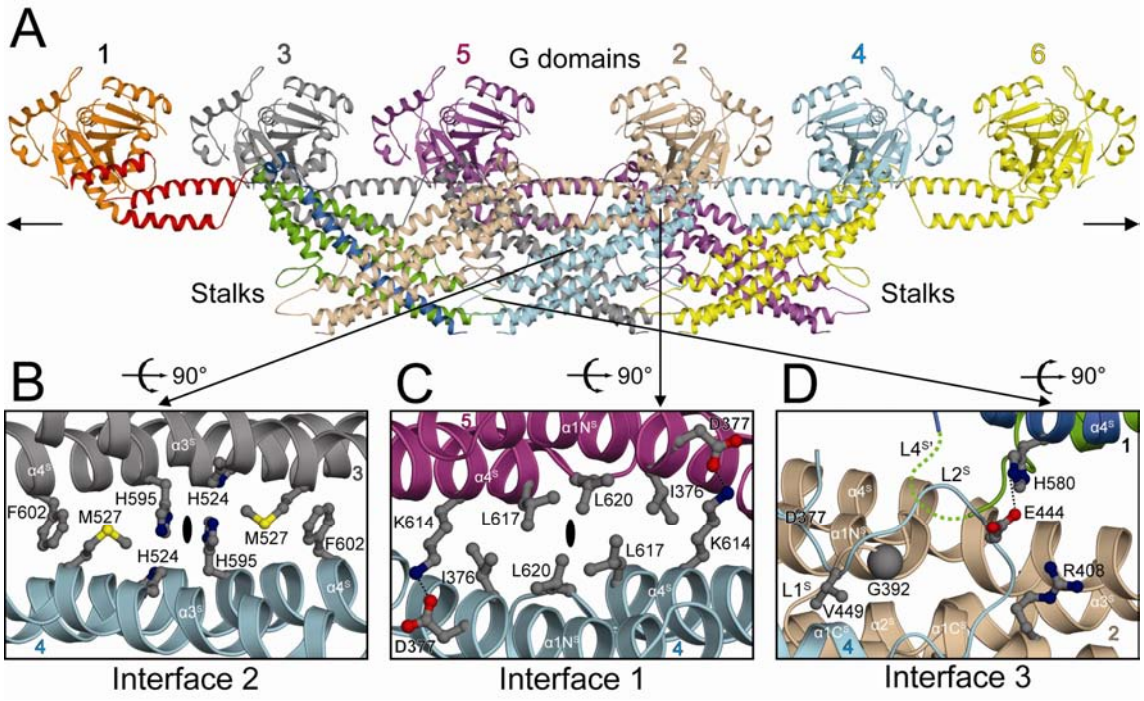

Figure 53. Assembly of the three-domain hsMxA. A) Ribbon-type representation of an hsMxA hexamer. The six monomers are individually colored and labeled in a way similar to those in Fig. 32. The overall architecture and the interfaces are consistent with the isolated stalk oligomer. B) Interface 2 is characterized by a symmetric interaction of Met527 and Phe602 which interact *in trans* with each other. A central histidine cluster is also involved in the interface. The corresponding residues are shown as ball-and-stick models. C) Interface 1 consists of a large hydrophobic network built up by conserved Ile376, Leu617, and Leu620, and two symmetric salt bridges formed by Asp377 and Leu614 *in trans*. The corresponding residues are shown as ball-and-stick models. For B and C the symmetry centre is indicated each by a black ellipse. D) Interface 3 details. $L2^S$ was completely resolved in our structure with the YRGR440-443AAAA mutation. The preserved Glu444 in the conserved YRGRE motif in $L2^S$, whose side chain is well covered by the electron density, might interact with a conserved His580 from the other monomer (as indicated by the numbers). The Val449 and Gly392 mediating the interaction between the parallel monomers are observed. The conserved Arg408 is located in the vicinity of $L2^S$ of the parallel monomer. The corresponding residues are shown as ball-and-stick models. The incompletely resolved artificial $L4^{S'}$ is shown as a dashed line.

In addition to the previously described interactions in the stalk, further contacts between neighboring hsMxA monomers became apparent in the three-domain hsMxA oligomer. In the isolated stalk structure, $L2^S$ was not visible (Fig. 30B), but in the three-domain structure the loop was fully resolved, contacted the anti-parallel stalk (Fig. 53) and might contribute in this way to oligomerization of hsMxA. Interestingly, the BSE of each monomer was in contact with the stalk of the neighboring parallel monomer. As suggested by the clear trace of electron densities, a number of side-chain contacts were found to mediate this interaction, i.e. one salt bridge between Asp478 from $\alpha2^S$ of the stalk and Arg654 from $\alpha3^B$ of the BSE, and hydrogen bonds between Asp467 from $\alpha2^S$ of the stalk and $\alpha2^B$ from the BSE. Besides these interactions, hydrogen-bonding between Lys503 from $\alpha2^S$ of the stalk and oxygens on the main chain of Ala658 and Phe660 also contributed to the stalk-BSE interface (Fig. 54).

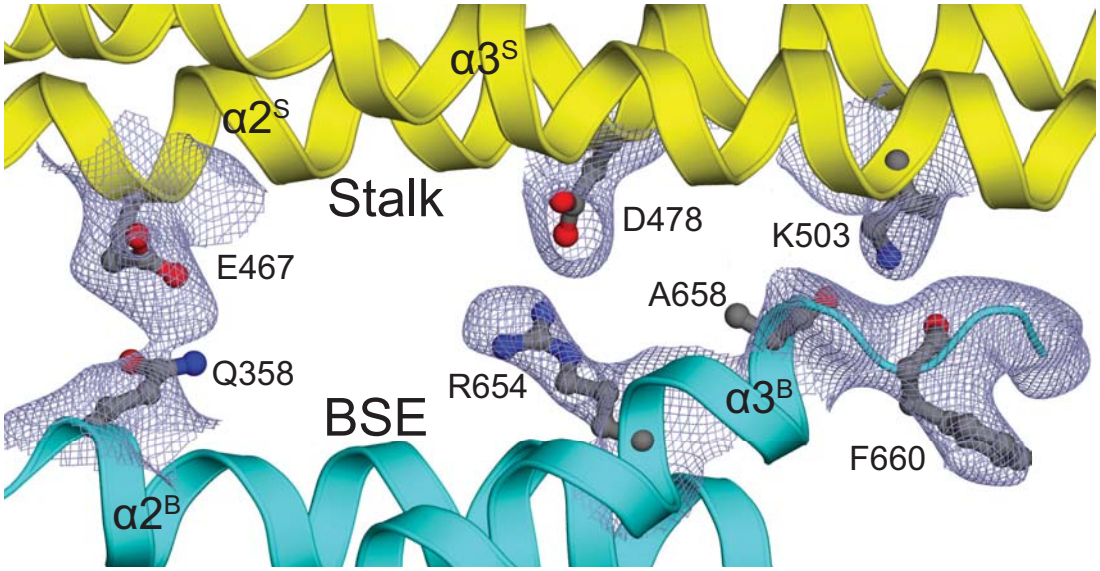

Figure 54. The interaction between the BSE and the stalk. Two parallel monomers (monomer 4 and 6 from Fig. 52A with the same colors) are shown with helices and residues involved in the interaction labeled, and the residues are shown as ball-and-stick models. The 2*Fo*-*Fc* electron density map around the interaction sites is shown at a level of 1.0σ as light blue mesh. Involved residues are shown. The side chains of these residues are clearly discernable in the electron density.

From the analysis of crystal packing it was discovered that large solvent channels were present in the crystal, which led to a solvent content of around 70%, compared to a normal value of 50%. The high solvent content made the crystal lattice instable and therefore challenged the freezing process as described in 3.4.2 and 4.5.1. It was also notable that G domains along the *c* axis of the crystal did not contact each other (Fig. 55A, B). This finding served as indirect evidence that the G domain dimerization

required the binding of nucleotide, and the release of nucleotide would lead to a dissociation of the G domain dimers. However, due to insufficient crystal contacts, the G domain was not defined as clearly as the stalk region, although the DEN refinement gave rise to greatly improved electron density maps.

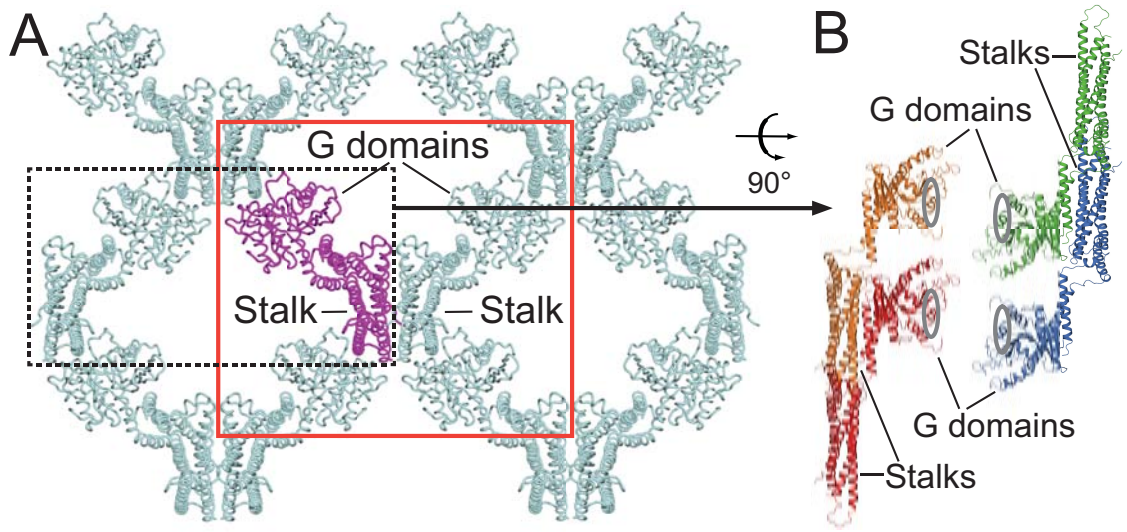

Figure 55. Crystal packing of the three-domain hsMxA. A) Crystal packing viewed along *c* axis: the T-bar shaped dimer can be seen. The unit cell is shown as orange block. One molecule is highlighted in magenta out of others colored in cyan. The G domains and the stalks are indicated. Large solvent channels can be seen. B) The interaction between the G domains from parallel linear oligomers. Four monomers are shown as ribbons from the crystal lattice in A. Two monomers belonging to the same linear oligomer are colored in red and orange, while the other two from the parallel linear oligomer are colored in blue and green. The G domains and stalks are indicated. The nucleotide binding sites are marked with gray ellipses. According to the dynamin G domain model (Fig. 13A) (Chappie, Acharya et al. 2010), the *trans* dimeric interfaces of the G domains are not facing each other, and there are no substantial crystallographic contacts between those G domains.

4.6 Chraracterization of the hinge and BSE-stalk interface

4.6.1 Mutations in the hinge and BSE-stalk interface

To investigate the function of the hinge region and BSE-stalk interface, corresponding point mutations were generated to full-length wt hsMxA according to 3.2.10. These mutants included E632A and R640A in the hinge region (Fig. 52D) and Q358A, D478A and K503A in the BSE-stalk interface (Fig. 54). Their oligomerization property and GTPase activity were subsequently assayed.

4.6.2 Oligomerization studies

The mutants were first tested in sedimentation assays together with wt hsMxA (see 3.3.15). Under these conditions, 50% of wt hsMxA oligomerized in the absence of nucleotide while more than 90% was sedimented in the presence of GTPγS (Fig. 56). Hinge region mutants E632A and R640A, showed strongly reduced oligomerization in the absence and presence of GTPγS indicating that an intact hinge region is important for native assembly. The K503A mutant in the BSE-stalk interface showed strong oligomerization deficits in the absence of nucleotides which could only partially be rescued by addition of GTPγS (Fig. 56), In contrast, the BSE-stalk interface mutants Q358A and D478A behaved similarly as wt hsMxA in these assay (Fig. 56).

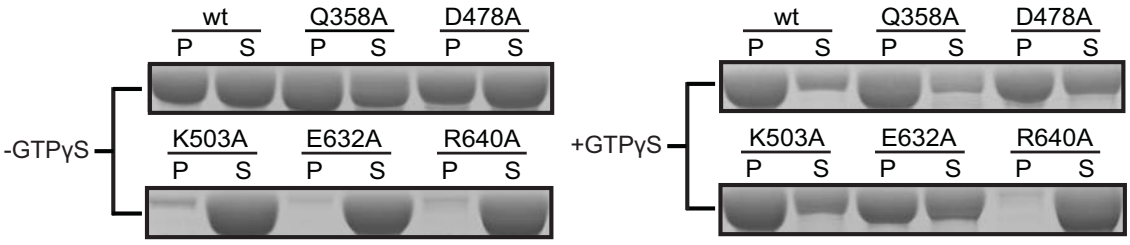

Figure 56. Sedimentation experiments of wt hsMxA and selected mutants. The assays were carried out both in the absence and presence of 1 mM GTPγS, as indicated in the figure. P and S: Pellet fraction and Supernatant.

The results from sedimentation assays were further corroborated by right angle light scattering (RALS) analysis (see 3.3.13). In the assay wt hsMxA showed a dimer-tetramer equilibrium, whereas the oligomerization defective mutant M527D (see 4.3.2) eluted predominantly as a monomer (Fig. 57). The Q358A and D478A mutants behaved similarly as wt hsMxA, whereas K503A, E632A and R640A showed a reduced tendency of tetramerization and eluted mostly as dimers (Fig. 57).

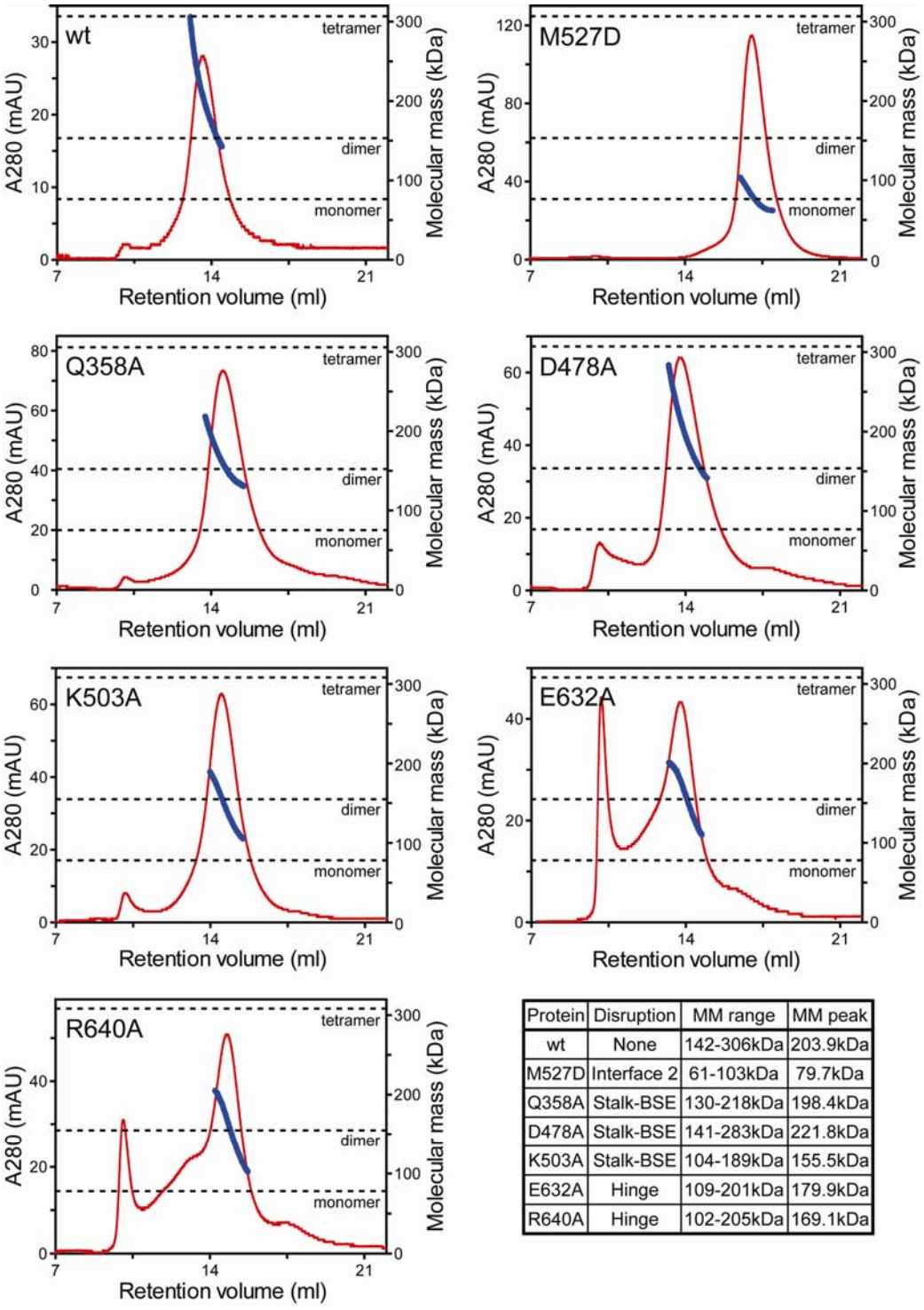

Protein	Disruption	MM range	MM peak
wt	None	142-306kDa	203.9kDa
M527D	Interface 2	61-103kDa	79.7kDa
Q358A	Stalk-BSE	130-218kDa	198.4kDa
D478A	Stalk-BSE	141-283kDa	221.8kDa
K503A	Stalk-BSE	104-189kDa	155.5kDa
E632A	Hinge	109-201kDa	179.9kDa
R640A	Hinge	102-205kDa	169.1kDa

Figure 57. RALS analysis of the hinge and BSE-stalk interface mutants. The 280 nm absorption curve was shown in red, and the determined absolute molecular masses are shown around the main peak in blue. Results are summarized in the table at the bottom. Note that mutations in the hinge region (E632A, R640A) might destabilize the protein leading to some aggregation after freezing/concentration of the protein.

Taken together, these data implied a decisive role for the hinge region and the BSE-stalk interface for oligomerization.

4.6.3 GTP hydrolysis assay

GTPase activity of the mutants was performed as described in 3,3,8. wt hsMxA showed a cooperative GTPase reaction with an estimated maximal k_{obs} of 6 min^{-1} (Fig. 58) (see also 4.3.4). In contrast, the Q358A and D478A mutants in the BSE-stalk interface showed 3-fold increased GTPase rates at higher protein concentration and the K503A mutant an even 5-fold increase (Fig. 58). Mutations in the hinge region, especially the R640A mutation, led to a dramatically accelerated GTP turnover already at low protein concentrations (Fig. 58). This result implied that the stability of the hinge region play an important role in the stimulated GTP hydrolysis of hsMxA.

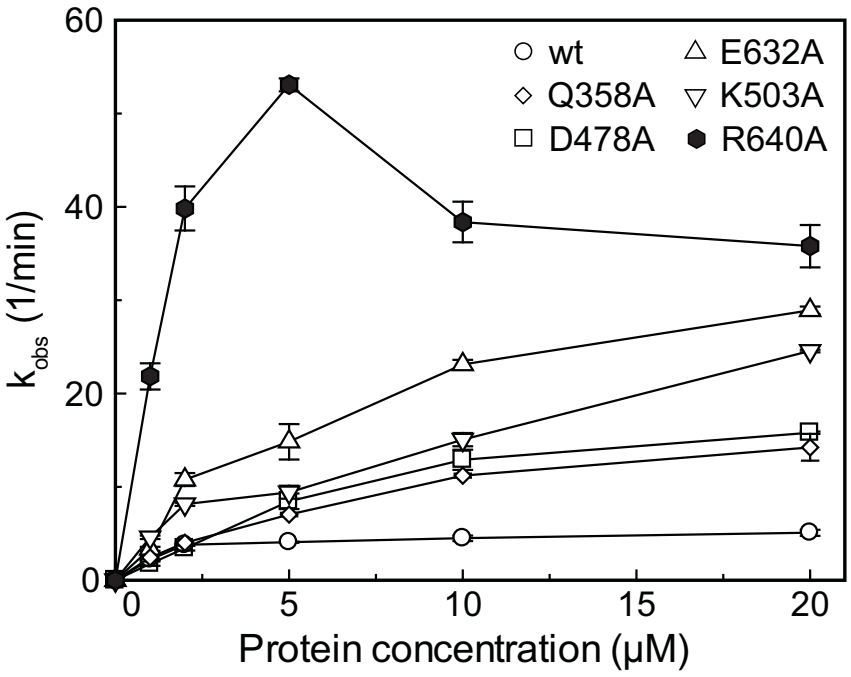

Figure 58. Results of GTP hydrolysis assay. Protein-concentration-dependent GTPase activities of wt MxA (○) and representative mutants E632A (△), R640A (⬢), Q358A (◇), D478A (□) and K503A (▽) were determined. The mean of k_{obs} calculated from two independent experiments is indicated with the error bars showing the range of the two data points.

5 DISCUSSION

5.1 Insights into the hsMxA stalk structure

5.1.1 Structural comparison of the human MxA stalk and other dynamin superfamily members

The architecture of the hsMxA stalk differs in detail from that of other dynamin superfamily members (Fig. 59A-D), but they are topologically similar and all have a long N-terminal helix pointing away from the G domain and a GED-like helix leading back to the G domain. In BDLP and EHD2, additional helices derived from residues N-terminal to the G domain participate in the helical assembly (Fig. 59C, D). Overall, the similar topology of the stalk regions in these proteins implies an evolutionary relationship.

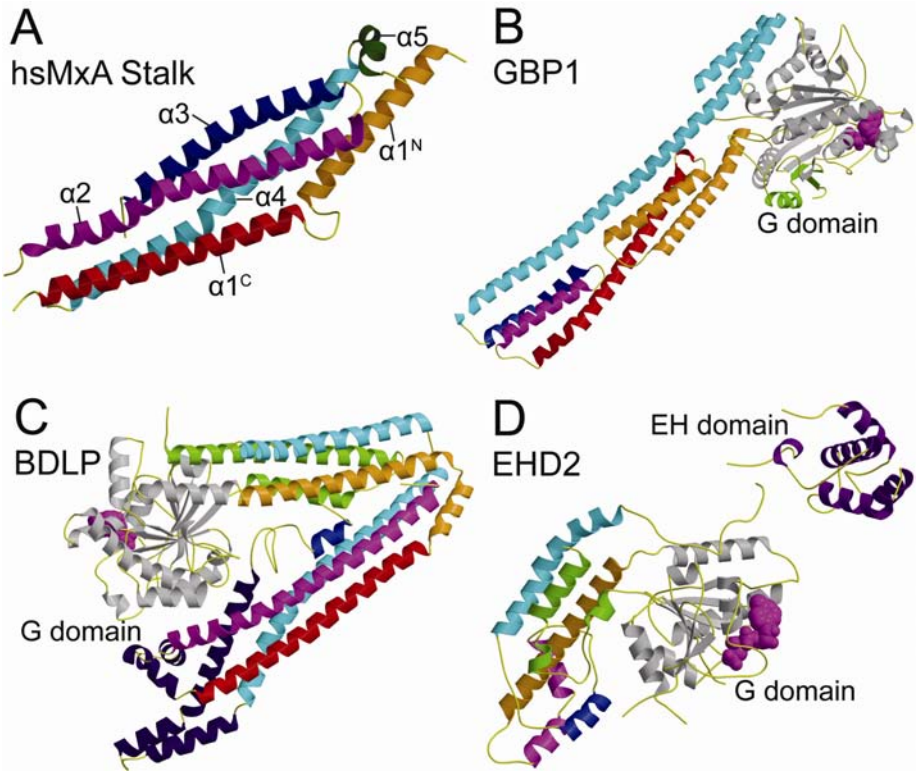

Figure 59. Structural comparison of the hsMxA stalk with other dynamin family members. A) hsMxA stalk (PDB code 3LJB). B) GMP-PNP bound GBP1 (pdb code 1F5N) (Prakash, Praefcke et al. 2000). C) GDP-bound BDLP (2J68) (Low and Lowe 2006). D) ATPγS bound EHD2 (2QPT) (Daumke, Lundmark et al. 2007). These protein structures (B-D) are shown in comparison with the hsMxA stalk. The helices in GBP1, BDLP and EHD2 corresponding to those in hsMxA are colored as A. The G domains of GBP1, BDLP and EHD2 are shown in grey with nucleotides in magenta. Additional elements such as the paddle in BDLP and the EH domain in EHD2 are shown in violet.

5.1.2 Implications of the human MxA stalk structure for the dynamin superfamily

For the last decades, many studies based on point mutations in the stalk region of dynamins and hsMxA have been performed to explore functionally important sites, when no high-resolution structure of the corresponding region was available.

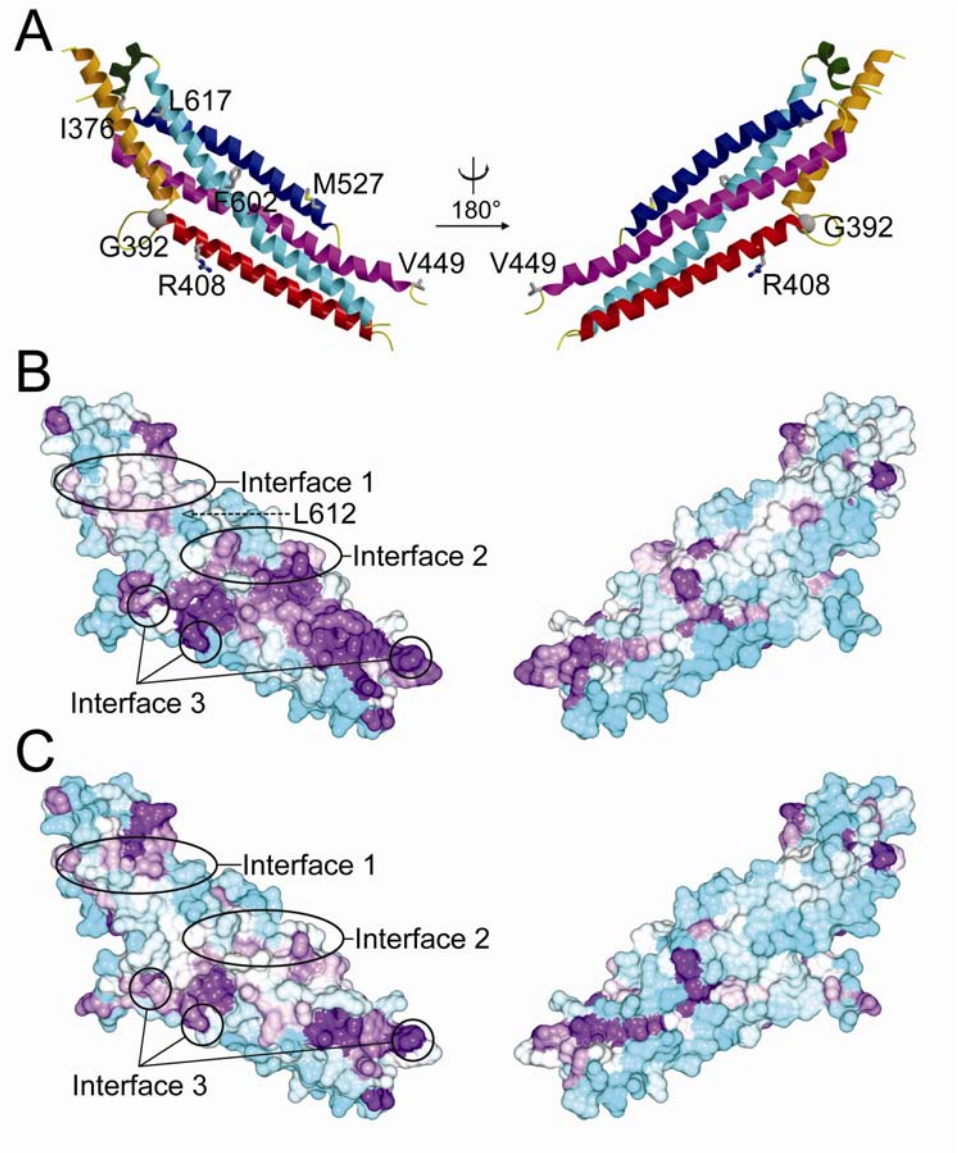

Figure 60. Amino acid residue conservation on the surface of hsMxA. A) Ribbon-type hsMxA stalk in two orientations, with selected residues of the interfaces shown in ball-and-stick representation. B) Sequence conservation in the Mx family. Sequence conservation surface plot (see 3.4.8) of the hsMxA stalk in the same orientations as in A where conserved residues are colored in a gradient from purple (highly conserved) to cyan (non-conserved). Sequences of 33 Mx proteins of different species were used to score the conservation. The approximate position of Leu612 is indicated. The positions of the three interfaces are labeled. C) Sequence conservation between Mx and dynamins. Models were oriented and colored as in A. The alignment in Fig. 31 was used to detect conserved surface patches.

The structure of the hsMxA stalk is the first high resolution structure of a conventional MD and GED for proteins closely related to dynamin. Therefore, the oligomerization interfaces observed in the hsMxA stalk structure may represent common features of these proteins. Surface conservation analysis of hsMxA stalk structure indicates that interface 1 is only partially conserved in dynamins and Mx proteins, whereas interface 2 is highly conserved (Fig. 60B, C). Interface 3 is more than 90% conserved among dynamins and Mx proteins. On the other hand, interface 1 and 2 appear to be stabilized by oligomerization in the crystal, as indicated by low temperature (B)-factors, while interface 3 shows higher B-factors reflecting increased flexibility in this region (Fig. 61).

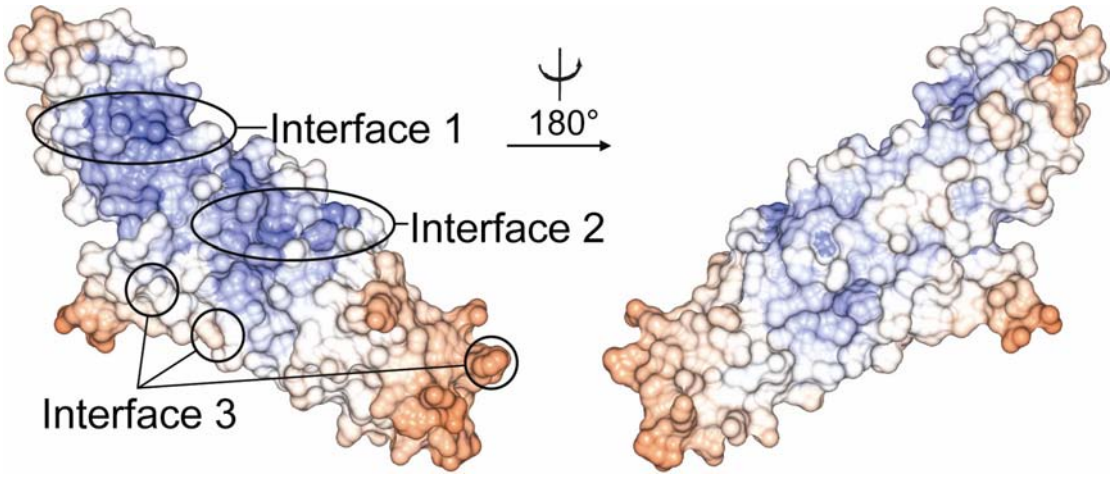

Figure 61. Surface B-factor plot of the hsMxA stalk. Regions with low B-factors are indicated in light blue and high B-factors in orange. Interfaces are indicated as Fig. 60B, C.

The hsMxA stalk structure provides explanations for some of the phenotypes found in previous mutagenesis studies. For example, Leu612 was reported to be critically involved in hsMxA oligomerization (Schumacher and Staeheli 1998; Janzen, Kochs et al. 2000). However, according to the hsMxA stalk structure, it is located in between interface 1 and 2, and does not directly participate in inter-molecular interactions but rather contributes to the hydrophobic core of the stalk (Fig. 60B). The L612K mutant in bacterial expression system was insoluble (data not shown). Consequently, this mutation may lead to unspecific destabilization of the stalk architecture. Additionally, the R361S and R399A mutations in dynamin interfere with its tetramerization into stable dimers (Ramachandran, Surka et al. 2007). Remarkably, these two dynamin residues correspond to the Arg408 and ^{440}YRGRE motif at interface 3 of the hsMxA stalk, respectively (Fig. 31, Fig. 60A-C), and their mutation also breaks hsMxA tetramer into stable dimers (Fig. 34A, H). Further, the mutation G385D in yeast

dynamin DNM1 also leads to the disruption of tetramer into stable dimers (Ingerman, Perkins et al. 2005). Interestingly, its counterpart mutation in hsMxA, G392D at interface 3 in the stalk, has the same phenotype for hsMxA (Fig. 34G, Fig. 60A-C).

5.2 Biochemical properties of human MxA

5.2.1 Oligomerization of human MxA

Most hsMxA interface and hinge region mutants presented in this work failed to form high-order oligomers as reported in 4.3.2 and 4.6.2. However, they showed distinct oligomerization states, depending on the location of the mutations in different interaction sites (Fig. 34A-I, 35, 36, 56, 57). M527D and F602D had the most severe phenotypes completely disrupting oligomerization. This implied that interface 2 is critical for formation of the dimeric building block, as suggested (Fig. 14A, see also 4.4.1) (Praefcke and McMahon 2004). This was also reflected in the behavior of the interface 3 and L4 mutants (Fig. 33, 34A, G-I, 35), which all led to a stable dimeric form of hsMxA. It is very likely that these mutants dimerize via the intact interface 2, and the localizations of interface 3 and L4 seen in the oligomer support this hypothesis (Fig. 32A, D). Moreover, interface 1 mutants exist either close to dimeric form or in a dimer-tetramer equilibrium (Fig. 34A-E), which can also be explained by the interface 2-mediated dimeric unit and an unspecific destabilization effect from the introduction of an charged aspartate in the center of the hydrophobic patch of interface 1.

It has been observed in previous studies and in 4.3.2 that nucleotide binding promote oligomerization of wt hsMxA (Fig. 35) (Kochs, Haener et al. 2002). This can be explained by the additional GTP-dependent association between G domains via the nucleotide binding interface, as observed in the crystal structures of the human dynamin 1 and dynamin 3 G domain, human GBP1, and BDLP (Prakash, Praefcke et al. 2000; Ghosh, Praefcke et al. 2006; Low and Lowe 2006; Chappie, Acharya et al. 2010; Yang, Tempel et al. 2010). For mutants that did not oligomerize in the spin assay in the presence of GTPγS (Fig. 35), it is unclear whether their G domains were still able to interact with each other. Therefore, analytical gel filtration was carried out on the M527D mutant in different nucleotide loading states. It was found that upon binding both GDP and/or GMP-PNP, M527D eluted at the same retention time as the nucleotide-free monomer, indicating that nucleotide binding failed to promote stable dimer formation via the G domains (Fig. 62). According to these results, it is concluded that the affinity for the G domain interface is relatively low, and efficient association of the G domains requires multiple interactions within a native assembly of hsMxA via undisturbed stalk region.

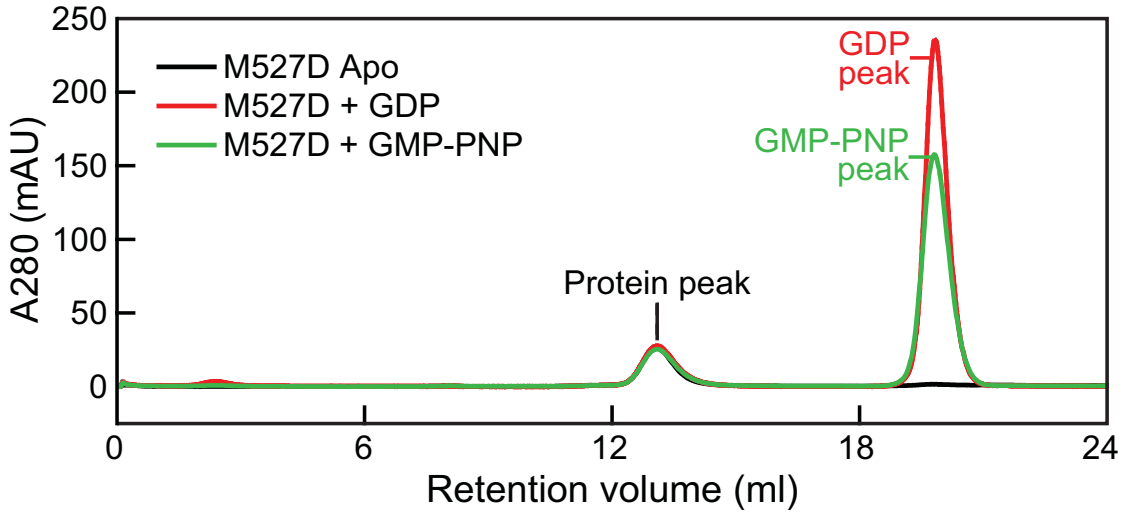

Figure 62. Analytical gel filtration assay for hsMxA M527D in different nucleotide bound states. 1 mg protein was used without nucleotide (black), with 1 mM GDP (red), or with 1 mM GMP-PNP (green). The result suggests that binding of nucleotide does not promote dimerization of the monomeric interface 2 mutant M527D via the G domains. To exclude the possibility that nucleotides may be dissociated from the protein due to the relative low binding affinity and a diluted condition caused during the experimental process, the assay was repeated also in nucleotide-containing buffers so that 1 mM GDP or GMP-PNP was constantly supplied to the column during the entire run to ensure the binding of nucleotides to the protein. M527D was eluted at the same retention volume as in the first assay shown in the figure.

5.2.2 The lipid-binding property of hsMxA

Albeit lacking the lipid-binding PH domain, hsMxA has previously been shown to bind to lipids and tubulate them (Fig. 26C) (Accola, Huang et al. 2002; Kochs, Reichelt et al. 2005). According to the result of the liposome co-sedimentation experiment as shown in 4.3.3, hsMxA also interacts with Folch liposomes in the absence of nucleotide. The positively charge amino acid cluster, $KKKK^{554}$ in L4 (Fig. 31, see also 4.3.1), was proposed to be the interaction site of hsMxA with negatively charged lipid membranes. However, compared to mEHD2 which also lacks a PH domain, this interaction is not very strong, as only 50% of hsMxA was co-sedimented with Folch liposome whereas under same conditions 100% mEHD2 co-sedimented with either PS or Folch liposomes (Daumke, Lundmark et al. 2007). Furthermore, hsMxA only exhibited association with unfiltered, but not filtered liposomes (which have smaller sizes and higher homogeneity) in the same experiment (data not shown). Given these facts, whether lipid binding is involved in the core functional mechanism of hsMxA becomes suspicious.

On the other hand, human dynamin 1 and mEHD2, both known to function in at lipid membranes, show a 1000-fold and 8-fold stimulation of nucleotide hydrolysis, respectively, upon lipid binding (Stowell, Marks et al. 1999; Daumke, Lundmark et al. 2007). In contrast, hsMxA did not show stimulated GTPase activity in the presence of either Folch or PS liposome (see 4.3.4, Fig. 39A, B). These results reflect the fact that lipids may not be the key physiological substrate for Mx proteins during their antiviral function.

5.2.3 High GTP hydrolysis rates of hsMxA mutants

In nucleotide binding and fast kinetic assays described in 4.3.5, wt hsMxA and M527D showed similar off-rates for mant-GDP which are much faster than GTP turnover (Fig. 40, 41A), suggesting that GDP release alone is not the rate-limiting step in the GTPase reaction. The k_{off1} values of mant-GMP-PNP for wt hsMxA and M527D were slower compared to those of mant-GDP (Fig. 41B). The difference between wt hsMxA and M527D in k_{off1} for mant-GMP-PNP (2.6-fold, Fig. 41B) is consistent with their observed affinity difference for GMP-PNP (3-fold, Fig. 40), indicating that wt hsMxA and M527D should have similar on-rates for GTP. The deduced on-rates for mant-GMP-PNP are both approximately 4 $min^{-1}\mu M^{-1}$ and are in a similar range as previously described (Richter, Schwemmle et al. 1995). In the GTPase assays in the presence of 1 mM GTP, the GTP binding rates are therefore fast (around 4,000 min^{-1}) and also not the rate-limiting step. Finally, the cleavage of the phosphoanhydride bond should be a transient step as well (Westheimer 1987).

Moreover, k_{off1} for mant-GMP-PNP approximates the maximal GTPase turnover number at high protein concentrations for both wt hsMxA and M527D (see 4.3.4, Fig. 40). Based on these results, it can be suggested that at low protein concentration, self-assembly of hsMxA via the G domains does not stimulate GTP hydrolysis in solution, resulting in a similar small increase in k_{obs} with increasing protein concentrations for each mutant. However, at higher protein concentrations/higher GTPase turnover, the off-rates for GDP●P_i after GTP hydrolysis or conformational changes associated with this step might be rate-limiting, as for example in the myosin system, where also the release of inorganic P_i was shown to be rate-limiting (Pollard and Ostap 1996). Similarly as for mant-GMP-PNP, these off-rates might be slower for wt hsMxA than for the monomeric/dimeric mutants leading to the observed differences in GTPase activity at higher protein concentrations. Therefore, it can be implicated that

oligomerization of hsMxA via the stalk region influences nucleotide release in G domains.

In the case of the hinge region and the BSE-stalk interface mutants, as they have similar effects in the GTP hydrolysis assays as the stalk mutant (see 4.6.3, Fig. 58), it is assumed that both an intact hinge and the BSE-stalk interface are required for efficient higher-order oligomerization of hsMxA in solution. The high GTP hydrolysis rate for R640 at low protein concentrations (1-5 µM) can be explained by the increased chance of G domain association in solution, which may result from the larger freedom of movement of the G domain provided by the loosened hinge region.

5.3 Model for the mechano-chemical function

5.3.1 The flexibility of the oligomer

As described in 2.3.2, the mechano-chemical function of dynamin requires the coordination of GTP hydrolysis and oligomerization. The dynamin oligomer model explains that promote GTPase activity is stimulated vial inter-helical-turn G domain association which is dependent on the native assembly (see 4.4.3, Fig 46). As a close relative to dynamin, Mx proteins are expected to have a similar mechano-chemical function.

For both dynamin and Mx proteins, the helical-shaped or ring-like oligomers were observed with varying diameters in previous EM studies (Oh, McIntosh et al. 1998; Kochs, Reichelt et al. 2005). The surface hydrophobicity analysis of hsMxA showed that both interface 1 and 2 form extensive interaction areas (Fig. 63A). Interface 2 area has a longer hydrophobic span and Met527 from each molecule of the dimer inserts into a socket formed by Leu598, Ile599, Phe602 and Phe603 from the other one, thereby confining the relative movement of the two monomers (Fig. 32C, 63A). In contrast, interface 1 has a central hydrophobic area that appears smoother, flanked by two flexible salt bridges, which might allow a certain extent of rotation without disrupting the original contacts (Fig. 63A, B).

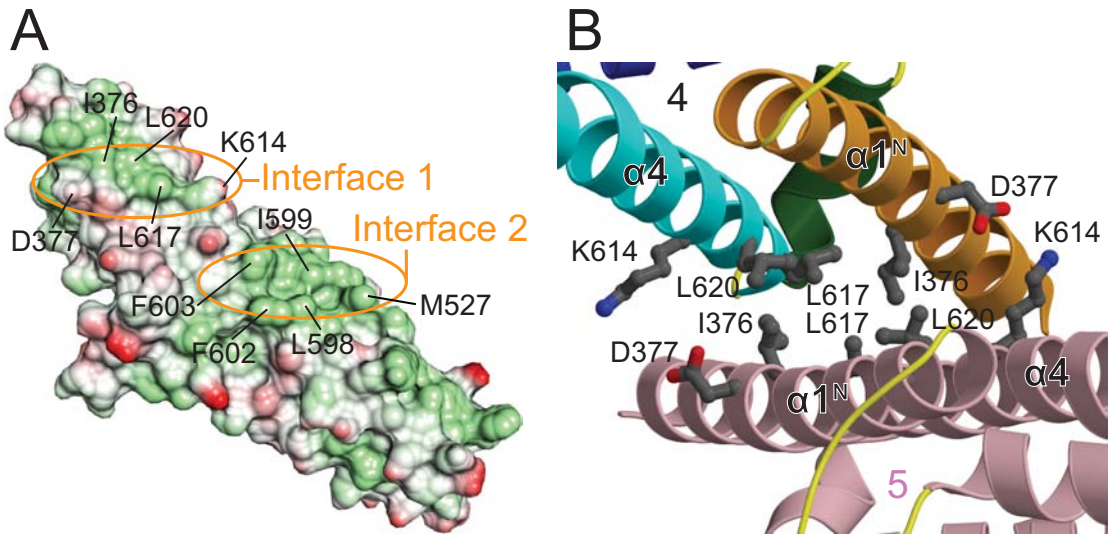

Figure 63. Features of the interfaces in the oligomer. A) Surface representation of the hsMxA stalk, with hydrophobic atoms in green and charged residues in red. Interface 1 and 2 are individually labeled. B) Details of interface 1 after rotation according to A. Residues and helices are labeled as in Fig. 32B. All the contacts found in the linear oligomer are maintained and no clash is introduced between the side chains.

Based on these features, it is proposed that neighboring constitutive dimers can adapt varying rotation angles between each other via the flexible interface 1 during the assembly (Fig. 64), thereby resulting in different diameters of oligomers. As described in 4.4.1, contacts between constitutive dimers at interface 3 may be strengthened by the rotation. In the hsMxA stalk and three-domain hsMxA crystals, the linear oligomer were supported by additional crystallographic contacts (see 7.1.1-2).

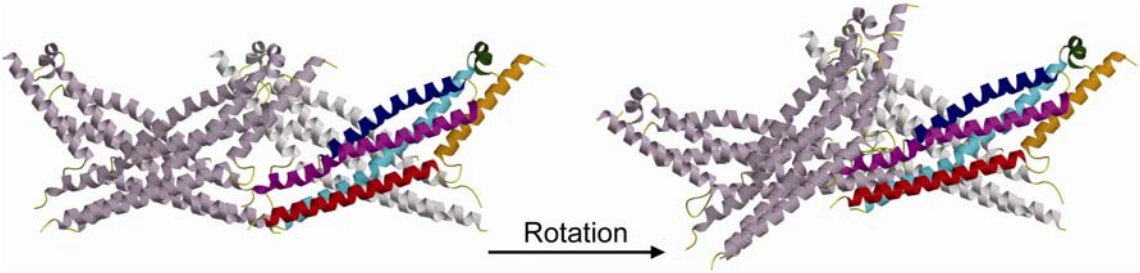

Figure 64. The rotation around interface 1. Shown are two constitutive dimers and their relative positions before and after rotation at interface 1. This flexible rotation movement provides freedom for dynamin or hsMxA oligomers with different diameters.

5.3.2 The human MxA oligomer model

Different from the helical dynamin assembly model yet with a similar architecture (see 4.4.1-3), an hsMxA oligomer model was built in a ring shape according to previous EM studies (Kochs, Haener et al. 2002). In this model, the rotation angle between neighboring constitutive dimers 1 is 23° (Fig. 65A), which is endorsed by the flexibility of interface 1 discussed in 5.3.1. The G domains are in the same position as in the dynamin model and the constitutive dimers also form a T-bar shape, in agreement with the TEM images in previous studies (Fig. 17, 44A, B, 45, 65A, B). The nucleotide binding pockets face away from the stalk (Fig. 65B).

A complete hsMxA oligomer ring comprises 16 constitutive dimers. It has an outer and inner diameter of 24 and 41 nm, respectively (Fig. 65C). It is envisaged that MxA oligomerization initially proceeds via association of the stalks, until a complete ring is formed. The stimulated GTPase activity from the oligomer is then proposed to be achieved only when a multiple number of such rings align closely with each other on their physiological templates so that the inter-ring G domain contacts can be formed, as exemplified in Fig. 65D. The molecular mechanism of the G domain interaction is predicted to be the same as for dynamins, since the residues found to be involved in the *trans* stabilization of the G domain interface, namely Gln40, Ser41, Gly62 and

Asp180 in dynamins are also conserved in the Mx proteins (Fig. 31) (Chappie, Acharya et al. 2010).

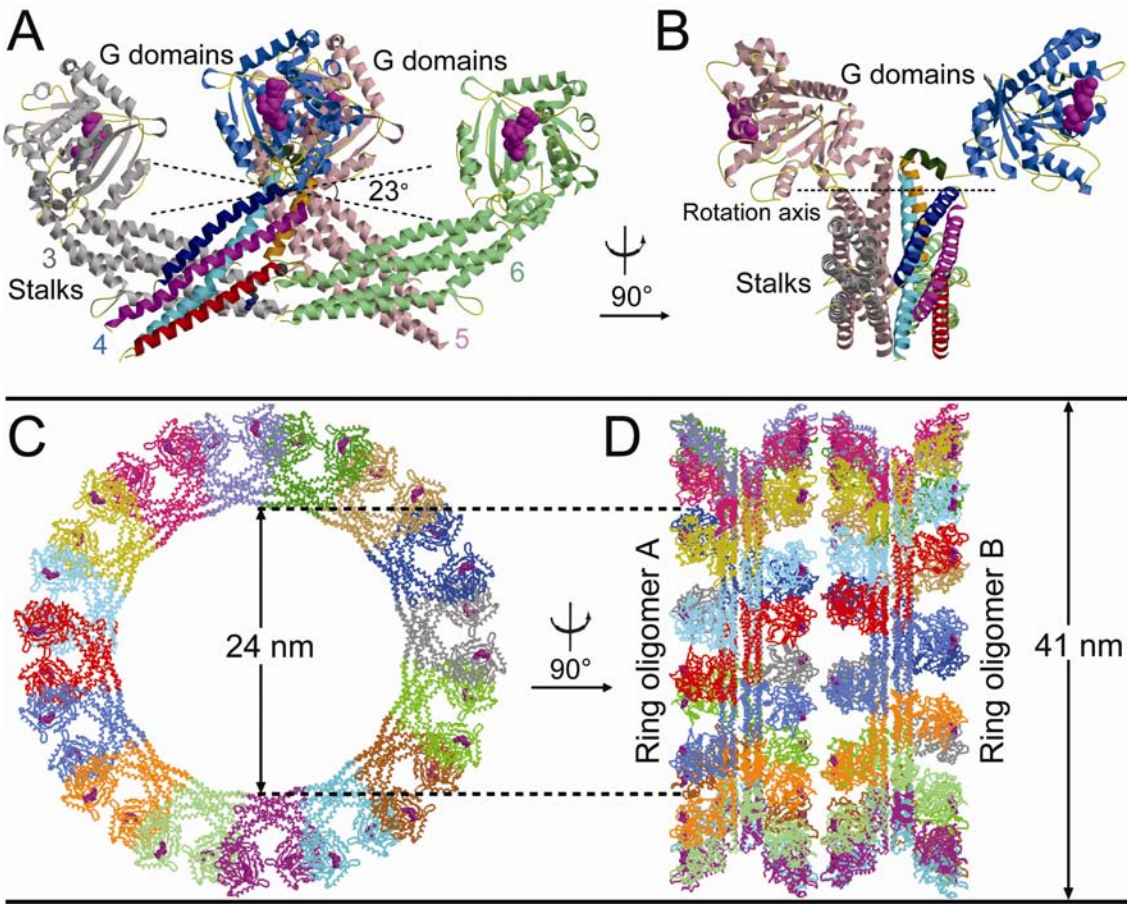

Figure 65. The ring-like hsMxA oligomer model. A) A tetrameric model comprising the hsMxA stalks and the dynamin G domains (described in 5.3.3). Monomers and GDP molecule are illustrated as in Fig. 32A, 44. A 23° rotation of constitutive dimers at interface 1 is indicated. B) The T-bar shape is also observed for the hsMxA model in the front view, with rotation axis labeled. The G domains of monomer 3 and 6 were removed for clarity. C) The hsMxA ring-like oligomer composed of 16 constitutive dimers. These dimers are depicted in different colors as C_α traces. D) The front view of the oligomer rings. Depicted here are two rings interacting via the G domain interfaces at the side of the oligomers as described in 5.3.3 and 5.3.4. The outer and inner diameters of the ring are indicated.

5.4 Human MxA as functional module in innate immunity

The hsMxA stalk crystal structure has clarified some previous experimental results based on point mutations (Haller, Stertz et al. 2007), but it is not yet sufficient to provide direct and detailed functional evidence about the antiviral mechanism of Mx proteins, partly due to the missing tentative template-binding loop L4 in the structure (see 4.2.3, Fig. 30A, B). Early work indicated that overexpression of the influenza polymerase subunit PB2 abolishes the antiviral effect of mouse Mx1, suggesting that PB2 might be a putative Mx1 target (Huang, Pavlovic et al. 1992; Stranden, Staeheli et al. 1993). However, such a role for PB2 could not be substantiated in subsequent work based on minireplicon systems and reverse genetics (Haller, Gao et al. 2010). In addition, cellular membranes may also not be the physiological substrates for hsMxA *in vivo* during the antiviral process as well (see 5.2.3) (Daumke, Gao et al. 2010). On the other hand, other evidence implies that viral RNPs are likely to be the targets of Mx proteins (mentioned also in 2.3.3) (Haller, Gao et al. 2010). The negatively-charged backbone of the viral RNA wrapped around NPs resembles the lipid tubule that was shown to associate with hsMxA (Accola, Huang et al. 2002). Moreover, the helical RNPs have a similar diameter as Mx-tubulated membranes, e. g. 15 nm for rabies virus (Albertini, Wernimont et al. 2006). All these observations imply that Mx proteins may form oligomeric rings around the elongated viral RNPs and bind to them via the positively-charged patches in L4, thereby blocking their function (Fig. 65C, D, 66). As a consequence, Mx proteins may directly suppress the transcription of the viruses by sequestering their RNPs. In addition, Mx proteins may also immobilize nucleocapsids or direct them to special sites in the cytoplasm where they will eventually be degraded.

It has been proposed that complex cellular functions arise from the interplay of protein ensembles which have been termed cellular modules (Hofmann, Spahn et al. 2006). Time ordered interactions and complex formation within these ensembles facilitate an autonomous function, allowing them to orchestrate cellular inputs and execute cellular tasks in a coordinated manner. Therefore, the current experimental results, the oligomer model and the proposed antiviral mechanism of hsMxA can be also generalized in a systematic context as follows. The studies in this thesis suggest hsMxA as part of such a cellular module regulating and executing the IFN-induced antiviral response. This antiviral module includes effector components such as hsMxA

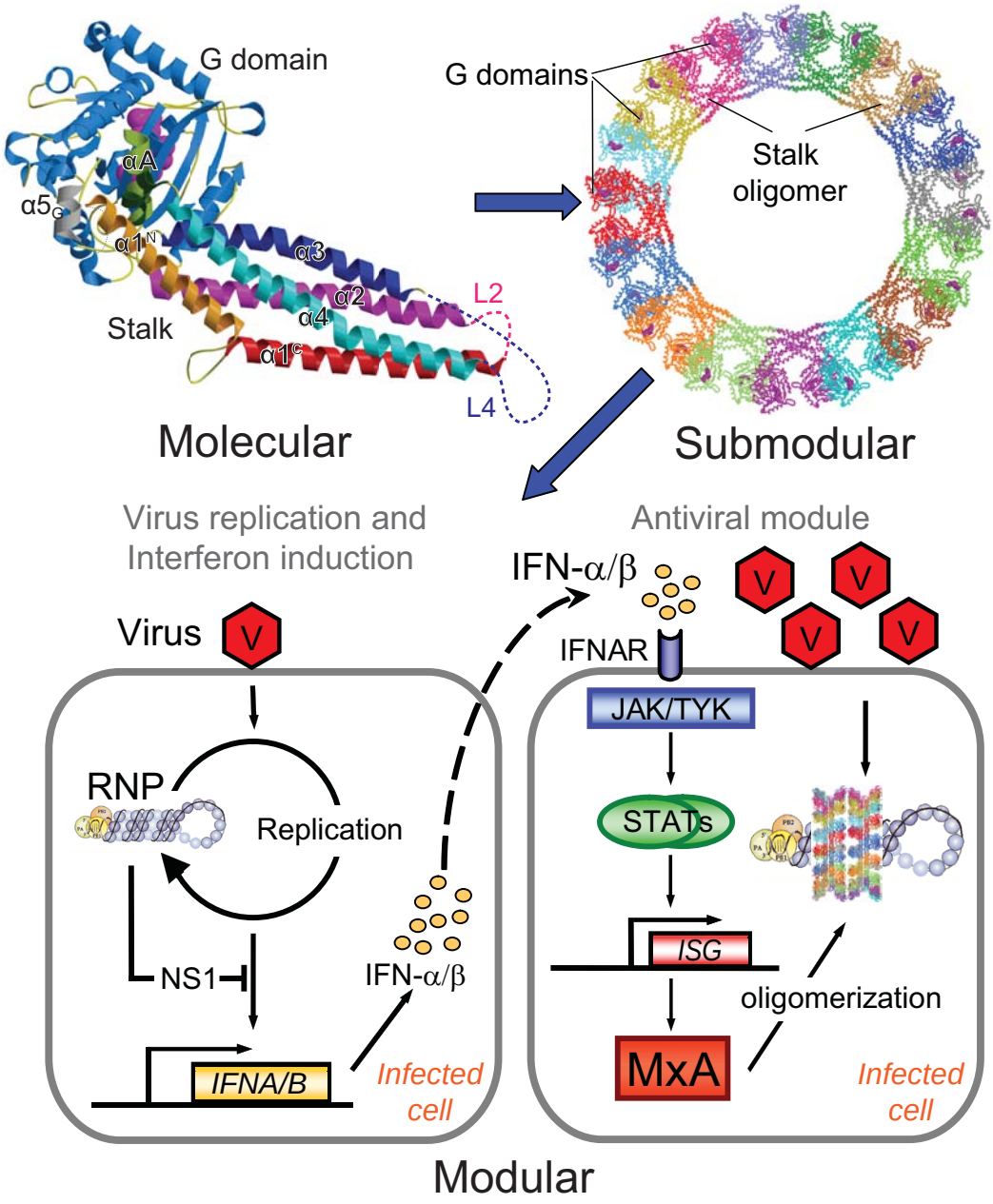

Figure 66. Functional organization of the antiviral module containing hsMxA. Upper left: hsMxA monomer corresponds to a molecular component of the antiviral module. Upper right: an hsMxA oligomer model represents a submodule with a defined subfunction in the antiviral module. Lower: the proposed antiviral module comprises components needed for the induction and regulation of hsMxA activity (e.g. Type I IFNs). IFNα/β are induced by viral RNA produced during viral replication leading to activation of a cascade of intracellular receptors and transcription factors that activate the IFN promoters. The FLUAV NS1 protein is an example of a viral antagonistic protein known to suppress IFN induction. Newly synthesized and secreted IFNs bind to IFNAR and activate the expression of ISGs including hsMxA via activation of JAK/TYK and STAT transcription factors. Upon infection, cytoplasmic hsMxA might recognize the incoming viral RNP structures and self-assemble into rings resulting in a stable complex that blocks viral RNP function. Figure modified from Daumke, Gao et al. 2010.

and regulatory components such as the IFN-system that tightly controls the expression of the effectors. The hsMxA monomers represent molecular components of this module, with relevant functions such as membrane and nucleotide binding properties (Fig. 66). They assemble into oligomeric hsMxA rings which constitute the next hierarchical level in the module, the so-called submodule that has a defined subfunction in the antiviral response (Fig. 66), as observed in hsMxA transfected cells. This subfunction is an intrinsic property of the hsMxA rings only, e.g., it is not present in the hsMxA monomers (Gao, von der Malsburg et al. 2010). It is proposed that the stalk constitutes a conserved building block in this submodule which allows flexible, dynamic and well controlled assembly and disassembly of the submodule. The individual contacts in interfaces 1, 3 (including L2) and L4 might be of low affinity and facilitate the transition from stable dimers into oligomers, as shown by single mutations at any of these sites. The ring-shaped architecture of the hsMxA oligomer guarantees a precise timing control of the assembly process. Full assembly and inter-ring contacts of the hsMxA rings might trigger GTPase activity initiating action and subsequent disassembly of the submodule. Thus, nucleotide binding and hydrolysis in the hsMxA monomers sets a time window for the assembly, the antiviral and/or mechano-chemical function and the disassembly of the hsMxA submodule. Notably, viruses have recently been shown to have modular character as well (Thaa, Hofmann et al. 2010) and they induce expression and serve as a template for the assembly of the antiviral module that executes the clearance of the viruses (Fig. 66). In contrast, viruses antagonize the expression of the antiviral module, e.g., via the FLUAV non-structural NS1 protein (Haller, Kochs et al. 2006; Kochs, Garcia-Sastre et al. 2007). Consequently, two cellular modules compete with and reciprocally regulate each other (Daumke, Gao et al. 2010). Eventually, the proposed application of the module concept to hsMxA is helpful for understanding the systemic organization of the antiviral response against pathogens.

5.5 Open questions and outlook

The three-domain hsMxA structure has confirmed the molecular mechanism of the oligomerization revealed by the isolated stalk structure (see 4.2.3). It also provides some more information about the mechano-chemical features of the protein. Firstly, the BSE was suggested to mediate the conformational changes between the G domain and the stalk (Chappie, Acharya et al. 2010). This mechanism can also be suggested for the BSE of hsMxA from three-domain structure (see 4.5.2). The BSE of nucleotide-free hsMxA is in a similar conformation relative to the G domain as the myosin-fused nucleotide-free rat dynamin G domain (Fig. 61A) (Reubold, Eschenburg et al. 2005). However, in the GDP●AlF_4^- bound structure of the dynamin G domain, the rigid $\alpha2^B$-$\alpha3^B$ network is rotated towards $\alpha1^B$ around the invariant Pro294 (Pro340 in hsMxA) (Fig. 61B) (Chappie, Acharya et al. 2010). Assuming that the minimal BSE structure is representive for the BSE in the full-length protein, it can be speculated that $\alpha1^B$ conveys nucleotide-mediated changes in the G domain to $\alpha2^B$-$\alpha3^B$, which is further relayed to the stalk. Similar conformational changes were also proposed for BDLP upon GMP-PNP binding (Fig. 20B) (Low, Sachse et al. 2009).

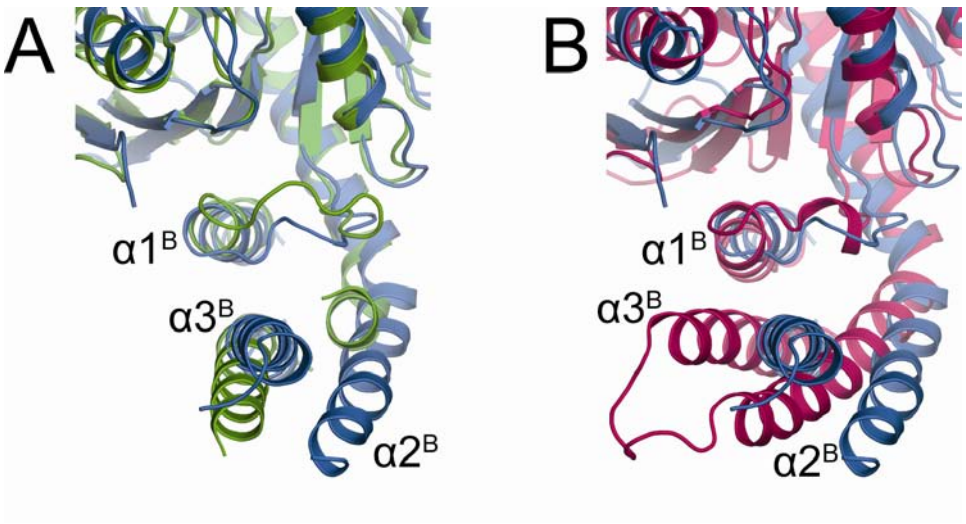

Figure 67. Comparison of the BSE conformations. A) Main chain superposition of the G domain and BSE from hsMxA (blue) with equivalent region of the nucleotide-free rat dynamin (PDB code 2AKA, green) (Reubold, Eschenburg et al. 2005) in front view. The helices of the BSE adopt similar relative position between the two structures, despite slight tilting difference at $\alpha2^B$ and $\alpha3^B$. B) Main chain superposition of the G domain and BSE from hsMxA (blue) with equivalent region of the GDP•AlF_4^- bound human dynamin (2X2E, pink) (Chappie, Acharya et al. 2010) in the front view. A big conformational change can be observed for the BSE in $\alpha2^B$ and $\alpha3^B$, as they move aside like a rigid body for 30° from the nucleotide-free hsMxA to the transition state of dynamin.

Second, the hinge region also appears to be stabilized by local interactions, especially the conserved via Glu632 and Arg640. It can be envisaged that the two loops in the hinge region at a certain period of the functional cycle may allow relative movements between the G domain and the stalk, since in the nucleotide-free state, the G domain interfaces are cannot face each other, as described in 4.5.3 (Fig. 55A, B). Mutations of these two residues which were expected to decrease the stability of the hinge region resulted in highly increased GTP hydrolysis rates of the protein (data not shown), implying that the flexibility of the hinge region may be necessary for the stimulated GTPase activity. The mutations also led to a defect in the oligomerization of hsMxA (data not shown), indicating that the stability of the hinge region is required for the native assembly of the protein, while GTPase activity is suppressed.

Third, BSE-stalk disruptions of the BSE-stalk interface via different point mutations also interfere with the natural assembly of hsMxA, and laid significant impact on the antiviral activity (data not shown). The fact suggests that this relatively weak interface might be important after the assembly via the stalks is finished. It may stabilize the hsMxA oligomers after the first round of nucleotide hydrolysis and thereby facilitate the re-establishment of the "initial state" for the next hydrolysis cycle.

Taken together, a possible functional cycle for hsMxA could be depicted as follows. First, the non-oligomerized hsMxA proteins are recruited to the target template and start to oligomerize. At this stage, the proteins should be loaded with GTP due to its high concentration in the cytosol and the binding affinity of hsMxA to nucleotide which is in low micromolar range (see 4.3.5). In the mean time, the G domain movement relative to the stalk is controlled via the hinge region and, possibly, the BSE-stalk interface (see 4.5.2-3), which may allow only certain degrees of flexibility. When a full ring is assembled and these rings approach each other as described in 5.3.2 (Fig. 65D), the G domains can contact each other and stimulated GTPase activity is triggered by multiple interactions, as suggested in 5.2.2. The local conformational change of the G domain upon GTP hydrolysis is then sensed by $\alpha 1^{B}$ from the BSE and subsequently passed to the stalk via the movement of $\alpha 2^{B}$-$\alpha 3^{B}$ and probably also the hinge region, resulting in specific sequesteration to the viral substrates via $L4^{S}$. This mechanism might also be applicable to dynamins.

Given this speculation, however, some details of the mechano-chemical function still remain unclear and many questions can be asked. How the G domain passes the force

generated from GTP hydrolysis to $\alpha 1^B$? To what extent can $\alpha 2^B$-$\alpha 3^B$ or the G domains rotate around the Pro340 or the hinge region? What exact conformational changes of the stalk occur during dimerization of G domains and GTP hydrolysis? To answer these questions, molecular structures of full-length Mx proteins or dynamins in different nucleotide-loading states will be indispensable. Higher resolution EM reconstructions of Mx or dynamin oligomers in different nucleotide-loading states will also reveal futher details of the oligomerization reaction. Furthermore, to unveil the complete functional scenario of the dynamin superfamily members, structural studies of the protein in complex with its specific substrates or binding partners will be required.

6 REFERENCES

Aaronson, D. S. and C. M. Horvath (2002). "A road map for those who don't know JAK-STAT." Science **296**(5573): 1653-5.

Accola, M. A., B. Huang, et al. (2002). "The antiviral dynamin family member, MxA, tubulates lipids and localizes to the smooth endoplasmic reticulum." J Biol Chem **277**(24): 21829-35.

Aebi, M., J. Fah, et al. (1989). "cDNA structures and regulation of two interferon-induced human Mx proteins." Mol Cell Biol **9**(11): 5062-72.

Afkarian, M., J. R. Sedy, et al. (2002). "T-bet is a STAT1-induced regulator of IL-12R expression in naive CD4+ T cells." Nat Immunol **3**(6): 549-57.

Ahmad, S., Y. M. Alsayed, et al. (1997). "The type I interferon receptor mediates tyrosine phosphorylation of the CrkL adaptor protein." J Biol Chem **272**(48): 29991-4.

Akarsu, H., W. P. Burmeister, et al. (2003). "Crystal structure of the M1 protein-binding domain of the influenza A virus nuclear export protein (NEP/NS2)." EMBO J **22**(18): 4646-55.

Albertini, A. A., A. K. Wernimont, et al. (2006). "Crystal structure of the rabies virus nucleoprotein-RNA complex." Science **313**(5785): 360-3.

Alonso-Caplen, F. V., M. E. Nemeroff, et al. (1992). "Nucleocytoplasmic transport: the influenza virus NS1 protein regulates the transport of spliced NS2 mRNA and its precursor NS1 mRNA." Genes Dev **6**(2): 255-67.

Anderson, S. L., J. M. Carton, et al. (1999). "Interferon-induced guanylate binding protein-1 (GBP-1) mediates an antiviral effect against vesicular stomatitis virus and encephalomyocarditis virus." Virology **256**(1): 8-14.

Ank, N., H. West, et al. (2006). "Lambda interferon (IFN-lambda), a type III IFN, is induced by viruses and IFNs and displays potent antiviral activity against select virus infections in vivo." J Virol **80**(9): 4501-9.

Arnold, K., L. Bordoli, et al. (2006). "The SWISS-MODEL workspace: a web-based environment for protein structure homology modeling." Bioinformatics **22**(2): 195-201.

Bach, E. A., M. Aguet, et al. (1997). "The IFN gamma receptor: a paradigm for cytokine receptor signaling." Annu Rev Immunol **15**: 563-91.

Baudin, F., I. Petit, et al. (2001). "In vitro dissection of the membrane and RNP binding activities of influenza virus M1 protein." Virology **281**(1): 102-8.

Beavis, R. C. and B. T. Chait (1989). "Matrix-assisted laser-desorption mass spectrometry using 355 nm radiation." Rapid Commun Mass Spectrom **3**(12): 436-9.

Behlke, J., O. Ristau, et al. (1997). "Nucleotide-dependent complex formation between the Escherichia coli chaperonins GroEL and GroES studied under equilibrium conditions." Biochemistry **36**(17): 5149-56.

Beutler, B. (2004). "Inferences, questions and possibilities in Toll-like receptor signaling." Nature **430**(6996): 257-63.

Bieniasz, P. D. (2004). "Intrinsic immunity: a front-line defense against viral attack." Nat Immunol **5**(11): 1109-15.

Blaas, D., E. Patzelt, et al. (1982). "Identification of the cap binding protein of influenza virus." Nucleic Acids Res **10**(15): 4803-12.

Boehm, U., T. Klamp, et al. (1997). "Cellular responses to interferon-gamma." Annu Rev Immunol **15**: 749-95.

Boivin, S., S. Cusack, et al. (2010). "Influenza A virus polymerase: structural insights into replication and host adaptation mechanisms." J Biol Chem **285**(37): 28411-7.

Bornholdt, Z. A. and B. V. Prasad (2008). "X-ray structure of NS1 from a highly pathogenic H5N1 influenza virus." Nature **456**(7224): 985-8.

Bourne, H. R., D. A. Sanders, et al. (1991). "The GTPase superfamily: conserved structure and molecular mechanism." Nature **349**(6305): 117-27.

Bradford, M. M. (1976). "A rapid and sensitive method for the quantitation of microgram quantities of protein utilizing the principle of protein-dye binding." Anal Biochem **72**: 248-54.

Brunger, A. T. (1992). "Free R value: a novel statistical quantity for assessing the accuracy of crystal structures." Nature **355**(6359): 472-5.

Brunger, A. T. (1997). "Free R value: cross-validation in crystallography." Methods Enzymol **277**: 366-96.

Brunger, A. T. (2007). "Version 1.2 of the Crystallography and NMR system." Nat Protoc **2**(11): 2728-33.

Brunger, A. T., P. D. Adams, et al. (1998). "Crystallography & NMR system: A new software suite for macromolecular structure determination." Acta Crystallogr D Biol Crystallogr **54**(Pt 5): 905-21.

Caplan, S., N. Naslavsky, et al. (2002). "A tubular EHD1-containing compartment involved in the recycling of major histocompatibility complex class I molecules to the plasma membrane." EMBO J **21**(11): 2557-67.

Chappie, J. S., S. Acharya, et al. (2010). "G domain dimerization controls dynamin's assembly-stimulated GTPase activity." Nature **465**(7297): 435-40.

Chappie, J. S., S. Acharya, et al. (2009). "An intramolecular signaling element that modulates dynamin function in vitro and in vivo." Mol Biol Cell **20**(15): 3561-71.

Chau, K. Y., A. M. Keane-Myers, et al. (2005). "IFN-gamma gene expression is controlled by the architectural transcription factor HMGA1." Int Immunol **17**(3): 297-306.

Chen, M. S., R. A. Obar, et al. (1991). "Multiple forms of dynamin are encoded by shibire, a Drosophila gene involved in endocytosis." Nature **351**(6327): 583-6.

Chen, V. B., W. B. Arendall, 3rd, et al. (2010). "MolProbity: all-atom structure validation for macromolecular crystallography." Acta Crystallogr D Biol Crystallogr **66**(Pt 1): 12-21.

Chen, Y. J., P. Zhang, et al. (2004). "The stalk region of dynamin drives the constriction of dynamin tubes." Nat Struct Mol Biol **11**(6): 574-5.

Cheng, A., S. M. Wong, et al. (2009). "Structural basis for dsRNA recognition by NS1 protein of influenza A virus." Cell Res **19**(2): 187-95.

Cheng, Y. S., R. J. Colonno, et al. (1983). "Interferon induction of fibroblast proteins with guanylate binding activity." J Biol Chem **258**(12): 7746-50.

Cheng, Y. S., C. E. Patterson, et al. (1991). "Interferon-induced guanylate-binding proteins lack an N(T)KXD consensus motif and bind GMP in addition to GDP and GTP." Mol Cell Biol **11**(9): 4717-25.

Chung, C. T., S. L. Niemela, et al. (1989). "One-step preparation of competent Escherichia coli: transformation and storage of bacterial cells in the same solution." Proc Natl Acad Sci U S A **86**(7): 2172-5.

Cippitelli, M., A. Sica, et al. (1995). "Negative transcriptional regulation of the interferon-gamma promoter by glucocorticoids and dominant negative mutants of c-Jun." J Biol Chem **270**(21): 12548-56.

Colman, P. M., J. N. Varghese, et al. (1983). "Structure of the catalytic and antigenic sites in influenza virus neuraminidase." Nature **303**(5912): 41-4.

Coloma, R., J. M. Valpuesta, et al. (2009). "The structure of a biologically active influenza virus ribonucleoprotein complex." PLoS Pathog **5**(6): e1000491.

Conklin, D. C., F. J. Grant, et al. (2002). "Interferon-ε."

Cros, J. F. and P. Palese (2003). "Trafficking of viral genomic RNA into and out of the nucleus: influenza, Thogoto and Borna disease viruses." Virus Res **95**(1-2): 3-12.

Cuff, J. A., M. E. Clamp, et al. (1998). "JPred: a consensus secondary structure prediction server." Bioinformatics **14**(10): 892-3.

Darnell, J. E., Jr. (1997). "STATs and gene regulation." Science **277**(5332): 1630-5.

Darnell, J. E., Jr., I. M. Kerr, et al. (1994). "Jak-STAT pathways and transcriptional activation in response to IFNs and other extracellular signaling proteins." Science **264**(5164): 1415-21.

Daumke, O., S. Gao, et al. (2010). "Structure of the MxA stalk elucidates the assembly of ring-like units of an antiviral module." Small GTPases **1**(1): 62-4.

Daumke, O., R. Lundmark, et al. (2007). "Architectural and mechanistic insights into an EHD ATPase involved in membrane remodeling." Nature **449**(7164): 923-927.

DeLano, W. L. (2002). "The PyMol Molecular Graphics System.".

Dias, A., D. Bouvier, et al. (2009). "The cap-snatching endonuclease of influenza virus polymerase resides in the PA subunit." Nature **458**(7240): 914-8.

Dittmann, J., S. Stertz, et al. (2008). "Influenza A virus strains differ in sensitivity to the antiviral action of Mx-GTPase." J Virol **82**(7): 3624-31.

Donnelly, R. P. and S. V. Kotenko (2010). "Interferon-lambda: a new addition to an old family." J Interferon Cytokine Res **30**(8): 555-64.

Drake, J. W. (1993). "Rates of spontaneous mutation among RNA viruses." Proc Natl Acad Sci U S A **90**(9): 4171-5.

Emsley, P. and K. Cowtan (2004). "Coot: model-building tools for molecular graphics." Acta Crystallogr D Biol Crystallogr **60**(Pt 12 Pt 1): 2126-32.

Engelhardt, O. G., E. Ullrich, et al. (2001). "Interferon-induced antiviral Mx1 GTPase is associated with components of the SUMO-1 system and promyelocytic leukemia protein nuclear bodies." Exp Cell Res **271**(2): 286-95.

Farr, B. M., J. M. Gwaltney, Jr., et al. (1984). "Intranasal interferon-alpha 2 for prevention of natural rhinovirus colds." Antimicrob Agents Chemother **26**(1): 31-4.

Fasler-Kan, E., A. Pansky, et al. (1998). "Interferon-alpha activates signal transducers and activators of transcription 5 and 6 in Daudi cells." Eur J Biochem **254**(3): 514-9.

Ferguson, K. M., M. A. Lemmon, et al. (1994). "Crystal structure at 2.2 A resolution of the pleckstrin homology domain from human dynamin." Cell **79**(2): 199-209.

Fleury, D., S. A. Wharton, et al. (1998). "Antigen distortion allows influenza virus to escape neutralization." Nat Struct Biol **5**(2): 119-23.

Flohr, F., S. Schneider-Schaulies, et al. (1999). "The central interactive region of human MxA GTPase is involved in GTPase activation and interaction with viral target structures." FEBS Lett **463**(1-2): 24-8.

Friesen, H. J., S. Stein, et al. (1981). "Purification of human fibroblast interferon by high-performance liquid chromatography." Methods Enzymol **78**(edn): 430-435.

Fu, X. Y., C. Schindler, et al. (1992). "The proteins of ISGF-3, the interferon alpha-induced transcriptional activator, define a gene family involved in signal transduction." Proc Natl Acad Sci U S A **89**(16): 7840-3.

Fukao, T., D. M. Frucht, et al. (2001). "Inducible expression of Stat4 in dendritic cells and macrophages and its critical role in innate and adaptive immune responses." J Immunol **166**(7): 4446-55.

Fukao, T., S. Matsuda, et al. (2000). "Synergistic effects of IL-4 and IL-18 on IL-12-dependent IFN-gamma production by dendritic cells." J Immunol **164**(1): 64-71.

Fushman, D., S. Cahill, et al. (1995). "Solution structure of pleckstrin homology domain of dynamin by heteronuclear NMR spectroscopy." Proc Natl Acad Sci U S A **92**(3): 816-20.

Gad, H. H., C. Dellgren, et al. (2009). "Interferon-lambda is functionally an interferon but structurally related to the interleukin-10 family." J Biol Chem **284**(31): 20869-75.

Gad, H. H., O. J. Hamming, et al. (2010). "The structure of human interferon lambda and what it has taught us." J Interferon Cytokine Res **30**(8): 565-71.

Gamblin, S. J. and J. J. Skehel (2010). "Influenza hemagglutinin and neuraminidase membrane glycoproteins." J Biol Chem **285**(37): 28403-9.

Gao, S., A. von der Malsburg, et al. (2010). "Structural basis of oligomerization in the stalk region of dynamin-like MxA." Nature **465**(7297): 502-6.

Ghedin, E., N. A. Sengamalay, et al. (2005). "Large-scale sequencing of human influenza reveals the dynamic nature of viral genome evolution." Nature **437**(7062): 1162-6.

Ghosh, A., G. J. Praefcke, et al. (2006). "How guanylate-binding proteins achieve assembly-stimulated processive cleavage of GTP to GMP." Nature **440**(7080): 101-4.

Golab, J., Zagozdzon, et al. (2000). "Direct stimulation of macrophages by IL-12 and IL-18--a bridge too far?" Immunol Lett **72**(3): 153-7.

Gold, E. S., D. M. Underhill, et al. (1999). "Dynamin 2 is required for phagocytosis in macrophages." J Exp Med **190**(12): 1849-56.

Goldstein, D. and J. Laszlo (1988). "The role of interferon in cancer therapy: a current perspective." CA Cancer J Clin **38**(5): 258-77.

Gonzalez, S., T. Zurcher, et al. (1996). "Identification of two separate domains in the influenza virus PB1 protein involved in the interaction with the PB2 and PA subunits: a model for the viral RNA polymerase structure." Nucleic Acids Res **24**(22): 4456-63.

Gottschalk, A. (1957). "Neuraminidase: the specific enzyme of influenza virus and Vibrio cholerae." Biochim Biophys Acta **23**(3): 645-6.

Grant, B., Y. Zhang, et al. (2001). "Evidence that RME-1, a conserved C. elegans EH-domain protein, functions in endocytic recycling." Nat Cell Biol **3**(6): 573-9.

Grigliatti, T. A., L. Hall, et al. (1973). "Temperature-sensitive mutations in Drosophila melanogaster. XIV. A selection of immobile adults." Mol Gen Genet **120**(2): 107-14.

Guenzi, E., K. Topolt, et al. (2001). "The helical domain of GBP-1 mediates the inhibition of endothelial cell proliferation by inflammatory cytokines." EMBO J **20**(20): 5568-77.

Guex, N. and M. C. Peitsch (1997). "SWISS-MODEL and the Swiss-PdbViewer: an environment for comparative protein modeling." Electrophoresis **18**(15): 2714-23.

Guilligay, D., F. Tarendeau, et al. (2008). "The structural basis for cap binding by influenza virus polymerase subunit PB2." Nat Struct Mol Biol **15**(5): 500-6.

Guu, T. S., L. Dong, et al. (2008). "Mapping the domain structure of the influenza A virus polymerase acidic protein (PA) and its interaction with the basic protein 1 (PB1) subunit." Virology **379**(1): 135-42.

Haller, O., S. Gao, et al. (2010). "Dynamin-like MxA GTPase: structural insights into oligomerization and implications for antiviral activity." J Biol Chem **285**(37): 28419-24.

Haller, O. and G. Kochs (2002). "Interferon-induced mx proteins: dynamin-like GTPases with antiviral activity." Traffic **3**(10): 710-7.

Haller, O., G. Kochs, et al. (2006). "The interferon response circuit: induction and suppression by pathogenic viruses." Virology **344**(1): 119-30.

Haller, O., G. Kochs, et al. (2007). "Interferon, Mx, and viral countermeasures." Cytokine Growth Factor Rev **18**(5-6): 425-33.

Haller, O. and J. Lindenmann (1974). "Athymic (nude) mice express gene for myxovirus resistance." Nature **250**(5468): 679-80.

Haller, O., P. Staeheli, et al. (2009). "Protective role of interferon-induced Mx GTPases against influenza viruses." Rev Sci Tech **28**(1): 219-31.

Haller, O., S. Stertz, et al. (2007). "The Mx GTPase family of interferon-induced antiviral proteins." Microbes Infect **9**(14-15): 1636-43.

Harris, A., F. Forouhar, et al. (2001). "The crystal structure of the influenza matrix protein M1 at neutral pH: M1-M1 protein interfaces can rotate in the oligomeric structures of M1." Virology **289**(1): 34-44.

Haslam, R. J., H. B. Koide, et al. (1993). "Pleckstrin domain homology." Nature **363**(6427): 309-10.

Hayden, F. G., J. K. Albrecht, et al. (1986). "Prevention of natural colds by contact prophylaxis with intranasal alpha 2-interferon." N Engl J Med **314**(2): 71-5.

He, X., J. Zhou, et al. (2008). "Crystal structure of the polymerase PA(C)-PB1(N) complex from an avian influenza H5N1 virus." Nature **454**(7208): 1123-6.

Hefti, H. P., M. Frese, et al. (1999). "Human MxA protein protects mice lacking a functional alpha/beta interferon system against La crosse virus and other lethal viral infections." J Virol **73**(8): 6984-91.

Hemmi, S., R. Bohni, et al. (1994). "A novel member of the interferon receptor family complements functionality of the murine interferon gamma receptor in human cells." Cell **76**(5): 803-10.

Henley, J. R., E. W. Krueger, et al. (1998). "Dynamin-mediated internalization of caveolae." J Cell Biol **141**(1): 85-99.

Hinshaw, J. E. and S. L. Schmid (1995). "Dynamin self-assembles into rings suggesting a mechanism for coated vesicle budding." Nature **374**(6518): 190-2.

Hiscott, J. (2007). "Triggering the innate antiviral response through IRF-3 activation." J Biol Chem **282**(21): 15325-9.

Hofmann, K. P., C. M. Spahn, et al. (2006). "Building functional modules from molecular interactions." Trends Biochem Sci **31**(9): 497-508.

Honda, K., H. Yanai, et al. (2005). "IRF-7 is the master regulator of type-I interferon-dependent immune responses." Nature **434**(7034): 772-7.

Horisberger, M. A., P. Staeheli, et al. (1983). "Interferon induces a unique protein in mouse cells bearing a gene for resistance to influenza virus." Proc Natl Acad Sci U S A **80**(7): 1910-4.

Horisberger, M. A., M. Wathelet, et al. (1988). "cDNA cloning and assignment to chromosome 21 of IFI-78K gene, the human equivalent of murine Mx gene." Somat Cell Mol Genet **14**(2): 123-31.

Huang, S., W. Hendriks, et al. (1993). "Immune response in mice that lack the interferon-gamma receptor." Science **259**(5102): 1742-5.

Huang, T., J. Pavlovic, et al. (1992). "Overexpression of the influenza virus polymerase can titrate out inhibition by the murine Mx1 protein." J Virol **66**(7): 4154-60.

Ihle, J. N. (1995). "The Janus protein tyrosine kinase family and its role in cytokine signaling." Adv Immunol **60**: 1-35.

Ingerman, E., E. M. Perkins, et al. (2005). "Dnm1 forms spirals that are structurally tailored to fit mitochondria." J Cell Biol **170**(7): 1021-7.

Isaacs, A. and J. Lindenmann (1957). "Virus interference. I. The interferon." Proc R Soc Lond B Biol Sci **147**(927): 258-67.

Iversen, M. B., N. Ank, et al. (2010). "Expression of type III interferon (IFN) in the vaginal mucosa is mediated primarily by dendritic cells and displays stronger dependence on NF-kappaB than type I IFNs." J Virol **84**(9): 4579-86.

Janeway, C. A. J., P. Travers, et al. (2005). Immunobiology: The immune system in Health and Disease. London & New York, Garland Science.

Janzen, C., G. Kochs, et al. (2000). "A monomeric GTPase-negative MxA mutant with antiviral activity." J Virol **74**(17): 8202-6.

Kabsch, W. (1993). "Automatic processing of rotation diffraction data from crystals of initially unknown symmetry and cell constants." Journal of Applied Crystallography **26**(6): 795-800.

Kash, J. C., A. G. Goodman, et al. (2006). "Hijacking of the host-cell response and translational control during influenza virus infection." Virus Res **119**(1): 111-20.

Kato, H., O. Takeuchi, et al. (2006). "Differential roles of MDA5 and RIG-I helicases in the recognition of RNA viruses." Nature **441**(7089): 101-5.

Kawai, T., K. Takahashi, et al. (2005). "IPS-1, an adaptor triggering RIG-I- and Mda5-mediated type I interferon induction." Nat Immunol **6**(10): 981-8.

Kay, B. K., M. P. Williamson, et al. (2000). "The importance of being proline: the interaction of proline-rich motifs in signaling proteins with their cognate domains." FASEB J **14**(2): 231-41.

Kelley, L. A. and M. J. Sternberg (2009). "Protein structure prediction on the Web: a case study using the Phyre server." Nat Protoc **4**(3): 363-71.

Kenniston, J. A. and M. A. Lemmon (2010). "Dynamin GTPase regulation is altered by PH domain mutations found in centronuclear myopathy patients." EMBO J **29**(18): 3054-67.

Key, L. L., Jr., W. L. Ries, et al. (1992). "Recombinant human interferon gamma therapy for osteopetrosis." J Pediatr **121**(1): 119-24.

Kiani, A., F. J. Garcia-Cozar, et al. (2001). "Regulation of interferon-gamma gene expression by nuclear factor of activated T cells." Blood **98**(5): 1480-8.

Klenk, E., H. Faillard, et al. (1955). "Enzymatic effect of the influenza virus." Hoppe Seylers Z Physiol Chem **301**(4-6): 235-46.

Kochs, G., A. Garcia-Sastre, et al. (2007). "Multiple anti-interferon actions of the influenza A virus NS1 protein." J Virol **81**(13): 7011-21.

Kochs, G., M. Haener, et al. (2002). "Self-assembly of human MxA GTPase into highly ordered dynamin-like oligomers." J Biol Chem **277**(16): 14172-6.

Kochs, G. and O. Haller (1999). "Interferon-induced human MxA GTPase blocks nuclear import of Thogoto virus nucleocapsids." Proc Natl Acad Sci U S A **96**(5): 2082-6.

Kochs, G., C. Janzen, et al. (2002). "Antivirally active MxA protein sequesters La Crosse virus nucleocapsid protein into perinuclear complexes." Proc Natl Acad Sci U S A **99**(5): 3153-8.

Kochs, G., M. Reichelt, et al. (2005). "Assay and functional analysis of dynamin-like Mx proteins." Methods Enzymol **404**: 632-43.

Kochs, G., M. Trost, et al. (1998). "MxA GTPase: oligomerization and GTP-dependent interaction with viral RNP target structures." Methods **15**(3): 255-63.

Kosaka, T. and K. Ikeda (1983). "Possible temperature-dependent blockage of synaptic vesicle recycling induced by a single gene mutation in Drosophila." J Neurobiol **14**(3): 207-25.

Kotenko, S. V., G. Gallagher, et al. (2003). "IFN-lambdas mediate antiviral protection through a distinct class II cytokine receptor complex." Nat Immunol **4**(1): 69-77.

Kraemer, A., T. Brinkmann, et al. (2002). "Fluorescently labeled guanine nucleotide binding proteins to analyse elementary steps of GAP-catalysed reactions." J Mol Biol **324**(4): 763-74.

Kraulis, P. (1991). "MOLSCRIPT: a program to produce both detailed and schematic plots of protein structures." Journal of Applied Crystallography **24**(5): 946-950.

Krause, C. D., E. Mei, et al. (2002). "Seeing the light: preassembly and ligand-induced changes of the interferon gamma receptor complex in cells." Mol Cell Proteomics **1**(10): 805-15.

Laemmli, U. K. (1970). "Cleavage of structural proteins during the assembly of the head of bacteriophage T4." Nature **227**(5259): 680-5.

LaFleur, D. W., B. Nardelli, et al. (2001). "Interferon-kappa, a novel type I interferon expressed in human keratinocytes." J Biol Chem **276**(43): 39765-71.

Lakadamyali, M., M. J. Rust, et al. (2003). "Visualizing infection of individual influenza viruses." Proc Natl Acad Sci U S A **100**(16): 9280-5.

Landau, M., I. Mayrose, et al. (2005). "ConSurf 2005: the projection of evolutionary conservation scores of residues on protein structures." Nucleic Acids Res **33**(Web Server issue): W299-302.

Larsen, R., T. P. Rokenes, et al. (2004). "Inhibition of infectious pancreatic necrosis virus replication by atlantic salmon Mx1 protein." J Virol **78**(15): 7938-44.

Laskowski, R. A., M. W. MacArthur, et al. (1993). "PROCHECK: a program to check the stereochemical quality of protein structures." Journal of Applied Crystallography **26**(2): 283-291.

Lenzen, C., R. H. Cool, et al. (1995). "Analysis of intrinsic and CDC25-stimulated guanine nucleotide exchange of p21ras-nucleotide complexes by fluorescence measurements." Methods Enzymol **255**: 95-109.

Li, M. L., P. Rao, et al. (2001). "The active sites of the influenza cap-dependent endonuclease are on different polymerase subunits." EMBO J **20**(8): 2078-86.

Lindenmann, J. (1962). "Resistance of mice to mouse-adapted influenza A virus." Virology **16**: 203-4.

Liu, C., M. C. Eichelberger, et al. (1995). "Influenza type A virus neuraminidase does not play a role in viral entry, replication, assembly, or budding." J Virol **69**(2): 1099-106.

Low, H. H. and J. Lowe (2006). "A bacterial dynamin-like protein." Nature **444**(7120): 766-9.

Low, H. H., C. Sachse, et al. (2009). "Structure of a bacterial dynamin-like protein lipid tube provides a mechanism for assembly and membrane curving." Cell **139**(7): 1342-52.

Lu, Y., M. Wambach, et al. (1995). "Binding of the influenza virus NS1 protein to double-stranded RNA inhibits the activation of the protein kinase that phosphorylates the elF-2 translation initiation factor." Virology **214**(1): 222-8.

Lundquist, P. G., S. Haglund, et al. (1984). "Interferon therapy in juvenile laryngeal papillomatosis." Otolaryngol Head Neck Surg **92**(4): 386-91.

Mach, B., V. Steimle, et al. (1996). "Regulation of MHC class II genes: lessons from a disease." Annu Rev Immunol **14**: 301-31.

Maher, S. G., F. Sheikh, et al. (2008). "IFNalpha and IFNlambda differ in their antiproliferative effects and duration of JAK/STAT signaling activity." Cancer Biol Ther **7**(7): 1109-15.

Maines, T. R., X. H. Lu, et al. (2005). "Avian influenza (H5N1) viruses isolated from humans in Asia in 2004 exhibit increased virulence in mammals." J Virol **79**(18): 11788-800.

Marie, I., J. E. Durbin, et al. (1998). "Differential viral induction of distinct interferon-alpha genes by positive feedback through interferon regulatory factor-7." EMBO J **17**(22): 6660-9.

Marks, B., M. H. Stowell, et al. (2001). "GTPase activity of dynamin and resulting conformation change are essential for endocytosis." Nature **410**(6825): 231-5.

Martin, K. and A. Helenius (1991). "Nuclear transport of influenza virus ribonucleoproteins: the viral matrix protein (M1) promotes export and inhibits import." Cell **67**(1): 117-30.

Matikainen, S., T. Sareneva, et al. (1999). "Interferon-alpha activates multiple STAT proteins and upregulates proliferation-associated IL-2Ralpha, c-myc, and pim-1 genes in human T cells." Blood **93**(6): 1980-91.

Matthews, B. W. (1968). "Solvent content of protein crystals." J Mol Biol **33**(2): 491-7.

Mayer, B. J. (2001). "SH3 domains: complexity in moderation." J Cell Sci **114**(Pt 7): 1253-63.

Mayer, B. J., R. Ren, et al. (1993). "A putative modular domain present in diverse signaling proteins." Cell **73**(4): 629-30.

Mazzella, G., G. Saracco, et al. (1999). "Long-term results with interferon therapy in chronic type B hepatitis: a prospective randomized trial." Am J Gastroenterol **94**(8): 2246-50.

McCoy, A. J., R. W. Grosse-Kunstleve, et al. (2007). "Phaser crystallographic software." Journal of Applied Crystallography **40**(4): 658-674.

Mears, J. A., L. L. Lackner, et al. (2011). "Conformational changes in Dnm1 support a contractile mechanism for mitochondrial fission." Nat Struct Mol Biol **18**(1): 20-6.

Mears, J. A., P. Ray, et al. (2007). "A corkscrew model for dynamin constriction." Structure **15**(10): 1190-202.

Melen, K., P. Keskinen, et al. (1996). "Human MxB protein, an interferon-alpha-inducible GTPase, contains a nuclear targeting signal and is localized in the heterochromatin region beneath the nuclear envelope." J Biol Chem **271**(38): 23478-86.

Melen, K., T. Ronni, et al. (1992). "Interferon-induced Mx proteins form oligomers and contain a putative leucine zipper." J Biol Chem **267**(36): 25898-907.

Melen, K., T. Ronni, et al. (1994). "Enzymatic characterization of interferon-induced antiviral GTPases murine Mx1 and human MxA proteins." J Biol Chem **269**(3): 2009-15.

Merritt, E. A. and M. E. P. Murphy (1994). "Raster3D Version 2.0. A program for photorealistic molecular graphics." Acta Crystallographica Section D **50**(6): 869-873.

Milburn, M. V., L. Tong, et al. (1990). "Molecular switch for signal transduction: structural differences between active and inactive forms of protooncogenic ras proteins." Science **247**(4945): 939-45.

Miller, M. M., K. Klucher, M., et al. (2009). "Interferon Lambda as a Potential New Therapeutic for Hepatitis C." Cytokine Therapies: Ann. N.Y. Acad. Sci.(1182): 80-87.

Munder, M., M. Mallo, et al. (1998). "Murine macrophages secrete interferon gamma upon combined stimulation with interleukin (IL)-12 and IL-18: A novel pathway of autocrine macrophage activation." J Exp Med **187**(12): 2103-8.

Murshudov, G. N., A. A. Vagin, et al. (1997). "Refinement of macromolecular structures by the maximum-likelihood method." Acta Crystallogr D Biol Crystallogr **53**(Pt 3): 240-55.

Nayak, D. P., E. K. Hui, et al. (2004). "Assembly and budding of influenza virus." Virus Res **106**(2): 147-65.

Nemeroff, M. E., S. M. Barabino, et al. (1998). "Influenza virus NS1 protein interacts with the cellular 30 kDa subunit of CPSF and inhibits 3'end formation of cellular pre-mRNAs." Mol Cell **1**(7): 991-1000.

Netherton, C. L., J. Simpson, et al. (2009). "Inhibition of a large double-stranded DNA virus by MxA protein." J Virol **83**(5): 2310-20.

Neumann, G., M. T. Hughes, et al. (2000). "Influenza A virus NS2 protein mediates vRNP nuclear export through NES-independent interaction with hCRM1." EMBO J **19**(24): 6751-8.

Newcomb, L. L., R. L. Kuo, et al. (2009). "Interaction of the influenza a virus nucleocapsid protein with the viral RNA polymerase potentiates unprimed viral RNA replication." J Virol **83**(1): 29-36.

Ng, A. K., H. Zhang, et al. (2008). "Structure of the influenza virus A H5N1 nucleoprotein: implications for RNA binding, oligomerization, and vaccine design." FASEB J **22**(10): 3638-47.

Nicholas, K. B., H. Nicholas, B, et al. (1997). "GeneDoc: Analysis and Visualization of Genetic Variation." EMBNEW. NEWS **4**.

Niemann, H. H., M. L. Knetsch, et al. (2001). "Crystal structure of a dynamin GTPase domain in both nucleotide-free and GDP-bound forms." EMBO J **20**(21): 5813-21.

O'Neill, R. E., J. Talon, et al. (1998). "The influenza virus NEP (NS2 protein) mediates the nuclear export of viral ribonucleoproteins." EMBO J **17**(1): 288-96.

Obar, R. A., C. A. Collins, et al. (1990). "Molecular cloning of the microtubule-associated mechanochemical enzyme dynamin reveals homology with a new family of GTP-binding proteins." Nature **347**(6290): 256-61.

Obayashi, E., H. Yoshida, et al. (2008). "The structural basis for an essential subunit interaction in influenza virus RNA polymerase." Nature **454**(7208): 1127-31.

Ochoa, G. C., V. I. Slepnev, et al. (2000). "A functional link between dynamin and the actin cytoskeleton at podosomes." J Cell Biol **150**(2): 377-89.

Oh, P., D. P. McIntosh, et al. (1998). "Dynamin at the neck of caveolae mediates their budding to form transport vesicles by GTP-driven fission from the plasma membrane of endothelium." J Cell Biol **141**(1): 101-14.

Onoguchi, K., M. Yoneyama, et al. (2007). "Viral infections activate types I and III interferon genes through a common mechanism." J Biol Chem **282**(10): 7576-81.

Ophir, J., S. Brenner, et al. (1995). "Effect of topical interferon-beta on recurrence rates in genital herpes: a double-blind, placebo-controlled, randomized study." J Interferon Cytokine Res **15**(7): 625-31.

Ortaldo, J. R., R. B. Herberman, et al. (1984). "A species of human alpha interferon that lacks the ability to boost human natural killer activity." Proc Natl Acad Sci U S A **81**(15): 4926-9.

Orth, J. D. and M. A. McNiven (2003). "Dynamin at the actin-membrane interface." Curr Opin Cell Biol **15**(1): 31-9.

Osterlund, P. I., T. E. Pietila, et al. (2007). "IFN regulatory factor family members differentially regulate the expression of type III IFN (IFN-lambda) genes." J Immunol **179**(6): 3434-42.

Palese, P., K. Tobita, et al. (1974). "Characterization of temperature sensitive influenza virus mutants defective in neuraminidase." Virology **61**(2): 397-410.

Pape, T. and T. R. Schneider (2004). "HKL2MAP: a graphical user interface for macromolecular phasing with SHELX programs." Journal of Applied Crystallography **37**(5): 843-844.

Pestka, S. (1997). "The human interferon-alpha species and hybrid proteins." Semin Oncol **24**(3 Suppl 9): S9-4-S9-17.

Pestka, S., B. Kelder, et al. (1983). "Molecular weight of the functional unit of human leukocyte, fibroblast, and immune interferons." J Biol Chem **258**(16): 9706-9.

Pestka, S., C. D. Krause, et al. (2004). "Interferons, interferon-like cytokines, and their receptors." Immunol Rev **202**: 8-32.

Pestka, S., J. A. Langer, et al. (1987). "Interferons and their actions." Annu Rev Biochem **56**: 727-77.

Pettersen, E. F., T. D. Goddard, et al. (2004). "UCSF Chimera--a visualization system for exploratory research and analysis." J Comput Chem **25**(13): 1605-12.

Pianko, S. and J. G. McHutchison (2000). "Treatment of hepatitis C with interferon and ribavirin." J Gastroenterol Hepatol **15**(6): 581-6.

Platanias, L. C. (2005). "Mechanisms of type-I- and type-II-interferon-mediated signaling." Nat Rev Immunol **5**(5): 375-86.

Poch, O., I. Sauvaget, et al. (1989). "Identification of four conserved motifs among the RNA-dependent polymerase encoding elements." EMBO J **8**(12): 3867-74.

Pollard, T. D. and E. M. Ostap (1996). "The chemical mechanism of myosin-I: implications for actin-based motility and the evolution of the myosin family of motor proteins." Cell Struct Funct **21**(5): 351-6.

Ponten, A., C. Sick, et al. (1997). "Dominant-negative mutants of human MxA protein: domains in the carboxy-terminal moiety are important for oligomerization and antiviral activity." J Virol **71**(4): 2591-9.

Poodry, C. A. (1990). "shibire, a neurogenic mutant of Drosophila." Dev Biol **138**(2): 464-72.

Portela, A. and P. Digard (2002). "The influenza virus nucleoprotein: a multifunctional RNA-binding protein pivotal to virus replication." J Gen Virol **83**(Pt 4): 723-34.

Potterton, L., S. McNicholas, et al. (2004). "Developments in the CCP4 molecular-graphics project." Acta Crystallogr D Biol Crystallogr **60**(Pt 12 Pt 1): 2288-94.

Praefcke, G. J., M. Geyer, et al. (1999). "Nucleotide-binding characteristics of human guanylate-binding protein 1 (hGBP1) and identification of the third GTP-binding motif." J Mol Biol **292**(2): 321-32.

Praefcke, G. J., S. Kloep, et al. (2004). "Identification of residues in the human guanylate-binding protein 1 critical for nucleotide binding and cooperative GTP hydrolysis." J Mol Biol **344**(1): 257-69.

Praefcke, G. J. and H. T. McMahon (2004). "The dynamin superfamily: universal membrane tubulation and fission molecules?" Nat Rev Mol Cell Biol **5**(2): 133-47.

Prakash, B., G. J. Praefcke, et al. (2000). "Structure of human guanylate-binding protein 1 representing a unique class of GTP-binding proteins." Nature **403**(6769): 567-71.

Prakash, B., L. Renault, et al. (2000). "Triphosphate structure of guanylate-binding protein 1 and implications for nucleotide binding and GTPase mechanism." EMBO J **19**(17): 4555-64.

Radhakrishnan, R., L. J. Walter, et al. (1996). "Zinc mediated dimer of human interferon-alpha 2b revealed by X-ray crystallography." Structure **4**(12): 1453-63.

Ramachandran, G. N., C. Ramakrishnan, et al. (1963). "Stereochemistry of polypeptide chain configurations." J Mol Biol **7**: 95-9.

Ramachandran, R., M. Surka, et al. (2007). "The dynamin middle domain is critical for tetramerization and higher-order self-assembly." EMBO J **26**(2): 559-66.

Reeves, R. H., B. F. O'Hara, et al. (1988). "Genetic mapping of the Mx influenza virus resistance gene within the region of mouse chromosome 16 that is homologous to human chromosome 21." J Virol **62**(11): 4372-5.

Reichelt, M., S. Stertz, et al. (2004). "Missorting of LaCrosse virus nucleocapsid protein by the interferon-induced MxA GTPase involves smooth ER membranes." Traffic **5**(10): 772-84.

Reubold, T. F., S. Eschenburg, et al. (2005). "Crystal structure of the GTPase domain of rat dynamin 1." Proc Natl Acad Sci U S A **102**(37): 13093-8.

Rhodes, G. (2006). Crystallography made crystal clear, Elsevier/Academic Press.

Richter, M. F., M. Schwemmle, et al. (1995). "Interferon-induced MxA protein. GTP binding and GTP hydrolysis properties." J Biol Chem **270**(22): 13512-7.

Robek, M. D., B. S. Boyd, et al. (2005). "Lambda interferon inhibits hepatitis B and C virus replication." J Virol **79**(6): 3851-4.

Roffi, L., G. C. Mels, et al. (1995). "Breakthrough during recombinant interferon alfa therapy in patients with chronic hepatitis C virus infection: prevalence, etiology, and management." Hepatology **21**(3): 645-9.

Rubinstein, M., S. Rubinstein, et al. (1978). "Human leukocyte interferon purified to homogeneity." Science **202**(4374): 1289-90.

Rubinstein, M., S. Rubinstein, et al. (1979). "Human leukocyte interferon: production, purification to homogeneity, and initial characterization." Proc Natl Acad Sci U S A **76**(2): 640-4.

Sambrook, J., E. F. Fritsch, et al. (1989). Molecular Cloning: A Laboratory Manual. New York, Cold Spring Harbor Laboratory Press.

Samudzi, C. T. and J. R. Rubin (1993). "Structure of recombinant bovine interferon-gamma at 3.0 A resolution." Acta Crystallogr D Biol Crystallogr **49**(Pt 6): 513-21.

Samuel, C. E. (2010). "Thematic minireview series: toward a structural basis for understanding influenza virus-host cell interactions." J Biol Chem **285**(37): 28399-401.

Saraste, M. and M. Hyvonen (1995). "Pleckstrin homology domains: a fact file." Curr Opin Struct Biol **5**(3): 403-8.

Saraste, M., P. R. Sibbald, et al. (1990). "The P-loop--a common motif in ATP- and GTP-binding proteins." Trends Biochem Sci **15**(11): 430-4.

Scheffzek, K., M. R. Ahmadian, et al. (1998). "GTPase-activating proteins: helping hands to complement an active site." Trends Biochem Sci **23**(7): 257-62.

Schindler, C., K. Shuai, et al. (1992). "Interferon-dependent tyrosine phosphorylation of a latent cytoplasmic transcription factor." Science **257**(5071): 809-13.

Schindler, H., M. B. Lutz, et al. (2001). "The production of IFN-gamma by IL-12/IL-18-activated macrophages requires STAT4 signaling and is inhibited by IL-4." J Immunol **166**(5): 3075-82.

Schnell, J. R. and J. J. Chou (2008). "Structure and mechanism of the M2 proton channel of influenza A virus." Nature **451**(7178): 591-5.

Schroder, G. F., M. Levitt, et al. (2010). "Super-resolution biomolecular crystallography with low-resolution data." Nature **464**(7292): 1218-22.

Schroder, K., P. J. Hertzog, et al. (2004). "Interferon-gamma: an overview of signals, mechanisms and functions." J Leukoc Biol **75**(2): 163-89.

Schumacher, B. and P. Staeheli (1998). "Domains mediating intramolecular folding and oligomerization of MxA GTPase." J Biol Chem **273**(43): 28365-70.

Schweins, T. and A. Wittinghofer (1994). "GTP-binding proteins. Structures, interactions and relationships." Curr Biol **4**(6): 547-50.

Schwemmle, M., M. F. Richter, et al. (1995). "Unexpected structural requirements for GTPase activity of the interferon-induced MxA protein." J Biol Chem **270**(22): 13518-23.

Schwemmle, M. and P. Staeheli (1994). "The interferon-induced 67-kDa guanylate-binding protein (hGBP1) is a GTPase that converts GTP to GMP." J Biol Chem **269**(15): 11299-305.

Scrima, A. and A. Wittinghofer (2006). "Dimerisation-dependent GTPase reaction of MnmE: how potassium acts as GTPase-activating element." EMBO J **25**(12): 2940-51.

Sen, G. C. (2001). "Viruses and interferons." Annu Rev Microbiol **55**: 255-81.

Senda, T., S. Saitoh, et al. (1995). "Refined crystal structure of recombinant murine interferon-beta at 2.15 A resolution." J Mol Biol **253**(1): 187-207.

Sever, S., A. B. Muhlberg, et al. (1999). "Impairment of dynamin's GAP domain stimulates receptor-mediated endocytosis." Nature **398**(6727): 481-6.

Sha, B. and M. Luo (1997). "Structure of a bifunctional membrane-RNA binding protein, influenza virus matrix protein M1." Nat Struct Biol **4**(3): 239-44.

Shao, Y., W. Akmentin, et al. (2002). "Pincher, a pinocytic chaperone for nerve growth factor/TrkA signaling endosomes." J Cell Biol **157**(4): 679-91.

Sheehy, A. M., N. C. Gaddis, et al. (2002). "Isolation of a human gene that inhibits HIV-1 infection and is suppressed by the viral Vif protein." Nature **418**(6898): 646-50.

Sheldrick, G. M. (2008). "A short history of SHELX." Acta Crystallogr A **64**(Pt 1): 112-22.

Sheppard, P., W. Kindsvogel, et al. (2003). "IL-28, IL-29 and their class II cytokine receptor IL-28R." Nat Immunol **4**(1): 63-8.

Shpetner, H. S. and R. B. Vallee (1989). "Identification of dynamin, a novel mechanochemical enzyme that mediates interactions between microtubules." Cell **59**(3): 421-32.

Shpetner, H. S. and R. B. Vallee (1992). "Dynamin is a GTPase stimulated to high levels of activity by microtubules." Nature **355**(6362): 733-5.

Shuai, K., C. Schindler, et al. (1992). "Activation of transcription by IFN-gamma: tyrosine phosphorylation of a 91-kD DNA binding protein." Science **258**(5089): 1808-12.

Sica, A., L. Dorman, et al. (1997). "Interaction of NF-kappaB and NFAT with the interferon-gamma promoter." J Biol Chem **272**(48): 30412-20.

Silberberg, D. H. (1994). "Specific treatment of multiple sclerosis." Clin Neurosci **2**(3-4): 271-4.

Silvennoinen, O., J. N. Ihle, et al. (1993). "Interferon-induced nuclear signaling by Jak protein tyrosine kinases." Nature **366**(6455): 583-5.

Skehel, J. J. and D. C. Wiley (2000). "Receptor binding and membrane fusion in virus entry: the influenza hemagglutinin." Annu Rev Biochem **69**: 531-69.

Staeheli, P., R. Grob, et al. (1988). "Influenza virus-susceptible mice carry Mx genes with a large deletion or a nonsense mutation." Mol Cell Biol **8**(10): 4518-23.

Staeheli, P. and O. Haller (1985). "Interferon-induced human protein with homology to protein Mx of influenza virus-resistant mice." Mol Cell Biol **5**(8): 2150-3.

Staeheli, P., O. Haller, et al. (1986). "Mx protein: constitutive expression in 3T3 cells transformed with cloned Mx cDNA confers selective resistance to influenza virus." Cell **44**(1): 147-58.

Staeheli, P., F. Pitossi, et al. (1993). "Mx proteins: GTPases with antiviral activity." Trends Cell Biol **3**(8): 268-72.

Staeheli, P. and J. G. Sutcliffe (1988). "Identification of a second interferon-regulated murine Mx gene." Mol Cell Biol **8**(10): 4524-8.

Stark, G. R., I. M. Kerr, et al. (1998). "How cells respond to interferons." Annu Rev Biochem **67**: 227-64.

Stein, S., C. Kenny, et al. (1980). "NH2-terminal amino acid sequence of human fibroblast interferon." Proc Natl Acad Sci U S A **77**(10): 5716-9.

Steinhauer, D. A. (1999). "Role of hemagglutinin cleavage for the pathogenicity of influenza virus." Virology **258**(1): 1-20.

Steinkellner, G., R. Rader, et al. (2009). "VASCo: computation and visualization of annotated protein surface contacts." BMC Bioinformatics **10**: 32.

Stertz, S., M. Reichelt, et al. (2006). "Interferon-induced, antiviral human MxA protein localizes to a distinct subcompartment of the smooth endoplasmic reticulum." J Interferon Cytokine Res **26**(9): 650-60.

Stoscheck, C. M. (1990). "Quantitation of protein." Methods Enzymol **182**: 50-68.

Stouffer, A. L., R. Acharya, et al. (2008). "Structural basis for the function and inhibition of an influenza virus proton channel." Nature **451**(7178): 596-9.

Stowell, M. H., B. Marks, et al. (1999). "Nucleotide-dependent conformational changes in dynamin: evidence for a mechanochemical molecular spring." Nat Cell Biol **1**(1): 27-32.

Stranden, A. M., P. Staeheli, et al. (1993). "Function of the mouse Mx1 protein is inhibited by overexpression of the PB2 protein of influenza virus." Virology **197**(2): 642-51.

Strong, M., M. R. Sawaya, et al. (2006). "Toward the structural genomics of complexes: crystal structure of a PE/PPE protein complex from Mycobacterium tuberculosis." Proc Natl Acad Sci U S A **103**(21): 8060-5.

Sugiyama, K., E. Obayashi, et al. (2009). "Structural insight into the essential PB1-PB2 subunit contact of the influenza virus RNA polymerase." EMBO J **28**(12): 1803-11.

Sweetser, M. T., T. Hoey, et al. (1998). "The roles of nuclear factor of activated T cells and ying-yang 1 in activation-induced expression of the interferon-gamma promoter in T cells." J Biol Chem **273**(52): 34775-83.

Sweitzer, S. M. and J. E. Hinshaw (1998). "Dynamin undergoes a GTP-dependent conformational change causing vesiculation." Cell **93**(6): 1021-9.

Szabo, S. J., S. T. Kim, et al. (2000). "A novel transcription factor, T-bet, directs Th1 lineage commitment." Cell **100**(6): 655-69.

Tarendeau, F., J. Boudet, et al. (2007). "Structure and nuclear import function of the C-terminal domain of influenza virus polymerase PB2 subunit." Nat Struct Mol Biol **14**(3): 229-33.

Tarendeau, F., T. Crepin, et al. (2008). "Host determinant residue lysine 627 lies on the surface of a discrete, folded domain of influenza virus polymerase PB2 subunit." PLoS Pathog **4**(8): e1000136.

Thaa, B., K. P. Hofmann, et al. (2010). "Viruses as vesicular carriers of the viral genome: a functional module perspective." Biochim Biophys Acta **1803**(4): 507-19.

Thompson, J. D., D. G. Higgins, et al. (1994). "CLUSTAL W: improving the sensitivity of progressive multiple sequence alignment through sequence weighting, position-specific gap penalties and weight matrix choice." Nucleic Acids Res **22**(22): 4673-80.

Thomson, S. J., F. G. Goh, et al. (2009). "The role of transposable elements in the regulation of IFN-lambda1 gene expression." Proc Natl Acad Sci U S A **106**(28): 11564-9.

Todd, P. A. and K. L. Goa (1992). "Interferon gamma-1b. A review of its pharmacology and therapeutic potential in chronic granulomatous disease." Drugs **43**(1): 111-22.

Uddin, S., B. Majchrzak, et al. (1999). "Activation of the p38 mitogen-activated protein kinase by type I interferons." J Biol Chem **274**(42): 30127-31.

Uddin, S., L. Yenush, et al. (1995). "Interferon-alpha engages the insulin receptor substrate-1 to associate with the phosphatidylinositol 3'-kinase." J Biol Chem **270**(27): 15938-41.

Uematsu, S. and S. Akira (2007). "Toll-like receptors and Type I interferons." J Biol Chem **282**(21): 15319-23.

Ulmanen, I., B. A. Broni, et al. (1981). "Role of two of the influenza virus core P proteins in recognizing cap 1 structures (m7GpppNm) on RNAs and in initiating viral RNA transcription." Proc Natl Acad Sci U S A **78**(12): 7355-9.

Urrutia, R., J. R. Henley, et al. (1997). "The dynamins: redundant or distinct functions for an expanding family of related GTPases?" Proc Natl Acad Sci U S A **94**(2): 377-84.

Uze, G., G. Lutfalla, et al. (1990). "Genetic transfer of a functional human interferon alpha receptor into mouse cells: cloning and expression of its cDNA." Cell **60**(2): 225-34.

Vagin, A. and A. Teplyakov (1997). "MOLREP: an Automated Program for Molecular Replacement." Journal of Applied Crystallography **30**(6): 1022-1025.

Vallis, Y., P. Wigge, et al. (1999). "Importance of the pleckstrin homology domain of dynamin in clathrin-mediated endocytosis." Curr Biol **9**(5): 257-60.

van Dam, E. M. and W. Stoorvogel (2002). "Dynamin-dependent transferrin receptor recycling by endosome-derived clathrin-coated vesicles." Mol Biol Cell **13**(1): 169-82.

van der Bliek, A. M. (1999). "Functional diversity in the dynamin family." Trends Cell Biol **9**(3): 96-102.

van der Bliek, A. M. and E. M. Meyerowitz (1991). "Dynamin-like protein encoded by the Drosophila shibire gene associated with vesicular traffic." Nature **351**(6325): 411-4.

Van Duyne, G. D., R. F. Standaert, et al. (1993). "Atomic structures of the human immunophilin FKBP-12 complexes with FK506 and rapamycin." J Mol Biol **229**(1): 105-24.

Varghese, J. N. and P. M. Colman (1991). "Three-dimensional structure of the neuraminidase of influenza virus A/Tokyo/3/67 at 2.2 A resolution." J Mol Biol **221**(2): 473-86.

Varghese, J. N., W. G. Laver, et al. (1983). "Structure of the influenza virus glycoprotein antigen neuraminidase at 2.9 A resolution." Nature **303**(5912): 35-40.

Vestal, D. J. and J. A. Jeyaratnam (2010). "The guanylate-binding proteins: emerging insights into the biochemical properties and functions of this family of large interferon-induced guanosine triphosphatase." J Interferon Cytokine Res **31**(1): 89-97.

Vetter, I. R. and A. Wittinghofer (2001). "The guanine nucleotide-binding switch in three dimensions." Science **294**(5545): 1299-304.

Wagner, R., M. Matrosovich, et al. (2002). "Functional balance between haemagglutinin and neuraminidase in influenza virus infections." Rev Med Virol **12**(3): 159-66.

Wallace, A. C., R. A. Laskowski, et al. (1995). "LIGPLOT: a program to generate schematic diagrams of protein-ligand interactions." Protein Eng **8**(2): 127-34.

Wallach, D., M. Fellous, et al. (1982). "Preferential effect of gamma interferon on the synthesis of HLA antigens and their mRNAs in human cells." Nature **299**(5886): 833-6.

Walter, M. R., W. T. Windsor, et al. (1995). "Crystal structure of a complex between interferon-gamma and its soluble high-affinity receptor." Nature **376**(6537): 230-5.

Wang, D. S. and G. Shaw (1995). "The association of the C-terminal region of beta I sigma II spectrin to brain membranes is mediated by a PH domain, does not require membrane proteins, and coincides with a inositol-1,4,5 triphosphate binding site." Biochem Biophys Res Commun **217**(2): 608-15.

Wang, D. S., R. Shaw, et al. (1994). "Binding of PH domains of beta-adrenergic receptor kinase and beta-spectrin to WD40/beta-transducin repeat containing regions of the beta-subunit of trimeric G-proteins." Biochem Biophys Res Commun **203**(1): 29-35.

Wang, J., R. Oberley-Deegan, et al. (2009). "Differentiated human alveolar type II cells secrete antiviral IL-29 (IFN-lambda 1) in response to influenza A infection." J Immunol **182**(3): 1296-304.

Wang, W., K. Riedel, et al. (1999). "RNA binding by the novel helical domain of the influenza virus NS1 protein requires its dimer structure and a small number of specific basic amino acids." RNA **5**(2): 195-205.

Weber, F., O. Haller, et al. (2000). "MxA GTPase blocks reporter gene expression of reconstituted Thogoto virus ribonucleoprotein complexes." J Virol **74**(1): 560-3.

Weiss, M. (2001). "Global indicators of X-ray data quality." Journal of Applied Crystallography **34**(2): 130-135.

Westheimer, F. H. (1987). "Why nature chose phosphates." Science **235**(4793): 1173-8.

Whittaker, G., M. Bui, et al. (1996). "Nuclear trafficking of influenza virus ribonuleoproteins in heterokaryons." J Virol **70**(5): 2743-56.

WHO (1980). "A revision of the system of nomenclature for influenza viruses: a WHO memorandum." Bull World Health Organ **58**(4): 585-91.

Williamson, M. P. (1994). "The structure and function of proline-rich regions in proteins." Biochem J **297 (Pt 2)**: 249-60.

Wingerchuk, D. M. and J. H. Noseworthy (2002). "Randomized controlled trials to assess therapies for multiple sclerosis." Neurology **58**(8 Suppl 4): S40-8.

Winn, M. D., G. N. Murshudov, et al. (2003). "Macromolecular TLS refinement in REFMAC at moderate resolutions." Methods Enzymol **374**: 300-21.

Wittinghofer, A. (1996). "Deciphering the alphabet of G proteins: the structure of the alpha, beta, gamma heterotrimer." Structure **4**(4): 357-61.

Wittinghofer, A. (1998). "Signal transduction via Ras." Biol Chem **379**(8-9): 933-7.

Xu, X., Y. L. Sun, et al. (1996). "Cooperative DNA binding and sequence-selective recognition conferred by the STAT amino-terminal domain." Science **273**(5276): 794-7.

Yang, S., W. Tempel, et al. (2010). "Crystal structure of the dynamin 3 GTPase domain bound with GDP." RCSB Protein Data Bank.

Yao, L., Y. Kawakami, et al. (1994). "The pleckstrin homology domain of Bruton tyrosine kinase interacts with protein kinase C." Proc Natl Acad Sci U S A **91**(19): 9175-9.

Ye, J., M. Cippitelli, et al. (1996). "The nuclear factor YY1 suppresses the human gamma interferon promoter through two mechanisms: inhibition of AP1 binding and activation of a silencer element." Mol Cell Biol **16**(9): 4744-53.

Ye, Q., R. M. Krug, et al. (2006). "The mechanism by which influenza A virus nucleoprotein forms oligomers and binds RNA." Nature **444**(7122): 1078-82.

Yoneyama, M., M. Kikuchi, et al. (2004). "The RNA helicase RIG-I has an essential function in double-stranded RNA-induced innate antiviral responses." Nat Immunol **5**(7): 730-7.

Young, H. A. (1996). "Regulation of interferon-gamma gene expression." J Interferon Cytokine Res **16**(8): 563-8.

Yuan, P., M. Bartlam, et al. (2009). "Crystal structure of an avian influenza polymerase PA(N) reveals an endonuclease active site." Nature **458**(7240): 909-13.

Yumerefendi, H., F. Tarendeau, et al. (2010). "ESPRIT: an automated, library-based method for mapping and soluble expression of protein domains from challenging targets." J Struct Biol **172**(1): 66-74.

Zhang, P. and J. E. Hinshaw (2001). "Three-dimensional reconstruction of dynamin in the constricted state." Nat Cell Biol **3**(10): 922-6.

Zhao, C., Z. Lou, et al. (2009). "Nucleoside monophosphate complex structures of the endonuclease domain from the influenza virus polymerase PA subunit reveal the substrate binding site inside the catalytic center." J Virol **83**(18): 9024-30.

Zheng, J., S. M. Cahill, et al. (1996). "Identification of the binding site for acidic phospholipids on the pH domain of dynamin: implications for stimulation of GTPase activity." J Mol Biol **255**(1): 14-21.

Zurcher, T., J. Pavlovic, et al. (1992). "Mechanism of human MxA protein action: variants with changed antiviral properties." EMBO J **11**(4): 1657-61.

7 APPENDIX

7.1 Additional crystallographic contacts

7.1.1 Other crystallographic contacts of the hsMxA stalk

Despite the close correlation of chain A and B of the hsMxA dimer in the asymmetric unit (see 4.2.2), the two chains have substantial differences at both tips of the stalk. These differences can be explained by the stabilizing effect of asymmetric crystallographic contacts other than the ones found in the described linear oligomer in the P1 crystal (see 4.2.4, Fig. 32A, 68A, B, C).

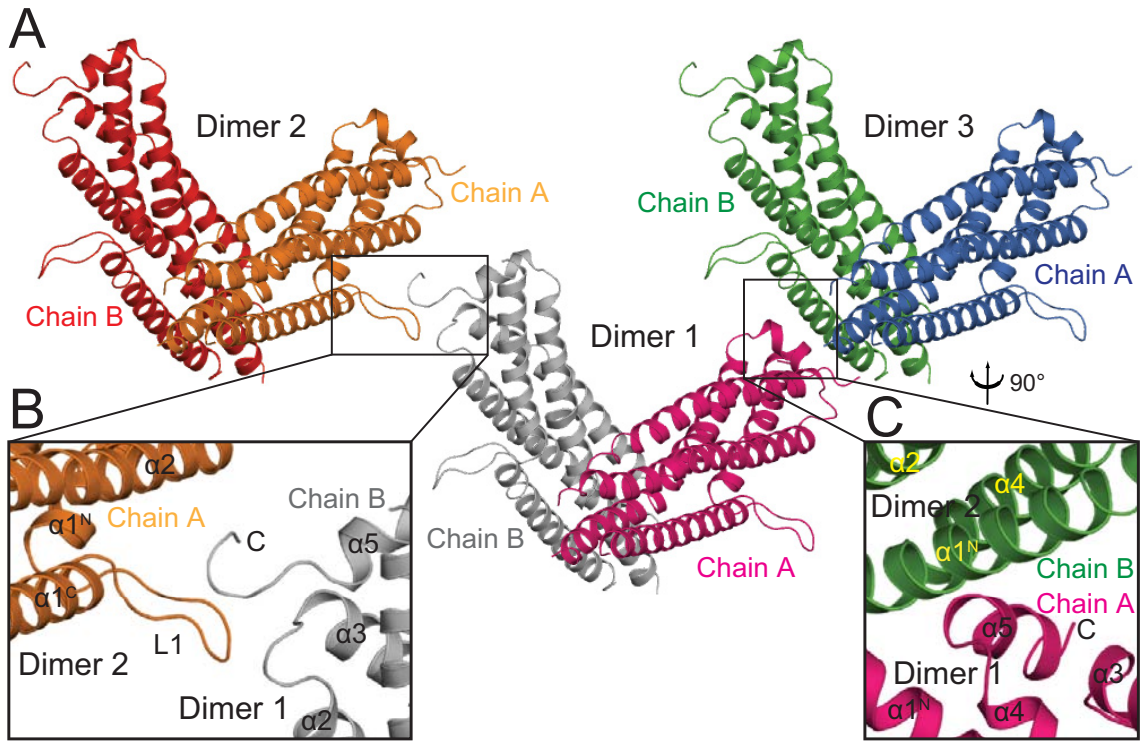

Figure 68. Crystal contacts stabilize interactions between dimers. A) Three dimers are shown with different colors for each chain. Chain A and B of dimer 1 are colored in pink and gray, of dimer 2 in orange and red, of dimer 3 in blue and green. B) Close-up of interaction site of chain B of dimer 1 and chain A of dimer 2. α5 of dimer 1 and L1 from dimer 2 make substantial contacts. C) Close-up interaction site for chain A of dimer 1 and chain B of dimer 3. In this case the α5 of dimer 1 associates with $\alpha1^N$ from dimer 3. All helices and L1 are labeled accordingly.

The C-terminus of the model is such an example. α5 is partially stabilized by hydrophobic contacts with α3 and α4; because of that, variations between the two

chains are found at the C-terminal extension of α5. The C-terminus of chain B (defined in 4.2.2) obtains extra stabilization from the L1 of the neighboring dimer chain A (Fig. 68B), which allowed modeling of three additional in this region and led to lower B-factors for certain residues in L1 of chain A. Similar effects are also observed for the tips of L2 (not shown).

7.1.2 Other crystallographic contacts of the three-domain hsMxA

In three-domain hsMxA crystals, no substantial contacts between G domains were observed (see 4.5.3, Fig. 55A, B) Instead, G domains are moderately stabilized by interaction with the stalks of the other two parallel monomers (Fig. 69). Interestingly, $L2^S$ from the stalk is also stabilized by this interaction, leading to clear corresponding election densities which are not present for the hsMxA stalk structure (see 4.2.3 and 4.5.2, Fig. 30B, 52B, 69).

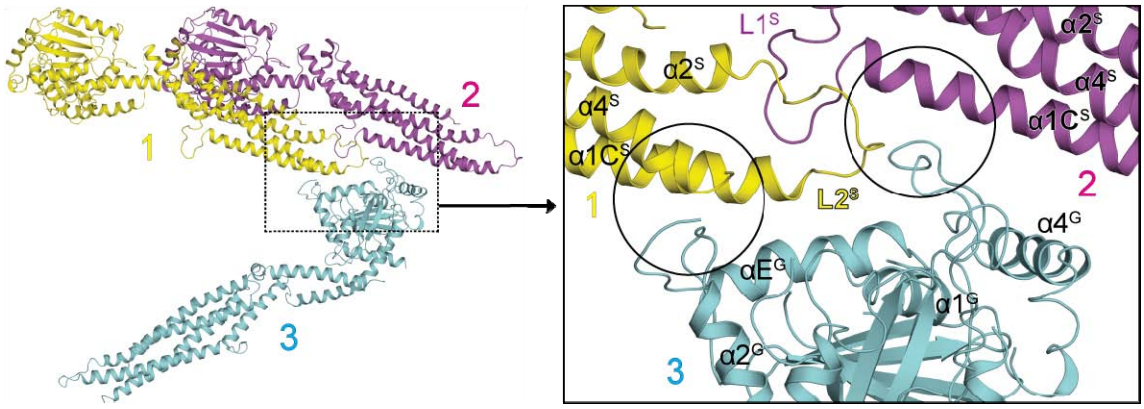

Figure 69. The crystallographic contacts between the G domain and the stalks. Three monomers exemplifying these contacts are individually colored in yellow, magenta, cyan and numbered accordingly. The interactions are shown in the left panel. In the right panel, the interaction sites are magnified and indicated by two circles. Secondary structural elements involved in the interactions are labeled accordingly.

Additionally, it is observed that the loops from the G domain of monomer 3 contacts $\alpha4^S$ from the stalk of monomer 1 (left circle), and $\alpha1C^S$ from the stalk of monomer 2 (Fig. 69).

7.2 The function for GTP hydrolysis assays

7.2.1 The motivation and the theoretical prerequisites of the function

The concentration-dependent GTPase activity stimulation effect was observed for both wt hsMxA and other mutants (see 4.3.4, Fig. 38). One speculation for this effect is that the increasing concentration leads to more chances for protein molecules to transiently interact with each other via the G domains, thereby resulting in more efficient GTP hydrolysis (see also 5.2.4 for relevant discussions). To generalize these data and testify the proposed mechanism, a mathematical function regarding the GTPase activity related to protein concentration was deduced and used for the fittings of the data for wt hsMxA and mutants shown in Fig. 38.

The deduction of the function is based on the following hypothesis:

i. Proteins must dimerize via the G domain interface to trigger the GTPase activity. At the particular moment when the GTP is being hydrolysed, the associating proteins are defined as dimers, and have their concentration termed accordingly as described in 7.2.2. This is supposed to applicable for both wt hsMxA and mutants.
ii. The intrinsic or the basal GTPase activity for both wt hsMxA and mutants, i.e. the hydrolysis of G domains that are not involved in the association, are negligible compared to the hydrolysis rate of the associated G domains.

7.2.2 The definitions of the parameters in the function

The definitions of the parameters used in the function are described as follows:

i. $[A_0]$: the initial protein concentration that is used in the experiment (µM).
ii. $[A_{dimer}]$: the concentration of the G domain mediated dimers (µM).
iii. $[A_{free}]$: the concentration of proteins with non-dimerizing G domains (µM).
iv. K_d: the modified dissociation constant for the G domains (µM).
v. V: the instant velocity of the GTP hydrolysis reaction (µM/min).
vi. V_{max}: the maximum of the velocity of the reaction (µM/min).
vii. k_{obs}: the absolute hydrolysis ability of the protein (min^{-1}).
viii. k_{obsmax}: the maximum of the absolute hydrolysis ability of the protein (min^{-1}).

One point to note is that all the proteins in the reaction system are classified either into dimers or free molecules. No matter what the oligomerization state of the molecule via the stalk region is, they are deemed as at same situations and having no

impact on the GTP hydrolysis. According to the 7.2.1, $[A_{dimer}]$ is solely responsible for the GTP hydrolysis, whereas $[A_{free}]$ is silent to the reaction. When all the protein molecules in reaction system are forming G domain mediated dimers, the maximum hydrolysis velocity is achieved.

7.2.3 The mathematical deduction of the function

Firstly, it is obvious that Equation 9 is intrinsically tenable:

$$[A_0] = 2 \cdot [A_{dimer}] + [A_{free}]$$

and it is easy to derive the Equation 10 therefrom:

$$[A_{free}] = [A_0] - 2 \cdot [A_{dimer}]$$

According to 7.2.1 and 7.2.2, Equation 11 is describing how the maximum velocity of GTP hydrolysis is achieved:

$$V = V_{max} \bullet \frac{2 \bullet [A_{dimer}]}{[A_0]}$$

It is obvious to see from Equation 11 that when $2 \cdot [A_{dimer}] = [A_0]$, the velocity will be at its maximum value. According to the definition, k_{obs} is related to V as in Equation 12:

$$k_{obs} = \frac{V}{[A_0]}$$

Based on Equation 11 and Equation 12, Equation 13 can be derived as:

$$k_{obs} = k_{obsmax} \bullet \frac{2 \bullet [A_{dimer}]}{[A_0]}$$

Moreover, the K_d in this case is defined as in Equation 14:

$$K_d = \frac{[A_{free}] \bullet [A_{free}]}{2 \bullet [A_{dimer}]}$$

According to Equation 10, the definition of K_d can be re-written as in Equation 15:

$$K_d = \frac{([A_0] - 2 \bullet [A_{dimer}]) \bullet ([A_0] - 2 \bullet [A_{dimer}])}{2 \bullet [A_{dimer}]} = \frac{([A_0] - 2 \bullet [A_{dimer}])^2}{2 \bullet [A_{dimer}]}$$

Equation 15 can be re-written as a quadratic formula about $[A_{dimer}]$ as in Equation 16:

$$[A_{dimer}]^2 - ([A_0] + \frac{K_d}{2}) \bullet [A_{dimer}] + \frac{[A_0]^2}{4} = 0$$

Therefore the $[A_{dimer}]$ can be solved from this formula and Equation 17 is derived

$$[A_{dimer}] = \frac{[A_0] + \frac{K_d}{2} - \sqrt{([A_0] + \frac{K_d}{2})^2 - [A_0]^2}}{2}$$

From Equation 17, it can be estimated that when $[A_0] \rightarrow \infty$, $[A_{dimer}] \rightarrow [A_0] / 2$, and clearly $(2 \bullet [A_{dimer}]) / [A_0] \rightarrow 1$, reflecting that increasing concentration of the protein promotes the formation of G domain mediated dimers, until this dimerization happens to every G domain. At this time, according to Equation 11 and Equation 13, the maximum hydrolysis rate is reached. This is mathematically consistent with the initial hypothesis. Equation 17 can be simplified to Equation 18:

$$[A_{dimer}] = \frac{[A_0] + \frac{K_d}{2} - \sqrt{K_d \bullet [A_0] + \frac{K_d^2}{4}}}{2}$$

Therefore, combining Equation 13, if $[A_{dimer}]$ is replaced, Equation 19 which is the fitting function used in the hydrolysis assay can be finally derived:

$$k_{obs} = k_{obsmax} \bullet \frac{[A_0] + \frac{K_d}{2} - \sqrt{K_d \bullet [A_0] + \frac{K_d^2}{4}}}{[A_0]}$$

A slightly simplified expression of Equation 19 can be presented in Equation 20, where the tendencies of the function are clearer when $[A_0]$ goes to extreme values:

$$k_{obs} = k_{obsmax} \bullet (1 + \frac{K_d}{2 \bullet [A_0]} - \sqrt{\frac{K_d}{2 \bullet [A_0]} + \frac{K_d^2}{4 \bullet [A_0]^2}})$$

The k_{obs} values can be measured at different given protein concentrations ($[A_0]$) in the experiments as described in 4.3.4. By plotting and fitting the sets of k_{obs} and $[A_0]$ data, the values of parameters k_{obsmax} and K_d can be obtained.

7.3 Animo acids abbreviations

Full-name	3-letter code	1-letter code
Alanine	Ala	A
Arginine	Arg	R
Asparagine	Asn	N
Aspartate (Aspartic acid)	Asp	D
Cysteine	Cys	C
Glutamate (Glutamic Acid)	Glu	E
Glutamine	Gln	Q
Glycine	Gly	G
Histidine	His	H
Isoleucine	Ile	I
Leucine	Leu	L
Lysine	Lys	K
Methionine	Met	M
Phenylalanine	Phe	F
Proline	Pro	P
Serine	Ser	S
Threonine	Thr	T
Tryptophan	Trp	W
Tyrosine	Tyr	Y
Valine	Val	V

In the thesis, the 1-letter codes are used for specifying individual amino acid residues in figures (e.g. M527), several consecutive amino acid residues (e.g. ^{440}YRGRE), and point mutations (e.g. M527D, YRGR440-443AAAA); the 3-letter codes are used for specifying individual amino acid residues in the text and figure legends (e.g. Met527).

ZUSAMMENFASSUNG

Das Interferon-induzierte MxA Protein ist ein zentraler Vermittler der angeborenen Immunität gegen gefährliche Pathogene, wie z.B. Influenzaviren. MxA gehört der Superfamilie der Dynamin GTPasen an, die eine essentielle Rolle in der Umformung von Membranen in der Zelle ausüben. Es wurde postuliert, dass die Mitteldomäne (MD) und die GTPase-Effektordomäne (GED) von dynamin-verwandten GTPasen einen Stiel ausbilden, der Oligomerisierung vermittelt und konformationelle Änderungen von der guaninbindenden (G-) Domäne auf die Zielstrukturen überträgt, aber der molekulare Aufbau des Stiels war nicht bekannt. Dadurch blieb der molekulare Mechanismus von MxA wie auch der gesamten Dynamin-Superfamilie unaufgeklärt.

Das Ziel meiner Arbeit war die strukturelle Charakterisierung des MxA Proteins und die Aufklärung des Mechanismus von MxA durch strukturbasierte funktionelle Studien. Im Rahmen dieser Arbeit wurde die Kristallstruktur des Stiels vom humanem MxA gelöst. Der Stiel hat eine Vier-Helix-Bündel Faltung und oligomerisiert im Kristall in einem Zigzag-Muster über drei separate Interaktionsflächen und eine Schleifenregion. Mutationen in diesen Interaktionsflächen beeinträchtigen die native Anordung in ein Tetramer, die Oligomerisierung, Membranbindung und die antivirale Aktivität von MxA. Basierend auf diesen Ergebnissen wurden strukturelle Modelle für Oligomerisierung und stimulierte GTP-Hydrolyse von MxA und Dynaminproteinen entwickelt, die mit vorherigen strukturellen Voraussagen über-einstimmen und funktionelle Bedeutung für alle Mitglieder der Dynamin Familie haben. Ausgehend von dieser Struktur wurde auch die Kristallstruktur des Voll-Länge MxA in der nukleotidfreien Form gelöst. Diese Struktur besteht aus drei Domänen, der G- domäne, dem Stiel und dem Bündelsignal-Element (BSE). Voll-Länge MxA oligomerisierte im Kristall über dieselben Interaktionsflächen wie der isolierte Stiel. Interaktionsstudien zwischen den einzelnen Domänen führten zu einem Modell des Mechanismus von Mx-Proteinen und der Dynaminsuperfamilie.

ACKNOWLEDGEMENT

I hereby would like to express my sincere gratitude to Prof. O. Daumke for the supervision, and the whole Daumke group for the support, especially S. Werner, (Dr.) D. Schwefel, S. Paeschke and A. Dick; Prof. U. Heinemann and the whole group; Prof. J. Behlke; Prof. O. Haller, Prof. G. Kochs and A. von der Malsburg from Universitätsklinikum Freiburg; Prof. A. Ziegler, Dr. Barbara Uchanska-Ziegler, C. S. Hee and the whole group from Charité; Dr. U. Müller and BESSY MX group; Ms. B. Cloos, Ms. S. Sibilak and Graduate Office at MDC; Embassy of the People's Republic of China in Germany; my family members and my friends. My thesis will not be accomplished without your kind help!

致谢:

感谢我的导师 O. Daumke 教授对我的指导，使我就读博士期间获益良多。也感谢我们组所有成员的关心和帮助，特别是技术员 S. Werner 女士，师兄 D. Schwefel (博士)，还有和我一起工作的 S. Paeschke 和 A. Dick。谢谢 U. Heinemann 教授及其研究组成员对我的支持，以及来自于 J. Behlke 教授 (MDC)，O. Haller 教授，G. Kochs 教授，A. von der Malsburg (弗莱堡大学) 以及 A. Ziegler 教授，C. S. Hee 及其研究组成员 (Charité 及柏林自由大学) 的合作。感谢柏林同步加速器的 U. Müller 博士及其工作组的技术支持。感谢 B. Cloos 女士，S. Sibilak 女士和研究生院的关心。感谢中国驻德国使馆教育处的帮助。感谢我的家人和朋友对我一直以来的鼓励与支持。

PUBLICATIONS

Hee CS*; **Gao S***; Loll B; Miller MM; Uchanska-Ziegler B; Daumke O; Ziegler A. (*Equal contribution)
Structure of a Classical MHC Class I Molecule That Binds "Non-classical" Ligands.
PLoS Biol. (2010) 8(12):e1000557

Haller O, **Gao S**, von der Malsburg A, Daumke O, Kochs G.
Dynamin-like MxA GTPase: Structural insights into oligomerization and implications for antiviral activity.
J Biol Chem. (2010) 285(37):28419-24

Daumke O, **Gao S**, von der Malsburg A, Haller O, Kochs G.
Structure of the MxA stalk elucidates the assembly of ring-like units of an antiviral module.
Small Gtpases. (2010) 1(1):62-4

Gao S; von der Malsburg A; Paeschke S; Behlke J; Haller O; Kochs G; Daumke O.
Structural basis of oligomerization in the stalk region of dynamin-like MxA.
Nature (2010) 465(7297):502-6

Hee CS*; **Gao S***; Miller MM; Goto RM; Ziegler A; Daumke O; Uchanska-Ziegler B. (*Equal contribution)
*Expression, purification and preliminary X-ray crystallographic analysis of the chicken MHC class I molecule YF1*7.1.*
Acta Crystallogr Sect F Struct Biol Cryst Commun. (2009) 65(Pt 4):422-25

ERKLÄRUNG

Ich versichere, daß ich die von mir vorgelegte Dissertation selbständig angefertigt, die benutzten Quellen und Hilfsmittel vollständig angegeben und die Stellen der Arbeit - einschließlich Tabellen, Karten und Abbildungen -, die anderen Werken im Wortlaut oder dem Sinn nach entnommen sind, in jedem Einzelfall als Entlehnung kenntlich gemacht habe; daß diese Dissertation noch keiner anderen Fakultät oder Universität zur Prüfung vorgelegen hat. Die Bestimmungen dieser Promotionsordnung sind mir bekannt. Die von mir vorgelegte Dissertation ist von Prof. Dr. O. Daumke und Prof. Dr. U. Heinemann betreut worden.

Berlin, Februar 2011

Song Gao